Detection and Measurement of Neutrino Interaction in a Cosmic Contaminated Environment

Inauguraldissertation
der Philosophisch-naturwissenschaftlichen Fakultät
der Universität Bern

vorgelegt von

Thomas Mettler

von Schwyz SZ

Leiter der Arbeit
Prof. Dr. M. Weber

Albert Einstein Centre for Fundamental Physics
Laboratory for High Energy Physics
Physics Institute

Detection and Measurement of Neutrino Interaction in a Cosmic Contaminated Environment

Inauguraldissertation
der Philosophisch-naturwissenschaftlichen Fakultät
der Universität Bern

vorgelegt von

Thomas Mettler

von Schwyz SZ

Leiter der Arbeit
Prof. Dr. M. Weber

Albert Einstein Centre for Fundamental Physics
Laboratory for High Energy Physics
Physics Institute

Von der Philosophisch-naturwissenschaftlichen Fakultät angenommen.

Bern, 17.05.2021

Der Dekan:
Prof. Dr. Z. Balogh

Abstract

Thanks to the good tracking and calorimetric capabilities of a Liquid Argon Time Projection Chamber (LArTPC), the Micro Booster Neutrino Experiment (MicroBooNE) provides precise measurements of ν-argon interactions at intermediate energies between $\mathcal{O}(100\,\mathrm{MeV})$ and $\mathcal{O}(2\,\mathrm{GeV})$. These are needed to improve our understanding of neutrino-nucleus interactions and to mitigate the uncertainties in the Monte Carlo simulation which needs to predict the signals of future experiments like Deep Underground Neutrino Experiment (DUNE) with great precision. A drawback of the LArTPC technology is the rather long charge readout in the of $\mathcal{O}(1\,\mathrm{ms})$. This means that a large amount of cosmic-induced particles will overlap the readout window for detectors placed on the earth's surface. To mitigate this problem in MicroBooNE, a Cosmic Ray Tagger (CRT) is built around the LArTPC. This work discusses the implementation of the CRT and shows its implication for a ν_μ Charged Current (CC) inclusive analysis. With a timing capability in the $\mathcal{O}(2\,\mathrm{ns})$ and a position resolution better than 2 cm, the CRT can reject cosmic background interactions without confinging the phase space of the selected neutrino interactions. On a newly developed ν_μ CC inclusive analysis using MicroBooNE data taken between December 2017 and Summer 2018, the cosmic contribution could be halved while maintaining the efficiency of 55.6% at the same level with respect to previous analysis. This leads to a higher signal purity of 72.0% and generally reduced uncertainties. The total flux-integrated inclusive cross section evaluated in this analysis is $\sigma = 0.770 \pm 0.005\ (\mathrm{stat})\ \pm 0.113\ (\mathrm{sys}) \cdot 10^{-38}\ \mathrm{cm}^2$. A double differential result in bins of muon momentum and the polar angle with respect to the beam direction is presented as a forward-folded event rate to avoid model dependence to a large extend. A comparison of the result to different neutrino generators commonly used results in χ^2-values larger than 10 per degrees of freedom for all models used here indicating a general discrepancy between models and data for neutrino-argon interactions. This work shows an effective way to further remove cosmic background interactions for a LArTPC on the earth surface using the CRT and presents a double differential cross-section analysis for further improvement of our understanding of ν-argon interactions.

Preface

With their very tiny cross-section, neutrino interactions are hard to measure. It took decades from the postulation to the first detection of these mysterious particles [1]. But after the final proof of neutrino oscillation in 2002 by Sudbury Neutrino Observatory (SNO) [2] and Super-Kamioka Nucleon Decay Experiment (KamiokaNDE) [3] and the measurement of all mass differences and mixing angles, measurements became progressively more precise. For more precise measurements more precise modeling of the interaction is necessary [4], therefore current experiments need to deliver data over a large variety of processes and target nucleons with minimal model dependence. Chapter 1 discusses this matter and motivates the work done here.

A short recap of the history of neutrinos and their detection is given in Chapter 2 up to the current and future experiments. Also, a small introduction to the formalism of neutrino oscillation is given along with how neutrino oscillation can be measured experimentally. The experimental aspects of a cross-section and the difficulties of its modeling are given before a description of the LArTPC technology which can provide detailed information of neutrino-argon cross-section over a large variety of different topologies.

Chapter 3 gives an overview of the MicroBooNE experiment [5]. Its data will be used for the analysis done in this work. First, the properties of the Booster Neutrino Beam (BNB) beam are discussed before the charge and the light readout systems of a LArTPC are described. The charge readout window of MicroBooNE's LArTPC is $\mathcal{O}(2\,\mathrm{ms})$ which introduces a lot of cosmic induced backgrounds, which motivates an additional system for cosmic rejection.

The CRT [6] for cosmic removal is discussed in Chapter 4. Here is my main involvement. I assembled the CRT modules in Bern, did the basic reconstruction to interaction points in 3D space and time including time calibration. While my contribution for the installation of the CRT at MicroBooNE was mainly on cabling and testing, I installed a test stand in the Short Baseline Neutrino Detector (SBND) detector pit. I wrote a large fraction of the reconstruction software which runs now in MicroBooNE by myself and ensured its stability over several years. I mitigated problems regarding timing either in the CRT system or the LArTPC ensuring the usability of the collected CRT data. With all the corrections applied I showed the performance of the CRT at MicroBooNE and the SBND test stand as well as introduce several possibilities for cosmic rejection at the end of this Chapter 4.

By applying a set of CRT rejection cuts along with others, I performed a ν_μ CC inclusive event selection. This is described in Chapter 5. Using MicroBooNE data from December 2017 to Summer 2018 where CRT data was available the first time, I

showed that the cosmic interactions are greatly reduced in a very model-independent way. The efficiency stays flat over a large phase space of the measurement when the CRT-cuts are introduced.

Finally I did a ν_μ CC inclusive cross-section analysis described in Chapter 6. Using the set of selection cuts developed in Chapter 5 I performed a double differential ν_μ CC inclusive cross-section measurement by comparing the expected event rate of different models to the actually measured one by using forward-folding. The representation of the result as an event rate brings several advantages while containing the same information as the commonly used cross-section normalized representation. Especially the clear separation of data points from simulation in the event rate representation minimize model dependences and allows the assignments of uncertainties only to simulated interactions.

Finally, the thesis is concluded in Chapter 7.

Contents

List of Figures

List of Tables

Acronyms

ADC Analogue-to-Digital Converter

ASIC Application-specific Integrated Circuit

BNB Booster Neutrino Beam

CC Charged Current

CP Charge conjugation Parity symmetry

CRT Cosmic Ray Tagger

CRTHit reconstructed Cosmic Ray Tagger event

DIS Deep Inelastic Scattering

DONUT Direct Observation of the Nu Tau

DUNE Deep Underground Neutrino Experiment

FEB Front-end Electronic Board

FNAL Fermi National Accelerator Laboratory

FPGA Field-Programmable Gate Array

FSI Final State Interaction

GENIE Global Analysis to Neutrino Scattering Data, a neutrino generator

GiBUU The Giessen BUU Project, a neutrino generator

GPS Global Positioning System

ICARUS Imaging Cosmic And Rare Underground Signals, the far detector in the SBN program

ICECUBE IceCube Neutrino Observatory

IBD Inverse Beta Decay

IMB Irvine-Michigan-Brookhaven

KamiokaNDE Kamioka Nucleon Decay Experiment

LAr Liquid Argon

LArTPC Liquid Argon Time Projection Chamber

LEE Low Energy Excess

LEP Large Electron-Positron Collider

MCS Multiple Coulomb Scattering

MEC Meson Exchange Current

MicroBooNE Micro Booster Neutrino Experiment

MiniBooNE Mini Booster Neutrino Experiment

MINOS Main injector neutrino oscillation search

MIP Minimum Ionizing Particle

NC Neutral Current

NEUT Neutrino interaction simulation library, a neutrino generator

NOνA NuMI Off-axis ν_{e} Appearance

NTP Network Time Protocol (server system time)

NuWro Wroclaw Neutrino Event Generator, a neutrino generator

Pandora Pandora Software Development Kit for pattern recognition

PCB Printed Circuit Board

PID Particle Identification

PMNS Pontecorvo-Maki-Nakagawa-Sakata

PMT PhotoMultiplier Tube

POT Protons On Target

PPS reference Pulse Per Second

QE Quasi-Elastic

R&D Research and Development

RES Resonant

RPA Random Phase Approximation

SBN Short Baseline Neutrino program at fermilab

SBND Short Baseline Neutrino Detector

SiPM Silicon PhotoMultiplier

SliceID reconstruction of a neutrino candidate slice by matching light and charge information

SM Standard Model

SNO Sudbury Neutrino Observatory

SVM Support Vector Machine

T0 time of an interaction

T2K Tokai To Kamioka

TPB TetraPhenyl Butadiene

VUV Vacuum Ultra-Violet

WLS WaveLength Shifter

1. Introduction

The study of neutrinos, first thought to be unmeasurable [7], has grown to a large field of research in particle physics. Since the discovery of neutrino oscillation in 2002 [2] and therefore evidence for physics beyond the Standard Model (SM), the experiments are no longer just looking for neutrino oscillations but also measure the neutrino mass differences and mixing angles with increasing precision. Nevertheless, several big questions regarding neutrinos remain unanswered. Although the mass of neutrinos is proven to be non-zero, the absolute masses remain unknown. Even the mass ordering is not known. Also, the question if there is Charge conjugation Parity symmetry (CP) violation in the lepton sector through neutrino interactions, which could help to explain the matter/antimatter asymmetry observed in our universe, is not answered [8]. Additionally, it is not known if a neutrino can act as its antiparticle, so if it is a purely Dirac particle or if it has also Majorana character. But, there is strong development for finding answers to these questions.

In 2012 the Daya Bay experiment measured the last and smallest mixing angle to be non zero enabling the possibility for CP violation through neutrino oscillation [9]. The Tokai To Kamioka (T2K) experiment excluded a CP violating phase to be zero with a 95% confidence level and further experiments like the Deep Underground Neutrino Experiment (DUNE) and the Hyper-Kamioka Nucleon Decay Experiment (KamiokaNDE) will help to answer these big questions about the CP violation and the mass ordering [10, 11]. Several anomalies are observed like the Mini Booster Neutrino Experiment (MiniBooNE) Low Energy Excess (LEE) measurement. Since there is some uncertainty on the origin of this anomaly, a dedicated measurement is on the way.

While the detectors are becoming heavier and more precise over a large phase space, a new problem arises: the precise modeling of neutrino interactions. Especially for energies between $\mathcal{O}(100\,\mathrm{MeV})$ to $\mathcal{O}(2\,\mathrm{GeV})$, where most of the accelerator based experiments do their research, the interaction cross-section is not known to better than $\sim$20% [4]. Nuclear effects and Final State Interaction (FSI) make the modeling hard and more data from experiments is needed to further improve the Monte Carlo simulations of the experiments.

The Micro Booster Neutrino Experiment (MicroBooNE) measures the neutrinos coming from the Booster Neutrino Beam (BNB) with a mean energy of around 800 MeV. The target nucleus is argon, a large nucleus that will also be used in the DUNE experiment. The Liquid Argon Time Projection Chamber (LArTPC) technology used in MicroBooNE can reconstruct charged tracks in great detail with calorimetric information that can separate Minimum Ionizing Particle (MIP) such as

muons from highly ionizing particles like protons. This allows a study of neutrino interactions over a large variety of topologies in great detail. Also, a LArTPC can separate photon-induced electromagnetic showers from electron-induced showers which is especially important for oscillation experiments.

A drawback of LArTPCs operating on the surface of the earth like MicroBooNE is the rather long charge readout window, $\mathcal{O}(2\,\mathrm{ms})$, during which a large amount of cosmic activity can enter the active detector volume. Even with advanced reconstruction tools like the Pandora Software Development Kit for pattern recognition (Pandora) [12] and good light to charge matching, cosmic interactions remained the leading background for a ν_μ Charged Current (CC) inclusive analysis [13] in MicroBooNE. To mitigate this cosmic background, a Cosmic Ray Tagger (CRT) was built to actively reject cosmic interaction occurring outside the time when the beam neutrinos are present in the detector. To do this effectively, the system needs to measure incoming muon tracks with a time resolution of $\mathcal{O}(1\,\mathrm{ns})$ and a spacial resolution of $\mathcal{O}(1\,\mathrm{cm})$ [14].

The CRT consists of multiple modules using plastic scintillator for the detection of thoroughgoing MIPs and was developed and assembled at the University of Bern [6]. The design is driven by the requirements for cosmic rejection and the fact that the tagger has to be installed around an already existing and operating experiment. The modules are read out by a Front-end Electronic Board (FEB) for each module. The information of all the FEBs has to be collected, calibrated, and reconstructed to an interaction point in 3D space with a corresponding timestamp. After the reconstruction, the actual performance of the system at the MicroBooNE detector can be evaluated. Eventual corrections have to be applied to reach the best performance, and a higher-level reconstruction that combines the CRT signals and the information of the LArTPC can be done.

With this additional information, LArTPC readouts can be rejected where the measured light signal probably comes from a tagged cosmic interaction either inside, or outside, the beam window. Depending on the signal one wants to analyze, different rejection possibilities are enabled using the CRT, from a complete veto of a LArTPC readout to more sophisticated rejection procedures considering also the topological and time information given by all the detector systems of MicroBooNE.

The performance is finally shown in a new ν_μ CC inclusive analysis using data where CRT information was available for the first time, from December 2017 to Summer 2018. A ν_μ CC selection can not rely on a cosmic rejection due to a specific neutrino interaction topology and is often used as an input for more exclusive channels. A variety of cosmic removal cuts using the CRT are discussed and most of them are implemented in the ν_μ CC analysis. Finally, a complete selection is developed which uses the information of all subsystems of MicroBooNE: light, charge, and CRT. The usage of the CRT allows less harsh cuts on the phase-space one wants to measure and reduces model dependences.

To use the data from this analysis for the improvement of neutrino models, the result is compared to a variety of commonly used neutrino generators. The data is

presented in a forward-folded way which avoids model dependence to a large extent. To provide maximal information while minimizing the workload for an external user, a script is provided with all the data which allows easy comparison of any event rate prediction to the data in this analysis, including all uncertainties.

2. Neutrinos and their Detection

This chapter gives an overview of the history of neutrinos and their detection. It covers the motivation for its initial postulation up to the modern problems we are hoping to solve using measurements of the properties of neutrino oscillations. A focus will be on the measurement techniques used for the different historical measurements as well as for current and future experiments. It concludes with an explanation of a LArTPC which is used as the detection technique for the experiment described in this work.

2.1. From first Hints to the Discovery of Neutrino Oscillation

In 1914, Chadwick measured the energy spectrum from the β-decay to be continuous [15]. A two-body decay would lead to a discrete spectrum and therefore this was a hint that another particle had to be involved in the β-decay. Motivated by this continuous energy spectrum, in 1930, Wolfgang Pauli proposed an additional neutral particle emerging from the nucleus [16]. A few years later, building on Pauli's proposal, Enrico Fermi developed the first theory of β-decay for nuclei [17]. After the discovery of the heavy neutron [18] not fitting the properties of the proposed particle, Fermi decided to call the new particle "neutrino". In the same year in 1934, Bethe and Peierls concluded that there is no practical way of measuring such a particle [7], but in 1946, Pontecorvo proposed a radiochemical method to measure neutrinos [19]. The reaction he proposed was:

$$\nu + {}^{37}\mathrm{Cl} \rightarrow e^- + {}^{37}\mathrm{Ar} \tag{2.1}$$

Pontecorvo's method allows the measurement of a small number of interactions inside a large volume (these are still the key points for neutrino detection today) by extracting the argon nuclei and measuring their radioactive decay. Pontecorvo also identified three intensive sources of neutrinos: the sun, nuclear reactors, and intense radioactive sources [19]. It took another 10 years until in 1956 Reines and Cowan reported the first measurement of neutrinos, or anti-neutrinos to be more precise, with a liquid scintillator loaded with $CdCl_2$ [1] through a process called Inverse Beta Decay (IBD). While Pontecorvo's proposed radiochemical method is sensitive to neutrinos, the IBD involves anti-neutrinos.

Shortly after the first measurement of neutrinos, Goldhaber could show that only left-handed neutrinos and right-handed anti-neutrinos are involved in the weak

interaction [20] and therefore parity is maximally violated in these processes. Up until then, only the electron neutrino was known, but in 1962 the second kind of neutrino, the muon neutrino was discovered [21]. As Pontecorvo pointed out, the sun should be a large source of neutrinos. These neutrinos were measured by Davis in 1968 [22] with the method suggested by Pontecorvo over 20 years earlier. The measured neutrino flux was always below the prediction of a detailed calculation by Bahcall called the 'Standard Solar Model', even after the improvement of both experiment and the model leading to the so-called 'solar neutrino problem' [23, 24].

The discovery of the tau lepton in 1976 by Perl [25] suggested that there should also be a third type of neutrino as there are for the other two leptons (electron and muon). The experiments KamiokaNDE [3] and Irvine-Michigan-Brookhaven (IMB) [26] measured neutrinos produced in the atmosphere in 1988 but their flux measurements were also below the expected rate. This was known as the atmospheric neutrino anomaly. At the Large Electron-Positron Collider (LEP) the total number of neutrino flavors was determined using the decay width of the Z-boson to be three which confirmed the expectations [27]. In 1998, the Super-KamiokaNDE experiment solved the atmospheric neutrino anomaly. By measuring an energy- and angle-dependent deficit of muon neutrinos produced in the atmosphere all around the globe, they provide strong evidence for neutrino flavor oscillations [3]. The propagation distance from the neutrino production in the atmosphere to the detection in Super-KamiokaNDE could be estimated by measuring the direction of the muon produced in the neutrino interaction inside the detector. In the year 2000, the Direct Observation of the Nu Tau (DONUT) experiment could observe the tau neutrino in a direct measurement [28] and therefore confirmed the prediction of three neutrino flavor states by LEP.

In 2002 the Sudbury Neutrino Observatory (SNO) solar neutrino experiment could finally bring the evidence for the solar ν_e disappearance by measuring the ν_e content coming from the sun through the so-called CC interaction as well as measuring the total ν flux through the Neutral Current (NC) interaction [2]. In a charge current interaction a $W^{\pm}$-boson is exchanged generating a charged lepton out of the neutrino according to its flavor. In a neutral current interaction a Z-boson is exchanged and the neutrino stays a neutrino but some of its momentum is transferred.

$$\text{Charged current interaction (CC)} = \nu_l + N \rightarrow l^- + X^+ \tag{2.2}$$

$$\text{Neutral current interaction (NC)} = \nu_x + X \rightarrow \nu_x' + X' \tag{2.3}$$

For a CC interaction to happen the neutrino needs to have enough energy to produce the charged lepton. Therefore one cannot measure the ν_τ and ν_μ content of the sun since these neutrinos are not energetic enough. With this interaction, the flavor of neutrinos can be measured while the neutral current interaction does not allow the determination of the flavor of the interacting neutrino. On the other hand, because no lepton has to be produced in the NC interaction low energy neutrinos of all kinds can be measured, enabling a measurement of the total flux.

So the solar, as well as the atmospheric neutrino problem, can be explained with neutrino oscillation. This was finally proven by the two experiments Super-KamiokaNDE and SNO which brought their leaders Kajita and McDonald the Noble Prize in 2015. This oscillation proves that neutrinos have a non-zero mass. Current experiments are focusing on precision measurements of the oscillation parameters as well as neutrino-nucleus cross-sections, and are discussed in the next section.

2.2. Neutrinos in the Standard Model

The SM describes the fundamental particles and their interactions. One can group these particles into fermions and bosons where the fermions have half-odd spins and the bosons have integer spin. The bosons in the SM are the force carriers that can couple to the fermions depending if they can feel that force. The photon carries the electric force, the gluon the strong force, and the $W^{\pm}$- and Z-boson carry the weak force. The Higgs-boson leads to the fact that some of the fundamental particles have a mass.

The fermions are grouped in quarks and leptons. All of these fermions feel the weak force and therefore couple to the $W^{\pm}$- and Z-boson. The quarks can couple to all forces, so additionally, they have a color charge coupling to gluons and an electric charge coupling to photons. The leptons do not feel the strong force but the charged leptons do couple to photons as well. This leaves us with the neutrinos which are electrically neutral and interact only via the weak force.

The fermions are grouped into three generations. The first generation contains the electron and the electron neutrino as well as the up and down quark. The second generation includes the muon, the muon neutrino, the charm, and the strange quark. Finally, the third generation in the SM contains the tau, the tau neutrino, and the top and bottom quark.

As seen in Section 2.1, the weak interaction can be split in CC and NC interactions. The first is described by the coupling by an electrically charged $W^{\pm}$-boson while the latter couples to an electrically neutral Z-boson. Figure 2.1 shows the fundamental Feynman graphs for these two kinds of interactions. The CC interaction also changes the electric charge by one unit. Therefore it changes a charged lepton to its neutrino of the same generation (as seen in Figure 2.1) or a positive electrically charged quark to a negative electrically charged quark. The electric charge of a quark is either +2/3 or -1/3. The interaction is also possible in the other direction (e.g neutrino to charged lepton or negative quark to positive).

The weak force was found to only act on left-handed particles and right-handed anti-particles. The handedness describes the projection of the spin of the particle to its momentum. For right-handed particles, the spin and the momentum point in the same direction. For left-handed particles, they look in the opposite direction. The SM describes the neutrinos as a massless particle, therefore the handedness is fixed since they will propagate always with the speed of light. Therefore, a neutrino

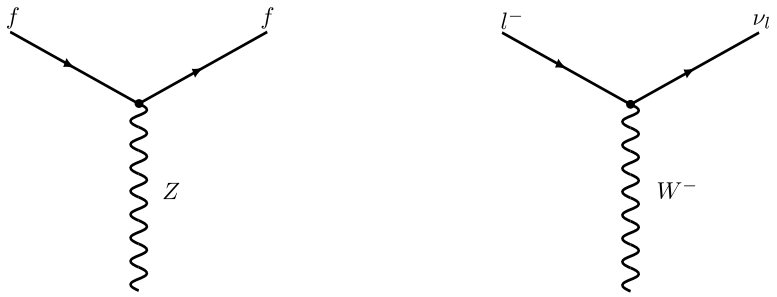

Figure 2.1.: The fundamental Feynman graphs for a NC interaction (left) and a CC interaction (right). The particle f can be any fermion. The CC interaction changes the charge of the fermion [29].

is always produced left-handed and an anti-neutrino right-handed. A right-handed neutrino would be sterile in the SM.

Since neutrinos are only weakly interacting they are not affected by large electric or magnetic fields. Also, they can pass through a large amount of matter without being absorbed. For this reason, they have a special role in astronomy. The first signal we can observe on earth coming from a supernova comes from a huge burst of neutrinos emitted during the explosion of a star. Additionally, the discovery of the cosmic microwave background radiation indicates that there should be similar background radiation of neutrinos emitted even before the photons in the cosmic microwave background. Therefore these particles can be subject to check astronomic or cosmological models.

The discovery of neutrino oscillation proved that the neutrinos have a non-zero mass. For this reason, the SM needs to be extended for including also the observed oscillation.

2.3. Current Experiments

Following the discovery of neutrino oscillation, neutrino experiments have made precise measurements of the oscillation parameters.

One to point out is the Daya Bay detector. This experiment was the first to finally prove that the mixing angle θ_{13} is not equal to zero [9]. Why is this important? By looking at the Pontecorvo-Maki-Nakagawa-Sakata (PMNS) matrix (see Eq. 2.8 in the next section) one sees that one needs all the mixing angles to be non-zero to observe a CP-violating phase δ_{CP}, which could help to explain the matter/antimatter difference as we have it in our universe today [30]. The other mixing angles θ_{12} and θ_{23} were already measured to be non-zero. The measured value of $\sin^2(2\theta_{13}) = 0.0856 \pm 0.0029$, updated in 2018 [31], is now measured enough away from zero to ensuring the possibility of measuring CP violation in the lepton sector. With all three mixing

angles non-zero, a CP-violating phase would manifest itself in different oscillation probabilities of neutrinos and anti-neutrinos.

Super-KamiokaNDE is a bigger version of the KamiokaNDE detector also located in the Kamioka Mine. It is also filled with water and equipped with PhotoMultiplier Tube (PMT)s but with a total mass of 50 kt. As mentioned, this experiment provided evidence of atmospheric-neutrino oscillations. The detector is now part of the T2K experiment where an artificial neutrino beam is going from Tokai to the Super-KamiokaNDE detector. With a baseline of 295 km and a mean neutrino energy of 600 MeV, it measures $\nu_\mu \rightarrow \nu_e$ oscillation of the initial ν_μ neutrino beam. This is called an appearance search and is sensitive to the θ_{13} angle. It also looks for ν_μ-disappearance and therefore provides very precise measurements of Δm^2_{23} and θ_{23}. But not only that, in 2017 the T2K experiment could exclude the CP-violating phase $\sin(\delta_{cp})$ to be equal to zero with a 95% confidence level [32]. They did this measurement by comparing the oscillation probabilities of neutrinos and anti-neutrinos. Also, the NuMI Off-axis ν_e Appearance (NOνA) experiment provided a measurement for the δ_{cp} value and there is an effort to combine the two results.

Several other experiments are active in the research of neutrino oscillation using neutrino beams produced using accelerators. Some using oxygen or hydrogen in water as a target (T2K [33]) or carbon in hydrocarbons (NOνA [34]). There are also different detectors using Liquid Argon (LAr) (Imaging Cosmic And Rare Underground Signals, the far detector in the SBN program (ICARUS), MicroBooNE, Short Baseline Neutrino Detector (SBND) [14]).

Different detectors looking for neutrino oscillation using reactor anti-neutrinos. These detectors often use liquid scintillator like Daya Bay [35], Double Chooz [36] or RENO [37]. Although these experiments have reached the end of their data-taking periods in the last few years, the analysis of the data taken is still ongoing. The KamLAND experiment which also measured reactor anti-neutrinos moved to a new phase and looks now for neutrino-less double-beta decay [38].

Several experiments in the field of neutrino astronomy are actively looking for a source of higher energy neutrino emission. Since neutrinos have a very small cross-section and do not interfere with electric or magnetic fields, they point directly back to an eventual source. They often use huge volume of water (antarctic ice in IceCube Neutrino Observatory (ICECUBE) [39], the Mediterranean Sea in ANTARES [40]) as a target material.

These experiments need a large target mass to counteract the very small cross-section of neutrinos. The physics goal of each experiment is slightly different, but all measure the neutrino properties like cross-section, energy, and direction to provide precise information about oscillation parameters or the origin of the measured neutrinos in the case of neutrino astronomy.

There is also a set of experiments that are looking for the absolute neutrino mass like KATRIN [41] or neutrino-less double beta decay like GERDA [42] or MAJORANA [43]. The current limit of neutrino-less double beta decay comes from Kamland-Zen [44] and a measurement by GERDA [45] and an eventual halflive needs to be

$>4 \cdot 10^{25}$ years, $>18 \cdot 10^{25}$ years respectively (at a 90% confidence level). These experiments measure the electron energy from a radioactive decay very precisely. The prove of neutrino-less double beta decay would prove that the neutrinos can act as their anti-particle. This would mean they are Majorana-particles and would not conserve the total lepton number as it is described in the SM.

The MiniBooNE experiment had reported an excess of low energy electron neutrinos [46]. Since MiniBooNE used a liquid scintillator combined with the Cherenkov cone of the outgoing lepton for the energy and flavor reconstruction of the neutrino, it could not distinguish single-photon events from the electron neutrino signal events. Therefore, there is an ongoing discussion of the source of this excess.

2.4. Oscillation Measurement

2.4.1. Oscillation Theory

By measuring ν_e in large detectors through CC interactions, it looked like a large amount of expected ν_e from the sun was missing. However, by measuring all neutrino flavors, the total solar-neutrino flux corresponds to the expected value [47]. The solution for this, and the atmospheric neutrino anomaly, was the theory of neutrino oscillation. Neutrino oscillation is a quantum mechanical phenomenon that can occur when the neutrinos have a non-vanishing rest mass. Such a mechanism cannot be described within the SM [48] where neutrinos are massless. In quantum mechanics, a particle is described by wave functions. For oscillation to occur, the flavor and the mass eigenstate must not coincide. The mechanism is similar to the mixing in the quark sector through the Cabibbo-Kobayashi-Maskawa matrix [49]. Let us assume that there are n orthogonal eigenstates of neutrinos. The weak (or flavor) eigenstates $|\nu_\alpha\rangle$ are connected to the mass eigenstates $|\nu_i\rangle$ via an unitary matrix U [48]:

$$|\nu_\alpha\rangle = \sum_i U_{\alpha i}|\nu_i\rangle \quad or \quad |\nu_i\rangle = \sum_\alpha U^\dagger_{\alpha i}|\nu_\alpha\rangle \tag{2.4}$$

with the matrix U. This matrix is in principle not limited by the number of mass and flavor eigenstates, which gives rise to light-sterile neutrinos. The propagation through time brings in the following time dependence:

$$|\nu(t)\rangle = \sum_i U_{\alpha i} e^{-iE_i t}|\nu_i\rangle = \sum_{i,\beta} U_{\alpha i}U^*_{\beta i} e^{-iE_i t}|\nu_\beta\rangle \tag{2.5}$$

And therefore the amplitude for a flavor change from α to β is given by:

$$A(\alpha \to \beta; t) = \langle \nu_\beta|\nu(t)\rangle = \sum_i U_{\alpha i}U^*_{\beta i} e^{-iE_i t} = \sum_i U_{\alpha i}U^*_{\beta i} e^{-i\frac{m_i^2}{2}\frac{L}{E}} \tag{2.6}$$

Here, the assumption is used that the neutrinos are relativistic and have a very small mass compared to the total energy, so L can substitute ct. The oscillation probabilities are then given by taking the absolute value squared of the amplitude.

$$P(\alpha \to \beta; t) = |A(\alpha \to \beta; t)|^2 = |\sum_i U_{\alpha i} U^*_{\beta i} e^{-i\frac{m_i^2}{2}\frac{L}{E}}|^2 = \sum_{i,j} U_{\alpha i} U^*_{\alpha j} U^*_{\beta i} U_{\beta j} e^{-i\frac{\Delta m_{ij}}{2}\frac{L}{E}} \tag{2.7}$$

with $\Delta m_{ij} = m_i^2 - m_j^2$. Therefore the oscillation probability is given by the mixing of the eigenstates and the mass differences.

For the three-flavor case this mixing matrix is known as the PMNS matrix and can be written in the following way:

$$U_{PMNS} = \begin{pmatrix} 1 & 0 & 0 \\ 0 & c\theta_{23} & s\theta_{23} \\ 0 & -s\theta_{23} & c\theta_{23} \end{pmatrix} \cdot \begin{pmatrix} c\theta_{13} & 0 & s\theta_{13}e^{i\delta} \\ 0 & 1 & 0 \\ -s\theta_{13}e^{-i\delta} & 0 & c\theta_{13} \end{pmatrix} \cdot \begin{pmatrix} c\theta_{12} & s\theta_{12} & 0 \\ -s\theta_{12} & c\theta_{12} & 0 \\ 0 & 0 & 1 \end{pmatrix} \cdot \begin{pmatrix} e^{i\frac{\alpha_1}{2}} & 0 & 0 \\ 0 & e^{i\frac{\alpha_2}{2}} & 0 \\ 0 & 0 & 1 \end{pmatrix} \tag{2.8}$$

Here s and c stand for the sine and the cosine of the mixing angle, δ is the CP-violating phase and α_i are two Majorana phases. While (as seen in Section 2.3) a sensitivity for δ could be reached in the T2K experiment, the Majorana phases do not affect the oscillation probability and will not be further discussed in this work.

The decay width of the Z-boson has shown that only three flavor eigenstates exist but this is only true under certain conditions. The neutrinos have to couple to the Z-boson and have to be lighter than half the Z mass. Therefore in principle light sterile neutrinos (non-weakly interacting) and neutrinos heavier than the Z-boson are allowed by the oscillation and the LEP constrains.

Since the oscillation probability (equation 2.7) depends on $\Delta m_{ij}^2 = (m_i^2 - m_j^2)$, the mass of a certain neutrino cannot be determined by measuring the oscillation, but their mass difference can be.

2.4.2. Measurement Technique

To measure oscillations in a neutrino beam, the beam can be sampled at a near detector, close to the source of the beam, and after some distance at a far detector. As one can see in equation 2.7, oscillation experiments need different ratios of the baseline (distance between near and far detectors) and the neutrino energy to be sensitive to specific values of the oscillation parameters. While the θ mixing angle sets the amplitude of the oscillation probability, the Δm^2 contributes to the oscillation frequency. Usually one chooses the distance between the production of the neutrinos and the detector and their energy spectrum and measures the oscillation parameters. Although the neutrino spectrum is constraint by the beam infrastructure. The oscillation parameters are then evaluated by comparing the expected event rate without oscillation with the measured event rate at specific energy and distance.

The oscillated event rate is given by:

$$R(x) = \Phi(E_\nu) \cdot \sigma(E_\nu, x) \cdot \epsilon(x) \cdot P(\nu_A \to \nu_B) \tag{2.9}$$

Where $R(x)$ is the event rate over some variable x at the detector, $\Phi(E_\nu)$ is the flux of neutrinos through the detector target material and $\sigma(E_\nu, x)$ is the cross section for this material. The $\epsilon(x)$ is the analysis specific efficiency and $P(\nu_A \to \nu_B)$ is the oscillation probability. Since all these inputs have large uncertainties assigned to them, a measurement of the oscillation parameters becomes hard. Additionally, the neutrinos have a certain energy spectrum over which the measured observables are averaged.

To measure the oscillation parameters as seen in Equation 2.7 one needs to know the distance from the neutrino production to the interaction point in the detector as well as the energy of the neutrino which has interacted. This is usually done with huge (since the cross-section is tiny) tracking or calorimetric detectors and the best would be having both capabilities.

The Daya Bay experiment measured the oscillation of $\overline{\nu_e}$ coming from different nuclear reactors a few kilometers away. The technique uses inverse beta decay, similar to the first successful neutrino detection by the experiment of Cowan and Reines. However, Daya Bay used a Gadolinium doped liquid scintillator as a target. The IBD $\overline{\nu_e} + p \to e^+ + n$ produces a positron and a neutron where the positron produces prompt light correlated to its initial energy and the neutron capture produces a delayed light pulse. The requirement of a prompt light flash and a delayed flash allows the rejection of background events and the amount of prompt light can be used to reconstruct the energy of the initial $\overline{\nu_e}$, which is needed for a precise oscillation measurement.

The Super-KamiokaNDE detector uses a 50 kt water tank which is equipped with large PMTs. The lepton, produced in the CC interaction of a neutrino originating from the atmosphere, propagates faster than the speed of light inside the water tank. This produces a Cherenkov light cone which gives information about the direction, energy, and flavor of the neutrino which has interacted in the detector. This technique works well as long as most of the energy goes into the lepton and starts to fail when a large number of daughter particles are produced, and is only partially sensitive to NC interactions. Super-KamiokaNDE also measures the neutrinos from an artificial neutrino beam in the T2K experiment. The initial properties of the neutrino beam are measured with a near detector to provide information on the unoscillated neutrino spectrum.

With an artificial neutrino beam, the energy and the baseline from the source to the detector can be chosen and can help reduce uncertainties in the measurement, but large uncertainties remain. The neutrino flux $\Phi(E_\nu)$ of a neutrino beam is usually not known better than 10% due to uncertainties of the production and reinteraction of the secondary particles (pion and kaons) within the beam target. The cross-section is only known with precision around $\sim$20% in the MeV to GeV region [4]. Therefore,

the neutrino interaction cross-section of the target nuclei of a specific detector has to be measured precisely to perform a precision oscillation measurement.

The $\epsilon(x)$ includes the uncertainties of the detector usually estimated from the detector simulation. On top of all of these uncertainties, there is statistical uncertainty due to the limited number of interactions measured as the neutrino cross-section is so low.

A way to reduce the flux-related uncertainties is to have a near and a far detector in an accelerator neutrino beam like the T2K experiment does with their near detector ND280 and Super-KamiokaNDE as the far. The cross-section uncertainties can be reduced by utilizing the same target material between near and far detectors, which allows for these uncertainties to be canceled out by looking at differences in the event rates measured between the near and the far detector. Also, with the implementation of a neutrino beamline, one can choose the energy spectrum and optimize the L/E ratio of Equation 2.7.

Nevertheless, as similar as the near and far detectors are, some uncertainty will always remain. Therefore, an oscillation experiment must also rely on an accurate simulation of the interactions between the target material and the beam neutrinos.

2.5. Future Experiments

There are two multi-kilotonne-scale long-baseline neutrino oscillation experiments planned for the near future. The goal of these experiments is not only to measure the oscillation parameters (mixing angle and mass difference) but also to measure the CP-violating phase [30]. Additionally, they have an astrophysical program and looking for proton decay signals.

Hyper-Kamiokande [11] will be an additional, even bigger successor of the Super-KamiokaNDE detector. It will use the same technology as the two KamiokaNDE experiments before. With an active mass of 217 kt, the water-Cherenkov detector will reach higher sensitivities and therefore be able to measure CP-violation and also probe the mass ordering.

The other big experiment will use LAr as a target. DUNE will use four 10 kt LArTPCs located at the Sanford Lab in South Dakota, 1300 km from the beam production point at Fermilab in Illinois [10]. DUNE will also measure the CP-violating phase as well as reveal the mass ordering of the neutrinos. DUNE has a goal of measuring the phase at 3 sigmas for 75% of its allowed values, which requires uncorrelated uncertainties (flux and cross-section) to be less than 2%.

As one can see in equation 2.9 several effects come into play by measuring neutrino oscillation. All of these have uncertainties associated with them. To constrain and keep the uncertainties as low as possible will be crucial for future experiments for reaching their physics goals.

One way to reduce uncertainties is the usage of a near detector. With a measurement of the neutrino flux before any oscillation, the flux uncertainties can be reduced. If

the near detector has the same target material some cross-section uncertainties can also be minimized. If the near detector has a similar detector response in general, also some detector-related uncertainties cancel when the oscillated spectrum at the far and unoscillated spectrum at the near detector is compared. But there is always some difference between the near and the far detector due to the spread of the neutrino beam as well as the far detector will see the oscillated spectrum.

Another way to reduce the flux uncertainties is the usage of a replica target in a test beam where the outgoing particles can be measured. This is done for example for the T2K experiment where the carbon target was put in front of the NA61 experiment [50].

The measurement of the neutrino beam at different angles of the beamline can also help to understand the beam content better. Such a concept is developed for the DUNE experiment.

While some uncertainties depend on the particular details of each experiment and cannot be constrained by outside neutrino measurements (like detector systematic and flux uncertainties), other experiments can help to bring down the cross-section uncertainties. For this reason, several experiments are measuring the neutrino cross-section on different targets and energies. For DUNE, the cross-section for neutrinos interaction on argon is of great importance. Without knowing the interactions between neutrinos and argon nuclei, precise modeling and therefore precise measurements will not be possible. For this reason, in the next section, it will be explained what a cross-section is and how it can be measured.

2.6. Cross Section Measurement

A cross-section gives the probability of a specific interaction and has units of area. It can be measured by simply counting the number of interactions $N^{\text{interaction}}$ for a given time-integrated flux ϕ and the number of target particles N_T, see Figure 2.2. The flux integrated total cross section can be calculated as follows:

$$\sigma = \frac{N^{\text{interaction}}}{\phi \cdot N_T} \tag{2.10}$$

For Equation 2.10 to have a unit of an area, the time-integrated flux ϕ is given as a number of particles per area. As one can also see, if the cross-section is very small, one needs a very big number of targets and a high flux to have multiple interactions.

Since most of the experiments will have some interactions which look like a signal but are not, one needs to subtract these as background events. Also, some signal events will be missed in a real measurement, therefore the cross section equation needs to be extended:

$$\sigma = \frac{N^{\text{data}} - N^{\text{bkgd}}}{\epsilon \cdot \phi \cdot N_T} \tag{2.11}$$

where N^{data} and N^{bkgd} are the number of selected data events and the estimated background events. The efficiency ϵ and the total flux ϕ as well as the total number of

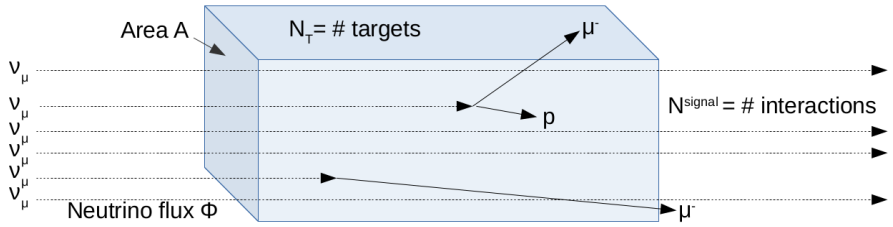

Figure 2.2.: Scheme of a cross section measurement. The cross section is given by the ratio of the number of interactions per number of targets and total flux as shown in equation 2.10.

nucleons N_T appear in the denominator. Therefore this method gives a cross-section per nucleon, so an average number of proton and neutrons in the target material has to be assumed. So the N^{data} is the total count of measured data events passing a given selection criteria while the number of background events is coming from the simulation and eventually partly from beam-off measurements. This can be calculated over a specific binned quantity X. The equation then looks like the following:

$$\left(\frac{d\sigma}{dX_\mu}\right)_i = \frac{N_i^{\text{data}} - N_i^{\text{bkgd}}}{\epsilon_i \phi \cdot N_T \cdot \left(\Delta X_\mu\right)_i} \tag{2.12}$$

Where $\left(\frac{d\sigma}{dX_\mu}\right)$ is the single differential cross-section and (ΔX_μ) is the bin width, both taken for the bin i. The cross-section is calculated for a certain interaction process.

From the interaction mechanism, one can distinguish different interaction modes. These modes are treated differently from the theoretical point of view. Since this work concentrate on CC ν_μ interactions, only these will be discussed:

- Quasi-Elastic (QE): $\nu_\mu + n \rightarrow \mu^- + p$
- Meson Exchange Current (MEC): $\nu_\mu + np \rightarrow \mu^- + pp$
- Resonant (RES): $\nu_\mu + p \rightarrow \mu^- + \Delta^{++} \rightarrow \mu^- + p + \pi^+$
- Deep Inelastic Scattering (DIS): $\nu_\mu + n \rightarrow \mu^- + X$

For the QE case, the initial neutrino energy can be calculated using only the information of the outgoing lepton, here the muon. This interaction mode dominates at low energies ($< 1\,\text{GeV}$). The energy reconstruction by looking only at the lepton is not possible for all other interaction modes. For these interactions, ideally, all particles involved in the interaction are taken into account to reconstruct the neutrino energy. There are difficulties to reconstruct particles like neutrons, therefore one often relies on simulation.

In the meson exchange current interaction, the neutrino interacts with a correlated proton-neutron pair resulting in two protons being emitted. As an additional proton is involved, the QE assumption is no longer valid. The same is true for the resonant interactions where one or more pions are produced. Additionally, this interaction mode is not easy to simulate due to several resonances for pion production. This mode becomes important for neutrino energies of a few GeV. The DIS interaction produces a lot of additional particles and becomes important at energies above a few GeV. Here, to reconstruct the neutrino energy, one also needs to take all outgoing particles into account.

An additional interaction is the coherent neutrino-nucleus scattering where the neutrino interacts with the whole nucleus. The charged lepton will be produced and a pion will be emitted. This interaction is significantly less probable and therefore not further discussed in this work.

The cross section for different interaction modes is shown in Figure 2.3.

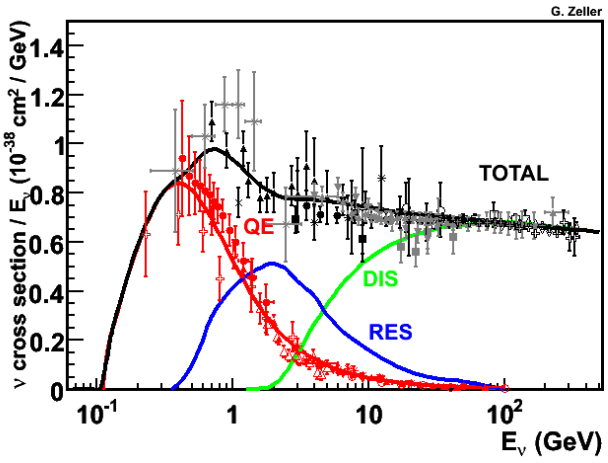

Figure 2.3.: Neutrino cross-section measurement for the different interaction modes QE, RES and DIS over a large range of neutrino energies [51]. Below 1 GeV more measurements are needed.

As one also can expect by looking at Figure 2.3, the differentiation between QE and the other channels can be made, while one cannot distinguish the other channels very easily. While this separation according to theoretical mechanisms makes sense, the experiments separate the interactions usually by the number and type of outgoing particles. This is what a detector can actually measure and still give an indication of which interaction channel mainly contributed to the measured signal. The measurement can again be used to improve the model of the neutrino cross-section and particle production during a neutrino interaction. But an additional difficulty comes into play by measuring the neutrino-nucleus cross-section. Several effects are happening inside a nucleus without a possibility to detect them, which can change the kinematics and the number of outgoing particles. For example, the

produced particles of the neutrino interaction can react inside the nucleus on their way out. These re-interactions of the daughter particles are called FSI. This and other effects are shown in Figure 2.4 and contribute to a large uncertainty to the cross-section.

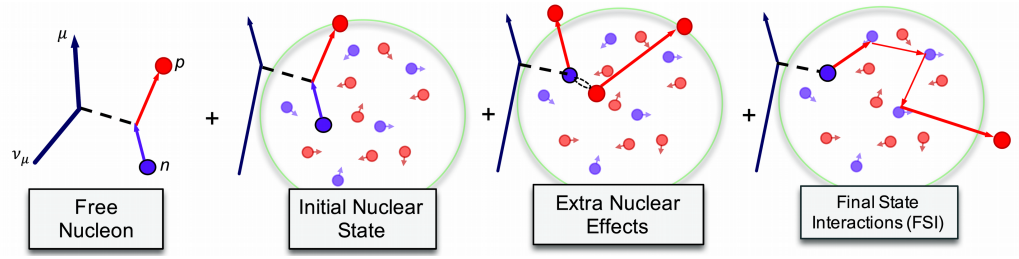

Figure 2.4.: Several effects happening inside the nucleus can change the kinematic distributions and the number of outgoing particles[1]. This makes the classification in interaction channels (QE, RES, MEC, and DIS) difficult as well as the reconstruction of the neutrino energy since only the outgoing particles can be measured.

These effects are less probable for small nuclei like hydrogen which makes the modeling of interaction simpler. The impact of these nuclear effects is not well measured for heavy nuclei, like argon. This is the reason why more precise cross-section measurements are needed for further experiments using heavy nucleons as a target to be successful.

While the liquid scintillator detectors do not have information about each track, there exists an uncertainty for the reconstruction of the neutrino properties depending on the number of particles leaving the nucleus. The same thing is true for Cherenkov detectors. They usually rely on the assumption that the neutrino undergoes a QE interaction when no additional particle to the lepton is detected. But, several effects can mimic the topology of this interaction. Therefore, a detection technique that can resolve all the tracks and their energy at the vertex is desirable. A LArTPC offers a possibility of resolving all the tracks while simultaneously providing calorimetric information. This technique is discussed in Section 2.7, but first I would like to discuss the modeling of neutrino interactions.

2.6.1. Modeling of Neutrino Interactions

The propagation of a particle through different detector media is done by the GEANT4 framework [52] and describes the signal which is produced by a certain particle in the active area of the detector. But the simulation of what particles to propagate has to be initially modeled by a generator. This generator uses theoretical models and predicts the outgoing particles for different interactions. It has to predict all the

[1]Figure by Patrick Stowell

particles leaving the nucleus for all interactions that can occur in the detector, not only for the targeted signal process but also for all kinds of backgrounds. Since we are interested in neutrino interactions, we will have a closer look at a few neutrino event generators. Of course, there exist other generators for other types of interactions.

Generally, the The Giessen BUU Project, a neutrino generator (GiBUU) and Wroclaw Neutrino Event Generator, a neutrino generator (NuWro) event generators are more theoretically oriented while the Neutrino interaction simulation library, a neutrino generator (NEUT) and Global Analysis to Neutrino Scattering Data, a neutrino generator (GENIE) generators are developed by experimentalists [53]. GiBUU differs mainly by the treatment of nuclear transport. A different set of models for different effects can be used within each generator. The models used are explained briefly for each generator as the measurement will be compared to these models later.

The models mentioned are stated here for completeness of the description without further details. More information about these can be found under the given citations.

GENIE V2 and V3

GENIE [54] v2.12.2 was mainly used for early analyses of MicroBooNE and is therefore listed here and also used for a comparison of the result [55]. The CC QE interaction use the Llewellyn-Smith model with the BBA05 elastic form factors [56]. The axial mass M_A is set to 0.99 GeV/c^2 [57]. The RES events are modeled using the Rein-Sehgal model including 16 resonances [58]. The DIS interactions are modeled by the Bodek-Yang model[59]. The transition region is treated by an extrapolation of the Bodek-Yang model. The nuclear modeling is done with a Fermi gas model with a high-momentum tail modeled by Bodek-Richie. The FSI interactions are modeled by INTRANUKE [57].

The Genie Version which is used for current analysis in MicroBooNE is the version v3.0.6 G18_10a_02_11a which includes tuning based on data from T2K [55]. The Local Fermi Gas is used for the nuclear model using the implementation of Nieves for the CC QE and CC multinucleon processes [57, 60]. The RES interactions using the Berger-Sehgal model, the DIS interactions make use of the Bodek-Yang model. For hadronization, the AGKY model is used and the intranuclear transport is simulated using the INTRANUKE hA 2018. This version is expected to agree better for neutrino interactions at the energies of MicroBooNE and is used for the simulation in the MicroBooNE experiment.

NEUT

This generator is developed for the KamiokaNDE detectors and is mainly used now in the T2K and Super-KamiokaNDE experiments [61]. Here the version 5.4.0.1 will be discussed [62]. This version uses the models of Llewellyn-Smith and Nieves treatment for the QE interactions [56, 60]. The nuclear model is the Local Fermi Gas. For coherent pion production, the model of Rein-Seghal is used and for the RES the model of Graczyk-Sobczyk is used [58, 63]. The DIS events are modeled by Bodek-Yang

[59]. A Random Phase Approximation (RPA) correction is applied to the CC QE interactions. The RPA describes the excitations in a many-body system which is the nucleus of the target material in this case [64].

NuWro

Models implemented in NuWro [65] were often adopted by GENIE and NEUT. The QE interactions are modeled according to the calculations of Llewellyn Smith with options for the vector form factors. Spectral functions are used for several nuclei. A spectral function describes the energy and momentum distributions of the nucleons in nuclei. The RES events are modeled by Jones and Scadron [66]. The pion production is newly implemented base on the work in [67]. The Bodek-Yang model is used to describe the DIS interactions [59]. The nuclear cascade used the work described in [68] and based on the Metropolis at al. algorithm [69]. FSI interactions are calculated using the work in [70]. Also, a phenomenological MEC model is used due to large discrepancies between different models [71].

GiBUU

GiBUU [72] can be used for the simulation of a variety of nuclear interactions including different scattering processes including neutrino scattering. Over a wide range of energies, a consistent physics model is used. The initial state distribution for momenta of the nucleons inside the nucleus is modeled with a local Fermi gas. The QE interactions make use of the impulse approximation which assumes the nucleons acting as free particles including Pauli-blocking [73].Measurements from electron-scattering experiments are used for the estimation of the MEC contribution as well as RPA. 13 resonances are used for the calculation of pion production but coherent pion production is not included. At a momentum transfer of more than 2 GeV, the DIS model takes over from the pion production. Final state particles are propagated simultaneously allowing interactions between them, as well as their decays and two- and three-body reactions. This sophisticated transport model is a strength of this generator.

2.7. Liquid Argon Time Projection Chamber

A neutrino detector needs a high target mass and the ability to reconstruct all particles emerging from the target nucleus including their energy to separate the contribution of the different interaction channels. Another crucial thing for most oscillation experiments is the separation of ν_e and ν_μ. While the ν_μ manifests itself by a muon track coming from the vertex, the ν_e leaves an electron in the final state which usually produces not a track but an electro-magnetic shower.

A LArTPC can provide all these measurements and can even distinguish electro-magnetic showers induced by an electron from the one initialized by a photon, see

Figure 2.8. More on that will follow, but first, a discussion of how particles interact in LArTPC , and how they are detected is presented.

Like most particle detectors a LArTPC can only measure charged particles propagating through the detector. They lose energy through ionization while propagating through the argon as described by the Bethe-Bloch equation:

$$\frac{dE}{dx} = -4\pi N_A r_e^2 m_e c^2 z^2 \frac{Z}{A}\frac{1}{\beta^2}\left[\frac{1}{2}ln\frac{2m_e c^2\gamma^2\beta^2}{I^2}T_{max} - \beta^2 - \frac{\delta}{2}\right] \tag{2.13}$$

where N_A is the Avogadro number, r_e and m_e are the classical electron radius, the electron mass respectively. z is the charge of the particle and Z is the atomic number of the medium the ionizing particle is propagation through and A its mass number. T_{max} is the maximal energy transfer per collision and δ is a correction due to polarization. The factors $\beta = \frac{v}{c}$ and $\gamma = \frac{E}{m_0 c^2}$ are used since the equation describes relativistic particles. And finally, $I = 16Z^{0.9}eV$ is the approximated mean excitation energy for material with $Z > 1$.

In the case where $\beta\gamma$ are $\mathcal{O}(1)$, the energy loss is minimal. So a charged particle with a $\beta\gamma$-factor around one is called Minimum Ionizing Particle (MIP).

The neutrino itself does not leave any signal in the LAr. But, when it eventually undergoes an interaction it can produce charged particles which then have enough momentum to propagate through the argon and leave a trace of ionized argon atoms and free electrons.

In a LArTPC, an electric field ($\mathcal{O}\left(100\,\mathrm{V\,cm^{-1}}\right)$) is applied which then cause the electrons and ions to drift in opposite direction. Since argon is a noble element, all the electrons in each shell are full so the ionization electrons can drift in the electric field without being reabsorbed until they reach the anode. While the electrons drift with a velocity around $1\,\mathrm{mm\,\mu s^{-1}}$, the argon ions drift around a million times slower. Therefore the charge readout is placed on the anode, where it is realized as a plane that can measure the position and time of the drifting electrons as induced or collected charge using sensitive wires or pixels.

In the LArTPC indicated in Figure 2.5 the readout is realized with three different wire planes, two induction and one collection plane where the electrons finally are absorbed. With the arrival time of the electrons and their 2D position on the wire planes, a 3D image of all the charged particle tracks can be reconstructed.

LAr is also a great scintillator. During the propagation of the charged particles through the argon, between 10^4 to 10^5 photons in the Vacuum Ultra-Violet (VUV) spectrum are emitted per centimeter. These photons can be measured by a light collection system and the time difference between the light signal and the arrival time of the electrons gives the absolute position in direction of the electric field, the projection of the Time Projection Chamber (TPC). The properties of argon relevant for LArTPC are given in the following Table 2.1.

With the numbers given in Table 2.1, one can see that LAr is pretty much transparent for its own scintillation light. The prompt component of the light

Specification	value
Atomic number	18
Molar mass	$(39.948 \pm 0.001)\,\mathrm{g\,mol^{-1}}$
Boiling point (BP)	87.26 K
Melting point (MP)	$(83.8 \pm 0.3)\,\mathrm{K}$
Density at BP	$(1396 \pm 1)\,\mathrm{kg/m^3}$
Dielectric constant	1.505 ± 0.003
Index of refraction (at 128 nm)	1.38
Rayleigh scattering (at 128 nm)	95 cm
Photon absorption length (for > 128 nm)	> 200 cm
W-value for ionization	(23.6 ± 0.3) eV / pair
W-value for scintillation	(19.5 ± 1.0) eV / photon
Molière radius	10.0 cm
Radiation length	14.0 cm
Minimum specific energy loss	$2.12\,\mathrm{MeV\,cm^{-1}}$
Scintillation emission peak	(128 ± 10) nm
Decay time	(6 ± 2) ns, (1590 ± 100) ns
electron drift velocity (at $500\,\mathrm{V\,cm^{-1}}$)	$(1.60 \pm 0.02)\,\mathrm{mm\,\mu s^{-1}}$
electron mobility	$(518 \pm 2)\,\mathrm{cm^2\,V^{-1}\,s^{-1}}$
Ar^+ drift velocity	$(8.0 \pm 0.4) \times 10^{-6}\,\mathrm{mm\,\mu s^{-1}}$
Ar^+ mobility	$6.0 \times 10^{-4}\,\mathrm{cm^2\,V^{-1}\,s^{-1}}$

Table 2.1.: Properties of argon [74].

is emitted within nanoseconds. The exact numbers of ionization electrons and scintillation photons depend on the magnitude of the electric field [75].

The electric wave-forms which are measured in the wires are indicated in Figure 2.6. The amplitude gives information of how many electrons were initially produced during the ionization process and therefore can be used for particle identification (PID) and the calculation of their energy and momentum. For these reasons a LArTPC is an excellent tracker as well as a calorimeter. So to say it can measure the charged particle tracks as well as the energy they have deposited in the detector.

As seen in Figure 2.7 the amount of energy deposited per length can be used for Particle Identification (PID). The scattering behavior can be used for the reconstruction of the momentum as one can see later in this section. For a particle stopping in the active volume of the detector, one can compare the energy loss at a certain point from the stopping position. By summing all the deposited energy from the stopping point to that certain point one can estimate the momentum. Also, the energy deposition before a particle stops depends on the type of particle and therefore allows particle identification.

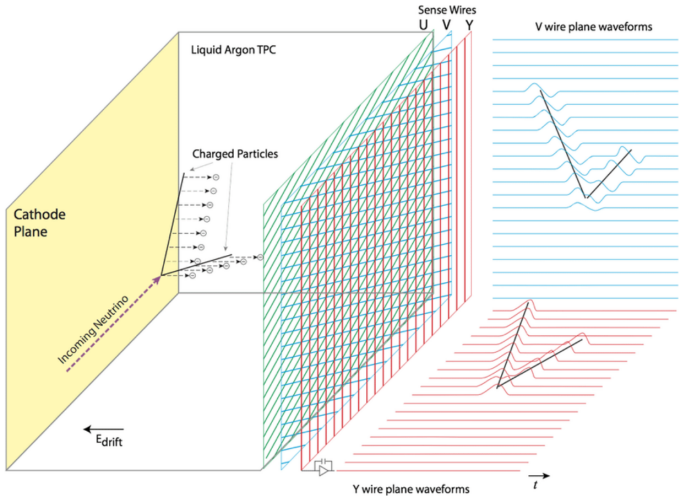

Figure 2.5.: The working principle of a wire LArTPC. The electrons from the ionized material inside the chamber are drift to the anode and readout by wire planes [76]. The 2D signals of each wire plane can be combined to a 3D signal of the interaction.

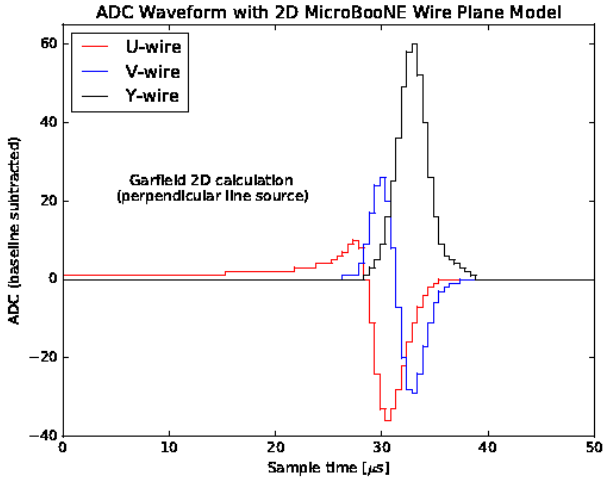

Figure 2.6.: The drifting electrons either induce a bipolar signal at the induction planes or a unipolar signal at the collection plane. The signal strength depends on the deposited energy by the charged particle which ionized the argon nucleons.

For a particle that starts and stops in the detector, one can calculate its total energy loss and therefore momentum by summing up all the energy deposited from the start to the end of the track. This is called momentum by range. As one can see in Figure 2.7, the energy loss increases dramatically below a certain momentum

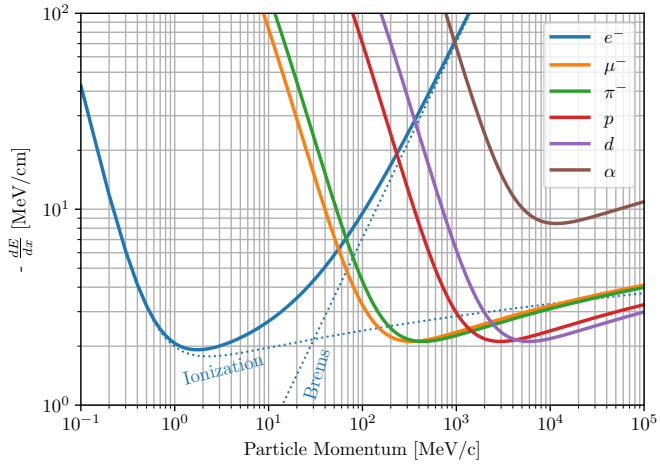

Figure 2.7.: Depending on the momentum and type of a particle it loses a different amount of energy while propagating through the LAr [29]. The energy deposition is described by the Bethe-Bloch equation explained at 2.13. This information can be used for particle identification of the reconstructed tracks.

leading to a peak of energy deposition at the end of each track. This is called the Bragg peak and can also be used to identify the start or endpoint of a track.

Since most experiments measure neutrinos of $\mathcal{O}(100\,\text{MeV})$ to $\mathcal{O}(1\,\text{GeV})$ the tracks in LAr are already tens of centimeters to several meters long, assuming they act as a MIP with an energy loss of $2.12\,\text{MeV}\,\text{cm}^{-1}$ [77]. For this reason, there is a substantial likelihood that the track will exit the detector, thus preventing a calorimetric or range-based momentum estimate. Such tracks can be reconstructed using the following behavior. The charged particle will undergo Coulomb scattering on its path through the detector multiple times, this is called Multiple Coulomb Scattering (MCS). The scattering angle depends on the momentum of the particle, therefore taking this information into account the momentum can be reconstructed even when the particle exits the active volume. The RMS width of the scattering angles is given by the Highland formula [78, 79]:

$$\Theta_{RMS} = \frac{13.6\,\text{MeV}}{\beta cp} \cdot z \cdot \sqrt{x/X_0}\,[1 + 0.038\log(x/X_0)] \tag{2.14}$$

where p is the momentum and X_0 is the radiation length, x stands for the distance through the particle has propagated and z Is the charge of the particle, so equal to one in the case of a muon. Because of this momentum dependency, the scattering behavior can be used to calculate the momentum for particles that exit the active volume of the detector

One other key feature of a LArTPC is that it can also reconstruct electromagnetic showers in great detail. An electromagnetic shower is a cascade made out of photons

and electrons initiated either by an electron or a photon above a certain energy. For the electron case, the electron loses energy, in addition to the ionization process, via the bremsstrahlung process where photons are produced. These photons then produce electron-positron pairs which again lose energy through bremsstrahlung. Like this, a cascade made out of photons, electrons, and positrons is produced until the photons have insufficient energy for further pair-production or the energy loss through bremsstrahlung becomes sub-dominant for the electrons.

While for photons above 10 MeV pair-production is the dominant effect, photons around 1 MeV will loos energy via Compton-scattering [29]. In this process, the photon only loses a part of its energy in the scattering process.

In the TPC only the energy depositions of the electrons and positrons are visible. By looking at the start of the shower, a TPC can distinguish the photon-induced showers from the showers induced by an electron or positron. Since the photon does not leave a signal in the detector until it produces an electron-positron pair, the start of such a shower consists out of two overlapping ionizing tracks while an electron or a positron already makes a single track by itself. Figure 2.8 shows a measurement of the electron/photon separation for a LArTPC , the two distributions are clearly separated.

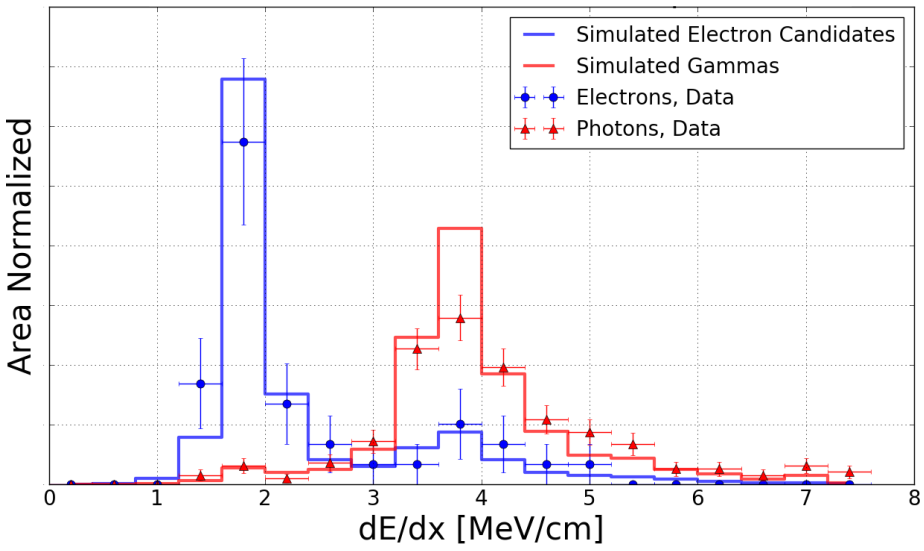

Figure 2.8.: A big advantage of the TPC is the good separation of electron vs. gamma induced showers. Here a measurement of ArgonNeuT is shown [80].

This is a very important ability for detectors that are looking for ν_e appearance in a ν_μ beam which is usually done in current experiments and will be done also in future experiments. Especially at low energies ($\mathcal{O}(100\,\text{MeV})$) the probability to detect the proton track of a charged current interaction is low and therefore the only signal of an ν_e is a single electron producing an electromagnetic shower. Exactly this topology can be mimic by a single photon. A photon can propagate through

a detector without undergoing any interaction for several centimeters until it also produces an electromagnetic shower. Photons can be produced by a π^0 decay which can be produced by a NC neutrino interaction where no lepton is produced. Such an interaction is a not fully reducible background for many experiments which do not have this good photon/electron separation.

The good electron-photon shower separation and the detailed 3D information including calorimetric information make a LArTPC an excellent detector for neutrino measurements. One does not rely on the kinematics of the outgoing lepton as many other detectors do, since it can reconstruct the neutrino energy taking all tracks and showers into account. The disadvantage of this technology is that the argon atom has 40 nucleons inside. This enables nuclear effects that are not well known and therefore difficult to correctly simulate. Another disadvantage is that charge readout in these detectors is rather slow. The duration of a read-out ends up in $\mathcal{O}(1\,\mathrm{ms})$ for the 3D charge signal. During this time background interactions can occur which makes the charge to light signal matching prone to errors.

3. The MicroBooNE Experiment

The MicroBooNE experiment is a LArTPC placed in the BNB at the Fermi National Accelerator Laboratory (FNAL) near Chicago in the US. It is one out of three LArTPC detectors in the Short Baseline Neutrino program at fermilab (SBN) program placed 470 m after the proton target for neutrino production [5, 81]. Besides neutrino oscillation studies in the SBN program, the main physics goal of MicroBooNE is the investigation of the LEE measured by the MiniBooNE collaboration in the same beamline as well as neutrino-argon cross-section measurements. The experience gained building and operating such a large LArTPC detector also supports the Research and Development (R&D) program of future LArTPC experiments like DUNE [5].

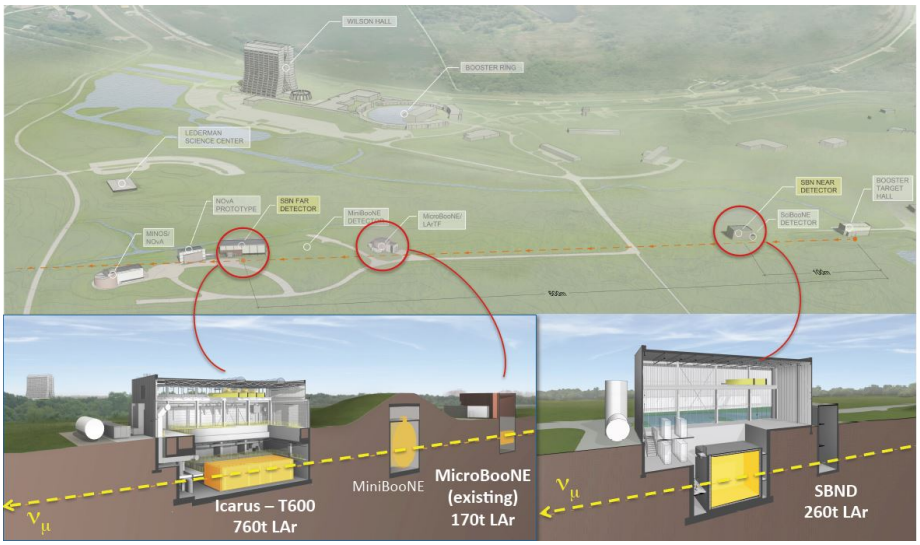

Figure 3.1.: MicroBooNE is one of the three detectors of the SBN program at FNAL near Chicago, USA [14]. These LArTPCs will measure the neutrinos of the BNB beamline.

In this chapter, a description of the neutrino beam is given to understand what the detector wants to measure. Then, the sub-components of the MicroBooNE detector are described as well as specific advantages and disadvantages of the detector system in MicroBooNE. Finally, the cosmic background that the detector will see is described.

3.1. Booster Neutrino Beam

The MicroBooNE experiment is located in the BNB at FNAL. The neutrinos are produced by directing a 8 GeV proton beam on a beryllium target. The protons interact with the nucleons in the target and produce secondary particles, mainly pions and kaons. These are then focused in a 50 meter long decay pipe using a magnetic horn where they finally decay. Charged pions decay to nearly 100% into a muon and its neutrino. While the muons are absorbed in the dirt after the decay pipe, the neutrinos will propagate through the downstream detectors of the SBN program.

By choosing the direction of the focusing field, either positively charged or negative charged pions and kaons can be guided into the decay pipe leading to a neutrino or anti-neutrino beam, respectively. In the neutrino configuration, a beam of mainly muon neutrinos is produced with only a small fraction of muon anti-neutrinos and even fewer electron neutrinos. The composition of the neutrino beam can be seen in Figure 3.2. This composition becomes important when an experiment is looking for oscillation of the neutrino flavors when the appearance signal is also part of the beam composition. Both, muon neutrino disappearance, as well as electron neutrino appearance searches, can be done with the BNB beam. In a disappearance search, one is looking for missing muon neutrino interactions, while in an appearance search one is looking for the appearance of electron neutrino interaction in an initial muon neutrino beam. The neutrino beam is provided in the form of a spill with an average

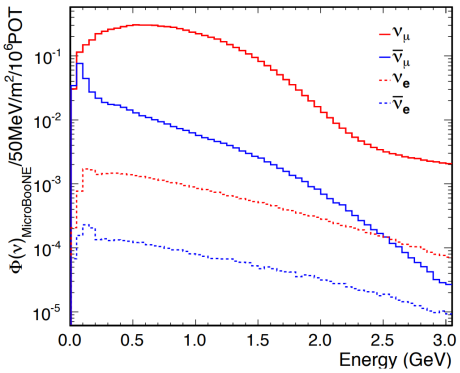

Figure 3.2.: The composition of the Booster Neutrino beam at FNAL. Mainly muon neutrinos are produces with a small contamination of muon antineutrinos and even less electron neutrinos [14].

frequency of 5 Hz. A spill consists of neutrinos produced by around 4×10^{12} Protons On Target (POT) and is structured in 84 bunches separated by 19 ns and with a width around 2 ns leading to a total beam duration of 1.6 µs, see Figure 3.3.

The mean neutrino energy is around 800 MeV. This means that all interaction channels (QE, MEC, RES, and DIS) will occur in neutrino interactions while the QE interactions will be dominant towards lower energies. The average muon track of a

CC muon neutrino interaction will have a momentum of several hundred MeV and therefore propagate several meters in the LAr of a LArTPC detector.

MicroBooNE utilizes [82] the framework for the beam simulation as well as for the calculation of the uncertainties developed by the MiniBooNE collaboration [83]. The prediction is based on a GEANT4 simulation [52] as well as data from the HARP experiment.

The timing of the beam becomes important when one wants to discriminate between beam events and non-beam-related interactions. The intensity of this beam is such that only around one neutrino event every 600 spills will interact in the LAr of the MicroBooNE detector [84]. Therefore, most events taken contain only signal from cosmic interactions. A minimum light level in the detector when the neutrinos pass through the detector is required to store the data from the event. This is done to minimize the amount of data taken without a neutrino interaction in the LAr.

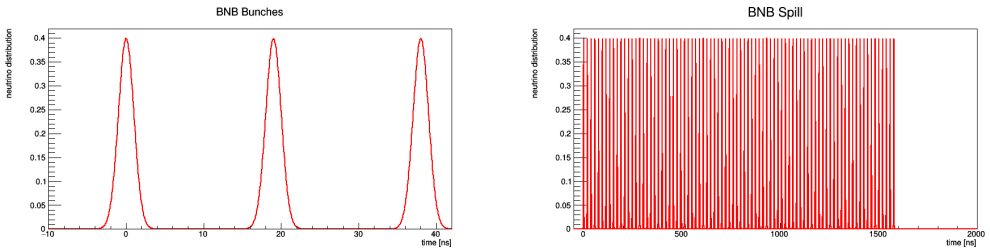

Figure 3.3.: The BNB beam structure (simulation) consists out of 84 bunches which from together one spill (right). On the left side one can see the separation of each bunch. Between each spill (around 5 Hz) and between each bunch, no neutrino interaction is expected. The vertical axis is in arbitrary units.

MicroBooNE will also see some of the Main Injector neutrino beam (NuMI) neutrinos [5]. The detector is around 8° off the beam axis. Since in this work only the neutrinos from BNB are used no detailed description about the NuMI beam is given here.

3.2. MicroBooNE's Time Projection Chamber

The LArTPC of MicroBooNE consists of the anode plane where the readout is realized, the cathode, and the field cage. In Figure 3.4 one can see the backside of the cathode plane as well as the field cage rings. All these parts are placed inside an insulated stainless steel vessel implemented as a cryostat to keep the argon liquid at the right temperature and pressure. Also part of the cryostat is the filtration system which ensures the number of impurities in LAr to be below a critical level.

Figure 3.4.: The field-cage of MicroBooNE with direct view on the back-side of the cathode plane. The anode plane is realized using three layers of wires which can be read-out [5].

The field cage is made out of metal rings connected by a voltage divider chain starting at a negative cathode voltage and ending at the grounded anode plane. The dimensions are stated in Table 3.1 and include a total mass of 85 t of LAr as a target material. The field cage ensures a uniform electric field from the cathode at $-70\,\mathrm{kV}$ to the anode at around 0 V resulting in total field strength of $273\,\mathrm{V\,cm^{-1}}$.

The readout at the anode plane is realized with three different wire planes referred to as the U, V, and Y plane. The U and the V plane are induction planes that measure the electrons without absorbing them while the Y plane is a collection plane that absorbs the electrons. The collection plane wires are oriented vertically while the induction planes have the wires oriented $\pm 60^\circ$ concerning the collection plane. The specifications of the MicroBooNE LArTPC are given in the Table 3.1.

The LArTPC is read out when triggered, which can either be a light signal over a certain threshold (self-triggering) or a trigger coming from an external source. One external source is the beam trigger, which fires every time BNB neutrinos are going through the detector. The location of the LArTPC is indicated together with the coordinate system and the definition of the angles θ and ϕ are shown in Figure 3.5.

The time of a interaction is given by the signal of the prompt scintillation light ($\tau = (6 \pm 2)\,\mathrm{ns}$, see Table 2.1) produced by charged particles ionizing the LAr. The detection time of the prompt scintillation light gives the so-called time of an interaction (T0). The time difference of this T0 and the arrival time of the drift electrons then leads to the proper projection and reconstruction of an interaction in the drift direction.

[1]Drawing by Wouter Van de Pontseele

Specification	value
LArTPC longitudinal dimension (along beam)	10.368 m
LArTPC vertical dimension	2.325 m
LArTPC horizontal dimension (drift)	2.560 m
LArTPC active mass	85 t
# collection plane wires (Y plane)	3456
# induction plane wires (U plane)	2400
# induction plane wires (V plane)	2400
Wire orientation (U,V,Y) w.r.t vertical	+60°, -60°, 0°
Plane spacing	3 mm
Wire pitch	3 mm
Cathode voltage	−70 kV
Bias voltages (U,V,Y)	−110 V,0 V,230 V
Drift field	273 V cm^{-1}
Maximal drift time	2.3 ms

Table 3.1.: Specification of the wire LArTPC in MicroBooNE [5] .

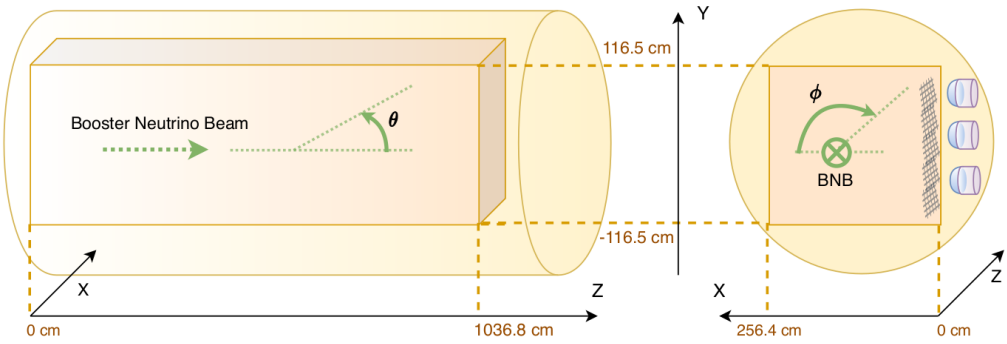

Figure 3.5.: The dimensions and the coordinate system of the LArTPC inside the cryostat, also the location of the PMTs is given in the figure. The angles θ and ϕ are also drawn[1].

The scintillation light is detected using 32 PMTs[2] sitting behind the three wire planes outside of the field cage of the LArTPC. Since these PMTs are insensitive to the VUV scintillation light with a wavelength of (128 ± 10) nm, a plate coated with wavelength shifting TetraPhenyl Butadiene (TPB) is mounted in front of each PMT. The TPB shifts the 128 nm scintillation light to (425 ± 20) nm, which the PMTs are sensitive to.

[2] 32 8" PMTs of the type: Hamamatsu 5912-02mod

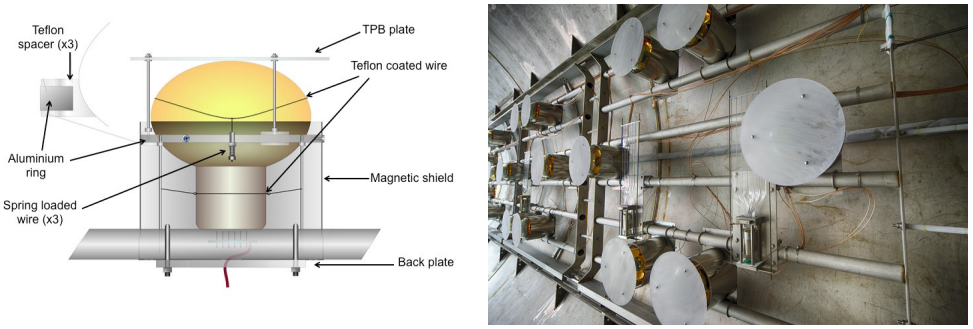

(a) PMT scheme (b) PMTs in Cryostat

Figure 3.6.: Left: a scheme of the PMT with the TBP coated plate in front of it. Right: the placement of the PMTs in the cryostat before the LArTPC installation [5].

In Figure 3.6 one can see the PMTs with the TPB coated plates in front of them. The total photo-cathode coverage is 0.9%. Since many photons are produced by a MIP, this coverage is enough and we end up with a light yield between 1 to 15 photons per MeV depending on the distance to the light read-out [85]. The signal of the PMTs is split into a high gain and low gain channel to have a bigger range with the Analogue-to-Digital Converter (ADC) readout.

When an external trigger arrives, a minimum of light has to be measured by the PMTs within a certain time window for the readout information of the LArTPC to be stored. The light can either come from a beam-neutrino interaction or a crossing-cosmic interaction within the specific time window.

For the interactions in this time window, the X position (position in drift direction) does not have to be corrected. However, all cosmic interactions outside this time window will have the wrong position in the drift direction and must be corrected to properly separate the interactions. This can be done by using the light information registered by the PMTs for all interactions during the readout if the light signal can correctly be assigned to the deposited charge registered by the wire planes.

The separation of charge signals coming from cosmic or beam-neutrino interactions by using the light information is not 100% efficient. A large amount of cosmic interaction overlaying an eventual beam-neutrino interaction leads to significant cosmic contamination in the analyzed interactions.

3.3. Data Acquisition

The analog signals of the total 8256 wires are readout by Application-specific Integrated Circuit (ASIC)s placed in the cold LAr inside the cryostat. Here the signal is

preamplified and shaped before being sent out of the cryostat for digitization in the warm. Before the digitization, in the feedthrough of the cryostat, an intermediate amplifier is mounted. Finally, in the rack on the platform above the cryostat, ADCs convert the analog signal to a digital one with a sampling rate of 16 MHz and a 12-bit ADC. Depending on the signal being bi- or uni-polar, a different baseline is chosen (low at 450 ADC counts for unipolar collection channels and in the middle of the range at 2055 for bipolar induction channels). After the digitization, the charge signals are fed into Field-Programmable Gate Array (FPGA)s for further data processing and reduction.

The signal of the PMTs is already strong enough for the propagation outside of the cryostat. For every PMT, a high gain and a low gain signal line go outside to a preamplifier and signal shaper. This signal is also digitized with a 12 bit ADC at a sampling rate of 64 MHz.

All the preprocessed and digitized signals are then collected by several servers to form subevent fragments. All these fragments are then sent to one event-building machine where one readout is constructed to an event and then finally stored on disk. One event corresponds to a readout of one trigger. It contains data from more than one readout cycle of the whole LArTPC so the signals induced before and after the beam window are also recorded. One readout is indicated by the red or gray boxes in Figure 3.7. One box corresponds to the size of the active LArTPC. In this event, no neutrino interaction is present. However, a lot of cosmic background tracks leave a signal in each event.

It is flux integrated

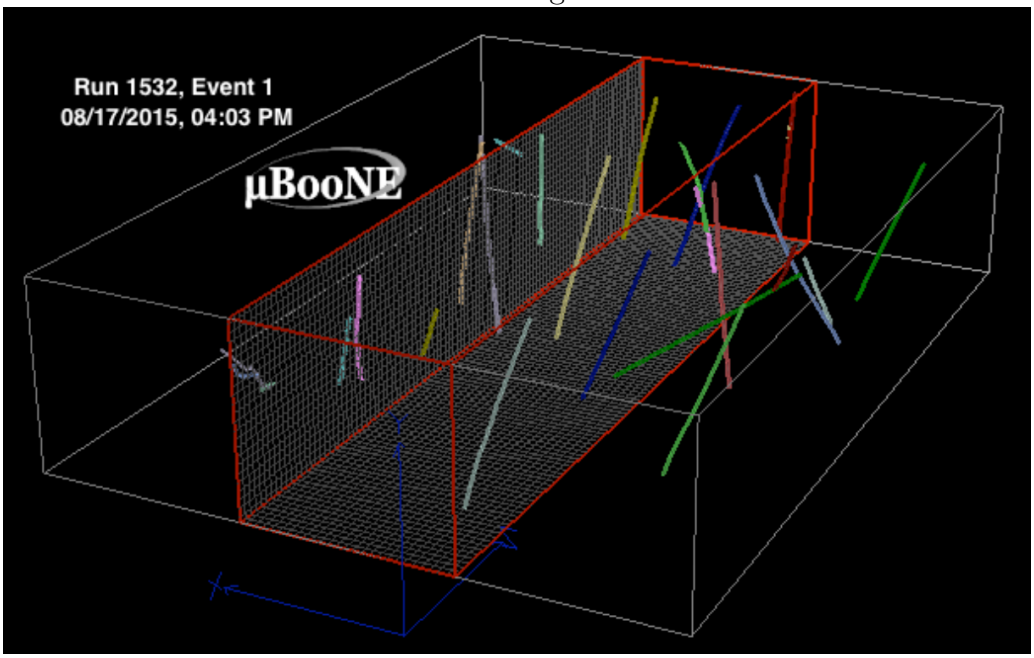

Figure 3.7.: A large amount of cosmic muon tracks will be present in each of the readouts of MicroBooNE. These can be mistaken as a neutrino interaction with a non-zero probability.

3.4. Cosmic Background

One feature of the LArTPC is the rather long charge readout time where background interactions can occur in the active volume of the detector. The main backgrounds which will enter the LArTPC are cosmic rays which consist mainly out of muons from pion and kaon decays in the atmosphere [86]. The flux of muons is around 2 orders of magnitude higher than the flux of other cosmic induced particles [87]. Around 8 muon tracks will enter the active volume of MicroBooNE each readout window [6] since the detector sits basically on the surface of the earth without any shielding, see Figure 3.7.

These muon tracks are surrounded by several delta electrons that originate from the muon track. Also, photons can be produced during the propagation of the cosmic muon through the LAr. Both the electrons as well as the photons can be mistaken for an electron neutrino interaction, especially when the cosmic-muon track is outside the active volume of the LArTPC, or somehow not fully reconstructed. There are several regions in the anode read-out plane of MicroBooNE's LArTPC where one or more wire plane contains bad- or non-responsive wires which cause that parts of a track might be not reconstructed.

Also, the cosmic-muon itself can act as a background for ν_μ CC events due to a large number of muons with respect to neutrino interactions and a small, but non-zero,

probability to misidentify them. Only in one out of 600 beam spills does a neutrino interact inside the active LAr on average, so a very large amount of cosmic tracks ($\approx 600 \times 8$ muon tracks per spill $= 4800$) are present per neutrino interaction if no time matching is made. Since ν_e interactions occur less often, the amount of cosmic entering the LArTPC with respect to ν_e interactions is even larger.

The largest rejection is obtained by the requirement to have a light signal in coincidence with a beam trigger but still, a large fraction of the background remains. These are either cosmic interactions in the beam window or a neutrino interaction that produces the light but a cosmic track is selected as the neutrino interaction. Therefore, there is a need for further rejection of cosmic interactions.

What makes it even harder to correctly identify cosmic tracks from neutrino interactions is that a fraction of the wires in MicroBooNE are non-functional as shown in Figure 3.8. Around 30% of the area of the readout plane has at least one wire in one of the wire planes which is not properly working [88]. This area is reduced to around 3% where two wires are malfunctioning. These less responsive or even dead areas lead to not fully reconstructed tracks or broken tracks. So a track might seem to start inside the TPC but comes from outside where one part is not properly reconstructed.

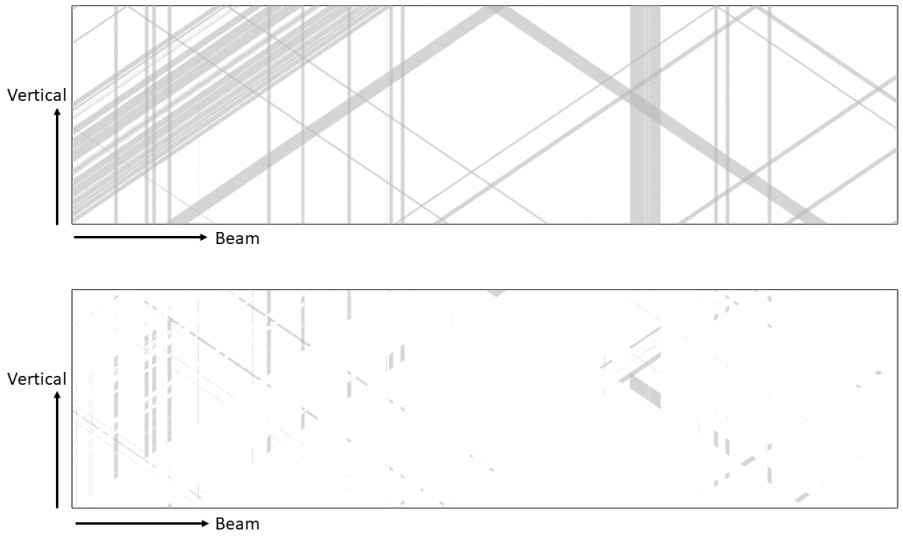

Figure 3.8.: Top: all wires which are non-functional in the MicroBooNE LArTPC. Bottom: the area which is not covered by at least two wire planes [88]. Non-responsive wires can lead to miss-reconstruction of the signals in the LArTPC.

Also, radioactivity can introduce a source of background. Since the most radioactive material sit in the cryostat or even outside, most radioactivity-induced signals will appear at the border of the LArTPC (outside the active volume). On top of that,

the energy of radioactivity is in the low MeV scale and therefore well separated from the energy of beam neutrino interactions.

A neutrino interacting in the surroundings of the LArTPC can also produce a background signal if the secondary particles reach the LArTPC. Most of these interactions happen upstream of the detector in the ground (dirt) or in the infrastructure around the LArTPC. Both of these sources (radioactivity and 'dirt' interactions) play a secondary role next to the intensity of the cosmic bombardment.

There are several possibilities of how to actively veto cosmic events in the LArTPC. One option is to tag the particles entering the LArTPC from outside since the interest is only on neutrino interactions happening inside the LArTPC. Such a tagging can be realized with a CRT which tags incoming particles.

With such a tagger one option would be to completely veto an event when the CRT registers an interaction in the beam window. This would only require good timing resolution, but not a good spatial resolution. Nevertheless, especially for ν_μ studies, one would also veto some amount of the exiting muons of the CC interaction.

Another option would be to tag all incoming particles from outside. This would need good timing and spatial resolution. Studies have shown [14] that >99% of the cosmogenic photons emerging from a muon track convert to a visible electron-positron pair within a 15 cm radius. Therefore a better spatial resolution than 15 cm is needed if one wants to apply such a cosmic rejection.

In any case, one needs to distinguish interactions with the CRT as on- or off-beam, so to separate the interactions happening in the 1.6 µs beam-window or outside this window is crucial for a CRT. As we saw in Section 3.1, one could even reject interactions happening between the bunches if nanosecond timing resolution is reached. To distinguish on- from off-beam events, a timing resolution around 100 ns is sufficient.

These timing requirements and also the spatial resolution of the $\mathcal{O}(1\,\text{cm})$ have driven the design of the CRT for SBND and MicroBooNE. The realization of the CRT is described in Chapter 4.

3.5. Laser System

The detector is permanently hit by cosmic muons ionizing the LAr. The free electrons propagate in the order of milliseconds to the anode where they are absorbed, but the positive ions drift much slower towards the cathode. By looking at Table 2.1, one can see that the mobility of the argon ions is $\mathcal{O}\left(10^6\right)$ lower, so the drift time for these is in the order of minutes. Since these ions are produced all the time, a cloud of positive ions starts to accumulate in the drift volume which deforms the electric field.

This deformation of the electric field is known as the Space-Charge effect and distorts the path of the ionization electrons as they propagate from the interaction to the anode. To measure these deviations a laser system is implemented which can introduce a straight line of light that ionizes the LAr in the field cage at different positions. Since the position of the laser beam is known a map between the true

position of the ionization point and the reconstructed position can be used to correct the position and the electric field strength.

A detailed description of how this is implemented in MicroBooNE is in [89] and a description of the principle is shown in [90].

4. CRT

My main contribution lies in the work for the CRT for the MicroBooNE and the SBND experiments. I was involved in the construction of the modules, the testing, and the installation for both experiments. I worked on the time calibration, reconstruction, and finally on the analysis of the CRT data.

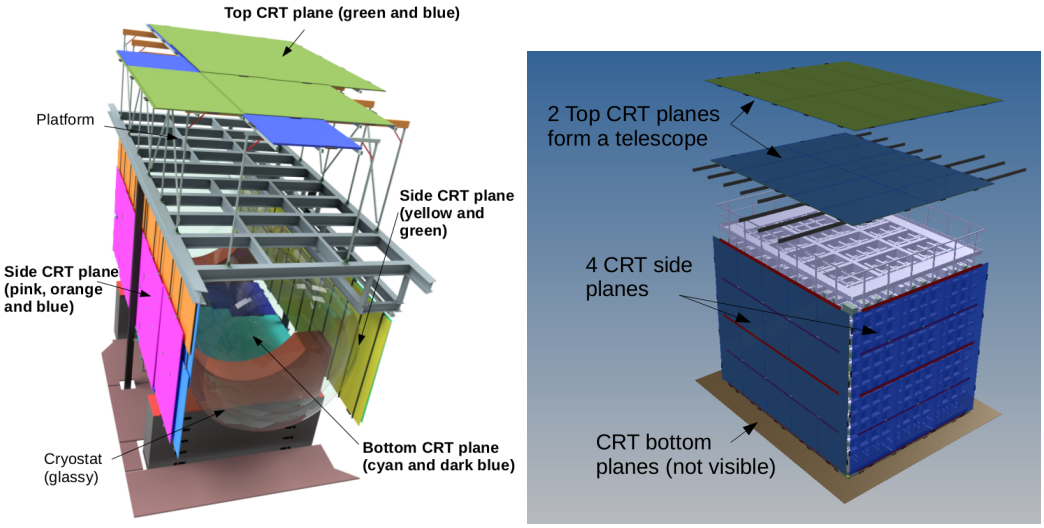

(a) CRT module (b) light collection

Figure 4.1.: Left: The location of the CRT modules around the cryostat of MicroBooNE. The modules of the CRT do not cover the active volume of the LArTPC symmetrically since they were built around the already existing MicroBooNE cryostat. Right: The CRT modules around the SBND detector with two Top CRT layers acting as a muon telescope. The planes cover all sides, at the bottom and the Top plane, there are some gaps needed for the infrastructure of the cryostat and the LArTPC.

One property of the LArTPCs of these two experiments is the rather long charge readout time where background interactions can occur in the active volume of the detectors (see Section 3.4). The main background which will enter the LArTPC are cosmic rays which consist mainly out of muons from pion and kaon decay in the atmosphere [86]. These muon tracks are surrounded by several delta electrons that

emerge from the muon track. Also, photons can be produced during the propagation of the cosmic muon through the LAr.

Both electrons and photons can act as a background for various analyses due to reconstruction errors (light mismatching, non-responsive wires, ...). Also, the muon itself can act as a background for ν_μ CC event due to a large number of muons with respect to neutrino interactions and a small but non-zero probability to misidentify them. Since ν_e interactions are even rarer, the amount of cosmic entering the LArTPC with respect to ν_e interactions is even larger. Therefore it is crucial for the SBN detectors, which are not underground, to reject these cosmic backgrounds.

There are several possibilities of how the cosmic interactions can be rejected for the LAr detectors of the SBN program. They are already introduced in section 3.4 and require a large coverage of active tagging around the LArTPC, a spatial resolution of $\mathcal{O}(1\,\text{cm})$ and a timing resolution of $\mathcal{O}(100\,\text{ns})$ to distinguish on- and off-beam events. If one wants to reject also the events between the bunches within a BNB spill (see section 3.1) a time resolution in $\mathcal{O}(1\,\text{ns})$ is needed. These requirements lead to the usage of plastic scintillator modules placed around the LArTPC.

For MicroBooNE, the system was built around the existing infrastructure of the cryostat, where the coverage had to be optimized to the space available, see Figure 4.1 (a). The CRT was included in the initial design phase of SBND, therefore a larger coverage could be reached for this detector as seen in Figure 4.1 (b).

Each CRT plane consists out of two layers of single CRT modules, an X layer, and a Y layer. With two such layers, a muon telescope can be realized as it will happen for the SBND detector. The design of such a module as well as the readout electronics is explained in the next section 4.1. After these explanations follow a discussion about the construction and assembly of these modules and their placement around MicroBooNE as well as the realization of a test stand for beam monitoring in the SBND detector pit in Section 4.2.

4.1. Design and Working-principle

The CRT will here be explained in the context of its application to the MicroBooNE experiment. The SBND experiment has a similar system with adapted sizes for the different detector dimensions.

The CRT of MicroBooNE consists of 73 individual modules (220 for SBND), where each module is made up of 16 mechanically-joined strips of scintillating plastic. The strips have a width of 10.8 cm and are sandwiched between two 2 mm thick aluminum sheets, which provide the necessary stability. This results in a module width of 1.75 m and lengths that vary from 2.3 m up to 4.1 m depending of the location of the module around the MicroBooNE cryostat.

As with the LArTPC, the CRT system can only measure particles interacting electromagnetically inside the modules. If a charged particle propagates through a CRT module, scintillation light is produced within the hit strip (figure 4.2, left).

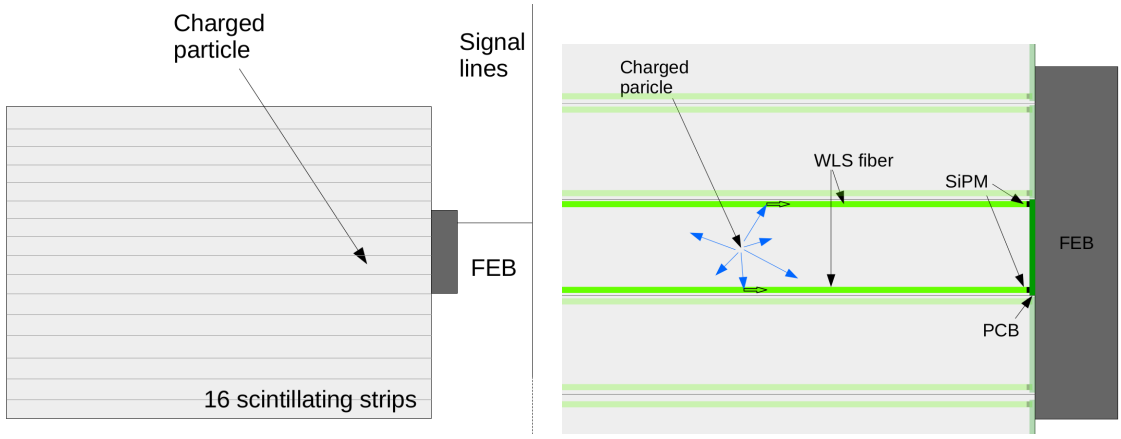

(a) CRT module (b) zoom inside

Figure 4.2.: Left: A CRT module containing 16 scintillating strips, right: the charged particle produces scintillation light with is trapped inside a WLS fiber and guided to the end with the SiPM readout mounted on a PCB on one side of the strip.

Some of the photons will eventually propagate into the WLS fiber, where they are guided to SiPMs (figure 4.2, right). The SiPMs are then read out by a FEB and eventually sent to a server for offline analysis.

Each strip is made out of the scintillating plastic USMS-03[1]. This is a mixture containing 1.5% of PTP (1,4 Diphenylbenzene, primary fluor) and 0.04% POPOP (1,4-Bis(5-phenyl-2-oxazolyl)benzene, secondary fluor). The main component of 98.46% is the Styrolution (base) PS GPPS. The whole strip has a highly reflective white outer layer. The emitted scintillation light has a wavelength in the blue region, and its absorption length in the USMS-03 is longer than 7.5 cm. To collect the light and guide it to the SiPMs, two WLS fibers are fixed with a glue that is transparent to the scintillation light. The WLS fibers absorb the scintillation light and re-emit it with a longer wavelength in the green spectrum, see Figure 4.3. The fibers are Kuraray Y11(200)M[2], which have an absorption length of more than 3.5 meter. The fibers are placed in a groove on the narrow long side of the strips and then covered with a layer of Mylar foil. The foil protects the cladding of the fibers and reflects exiting photons back into the fiber or scintillator.

The readout is realized with two Hamamatsu S12825-050P[3] SiPMs. On the other end of the fibers, a highly reflective aluminum mirror is evaporated which reflects the photons towards the SiPMs. The SiPM signal is read out by the FEBs mounted on one end of each module.

[1]USMS-03 by UNIPLAST Inc, Vladimir, Russian Federation
[2]fiber manufacture website: `http://kuraraypsf.jp`; November 26, 2020
[3]Hamamatsu S12825-050P: `http://www.hamamatsu.com/jp/en/S12571-050P.html`

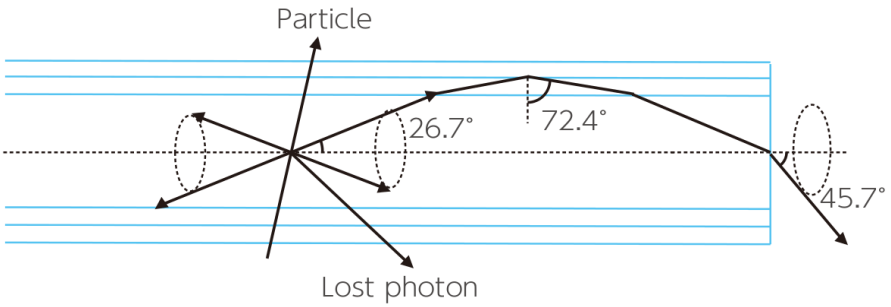

Figure 4.3.: Photons can be absorbed and re-emitted in the WLS fiber. The photons emitted in a certain angle are trapped inside the fiber and can therefore be guided to the readout[2].

4.1.1. Front-end Electronic Board

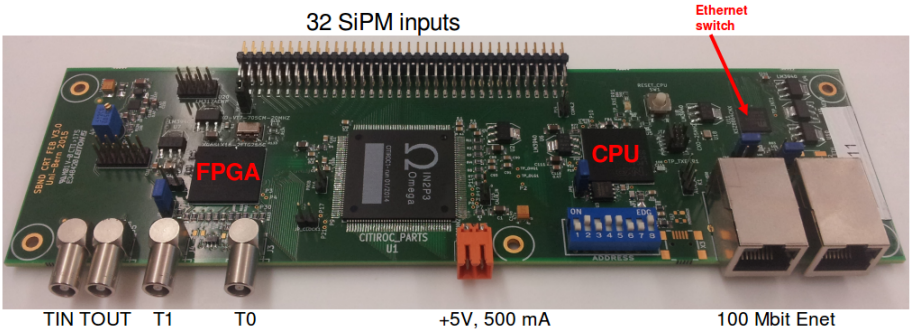

Figure 4.4.: The FEB and its electronic components [91].

The FEB was designed at the University of Bern to read out the CRT modules and is now commercially available from CAEN[4]. The electronic readout of a CRT module needs to fulfill several requirements coming from the technical construction of a CRT module and the physical purpose of the system. Since each module has 32 individual SiPMs, the FEB provide individually adjustable readout channels as well as bias voltages for each SiPM. The SiPM signals are also amplified, shaped, and digitized in the FEB. Since two signals from two perpendicular (X and Y layers) modules are needed, a trigger logic has to be implemented to ensures that the two signals are over their separately adjustable thresholds. Finally, the digitized signals need to be sent out to a host computer for further processing.

A physics requirement is the ability to generate accurate timestamps for the cosmic interactions in with resolution $\mathcal{O}(1\,\text{ns})$. To distinguish interactions between on- or off-beam (or even on- or off-bunches) one needs to match the signals from the CRT with the light signal from the PMTs, which requires the CRT to have time accuracy

[4] `https://www.caen.it`

of $\mathcal{O}(1\,\text{ns})$. Therefore, also the resolution has to be in the $\mathcal{O}(1\,\text{ns})$ for the electronic readout.

All this is realized on the FEB shown in Figure 4.4. A 32 channel CITIROC ASIC from Omega[5] shapes and digitizes the signals. The signals are then routed into a XILINX Spartan-6[6] FPGA where the triggering is managed. The CPU finally stores the triggered events which then can be sent out via an Ethernet connection. The two Ethernet sockets enable a daisy-chain of multiple FEBs in a single line. The LEMO connections TIN/TOUT provide the necessary signals for the X-Y triggering and the T0 and T1 connections can take reference pulses for the two internal clock counters. A detailed description can be found in [91].

4.1.2. Triggering

The goal is to record through going charged particles like cosmic muons. Therefore, the trigger system is built such that only interactions that leave a signal in two perpendicular modules are recorded (see Figure 4.5). This reduces the trigger rate significantly due to the suppression of small energy deposits in only one module e.g. from natural radioactivity in the surroundings.

One module can reconstruct an interaction in $\mathcal{O}(1\,\text{cm})$ in two spatial dimensions. The location of the module together with the 1 cm-thick scintillator strips define one dimension and the amplitudes of the two SiPM signals in the strip hit by the charged particles are used to reconstruct the second dimension. By placing two modules perpendicular to each other, the third spatial dimension can be reconstructed from the information of the particle interaction in each module resulting in a 3D reconstructed interaction point.

This trigger scheme is realized by using the TIN and TOUT connections on the FEB (see Figure 4.4). When the signal in the two SiPMs in one strip crosses the threshold, the FEB digitizes the signal of all 32 SiPMs and sends a signal out through the TOUT line. This line is plugged into the TIN connection of the FEBs in the perpendicular module. The signal is only stored when the FEB also receives a signal at the TIN input within a configurable time window. For SBND and MicroBooNE this time window is set to 150 ns [91]. This ensures that the X-Y trigger rate is minimized while allowing for good reconstruction in 3D space.

To reconstruct these interactions off-line, one needs to find the corresponding signals stored in the different FEBs. This is done by looking for signals occurring simultaneously and requires that all the internal clocks of each FEB are synchronized. The FEB has two internal counters, each with a resolution of 1 ns. The synchronization is achieved by sending a reference Pulse Per Second (PPS) to each FEB through the T0 signal line. This PPS originates from a Global Positioning System (GPS) controlled module which sends out the PPS as a global time reference. At the arrival of this reference pulse, the internal clock is reset and the FEB internal clock

[5] `http://omega.in2p3.fr/`

[6] `https://www.xilinx.com/products/silicon-devices/fpga/spartan-6.html`

speed is corrected. The source of the clock is a 20 MHz temperature-compensated voltage-controlled crystal oscillator. The T1 line does the same with a second counter and can be used e.g. for beam triggering.

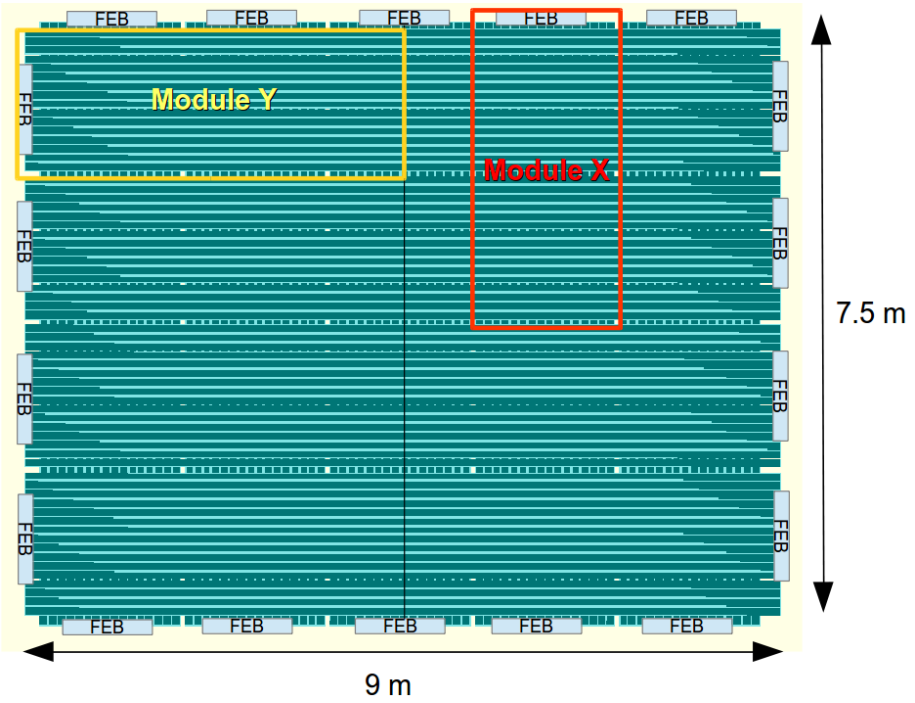

Figure 4.5.: The CRT stores only events where two perpendicular modules (X and Y layer) gave a signal over the threshold. If a module gives a signal over the threshold, a pulse is sent out through its TOUT line which is connected to all TIN lines of the FEBs in the perpendicular layer. Only if a FEB also receives a signal through the TIN, the signals of all SiPMs in that module and the two timestamps are stored in the internal buffer [6].

4.2. CRT Construction and Installation

I was heavily involved in the construction of the CRT modules for MicroBooNE as well as for SBND. At the University of Bern, I assembled a significant portion of the CRT modules. After the CRT production and initial testing, the modules were shipped to FNAL where I assembled and commissioned the SBND CRT test stand. Additionally, I was involved in the installation of the CRT for MicroBooNE, mainly in cabling and commissioning of the readout electronics.

Here, a description of the module assembly at the University of Bern and finally the installation of the CRT at MicroBooNE and the SBND test stand are presented.

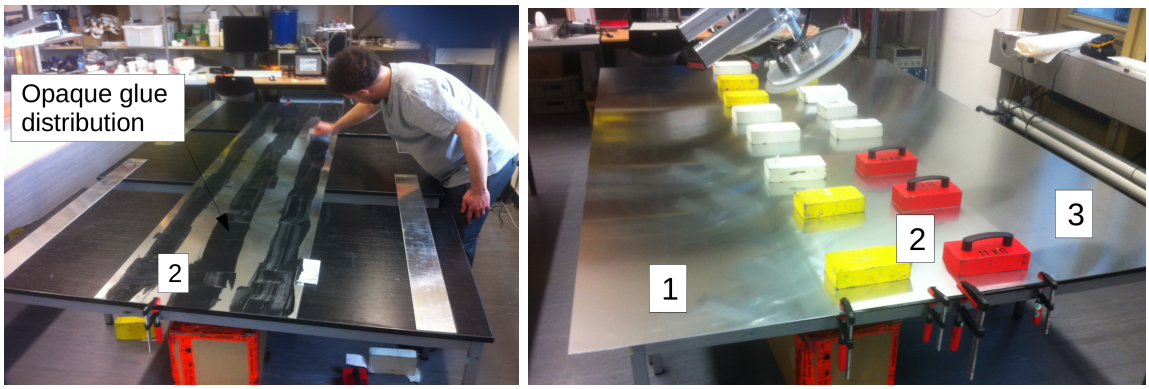

(a) Glue distribution (b) Big sheet assembly

Figure 4.6.: Usually, one aluminum sheet covers a side of a module but for the largest modules three aluminum sheets (1,2 and 3) are glued together in order to reach the size for the larges modules of MicroBooNE. Left: The glue is distributed on the middle aluminum sheet. Right: the tree aluminum sheets are glued together, the lead bricks provide the needed pressure.

4.2.1. Module Assembly

All modules are similar, with the only difference being the dimension of the modules and the length of the scintillating bars. The assembly of one module takes around 2 to 3 working days with 2 people involved. Since some steps can be done easily for more than one module, several modules at different stages were in production at the same time.

First of all, the aluminum sheets had to be prepared. For the largest modules for the MicroBooNE experiment, the sheet covering a module was made out of three single sheets on each side, glued together with an opaque glue ensuring light-tightness. This can be seen in Figure 4.6. After the glue has dried, the aluminum end pieces which are placed at the shorter sides of the modules between the aluminum sheets can be prepared. They are fixed at the right position between the aluminum sheets. The holes and threads can directly be drilled through the aluminum sheets into the end bars. One end bar has a gap to accommodate the FEB connector for the SiPM cables. The FEB will be mounted on the outer side of the module on that end bar. In this gap, a PCB with the connectors for the cable on one side and the connectors for the FEB on the other side is also glued in a way that no light can penetrate.

Next, the scintillation bars need to be prepared. They are delivered at the right length with a small groove at the sides for the WLS fibers. First, the side where the SiPMs will be mounted was milled to provide a flat surface, and threads are cut into the scintillating plastic with great care not to melt the plastic (see Figure 4.7, (a)). To couple the fibers to the SiPMs, the groove has to be enlarged at the readout end of each strip (see Figure 4.7, (b)). Also, the groove had to be cleaned so that the

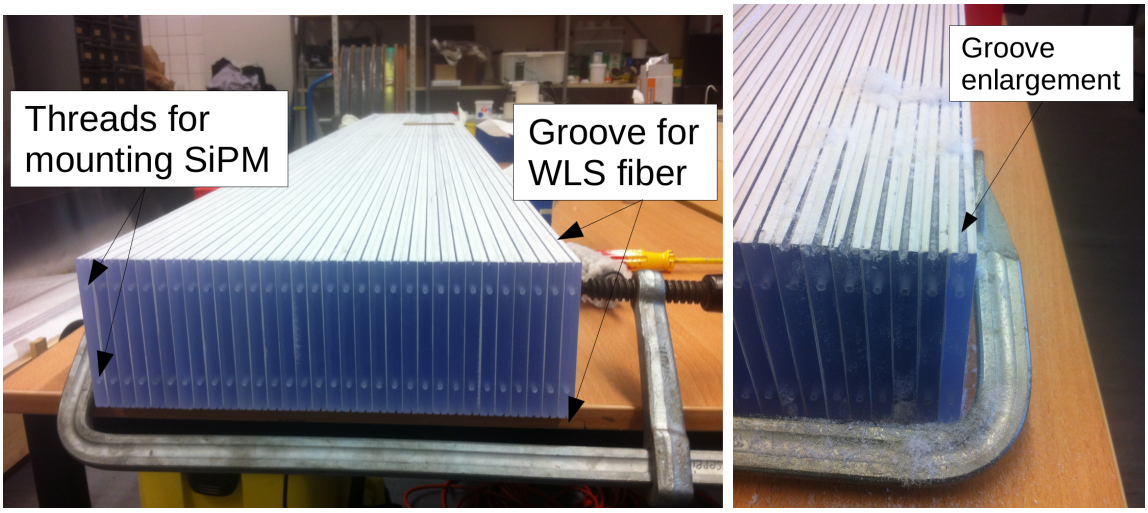

(a) milled scintillator strips (b) Enlargement at readout end

Figure 4.7.: The readout end of the scintillator strips was milled and threads were drilled for the SiPM assembly later on (left). In order to fit the WLS fibers nicely in front of the SiPMs the groove as to be cleaned and enlarged at the readout end (right).

fiber fits nicely along the length of the strip, as there were some residue leftovers from the machining inside the grooves.

The SiPMs were attached to the scintillation strips with a plastic mounting bracket that also locates the fibers (see Figure 4.8 (a) and 4.7 (a)). This mounting bracket ensured that the fiber is directly placed in front of the light readout. Before the fibers could be glued in the grooves at the side of each scintillator bar they were cut to length and then diamond polished at each end. One end of the fiber is placed into the mounting bracket and guided directly in front of the SiPM. On the other end of fiber, a mirror is evaporated (see Figure 4.8 (b)).

The fibers are then glued into the groove using an optical glue that does not absorb the scintillation light and does not damage the cladding of the fibers even when the bar is mechanically stressed. To protect the fiber and to further decrease the light loss, a reflective Mylar foil covers the fiber in the groove of the scintillator bar (see Figure 4.9 (a)). After these steps, the scintillator strips are ready to be assembled on the prepared aluminum sheet. For this, the bars are fixed on one aluminum sheet using double sided tape (see Figure 4.9 (b)).

With the scintillator strips fixed on one aluminum sheet, the SiPM cabling could be installed. For this, the pre-drilled aluminum end bars are mounted onto the same aluminum sheet, the bar with the PCB is placed on the readout end. Cables are connected between each SiPM and the PCB. Maintaining the correct order is vital (Figure 4.10 (a)), since the FEB will only trigger when both SiPMs of a scintillator

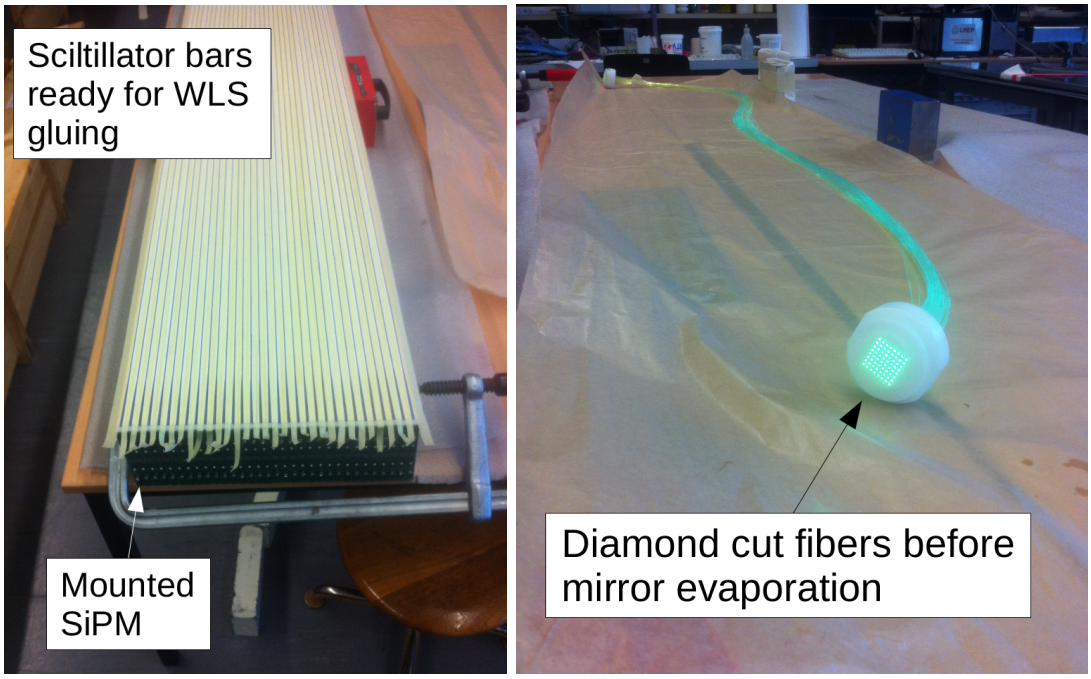

(a) SiPM mounted on bar (b) WLS fiber ready for evaporating

Figure 4.8.: Left: The SiPMs are mounted on one end of the scintillator bar with the fiber holder in between before gluing the WLS fibers into the groove. Duct tape prevents the optical glue to go in between the bars. Right: The WLS fibers are paced in a nest for diamond cutting and on one side a mirror is evaporated directly on the fiber in order to increase the light at the readout side.

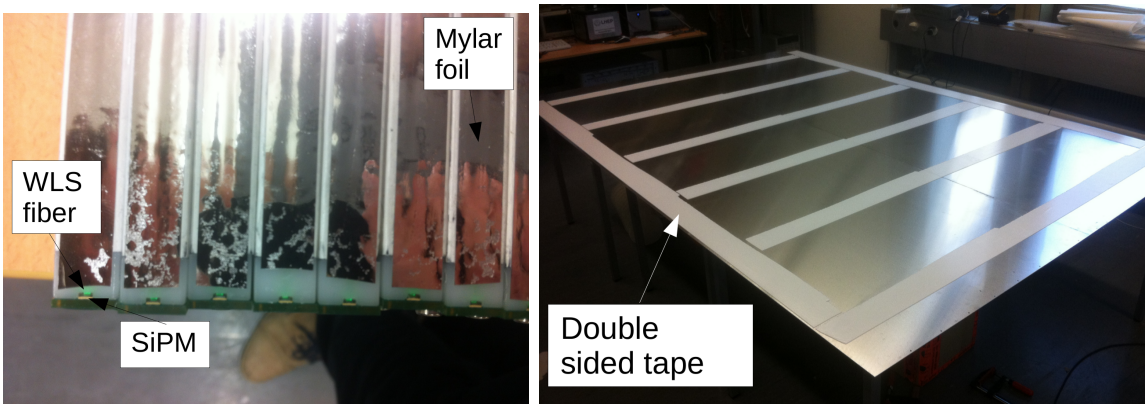

(a) Glued WLS fibers (b) Double sided tape on aluminum sheet

Figure 4.9.: Left: The WLS fibers are glued into the groove of the scintillator bar using an optical glue and then covered with reflective Mylar foil. Right: The bars are then fixed on one aluminum sheet using double sided tape, here the tape on the aluminum sheet is shown.

strip have a signal above a threshold. If a SiPM is connected to the incorrect channel, this trigger logic will not be fulfilled by a single through going MIP. A working connection can be tested with a multimeter, checking a small voltage in one direction at the connection outside of the aluminum end bar and zero voltage in the other direction. This ensures a working connection from the connector outside the aluminum bar to the SiPM but does not check if the order is correct. This check is done by eye.

After the cabling is complete and tested, the second aluminum sheet is mounted on the scintillator strips also using double-sided tape. Glue is applied between the aluminum end bars and the sheet to ensure no light can enter the module from outside and the screws are placed for fixing the end bar to the aluminum sheet.

Now, the long sides of the module can be covered using an aluminum U-profile. This is also glued onto the aluminum sheets and fixed using screws at each end to the aluminum end bars (see Figure 4.10 (b)). With this last step, the module is finally assembled and can be tested.

This is done by connecting the FEB to the module and running a test software. The event rate is checked to see obvious light leaks and all the junctions are surveyed with a flashlight by checking the event rate stays stable. Also, the light propagation in the WLS fibers is tested by using a radioactive source[7] to introduce signals in the scintillator at the near and far end of the module with respect to the readout. After the testing, the module is ready to be shipped.

[7] A ^{60}Co source, activity: 74 kBq

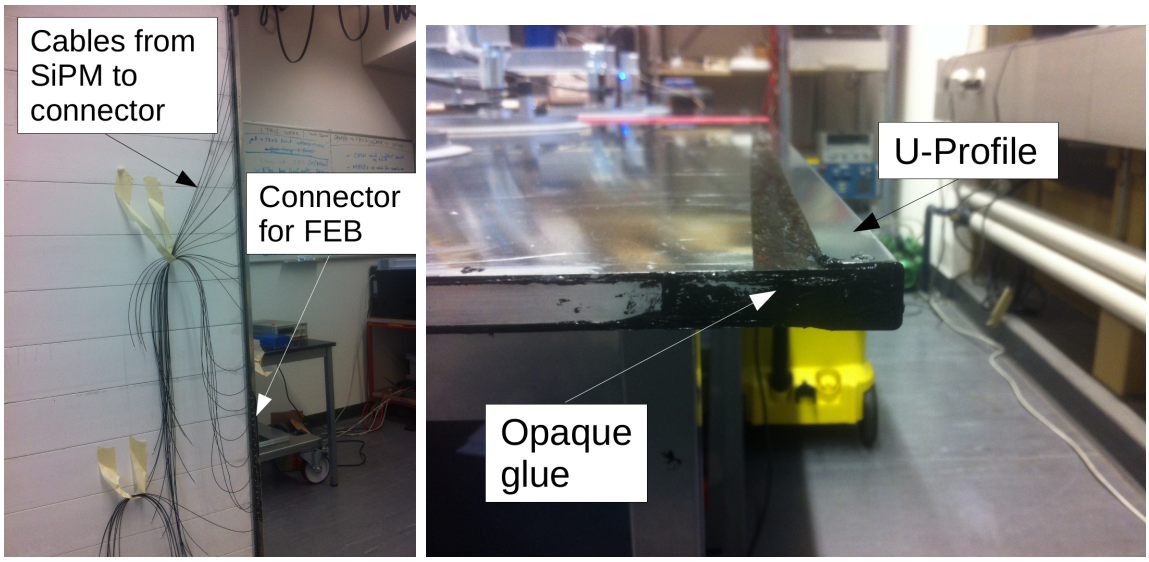

(a) Cabling (b) Long side cover

Figure 4.10.: Left: 32 cables connect the 32 SiPMs to a connector for the FEB sitting in the aluminum end bar. Right: The long sides of the module are closed by gluing an aluminum U-profile over the gap between the aluminum sheets. All eventual gaps have to be closed light tight using the opaque black glue.

4.2.2. CRT Installation at MicroBooNE

The modules were shipped to FNAL and then tested again on arrival. If a malfunctioning channel was discovered, the module would still be used but at the border of the MicroBooNE detector where the coverage is less important. In total, there are 7 dead channels in the CRT plane on the Pipe side, 3 on the Feed-thorough side and 5 in the Top plane. The Bottom plane is fully functional. These dead channels are only a minor drawback in the performance since the majority of the 1168 total channels are fully functional. Finally, the modules are placed around the MicroBooNE detector with help of a crane and lifting platforms placed in the detector pit. While I was not involved in placing the modules themselves, I did part of the cabling, see Figure 4.11. Also, I performed a test measurement using four modules, two at the pipe side and two at the feed-through side of the detector.

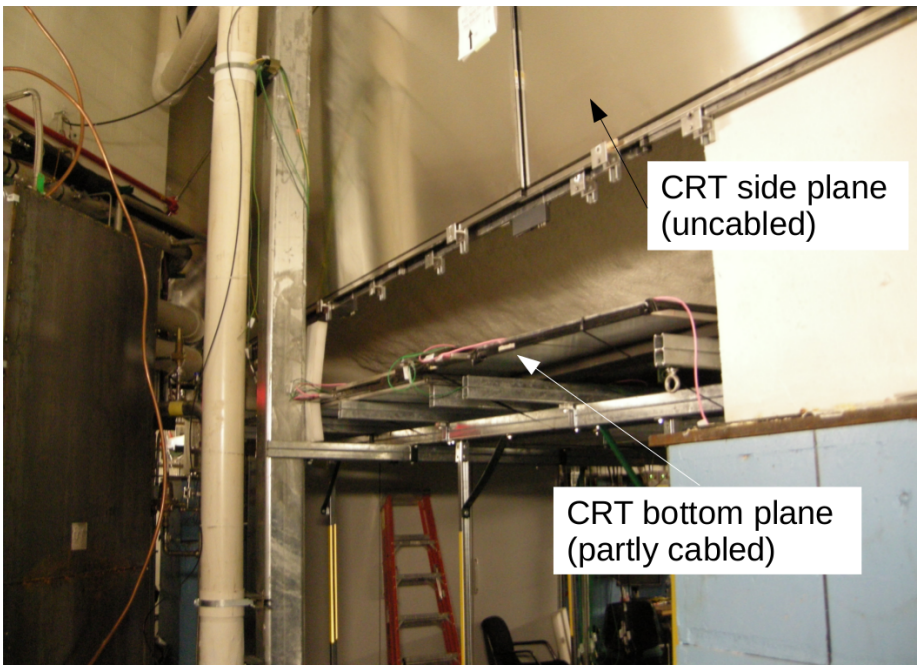

Figure 4.11.: Picture of the mounted modules of the bottom plane and the feed-through side plane. Only partly of the cabling is done in this picture.

A test rack was built in the D0 building a few kilometers away from the MicroBooNE detector building. There, I was involved in equipping the rack and the internal cabling. Also, I prepared it for the first steps of the commissioning.

4.2.3. CRT Installation at the Test Stand in the SBND Detector Pit

Since a large fraction of the CRT modules for the SBND detector were ready long before the detector will be assembled in the pit, it was decided to put the CRT

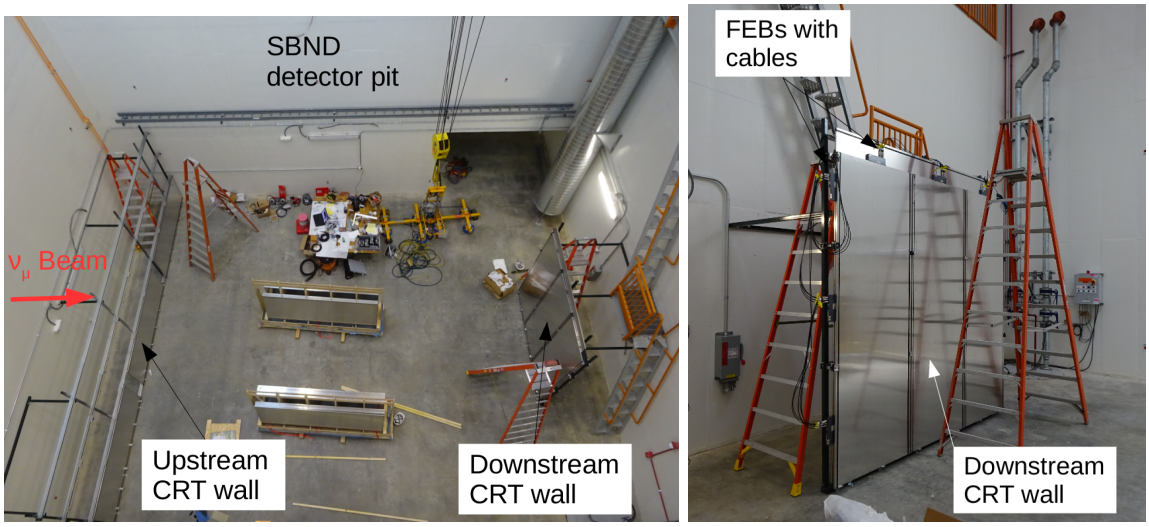

(a) SBND CRT placing

(b) Cabling of the down stream CRT wall

Figure 4.12.: Left: The partly placed CRT modules in the SBND detector pit. 18 modules will be placed on the upstream side and 6 (already in place) are on the downstream side. Right: The cabling for the downstream wall of CRT modules.

modules by themselves into the pit beforehand. By doing this, the modules could be tested and a measurement of the muons produced by neutrino interactions in the ground could be made only using the CRT modules. A muon telescope was built with one wall consisting of 18 CRT modules at the upstream side of the pit and 6 modules at the downstream side of the pit. With this configuration, the neutrino beam profile in time and space can be measured by detecting the muons from CC interactions in the dirt upstream of the CRT modules. I was involved with all aspects of this measurement, from installing the modules to cabling and commissioning of the system and the analysis of the data taken.

4.3. Detector Integration and DAQ

The CRT system of MicroBooNE was commissioned after the rest of the detector was already taking data. Therefore, the DAQ chain of the CRT is completely independent of the DAQ chain for the rest of the detector.

As described in the description of the CRT design in section 4.1 each FEB stores the triggered interactions in its internal memory. The information stored for each triggered interaction is all of the 32 SiPM amplitudes as well as two timestamps from the two internal clocks of the FEB. Rather, these clocks are counters which count the

nanoseconds since the last reference pulse. These counters will overflow at a count of 1024 ms. Since one counter receives the PPS reference pulse, the count of this clock represents the number of nanoseconds since the last second in a global time reference. The global time in seconds needs to be added to these timestamps containing only the number of nanoseconds. For this reason, the FEBs are read out by a host server for each plane (so four servers for the four planes at MicroBooNE) multiple times per second (see Figure 4.13). When the data is read out, the Network Time Protocol (server system time) (NTP) time of the server during the readout is added to the interaction time stamp.

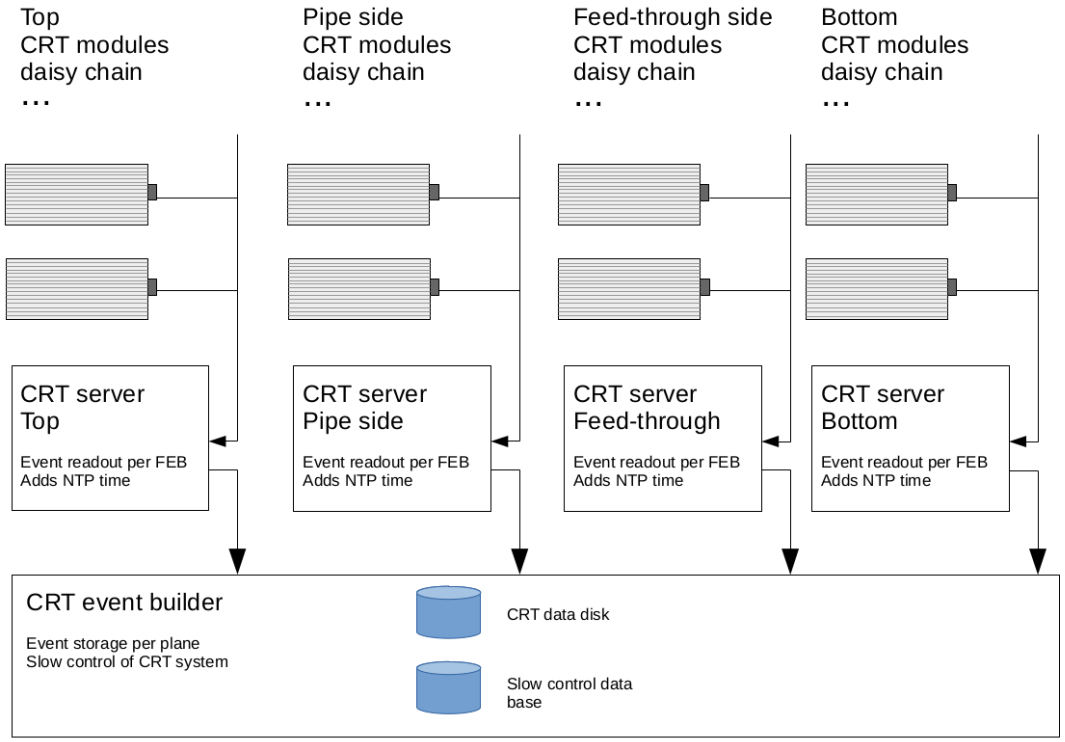

Figure 4.13.: The DAQ of the CRT works as a standalone process. Each CRT plane is connected in a daisy-chain to a server which reads out all FEBs in one line one by one and adds NTP time of start and end of the read out to the data stream which is stored on the CRT event builder machine. Each plane is stored in a separate file.

All the FEBs of one plane are connected to a DAQ server in a daisy-chain. In each server a driver is running which reads out all the FEBs in the line within a configurable time interval (210 ms and 270 ms for the MicroBooNE planes). The driver reads all the interactions stored in each FEB and adds the server NTP to it before sending them to a shared DAQ machine for storing all the data from all the CRT planes. The driver sends out not only the data from each interaction but also additional information which is used for the slow monitoring. The slow monitoring

checks the status of the CRT system and eventually sends out alerts if something is not in a preset nominal state. This is implemented in a Grafana[8] dashboard taking the information from an InfluxDB[9] data base where the status about the CRT is stored as an time series. An example of the slow monitor is shown in Figure 4.14.

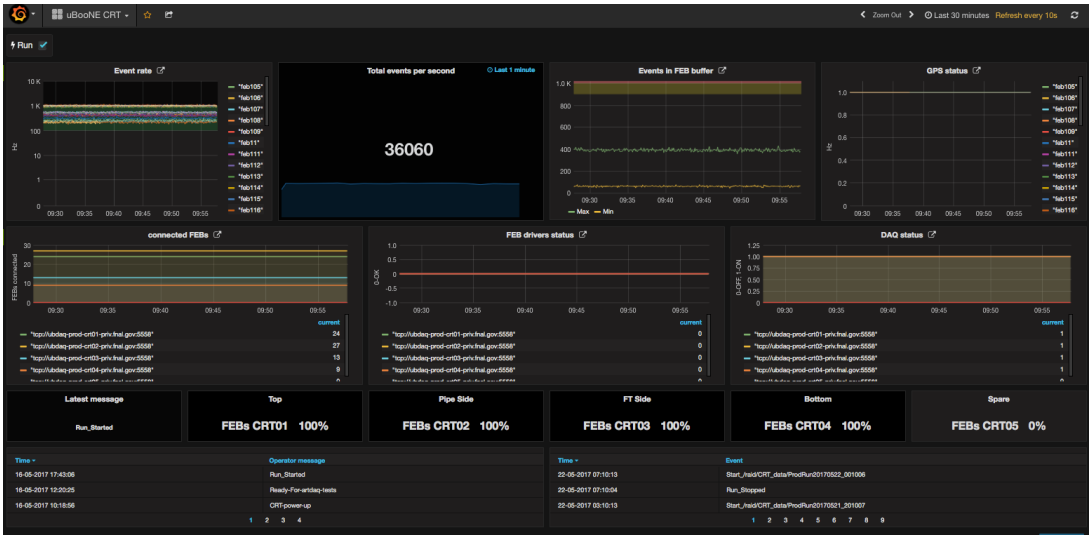

Figure 4.14.: One dashboard of the slow monitor for the surveillance of the status of the CRT. The DAQ driver stores information about the status of the system in a database which then is shown as a time series.

The data of each plane is stored on central storage in a binary format for later offline processing. During the off-line processing, first, a basic reconstruction is done as well as formatting into the commonly used 'artroot'[10] data format. Finally the corresponding CRT information is merged to the LArTPC events using the time stamps of the recorded CRT interactions and the LArTPC event trigger time. This procedure is explained in the next Section 4.4.

4.4. Reconstruction

As described in Section 4.3, the information of a triggered interaction in the CRT is stored for each plane individually. Also, within one plane, the information is grouped by each FEB and readout.

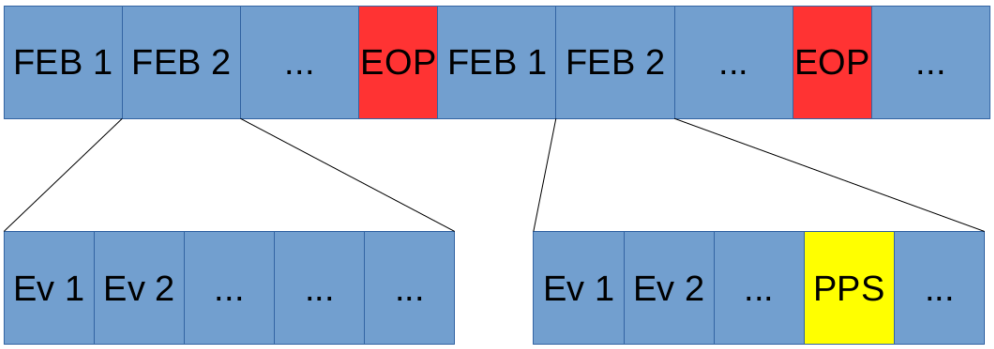

Figure 4.15.: After all registered events (Ev x) of all FEBs in a line the NTP time during the readout is stored in the end of poll event (EOP). With this information all the events between two PPS can be assigned to the same second as long the NTP time and the PPS GPS clocks are synchronized.

4.4.1. Second Assignment

First of all the correct second has to be assigned to each timestamp since it only includes the number of nanoseconds since the last reference pulse in a global time reference. For this, the information of the beginning and end time of a data poll is used, see Figure 4.15. A data poll is defined as the readout cycle of all FEBs in one plane. This only works when the GPS PPS time reference agrees with the NTP time of the servers within $\mathcal{O}(10\,\text{ms})$. Usually, the time accuracy of the NTP time agrees within $<1\,\text{ms}$. In the first phase of the data taking with the CRT of MicroBooNE, a problem with the GPS time was discovered which required additional steps for the second assignment. See Section 4.5 for more information about this topic.

4.4.2. Pair Finding

The next step is to find for each recorded interaction of a module the corresponding one in the perpendicular plane. This is done by comparing the timestamps of each second to all the timestamps in the other FEBs of the same second, see Figure 4.16. When two timestamps are found within a certain time window (taking also the time delays of the cables into account), cross-checks are carried out to confirm if such a pair comes from overlapping modules. If a valid pair is found, the information of the amplitudes and the locations of the SiPM is used to reconstruct a so-called CRTHit in 3D space and time. Since two SiPMs collect the light of each scintillator bar within one module the interpolated position between the two SiPMs of one bar with the highest amplitudes are used for the reconstruction of the position of the

[8] https://grafana.com/
[9] https://www.influxdata.com/
[10] https://art.fnal.gov/art-workbook/

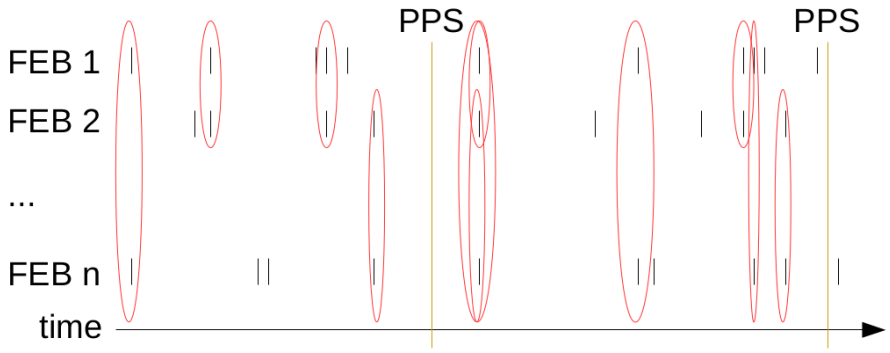

Figure 4.16.: All recorded interactions per FEB and plane of the same second are compared to each other in order to find corresponding timestamps which belong to the same interaction. Further consistency test are done before a proper 3D CRTHit is reconstructed.

interaction. So, the interpolation is done for the position between the two SiPMs in one scintillating bar but not along the bar. One module can measure the position well along the SiPM readout but not so well along the scintillator bars. Therefore the second signal from the perpendicular module is used for the reconstruction along this dimension. Together the two signals can reconstruct an accurate position in 3D and time.

Cosmic rays often lead not only to a single muon but a bunch of muons that can hit the detector at the same time. Therefore a signal of one FEB can potentially be used for more than one pair. This can lead to ambiguities in the reconstruction of the single CRTHits. These ambiguities are not a problem in the way the CRT data is used for analysis. For a veto, the analyzer usually does not care about the number, or position, of the CRTHits, but the time. For the track - CRTHits matching (see later in this Section 4.4.4) the ambiguous hits are leading to a negligible increase of accidental matchings. Therefore, cuts using these variables will not or only very small be affected, leading to a small increase of inefficiency of a signal selection.

4.4.3. Merging

The reconstructed CRTHits build the basic information which can be used for analysis and are stored in an 'artroot' file. These 'artroot' files are then later used when the LArTPC events are further processed. The merging is done based on the timestamp of the LArTPC event and the CRTHits. A CRTHit has to be in a time window of $-4.2\,\text{ms}$ to $5.0\,\text{ms}$ around the trigger time stamp of the LArTPC event. This ensures the possible matching of all tracks in the LArTPC with a CRTHit.

4.4.4. CRT Veto and Track Association

By including the CRT information to the LArTPC data stream one can look for signals which were reconstructed in all systems. A cosmic particle going through the CRT and then entering the LArTPC leaves a signal in all of the detector systems: a CRTHit, a charge signal as well as a light signal.

The CRT reconstructs interactions as single points in 3D space and precise time. This can be compared to the light signals which have good timing but lowers spatial resolution as the charge readout. The charge readout on the other hand gives precise spatial information but reconstructed energy depositions can be shifted due to not correctly account the initial drift time.

By comparing the CRTHit times to the light signal which has triggered the light system one can check if the interaction has also left a signal outside the LArTPC. Depending on the interaction, it is very unlikely that a signal in the CRT is induced by this interaction. Especially for low energy electron neutrino interactions in the active volume of the LArTPC a veto can be applied and reject all events when at the time of the light flash also a CRTHit is registered. A low energy electron neutrino interaction is very unlikely to trigger also the CRT since a particle would need to propagate all way out of the LArTPC and the surrounding LAr to the CRT which is meters apart from the LArTPC. This can lead to a great reduction of cosmic contamination for an analysis of neutrino interactions and is further called the CRT veto.

The other possibility to combine the CRT information is to use the reconstructed energy depositions of the charge readout. For these, only precise timing information is available when the charge signal is matched to the light signal which does not work perfectly.

Assuming a charge-light matching using the flash in the beam window, a correct matching can be either a beam-induced neutrino interaction or a cosmic hitting the detector in the beam window. By extrapolating the position of a track reconstructed with the charge signal to the CRT, one could confirm the matching if there is a CRTHit at this time, see Figure 4.17. If there are no CRTHit at this time, one can shift the track location in drift direction and check if one finds a CRTHit at the extrapolated shifted direction to check if the charge initially was wrongly matched to the light signal in the beam window. If this is the case one can again check if the shift in drift direction corresponds to the time of the CRTHit times the drift velocity of the charge. In case of such a matching one can further reject the event if the CRTHit time of the track-CRTHits matching is outside the beam window. This will be called CRT-track association or tagging and can be used for analysis where a neutrino signal is not necessarily contained in the LArTPC or a wrongly light-matched cosmic.

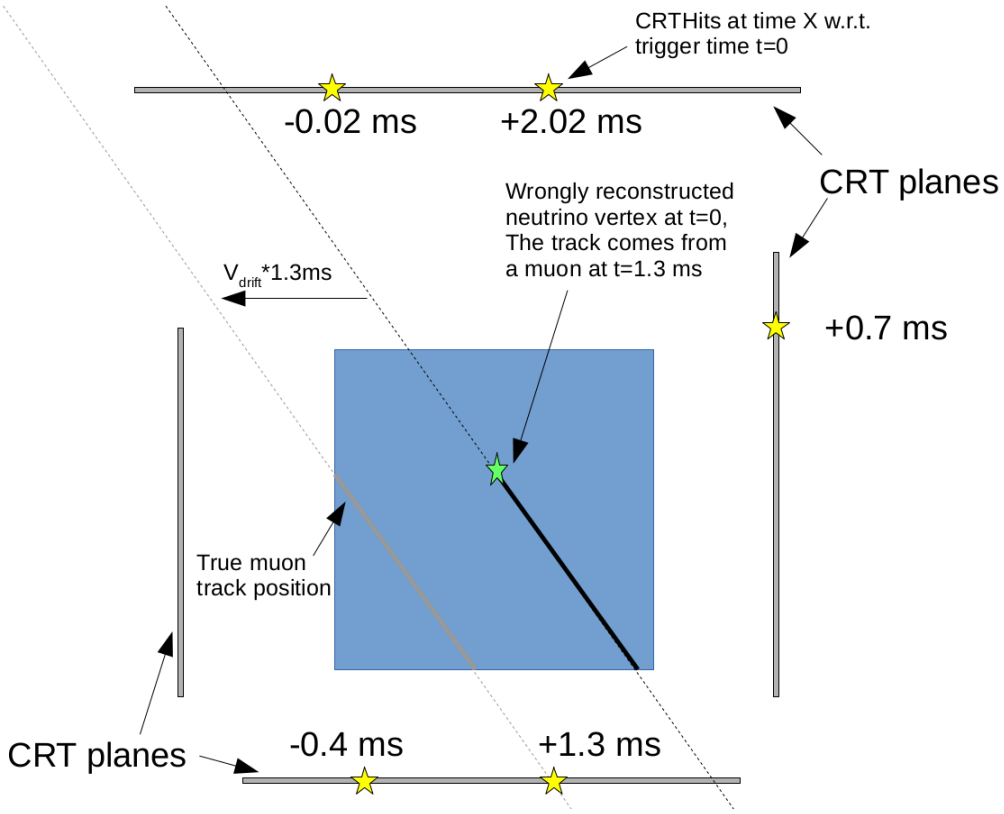

Figure 4.17.: CRTHit - track association: A track is shifted to different times of the CRTHits in the event. If the extrapolated track matches the position of a CRTHit if the track is shifted according to the time of the CRTHit, a association between the track and the CRTHits is formed.

4.5. CRT Time Corrections

The procedure as described in the previous section 4.4 theoretically allows a comparison of the timestamps of the different systems with the convoluted time resolution of each system. By analyzing the actual data three different problems were discovered which lowered the performance of the CRT for cosmic rejection significantly: A GPS time problem in the CRT system, a problem in the memory buffer of the FEB, and problems in the trigger time calculation of an event in the LArTPC.

First the GPS problem in the CRT is discussed. As described in the section 4.1, each FEB receives a PPS reference pulse each second which enables the generation of a time stamp in a global time reference. This pulse comes from a GPS receiver module in the rack which needs to be connected to an antenna to receive the GPS signal. For testing of the CRT during the installation phase, the module was configured to not rely on a GPS signal but simply stream out a PPS with respect to an internal clock not synchronized to any reference. The reconfiguration of the module to provide GPS driven PPS was forgotten at the commissioning of the CRT. For this reason all FEBs

of the CRT in MicroBooNE received the PPS pulse of an independent free running clock since the commissioning until the 1st of December 2017 where this error was resolved. The effect of this mistake was that the CRT had a unique timing by itself but not with the rest of the detector.

The CRTHits can be formed without any problems but the merging to the LArTPC data stream leads to no meaningful CRT data added to each event. A way to resolve this issue is given by the fact that the CRT also receives the beam trigger reference pulse as the LArTPC does. The time the reference pulse is received is registered in the CRT and the matching of the arrival time pattern of these triggers can be used for correction of the global timestamp of the CRTHits.

I did this for the data where there are beam triggers available. But every year there is a break during summer where no beam is delivered. For this time one can look at the difference of the NTP server time and the free-running clock and use this difference for the correction. The NTP time matching depends on the accuracy of the NTP time itself which is only in $\mathcal{O}(1\,\mathrm{ms})$. Beam-off data is needed for estimation of the purely cosmic contamination in the beam-on data but this can also be taken between beam spills. Therefore this data is less important than the data when the neutrino beam is operating.

Nevertheless, a correction can be applied and a first agreement within a few microseconds can be reached when a correction map based on the beam triggers is used. This is good enough for the matching of the CRT data to the LArTPC data stream as shown in Figure 4.18. The resolution without this GPS problem is shown in the section 4.7. Since this correction leads to a time-dependent CRT time resolution, this data is not used in the analysis presented in this work.

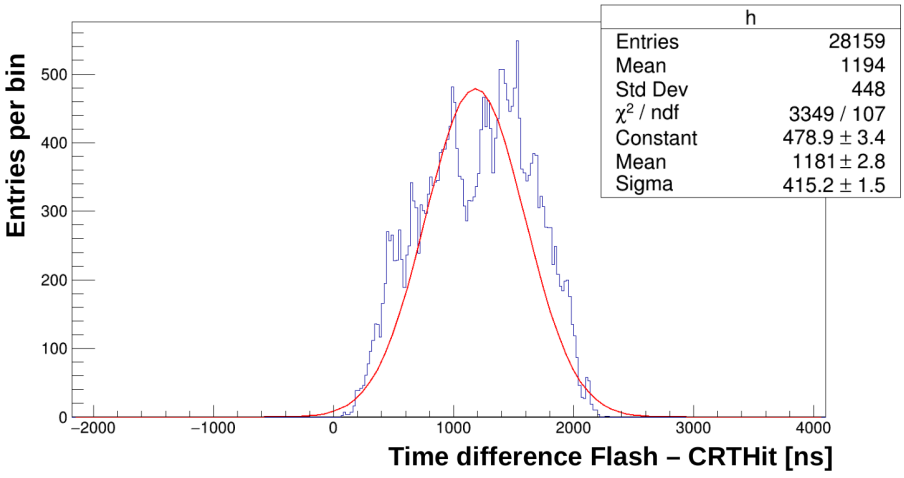

Figure 4.18.: The time difference between the light signal and the CRTHits for the time where no GPS signal was delivered to the CRT. A correction map was build based on times of beam triggers and applied in order to reach again the synchronization of the clocks in the $\mathcal{O}(1\,\mu\mathrm{s})$.

Rarely some spikes appeared in the distribution of the timestamps of one or more modules. This was already seen in the testing phase of the first modules during the CRT production at Bern. It was first believed that these are some old interaction times coming from the buffer in the FEB where they got stuck. Since they seemed not to harm the rest of the DAQ and occurred very rarely they were considered as not a problem. After a while, it was discovered in the CRT of MicroBooNE that the second assignment starts to fail for some part of the CRT data taken, mostly at the end of a four-hour data-taking period. By checking what causes this behavior I checked the time of the polls and compared them to the time of the registered CRT interaction in this readout. I saw that the time difference between the first interactions of a readout and the time of the poll starts to increase over time since the data run was started. This can be seen in Figure 4.19. A restart of the CRT DAQ reset the deviations.

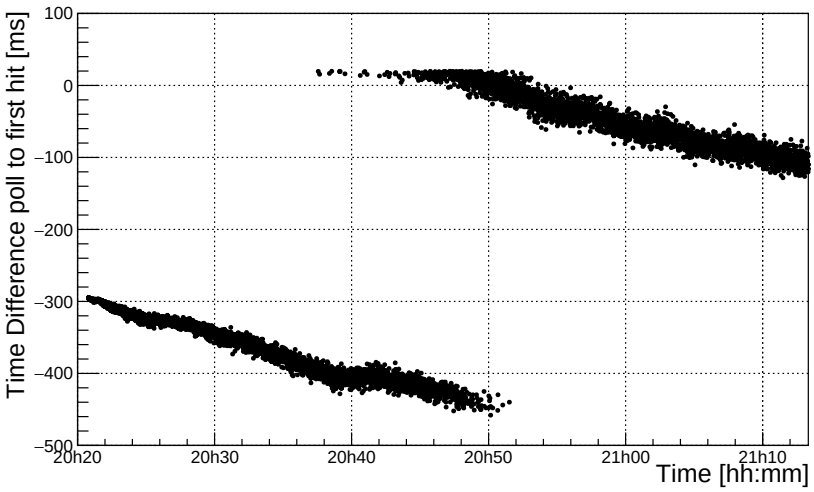

Figure 4.19.: The time difference between the first CRT interaction in a poll and the start of the poll time in millisecond. The poll time for this test measurement in Bern was set to 300 ms. As one can see the absolute time difference increases up until the first interaction is overwritten by a newly registered one. The slight offset at the start and for the first overwritten timestamp comes from the duration of the poll and eventual differences between NTP and GPS time.

The issue causing this feature turned out to be a memory problem inside the FEB. Each FEB has two CPUs, one for writing newly registered interactions and one for sending them out during a poll. When a FEB is read out it sends out all triggered interactions in the ring memory buffer since the last readout. It can happen that this number is not reflecting the actual number of new interactions and therefore the buffer which is readout becomes misaligned by one memory slot. This happens from time to time and starts to accumulate so that the part which is read out is not anymore

the part which is newly written causing an increasing difference which can lead to an overwriting of not yet readout interactions with new ones and therefore results in a loss of interactions. I observed that this behavior depends on the interaction rate in the specific CRT module. For the interaction rates at MicroBooNE the overwriting does not occur within the four-hour data run but the second assignment can run into problems. Therefore only the second assignment had to be corrected to fix the problem for MicroBooNE, and to be sure, the run time for the CRT is restarted every 2 hours instead of every 4 hours. For the SBND CRT another solution will be applied. Since this experiment is not yet assembled, the firmware of the FEBs will be changed so that they do not use a ring buffer but a linear one where this problem will be reset after each poll.

Another feature observed was that the event trigger time difference of the LArTPC data stream and the CRT system showed a time dependent disagreement in the $\mathcal{O}(1\,\mu s)$, see Figure 4.20. The cause of this was tracked down to the trigger timestamp of the LArTPC event. Since the disagreement does not cause any problems for the CRT merging to the LArTPC data stream this problem can be solved by actually matching the timestamps of the light signals and the CRTHits for each event individually. I use for this correction the CRTHit times of geometrically matched CRTHit - track associations and the matched light signals of these tracks. This ensures that only times are compared which coming from the same interaction. This correction leads to the agreement of all the timestamps on a level comparable to the time resolution of each system. The time the particle needs to propagate from one system to another is negligible for the time performance of the reconstruction of the PMT signals in MicroBooNE.

These corrections are among other things a reason for the difference in the performance of the CRT system in the experiment and its performance as a stand-alone tool in the lab.

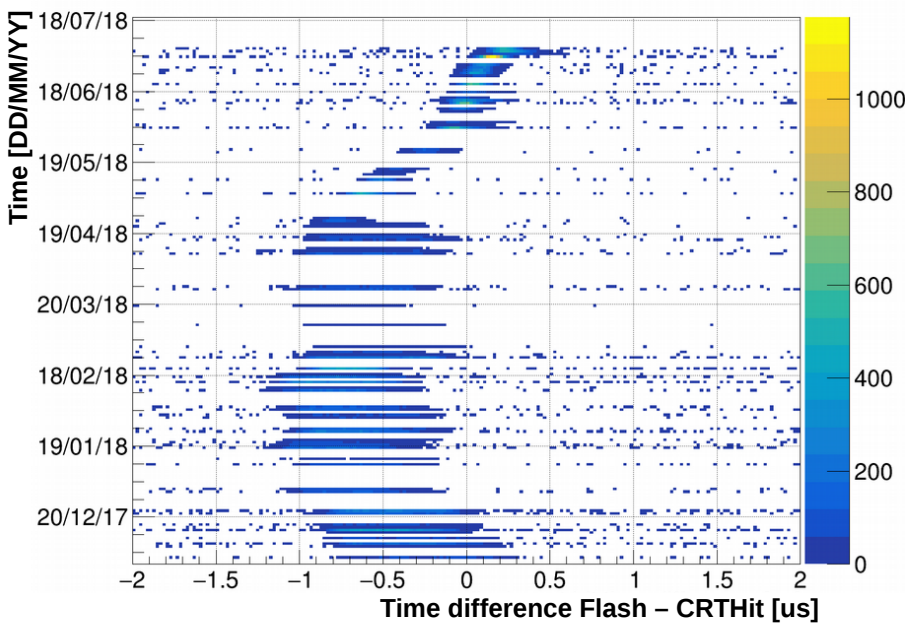

Figure 4.20.: There is a time dependent time shift of the trigger time stamp leading to a shift of the time stamps of the CRT and the LArTPC.

4.6. CRT Simulation in MicroBooNE

While the performance of the CRT by itself can be largely estimated by measurements, the impact on a neutrino analysis has to be simulated. The simulation described here is based on the implementation in the MicroBooNE experiment.

The data of the CRT is generated in the FEBs and include only SiPM amplitudes and time stamps which are first reconstructed to CRTHits in 3D space and time and brought in a common data format. The simulation follows a slightly different workflow. A CRTHit is directly simulated including already the time corrections and the detector response. The amplitudes on the SiPMs are calculated by taking the angle of a track with respect to a CRT module into account. Also, dead channels are considered coming from a database that includes changes in time, for example when a channel suddenly appears to be non-responsive. For this reason, the simulated interactions are not treated by the same pair building reconstruction algorithm and several time corrections as done for the data are not needed.

The position of the SiPMs is taken from the position file which is also used for the reconstruction. So changes between the real CRT module position and a reconstructed CRTHit would only show up in data but not in the simulation since we assume that the CRT modules are exactly placed as they are in the reconstruction. Therefore some difference between simulated CRTHits and data is expected when a TPC-reconstructed track is projected to the CRT.

The simulation is validated by comparing it to data. The differences between the simulation and data regarding the position are small and not expected to have an impact on an analysis. Small differences in the track to CRTHit association were found at a 1% level for tracks where more than 20 cm is reconstructed in the LArTPC. This is caused by effects not included in the simulation like the dead time of the FEBs after receiving a reference signal (T1 or T0) or the small differences in the geometry.

The energy deposition is smeared according to the smearing observed in the CRT data. The simulation reproduces the energy spectrum of measured CRTHits except a low energy tail. For this reason, in this analysis, only simulated CRTHits are used above 70 photo-electrons where the spectrum of the simulation agrees with the measured one.

4.7. CRT Response and Performance

In this section, the result of the measured performance is presented, first for a single module and then for the CRT system as implemented and reconstructed in the MicroBooNE experiment. The performance for other experiments like SBND can deviate from the numbers stated for MicroBooNE since the physical realization is different as well as eventual differences of the reconstruction chain in the experiment.

4.7.1. Single Module Performance

The performance of a single module was tested at Bern by using a 1.8 meter × 4.1 meter prototype. The spatial resolution was derived from a measurement with a muon telescope placed at different positions within one scintillator bar. Figure 4.21 shows the true versus reconstructed location between the two WLS fibers within one scintillation bar on the left side. On the right side, the RMS is given for the different positions. The resolution is better than 2 cm for every position in one scintillator bar.

For the measurement of the timing capabilities, a pulsed laser was used. The trigger of the laser was also sent and recorded by the FEB. The laser pulse was induced to the module at two different distances from the readout. Like this, also the light propagation velocity inside the module can be measured by taking the time difference and the distance of the laser injections into account. The result of this study is shown in Figure 4.22. By taking the RMS of the time difference between the laser injection and measurement of the signal in the FEB one can check the time resolution of the system. While Figure 4.22 (a) shows the absolute measurement of the arrival time of the signal as registered by the FEB, Figure 4.22 (b) shows the resolution as a function of the signal amplitude.

Of course, this time resolution is given as a convolution of various effects. As Figure 4.22 already indicated, the photo statistic plays a role. The first photon bringing the signal at the SiPM over the threshold triggers the time, therefore the

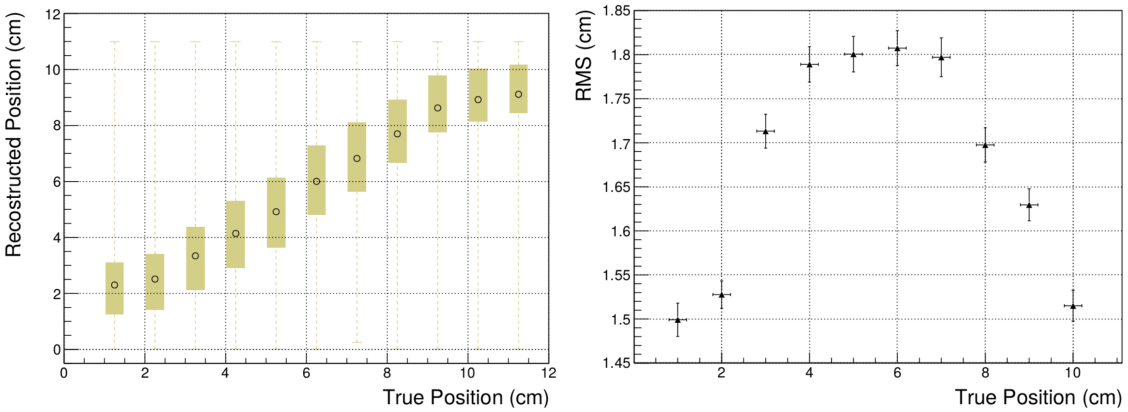

(a) reco. vs. true position (b) Spatial resolution

Figure 4.21.: Left: Reconstructed over true position of an interaction in one scintillator bar of one CRT module. The measurement is performed with an external muon telescope. Right: the RMS of the difference between the reconstructed and the true position between the two WLS fibers is below 2 cm [6].

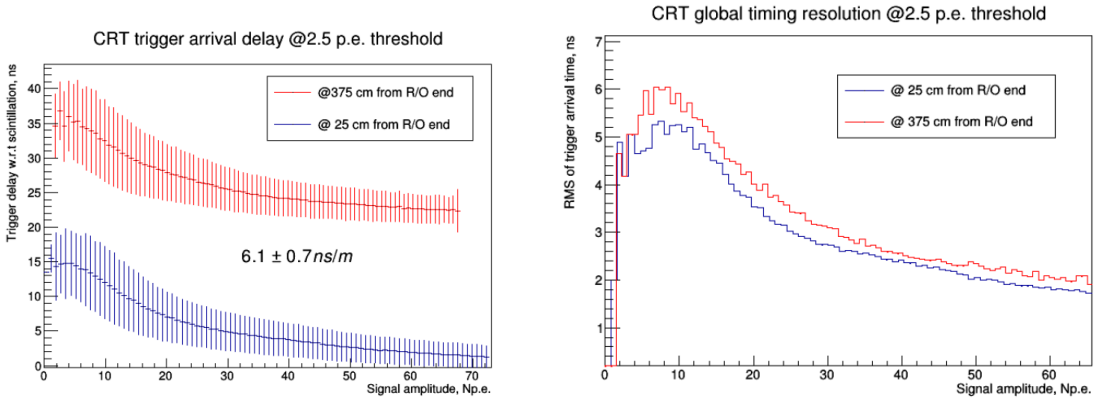

(a) light arrival time (b) time resolution

Figure 4.22.: With a pulsed laser at two position the arrival time can be measured (a) as well as the resolution (b). Here both values are given as a function of signal strength in numbers of photoelectrons detected in the SiPMs [6].

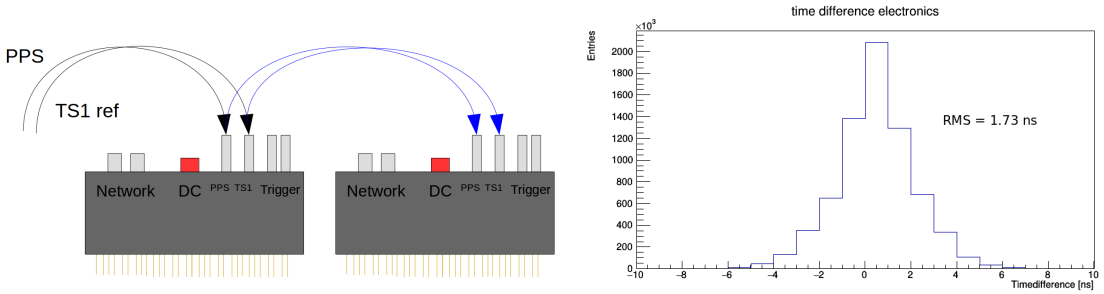

(a) Chain of FEB

(b) Time difference

Figure 4.23.: (a) The intrinsic time resolution of a FEB measured by a chain of FEBs connected to a reference pulse. (b) The resolution is given by the time difference of the time stamps of the reference pulse.

more photons are produced the less is the jitter coming from the different time constants of the various absorption and re-emitting processes inside the module. An intrinsic limit is the time resolution of the FEB itself. This was also measured by sending a reference pulse through the TS1 input on the FEB to two different FEBs and then checking the time difference between the registered arrival time. Since the signal cables are short ($\approx 20\,\text{cm}$) and have the same length, the timing resolution of one FEB is directly given as the time difference of the reference pulse registered in the two different FEBs divided by the $\sqrt{2}$. The setup and the result is shown in Figure 4.23.

As one can see in Figure 4.22, the time resolution depends on the light yield. The intended particle to measure is a muon and the minimal signal it leaves in one module is when it hits the module perpendicular. The light yield of a perpendicular crossing muon is measured again with the help of the muon telescope at different distances from the readout. The result of this is shown in Figure 4.24 (a). In (b) the detection efficiency is shown for different distances from the readout. The efficiency is for all locations higher than 95% and in average 30 PE are measured for a muon crossing the module perpendicular.

These measurements have all been made by using a single module in the lab. Of course, the performance of the fully installed CRT differs from a single module in the lab. Now follows the measured performance of the CRT installed at MicroBooNE.

4.7.2. CRT Performance at MicroBooNE

One single module has a spatial resolution better than 2 cm and a time resolution of $\mathcal{O}(1\,\text{ns})$ and detection efficiency of more than 95% at more than 4 m from the read out. But this is not what counts since the CRT will not consist out of just a single module. The more complex cabling with longer cables could lower the time

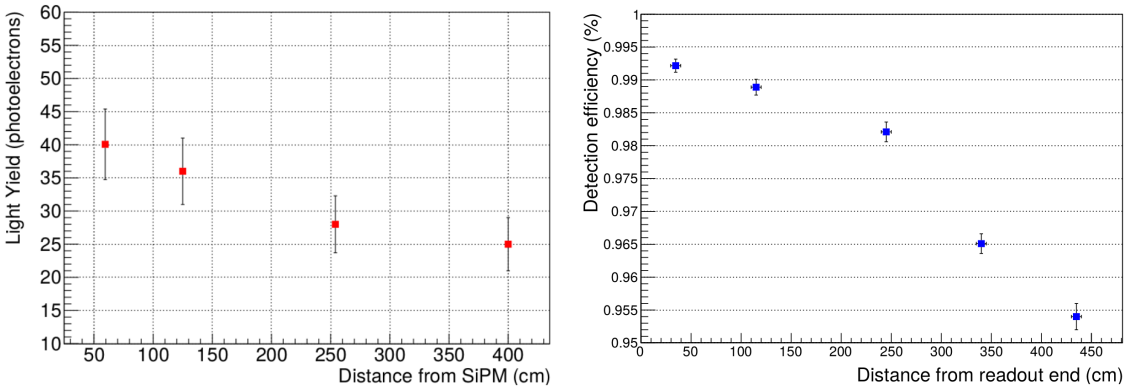

(a) Light yield

(b) Detection efficiency

Figure 4.24.: The light yield and the muon detection efficiency of one CRT module as measured in the lab using a muon telescope [6].

performance and an eventual misalignment between the actual and reconstructed position of a module leads to a lower accuracy of the position. The requirement to have at least two signals, one in an X module and one in a Y, leads to a lower detection efficiency but provides two measurements of the same particle. So, the time resolution will profit from the second measurement.

To measure the performance of the CRT system, one has to compare it to another value. For this, the measurement of the LArTPC is used, which also does not have infinite resolution. In Figure 4.25 (b), one can see the time difference of the flash measured in the beam time and the CRTHit time if there was any. Only cosmic induced events are used for this measurement. A Gaussian fit is applied and the sigma is 32 ns which is a convolution of the CRT resolution and the resolution of the reconstructed light signal. Since the light signal reconstruction has an intrinsic resolution of around $100\,\text{ns}/\sqrt{(12)} = 29\,\text{ns}$ it contributes in a major way to this. The offset of the distribution comes from an offset in the reconstruction of flashes inside the beam window and outside the beam window. The median of the difference in time of light-matched tracks and CRTHits is used for the time correction explained in Section 4.5. Therefore a shift between out of beam signals and in-beam signals shows up.

To see the time resolution of the CRT itself one can look at Figure 4.25 (a) where the time difference between the signal in an X and a Y module is shown. The histogram contains CRTHits of the bottom plane. A single CRTHit has therefore a time resolution of $5/\sqrt{2}\,\text{ns}$.

To see how the CRT performs is in terms of position, a track that goes through the anode or cathode was extrapolated to the CRT. Of course, by doing this, uncertainties of the track reconstruction and the extrapolation are added in, so this represents not the position capabilities of the CRT but more of the CRT+LArTPC. To illustrate

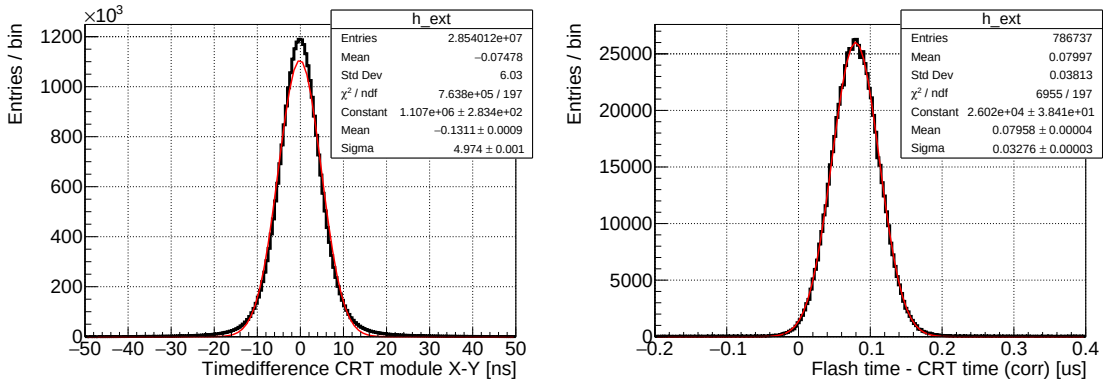

(a) time difference X-Y CRT module (b) corrected time difference Flash - CRTHit

Figure 4.25.: The time difference of the light signal and the CRTHit in the beam window of a sample containing only cosmic signals. All the described corrections are applied.

the performance anode or cathode piercing tracks (as for the timing) are used. In Figure 4.26 one can see the difference in the bottom plane of the CRT. Some offsets are different for each CRT plane but the resolutions are similar as expected.

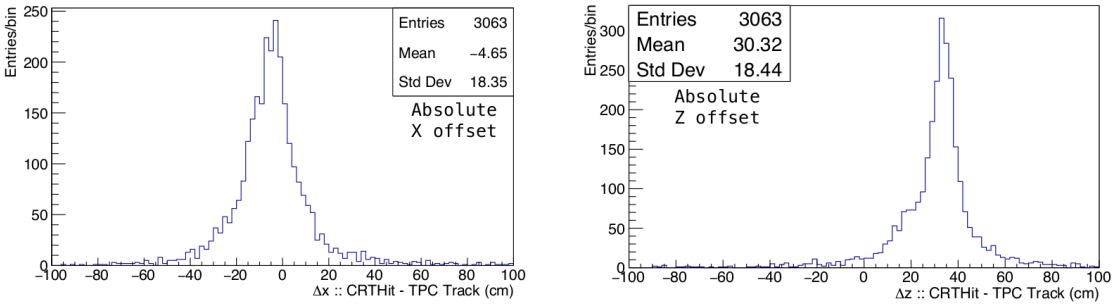

Figure 4.26.: The difference of the extrapolated track position on the CRT bottom plane and the CRTHit in coordinates of X and Z.

Here, only the example of the bottom plane is shown but the resolution and offsets for the side planes are very similar. The Top plane comparison performs the worst but also the extrapolation has the biggest effect for this plane since it is the plane furthest away from the LArTPC, see Figure 4.27.

So as one can see in Figure 4.25 and 4.26, the performance of the CRT itself is within its expectations. The time resolution is in the $\mathcal{O}(1\,\text{ns})$ but the time reconstruction of the rest of the detector lowers the performance to the $\mathcal{O}(30\,\text{ns})$. The spatial resolution is here only compared between the CRT and LArTPC system, both contribute to the

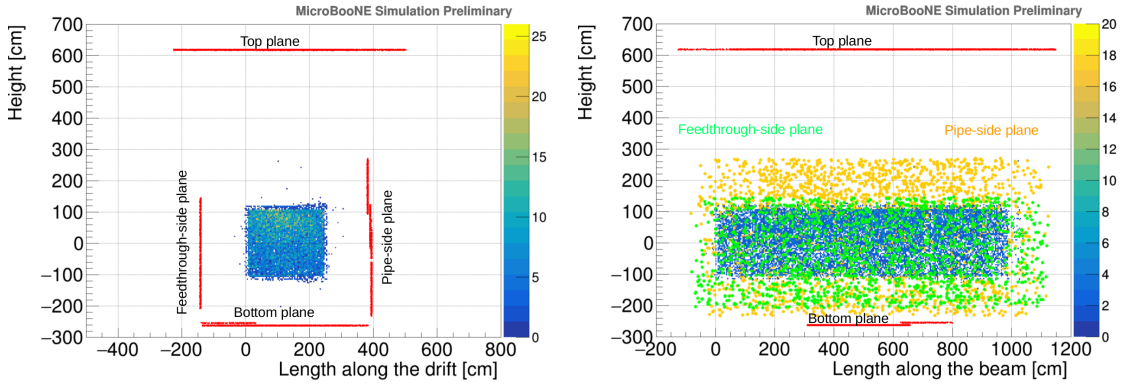

(a) Front view (b) Side view

Figure 4.27.: The CRTHits in the beam window and the start of the tracks in the LArTPC. The Top plane is 5 m above the LArTPC while the side planes are separated around 1.4 m. The bottom plane covers only a part of the bottom of the LArTPC and is 1.5 m below the LArTPC.

uncertainty of this measurement. But the positions agree within tens of centimeter allowing the tagging of tracks inside the LArTPC as it was intended to.

The matching efficiency for tracks is around 50%[11]. So half of the tracks as seen in the MicroBooNE detector also leave a signal in the CRT. The reasons why it is not close to 100% are diverse. One main reason is the coverage. There are huge gaps between the planes where cosmic muon tracks can enter the LArTPC undetected as it can be seen in Figure 4.27. Other reasons are the detection efficiency, the dead time of the electronics after recording a signal, and errors during the reconstruction. While the dead time and eventual reconstruction failures might are not fully simulated (see Section 4.6), the coverage and detection efficiency are. There is only a difference in the 1% level for >20 cm long reconstructed tracks indicating that the effects eventually missed by the simulation are only minor and the largest fraction indeed comes from the coverage.

4.7.3. CRT Performance at SBND

The test stand in the SBND pit allows a good measurement of the bunch structure in a beam spill. The CRT planes here are perpendicular to the beam axis so they see more signals coming from the BNB beam direction. Also, the planes are vertically and therefore do not cover so much of the cosmic flux as the Top and Bottom plane of MicroBooNE. On top of that, the beam signal should arrive at the same time at each plane in the CRT since they are not oriented along the beam direction. Since no

[11]Study was done by Michelle Stancari

other detector part was installed, only the CRTHits were analyzed, and therefore only its capabilities matter. No matching between different systems had to be performed.

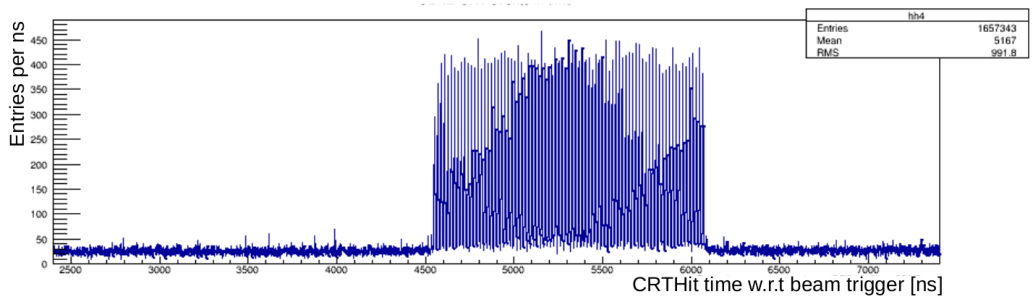

Figure 4.28.: The spill structure measured with CRT planes in the SBND pit. The signal coming from the beam is clearly over the in time cosmic background.

In Figure 4.28 one can see the signal coming from the BNB beam clearly sticks out of the continuous cosmic background with no specific time structure. One can not only recognize the spill duration of 1.6 µs but also the bunch structure within the spill. This shows that the CRT can very effectively separate beam signals from off-beam cosmic signals by timing.

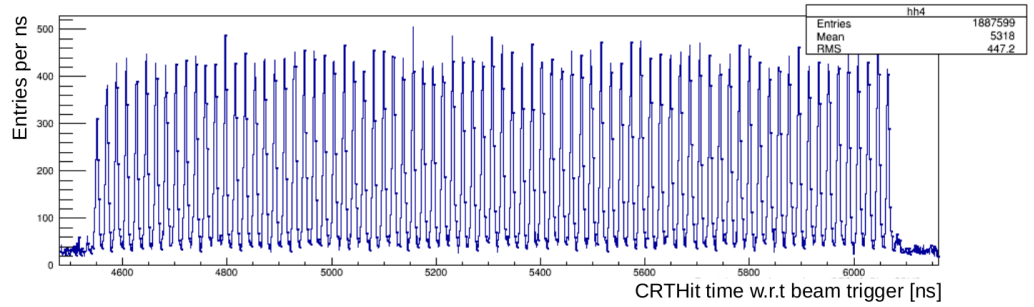

Figure 4.29.: By zooming in the spill one can even recognize the single bunches in the spill. This shows the timing capabilities possible with the CRT.

Figure 4.29 shows a zoom of Figure 4.28. In this figure, one can recognize the single bunches inside the beam spill. The cosmic background contamination is orders of magnitudes lower. This figure proves that the CRT can indeed separate interactions as within a beam bunch and outside a beam bunch at it was designed for.

Taking into account also the position of the CRTHit one can see the beam spatial distribution in Figure 4.30. Here, the background cosmic CRTHits are subtracted based on beam-off data. Since SBND is only 100 m after the beam dump of the BNB beamline, the beam will even more spread out at the MicroBooNE position at 470 m after the target.

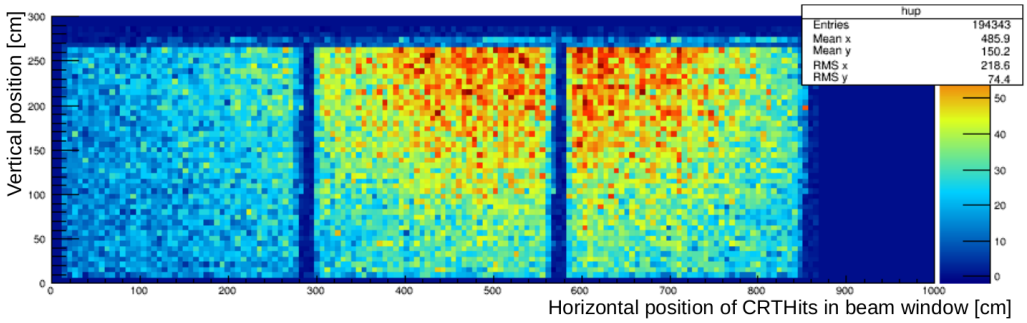

Figure 4.30.: By subtracting the cosmic contribution one can also measure the spatial beam profile. One can see that the CRT modules are not centered with respect to the beam. A fit of the profile to get the beam center agrees with the expected beam center [92].

4.8. Improvements for Neutrino Event Selection

The additional possibility to tag cosmic interactions with the CRT allows further reduction of the cosmic background. How this is done for a specific analysis depends on the choices of the analyzer but here are some general ideas and estimation of how much cosmic background can be rejected. Depending on the signal and background topology for a specific analysis, some rejection methods are more reasonable than others. In Chapter 5, some of the ideas mentioned here are applied and the specific numbers are given for the case of the specific analysis.

An estimation [6] has shown that around 8 cosmic muons enter the LArTPC of MicroBooNE in a 2.2 ms readout window. Taking the 1.6 µs beam window into account, around every 1 in 172 events have a cosmic muon in the time window of the beam passing through the LArTPC. This makes a cosmic interaction in the beam window more probable than a neutrino interaction from the BNB beamline.

With a veto of all events where there is a CRTHit inside the beam window, a large fraction of the in-beam cosmic interactions can be rejected. Of course one has to estimate the loss of signal. A cause of signal loss can be either the neutrino interaction itself has triggered the CRT or a cosmic has triggered the CRT while a neutrino interacts inside the LArTPC. Due to the larger area of the CRT, it will tag more cosmic interactions than the LArTPC in the beam window.

To minimize an eventual signal loss one can apply the CRT veto only for certain panels. Figure 4.31 shows the CRT activity inside the beam window for cosmic interactions (green), neutrino interacting inside the LArTPC (read) and outside the LArTPC (blue). One can for example only use the Top plane of the CRT as a veto since it will mainly detect cosmic interactions and only a small amount of neutrino-induced signals due to its location and orientation.

There is also a distinct distribution of the CRT hits by looking at the positions of the CRTHits with respect to the reconstructed interaction vertex. Figure 4.32 shows

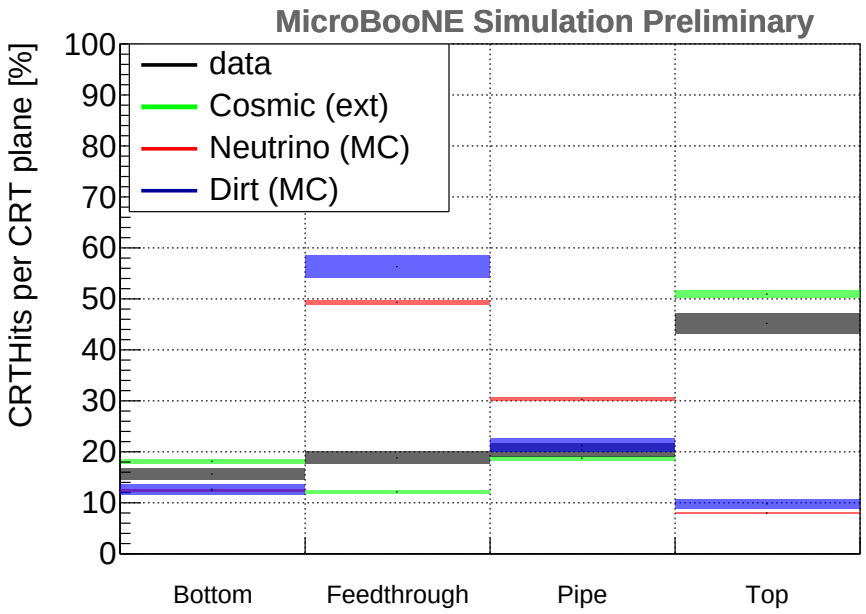

Figure 4.31.: Difference between origin of the signals showing up in the plane by plane comparison, each origin is scaled to 100%. For example, for purely cosmic signals (ext) around 50% of the CRTHits occurring in the Top plane while the Bottom plane accounts for around 18%. Since the data contains fractions of all the other samples, one can see that the amount of CRTHits is always between the purely cosmic and the neutrino sample.

the distribution of the difference in the Y coordinate (horizontal) and Z coordinates (beam direction). While cosmic tracks come from the sky above, the CRTHits are mainly below or above the interaction vertex while neutrino interactions produce the secondary particles uniformly (4.32, left). One could also use the fact that the secondary particles of a neutrino interaction are forward boosted. Due to this fact, CRTHits of a neutrino interaction are mainly downstream of the vertex while cosmic interaction has no preferred direction, the difference of the CRTHit position and the reconstructed vertex is distributed around zero for cosmic interactions, there is only a small bias due to a bias of the vertex reconstruction (see 4.32, right). What one also can see in 4.32 (b) is that most of the neutrino interactions happening outside of the cryostat (dirt) produce a CRTHit upstream of the vertex if any since these interactions happen often in the ground in front of the detector with low CRT coverage. With this distribution one can not only separate cosmic from neutrino interaction in the LArTPC but also one can separate neutrinos interaction outside the cryostat which eventually have triggered the LArTPC.

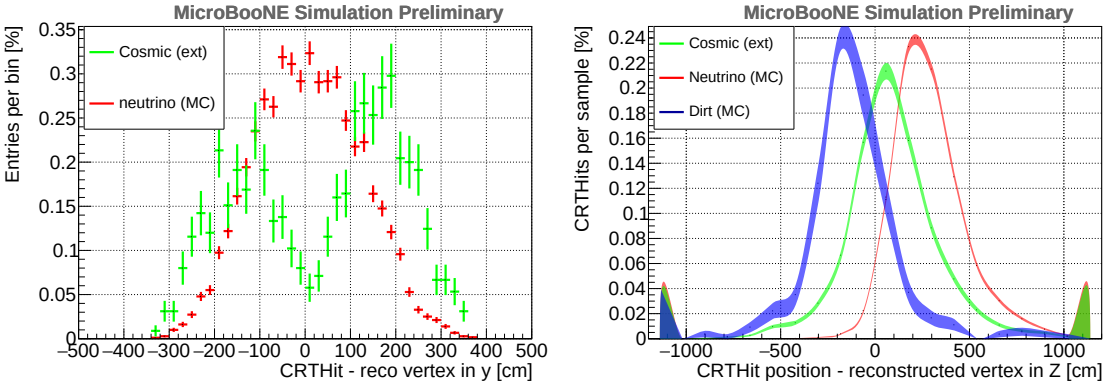

(a) Rejection on Y position

(b) Rejection on Z position

Figure 4.32.: Difference in the topology of neutrino and cosmic signals showing up in the CRT data by comparing the reconstructed vertex position in y (horizontal) and z (along beam) coordinates with CRTHits in the beam window. This allows some separation between neutrino interactions and cosmic background events. The difference along the beam even allow separation from dirt neutrino interactions from the others.

Further possibilities are to check if a track of the reconstructed neutrino interaction is tagged by the CRT. A matching to a CRTHit in the beam window can confirm the correct light-charge matching while a matched CRTHit outside the beam window indicates a wrong light-charge matching. If the reconstructed CRTHit-tagged track is contained, the matching suggests that a part of the track is not properly reconstructed. These two indications can be used for further rejection of possible cosmic backgrounds.

The suggestion of the SBN proposal [14] can also be done. 50% of all the tracks can be tagged and identified therefore as cosmic muons if they are out of the beam window. Now the correct position of these tracks is known and the distance to the reconstructed neutrino vertex can be checked. If the distance is below a certain value one can reject also these events.

As already mentioned, the advantage of background rejection and the disadvantage of an eventual signal loss has to be evaluated for each analysis individually. Generally one can say that a CRT veto is probably more suitable to electron neutrino searches than for muon neutrino searches since the probability for a muon to induce a signal in the CRT is much higher than for an electron.

In the next Chapter 5 several cuts are applied involving the CRT for a muon neutrino CC inclusive cross-section analysis. The specific rejection power and loss of signal events are stated for each cut.

5. Muon Neutrino Selection with Cosmic Removal

We want to perform a cross-section measurement using the MicroBooNE data including the CRT. The improvements by using the CRT for a measurement depend on each analysis separately. Here, the performance is shown on an analysis of the ν_μ CC inclusive cross-section. Improved measurements of neutrino cross-section, especially on argon, are needed by the neutrino community as was described in Section 2.4.

A ν_μ CC inclusive cross-section measurement only requires the identification of a muon in the final state and is, therefore, a relatively simple topology for the comparison to different models or experiments. There are no detector-specific thresholds for a variety of particles except for the muon track as more inclusive studies have.

From the technical point of view, a ν_μ CC interaction can also leave a signal in the CRT. Therefore, it is worth looking into in detail how a neutrino interaction differs from a cosmic interaction in the CRT. While for other interactions (e.g ν_e), a CRT veto is well-motivated in MicroBooNE, I wanted to use also CRTHits in the beam window for more than just a veto of the event to keep more signal events.

5.1. Data Sample

The data used in this analysis was taken from the period between December 2017 and Summer 2018 at the time where the CRT data is available in good quality for the first time. Before this period, the CRT was either incomplete (Top plane commissioning was a few months after the other CRT planes in Spring 2017) or the timing was treated differently (see Section 4.5).

The data set on which the analysis is developed contains $7.6 \cdot 10^{18}$ POT while for the final result a data set of $2.1 \cdot 10^{20}$ POT is used. This procedure is motivated by two points. First, by only looking at a small subset of data the risk of introducing a bias in the analysis is smaller, and secondly, the blinding for other analyses will not be spoiled.

The data taken during the neutrinos were present (beam-on) in the 1.6 microsecond beam window can be separated into three different groups. The first group involves all events where no neutrino has triggered the detector (cosmic). As one could see in Section 3.1, only 1 event in around 600 contains a neutrino interacting in the LArTPC. For events in this group without a neutrino interaction, the light needed for triggering

comes from a cosmic interaction, either in the LArTPC or in the surrounding argon in the cryostat.

The next group of events contains only interactions where a neutrino interaction outside the cryostat has triggered the event. The secondary produced particles have then induced a signal in the LArTPC, either in the active volume or in the liquid argon around it. These events can not be fully reconstructed and have not interacted on an argon nucleus.

Finally, the third sample contains the neutrino events where a neutrino has interacted inside the liquid argon, either inside the active LArTPC or outside. The interactions inside the LArTPC are the ones of interest since these are the interactions that can be measured. This sample can then eventually further be split into signal and background interactions, (e.g here ν_μ CC interaction and other processes).

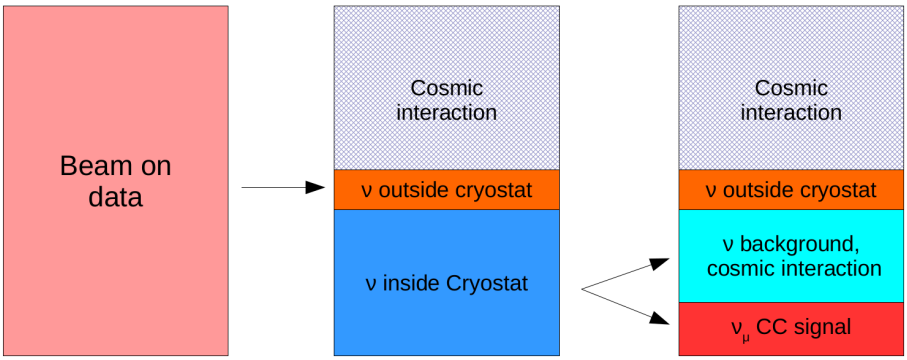

Figure 5.1.: The events measured while the neutrinos from the beam are present in the detector can be grouped in different categories: a cosmic interaction has triggered the detector without a neutrino interaction present, a neutrino interaction with the vertex outside the cryostat has triggered the LArTPC or a neutrino with vertex inside the cryostat has triggered the LArTPC. The last category can be split into signal and background events (e.g ν_μ CC and NC background).

A graphical illustration of the separation of the data in these three subgroups is shown in Figure 5.1. The reason why the beam-on data events are split into these subgroups comes from the different estimations of the number of events for each subgroup in the analysis. To calculate the cross-section one needs to know how many of the events in the final selection come from signal events and how many from background events. In MicroBooNE, we use different data sets for each group: purely cosmic interactions, interactions in the surrounding material (further called 'dirt' interactions), and neutrino interactions inside the cryostat.

The purely cosmic background is estimated by taking data in the same configuration as the beam-on data but without beam neutrino present in the detector. Therefore this is called the beam-off sample. By counting the number of beam-on events taken (ignoring whether the LArTPC has reached a signal over the threshold to store the

event or not) one can scale the beam-off sample to the same number of purely cosmic events expected in the beam-on sample. It is important that the beam-off events are taken in the same configuration as the beam-on events and the detector should be in the same state. Therefore MicroBooNE takes several beam-off events after each beam-on event.

For the other events, a neutrino interaction happened either in the surroundings or inside the cryostat. For this reason, the neutrino interactions have to be simulated to estimate the contribution of background and signal events in the final beam-on sample. The simulation is done using GENIE version v3 G18_10a_02_11a with a preliminary MicroBooNE-specific tune [54], [55]. Since MicroBooNE sees so many cosmic interactions also for events where a neutrino interaction is present, the simulated neutrino event is overlayed with cosmic data [93].

The samples used in this analysis are listed here.

- **beam on:** (open dataset)
  uboonecode: v08_00_00_25
  POT: $7.644 \cdot 10^{18}$
  Number of triggers: 1838700
- **beam on:** (full Run3)
  uboonecode: v08_00_00_50
  POT: $2.144 \cdot 10^{20}$
  Number of triggers: 51546294
- **beam off:**
  uboonecode: v08_00_00_25
  Number of triggers: 18997529
- **Dirt overlay:**
  uboonecode: v08_00_00_26
  POT equivalent: $1.25 \cdot 10^{20}$
- **BNB overlay:**
  uboonecode: v08_00_00_26
  POT equivalent: $1.268 \cdot 10^{21}$

The uboonecode version number states which specific detector software version is used during the reconstruction of the data. This is only mentioned here for completion and for the case someone wants to use the same samples.

5.2. Reconstruction

How a LArTPC can reconstruct neutrino interactions is described generally in Section 2.7. What follows is a short description of how it is done for variables specifically used in this analysis.

For the light signal, the reconstruction sums up the signal within 100 ns which defines the resolution of the system to around 29 ns. This information is further grouped to a flash which contains the mean position in the YZ-plane and the number of photo-electrons produced together with the time information.

The three wire planes of MicroBooNE read out the charge signal of the LArTPC. The charge peaks (either induction or collection) are reconstructed to a series of wire hits which are then input for various reconstruction algorithms [94] [95].

First, a topological reconstruction is performed using the Pandora framework, which inputs wire hits from the LArTPC and reconstructs potential interactions as vertices with associated track and shower particles. The charge signals from all three wire planes are clustered and a Support Vector Machine (SVM) classifies each cluster with a score between 0 and 1 [96]. By default, all clusters with a score below 0.5 are reconstructed as shower objects while all the other clusters are reconstructed as track objects.

Of these potential interactions, the one most likely to come from a neutrino interaction, as opposed to a cosmic background, is then selected by Pandora using both topological and PMT information during the 'so-called' reconstruction of a neutrino candidate slice by matching light and charge information (SliceID) process. A slice is a cluster of grouped charge depositions. During that process, the light signal is matched to the charge signal by rejecting charge clusters that are incompatible with the position (YZ) of the flash. Further, the charge signal at its position in the drift direction has to agree with the flash intensity. Since the time when a neutrino interaction can occur is known (beam window), the position in drift direction is fixed for a real beam neutrino interaction.

More events are rejected when one of the following requirements is fulfilled:

- One track of the slice hits the anode or cathode when shifted to a light signal out of the beam window
- One track can be identified as a decaying muon with wrongly reconstructed direction (points towards vertex using Multiple Coulomb Scattering (MCS) likelihood) and there is a Michele electron when the slice is reconstructed under the cosmic assumption
- If a cosmic track also matched the light, the χ^2 of the neutrino candidate slice is not at least 5 times larger
- The topology suggests a cosmic (topological score < 0.06)

A detailed description is available in the Appendix A.2 and in [12]. The Pandora framework uses the reconstructed objects and returns a neutrino candidate including the tracks and showers originating from the candidate.

To distinguish between interactions originating from cosmic rays and neutrinos interaction inside the LArTPC, a topological score is calculated using a SVM. The input is based on various reconstructed quantities like the number of reconstructed

direct daughter particles of the neutrino, the position of the reconstructed vertex and daughter particles as well as the direction of the daughter particles. From the longest track, the total and fractional wire hits and directional information are also fed in. More details are given in the Appendix A.3 or in [97].

For the particle identification, a PID variable is calculated by comparing the energy deposited as a function of distance along the track to several different particle assumptions. A detailed description can be found in [98]. The deposited energy is calculated by combining information from the three wire planes: information is used from all planes where possible, but information from planes in which the wires are parallel to a track direction is discarded since parallel tracks can lead to difficulties during the reconstruction. The total χ^2 is calculated in the following way:

$$\chi^2_{3pl} = \frac{\chi^2_{pl0} \cdot \omega_{pl0} + \chi^2_{pl1} \cdot \omega_{pl1} + \chi^2_{pl2} \cdot \omega_{pl2}}{\omega_{pl0} + \omega_{pl1} + \omega_{pl2}} \tag{5.1}$$

where χ^2_{plx} is the PID χ^2 for each wire plane and ω_{plx} is the binary weight calculated using the angle between the reconstructed track and the wire orientation of each plane:

$$\omega_{plx} = \begin{cases} 1 & \text{if } sin^2(\omega_{wirex}) \geqslant 0.05 \\ 0 & \text{if } sin^2(\omega_{wirex}) < 0.05 \end{cases} \tag{5.2}$$

The momentum for exiting tracks is calculated using the MCS behavior of muons inside LAr. This is generally described in Section 2.7 and how it is realized in MicroBooNE is described in [99]. The Highland equation given in Equation 2.14 is modified to take the angular resolution of the detector into account as well as a fit of the GEANT4 simulation. The momentum is reconstructed by range for tracks that are fully contained. A track is labeled as contained or uncontained according to the following condition:

- **Contained:** Track end is within a volume of 5 cm inside of the active LArTPC
- **Uncontained:** Track end is outside a volume of 5 cm inside of the active LArTPC

The reconstruction of all CRT related variables used in this work is described in the CRT Chapter 4 in Section 4.4. Additionally, the beam window is slightly shifted for different samples. The following definitions are used to define a CRTHit as on- or off-beam; the windows are slightly larger than the nominal beam window:

Sample	Beam window
beam-on	[3.1 us, 4.9 us]
beam-off	[3.475 us, 5.275 us]
BNB overlay	[3.05 us, 4.85 us]
dirt	[3.05 us, 4.85 us]

Table 5.1.: The time window used with respect to the trigger time in order to classify CRTHits as on- or off-beam. The windows are slightly different by a constant offset.

5.3. Simulation

The most seen signals in MicroBooNE are cosmic induced background tracks. To take these into account when predicting a beam neutrino event, a simulated neutrino interaction is overlayed over a cosmic beam-off event. The beam-off event is taken without applying any trigger condition in order not to introduce any bias regarding the cosmic part of the event.

The neutrino interaction is modeled by the GENIE version v3 G18_10a_02_11a with a preliminary MicroBooNE-specific tune and the out-going particles are then propagated using GEANT4. The energy deposition of each particle is then translated into a number of electron-ion pairs taking into account recombination. The electrons are then transported to the wire planes including attenuation as well as diffusion. Finally, the wire response to the arriving electrons is simulated. A signal on up to ten neighboring wires in both directions is taken into account for proper simulation of induced charge on neighboring wires. Unresponsive wires can be masked based on a database. The electronic response of the induced charge on the wires includes also the simulation of electronic noise. A detailed description can be found in [94] and a validation study using simulation-data comparison is described in [95].

The waveforms for the light signal on the PMTs are simulated and overlayed on the waveforms of the underlying cosmic event. Also for these signals, the gain of the PMT signals can be adjusted according to a database since a degrading over time is seen in the data.

Further reconstruction is then done similarly as for data. One difference is that the simulated signals can be backtracked from the reconstructed objects to the originally simulated ones. For this reason, one can always check if a reconstructed object originates from the simulation or the underlaying cosmic event. These events are neither data nor purely simulation but a mixture of both.

The CRTHits are also partly coming from cosmic data and simulated energy depositions from a neutrino interaction. This is described in Section 4.6.

The cosmic data used for the overlay is taken by simply reading out the detector when no beam neutrino is present and without any trigger conditions applied in order not to introduce a bias. The mixture of real unbiased cosmic data and simulated

neutrino events corresponds to the best knowledge of our events where a neutrino interaction is present. The number of these interactions is calculated using the equivalent POT for a simulated event and is then scaled to the POT in the beam-on sample. A detailed description of the overlaying process can be found in [93]. The simulation of the initial neutrino interactions inside the cryostat differs from the simulation of the interactions outside due to different target materials. For this reason, these two types of interactions are separated into different samples: a 'dirt' overlay sample and a BNB overlay sample. Both containing real cosmic events overlayed with simulated neutrino interaction either outside the cryostat (dirt) or inside the cryostat (BNB).

5.4. Signal Definition

Now we have all our samples in hand: beam-off for the estimation of the purely cosmic background, the dirt sample for the neutrino-related background for interactions outside the cryostat, and the BNB sample for the estimation of the interactions happening inside the cryostat. The next step is to look into the different interactions and try to select only the one wanted: the signal events. The **true definition** for this ν_μ CC inclusive analysis is the following:

- A true ν_μ CC interaction
- The interaction happens inside the true fiducial volume
- The muon produced in the CC interaction has to have a true momentum > 150 MeV/c

The fiducial volume is defined as at least 10 cm from all sides of the active LArTPC volume and 50 cm from its end of the active LArTPC with respect to the beam direction. This ensures that the vertex and with the start of all the direct produced particles can be reconstructed and avoids wrongly reconstructed cosmic tracks to be mistaken as tracks originating from a neutrino interaction. The stronger cut at 50 cm is motivated by the momentum reconstruction. Since most muon tracks are forward boosted, there is more space where the track can be reconstructed which leads to better momentum reconstruction.

The minimum momentum of 150 MeV is required since the efficiency for lower momentum muons is basically zero for the selection developed in this analysis. This requirement introduced after the selection was developed to restrict the measurement to the phase space where it actually can measure a signal. Other MicroBooNE analysis have no or different restrictions. More discussion about the efficiency at different momenta is in the following section (5.6) about the performance.

Every simulated interaction corresponding to the true definition, even if not reconstructed at all, is accounted for in the number of generated interactions $\nu_\mu^{\text{generated}}$.

The **true selected** interactions have to fulfill requirements both the true definition as well as the correct selection of the primary muon track from the ν_μ CC interaction:

- A true ν_μ CC interaction
- The interaction happens inside the true fiducial volume
- The muon produced in the CC interaction has to have a true momentum > 150 MeV
- The muon produced in the CC interaction is the one selected
- The interaction passes the event selection

The requirement that the selected track is a muon from the ν_μ CC interaction is realized by requiring that at least 50% of the hits of the track in the LArTPC originate from energy depositions of the simulated muon. All interactions fulfilling the true selected requirements are accounted in the number $\nu_\mu^{\text{selected}}$.

All interactions which are reconstructed, passing the selection, and do not fulfill the requirements of the true definition or failing the muon matching, are regarded as background.

With these definitions, one can define some measures of the performance of a selection: efficiency and purity. The efficiency is defined in the following way:

$$\text{efficiency} = \frac{\nu_\mu^{\text{selected}}}{\nu_\mu^{\text{generated}}} \tag{5.3}$$

Where $\nu_\mu^{\text{selected}}$ corresponds to the number of ν_μ CC signal events passing the selection cuts and $\nu_\mu^{\text{generated}}$ corresponds to the total number of ν_μ CC true events initially generated in the simulation.

The definition of the purity which is used in this analysis is given by:

$$\text{purity} = \frac{\nu_\mu^{\text{selected}}}{\nu_\mu^{\text{selected}} + \sum \text{background}^{\text{selected}}} \tag{5.4}$$

To give an overview of the different background grouped in the analysis follows here a short list:

- $\boldsymbol{\nu_\mu}$ **CC (not** $\boldsymbol{\mu}$**)**: ν_μ CC interactions where the primary muon track from the ν_μ CC is not selected
- $\boldsymbol{\nu_e}$ **,** $\boldsymbol{\overline{\nu_e}}$ **CC**: ν_e and $\overline{\nu_e}$ CC interactions
- $\boldsymbol{\overline{\nu_\mu}}$ **CC**: $\overline{\nu_\mu}$ CC interactions
- **NC**: Neutral current interactions of any neutrino type
- **OUTFV**: Interactions which happen outside the fiducial volume but are reconstructed inside

- **Cosmic**: A neutrino interaction is present but a cosmic interaction is selected
- **Dirt**: Passing event of the dirt sample where a neutrino interaction outside the LArTPC is present
- **Beam-off**: Passing event where no neutrino interaction is present

Since the efficiency cares only about signal events it is higher the fewer events are cut away while the purity is maximal when all the backgrounds are rejected and more than one signal event remains. To find a good balance between these two often their product is optimized during the selection development. This minimizes the statistical uncertainty on the measurement under the assumption that the statistical uncertainty of the background prediction is negligible [100]. The number of simulated interactions and for this analysis also the number of off-beam cosmic interactions is much larger than the number of measured interactions, therefore this is true for many analyses like this one. Purity times efficiency is used as an optimization criterion for a few other cuts in this analysis.

5.5. Event Selection

We start from a large sample of events corresponding to a BNB beam pulse which have a small purity in terms of muon neutrino interactions due to the small interaction cross-section and a sizable contribution from cosmic ray interactions. Then, we apply a series of event selection cuts to increase the purity.

As a first step, we require that the Pandora-based reconstruction has identified a neutrino interaction from the 3D event topology with at least one track present (see previous Section 5.2). The application of this step results in a sample containing largely neutrino interactions and the cosmic background is reduced significantly. The charge to light signal matching is done at this step to ensure that the selected charge signal has triggered the LArTPC. On top of that, several requirements are applied which reject cosmic signals, the details are in the reconstruction Section 5.2. This first selection acts as a start point for all further cuts.

Out of such a reconstructed event, one track has to be selected as the muon candidate track which will then further be used for cuts. Also, the kinematic variables over which the cross-section is made are coming from the reconstruction of this track. The muon candidate selection procedure goes as shown in Figure 5.2. The criteria are based on a two-dimensional purity times efficiency optimization for the χ^2 values of the PID under the different assumptions. This procedure selects a muon if there is one in the simulation in >95% of the cases if the reconstructed track length is >8 cm and more than half of the hits of the track are traced back to the muon. The wrongly selected tracks are mainly pions (1.6%) and protons (1.3%). No event is rejected during this process.

With the Pandora-based neutrino reconstruction and the muon candidate track selection, one can first look into several properties of the data and the muon kinematics.

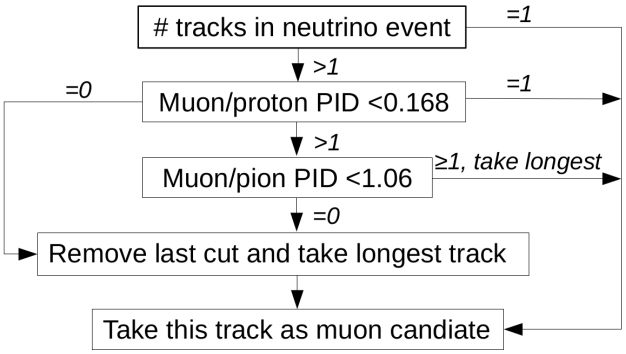

Figure 5.2.: Selection and identification of the muon track candidate from the neutrino interaction for different number of track. No event is rejected with more than zero tracks.

This, along with the requirement that the vertex is within the fiducial volume, builds what will be called the preselection. The distributions of the events after this first selection and the choice of one muon candidate track are shown in Figure 5.3.

The cases where not the muon track from the neutrino interaction but another (mainly a proton or a pion) is selected as the muon track are labeled as "ν_μ CC (not μ)". These events are in principle ν_μ CC events, but since in this case, we do not measure the muon properties these events are labeled as background. Further, there are two groups accounting for other CC neutrino interactions ("$\overline{\nu_\mu}$,ν_e and $\overline{\nu_e}$") and a group for neutral current background ("NC"). All neutrino interactions where a track from the interaction is selected but the true vertex is outside the fiducial volume are grouped as out of fiducial volume ("OUTFV"), while all cases where no track from the simulated neutrino interaction was chosen but a cosmic track from the overlaid off-beam event are going in the "Cosmic" group. The interactions passing the selection from the simulation of neutrinos in the surrounding the active LArTPC are grouped as "Dirt" and the contribution from the "beam-off" sample is the data part of the stacked histogram.The relative fraction with respect to the total number of events after each cut for each group is given in the figure indicates the purity at this stage.

As one can see, already one third of the events are signal events, and around 50% (accounted in the "Beam-off" + "Cosmic" group) are cosmic interactions. The distributions show good agreement between data and the stacked signal and background estimations which indicates the correct application of the scaling factors using the POT information or the number of triggers taken. While the $\cos(\theta)$ distribution shows a data/MC ratio around 1 for all bins, the momentum distribution shows an excess around 600 MeV of less than 10% and an overestimation of the number of events at 1 GeV and above.

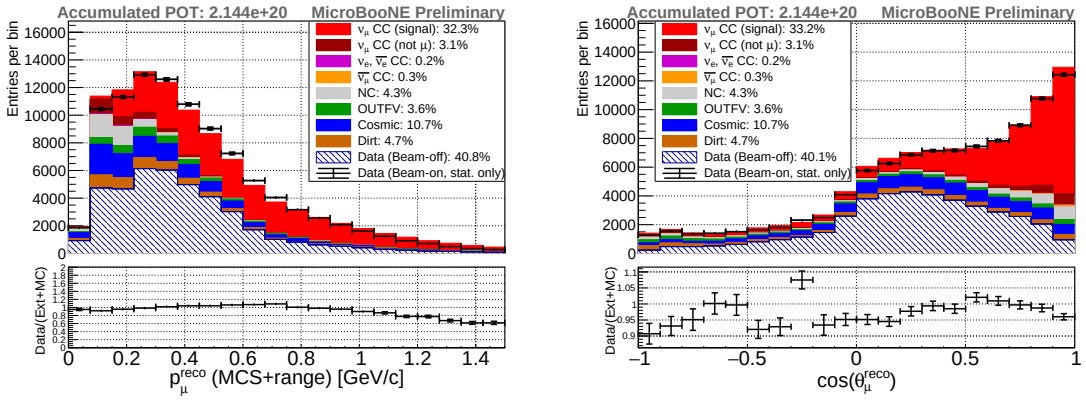

(a) Muon momentum

(b) $\cos(\theta)$

Figure 5.3.: The distribution of the neutrino interaction over reconstructed momentum (MCS and range-based, left) and over the $\cos(\theta)$ angle (right). Both variables are calculated for the muon candidate track of the event. Next to the signal in red, different groups of background interactions are listed (see Section 5.4.)

After this preselection, still, around 50% of the selected muon candidate tracks originate from cosmic interactions. This background is now reduced with several cuts making use of the CRT. As one can see in Figure 4.31 in Section 4.8, 50% of the cosmic induced CRTHits happening during the beam window occur in the CRT Top plane while only <10% are induced by a neutrino interaction. Therefore a cut is introduced which rejects all events when there is a CRTHit in the beam window in the Top plane. The separation of neutrino induced events and purely cosmic events is clearly visible in Figure 5.4 with the cut drawn into the histogram. With this cut, nearly no signal events are rejected but a good fraction of the beam-off events are. Also, most of the neutrino-related background passes this cut which can be interesting for an analysis looking for a different neutrino signal.

Now there are only CRTHits in the side planes and the bottom plane in the beam window available for further cuts. These planes are, different from the Top plane, only around 1.5 m away from the LArTPC instead of over 5 m. As shown in Section 4.8, Figure 4.32, the position of the CRTHits with respect to the interaction vertex separates between cosmic interactions and neutrino induced events. While the distribution for the Y-difference of the CRTHits and vertex for cosmic and neutrino induced interactions overlaps largely, there is a clear separation in the distribution of the difference in Z. Not only are nearly all of the neutrino induced CRTHits downstream of the vertex and the cosmic distribution is symmetrically located at nearly zero but also the dirt background distribution is clearly different from the neutrino case. Therefore one can reduce the cosmic as well as the dirt background

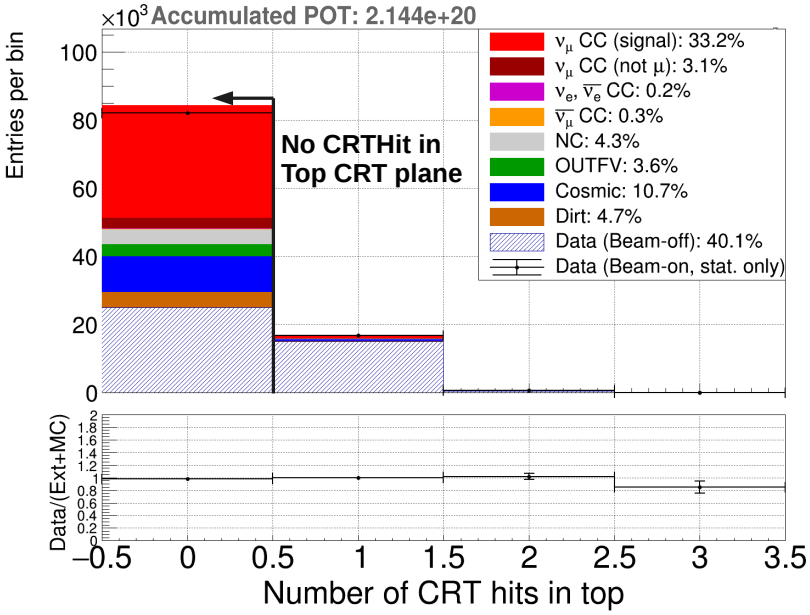

Figure 5.4.: After the preselection a veto is introduced rejecting all events where a CRTHit in the beam window in the top plane is present. Mostly cosmic interactions from the beam-off sample are rejected.

significantly by a cut of this difference. The chosen cut value is at zero, so for an event to be kept, a CRTHit has to be downstream of the vertex if there are any in the beam window. As one can see in Figure 5.5 also with this cut a large fraction of the remaining cosmic off-beam background can be eliminated as well as a part of the dirt.

After these two CRT cuts, there are still some interactions that are triggered by a cosmic in time with the beam. As a final cut for CRTHits in the beam window a complete veto is applied for events where the muon candidate track is contained as defined in Section 5.2. The probability that a particle from the neutrino interaction reaches the CRT is low, especially for non-muons since they have to propagate several meters. In order not to lose events where the interaction happens close to the border of the active LArTPC but the muon track still points inside, the containment requirement is only for the muon candidate track. After the two CRT cuts and the containment requirement, this cut rejects only a small amount of events, mainly purely cosmic interactions and some neutrino interactions where a cosmic track is selected as one can see in Figure 5.6.

After the CRTHits inside the beam window could be used to reduce the cosmic background by a large fraction, now the CRTHits outside the beam window are taken into account. In order to associate the CRTHits to the charge information inside the LArTPC the track-CRTHits matching is used as described in Section 4.4. Again only the muon candidate track is used and if this track points to a CRTHit outside of the

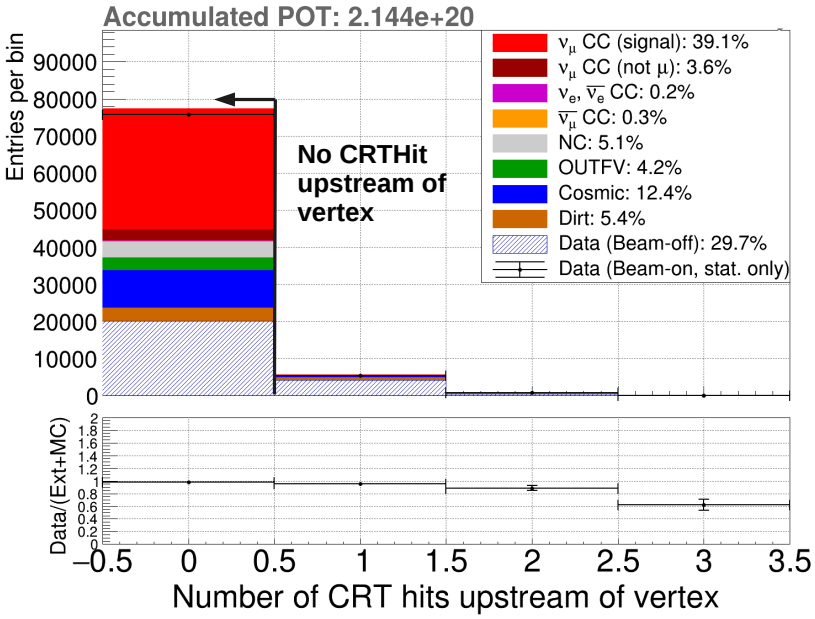

Figure 5.5.: After the preselection and the Top CRT veto, all events are rejected where there is a CRTHit inside the beam window upstream of the interaction vertex. Mainly the beam-off cosmic interactions as well as neutrino interactions from outside ('dirt') are reduced.

beam window, the event is rejected. A cosmic out of the beam window appears at the wrong X position in the LArTPC and can therefore be mistaken as a neutrino candidate, even contained. If the interaction is truly an out-of-time cosmic track the probability that the cosmic muon is selected as the muon candidate track is high and there is also a probability that this track is tagged by the CRT when entering the detector. For this reason, it makes sense to use this cut to reduce the out-of-time cosmic background. When one takes all tracks of the neutrino candidate interaction into account the probability of wrongly matched CRTHits increases, therefore only the muon candidate track is taken into account. As one can see in Figure 5.7, indeed this cut rejects a large fraction of the out-of-time cosmic where the wrong vertex is taken as the neutrino candidate.

So now the CRTHits in the beam window are used in such a way that a muon coming from the ν_μ interaction should not be rejected if it hits the CRT. Of course, especially since the CRT sees a higher cosmic flux than the LArTPC, there are some accidental rejections. The CRTHits outside the beam window are also used via the track-CRTHit associations. The only thing which was discussed in Section 4.8 but not applied in this analysis is a distance tagger. Since this is a ν_μ CC analysis a muon track is always required. Since the chance that a tagged cosmic track close by can mimic such an interaction is small, the distance tagger intends to be applied to a ν_e analysis rather than a ν_μ.

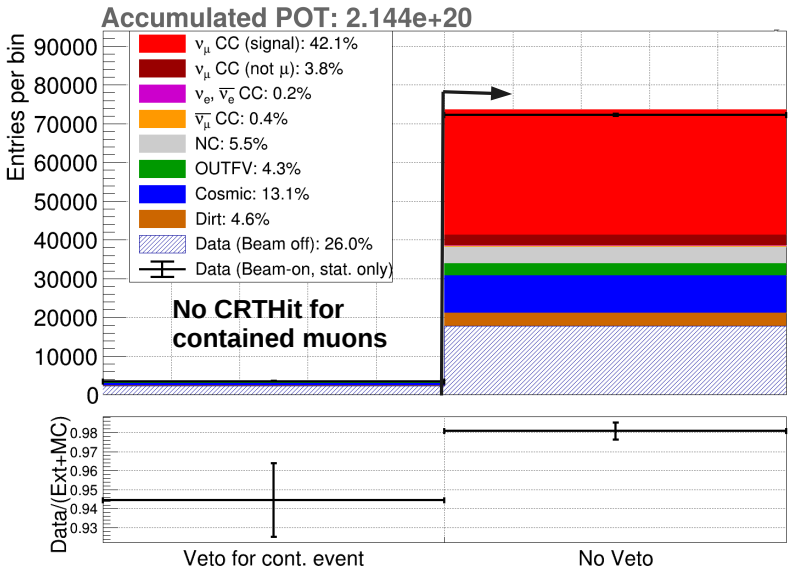

Figure 5.6.: A complete CRT veto is applied for events where the muon candidate track is contained. Only a small fraction of events is rejected, where either no neutrino is present or a cosmic track has been selected instead of the neutrino induced tracks.

With these cuts, the cosmic contamination has been largely reduced. Now the next series of cuts will try to select only a muon track from a ν_μ interaction.

A muon leaves a very track-like signal in the LArTPC. The track score is assigned by the Pandora pattern recognition framework and assigns to every cluster a number between 0 and 1. Here, a cluster to be regarded as a track object has to have a score >0.5. Further a cut is applied to reject clusters that are reconstructed as a track but are still not very track-like. All tracks which have a track-score below 0.8 are rejected as can be seen in Figure 5.8. This cut value is evaluated by optimizing purity $\cdot$ efficiency.

The muon momentum is reconstructed using a range-based calculation for contained muons and the MCS method for muons which leave the active volume of the LArTPC. However, the MCS method performs badly for very short tracks, therefore a minimum track length needs to be applied. Also, by looking at the track length distribution of the remaining tracks it is clear that nearly no signal events are present but a lot of background at short track length as it can be seen in Figure 5.9. Therefore a cut on the track length is also desirable. To evaluate the best cut value, again purity $\cdot$ efficiency was optimized, which resulted in a value of 32 cm. Since the track length can be more or less directly associated with a certain muon momentum for the signal events, such a cut removes a lot of the low muon momentum events. Therefore to

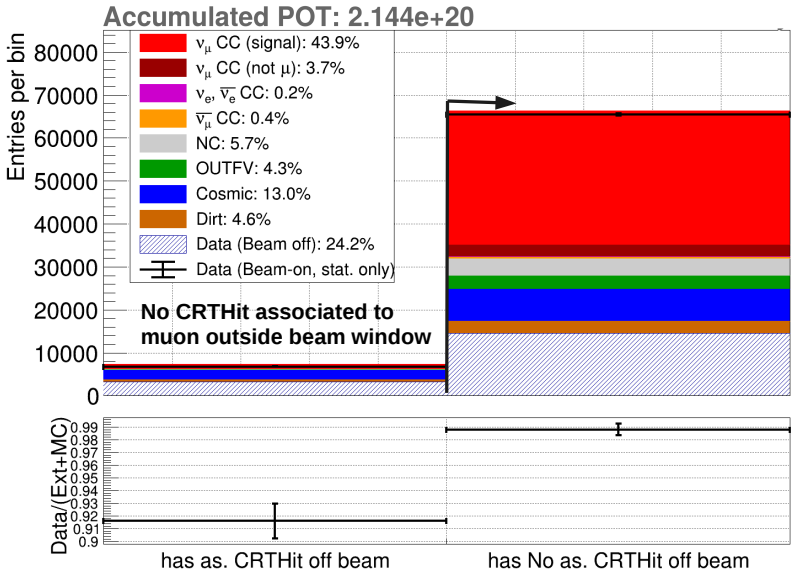

Figure 5.7.: If the muon candidate track points to a CRTHit outside the beam window, there is a good chance that this track is a misidentified out-of-time comic track. Therefore these events are rejected.

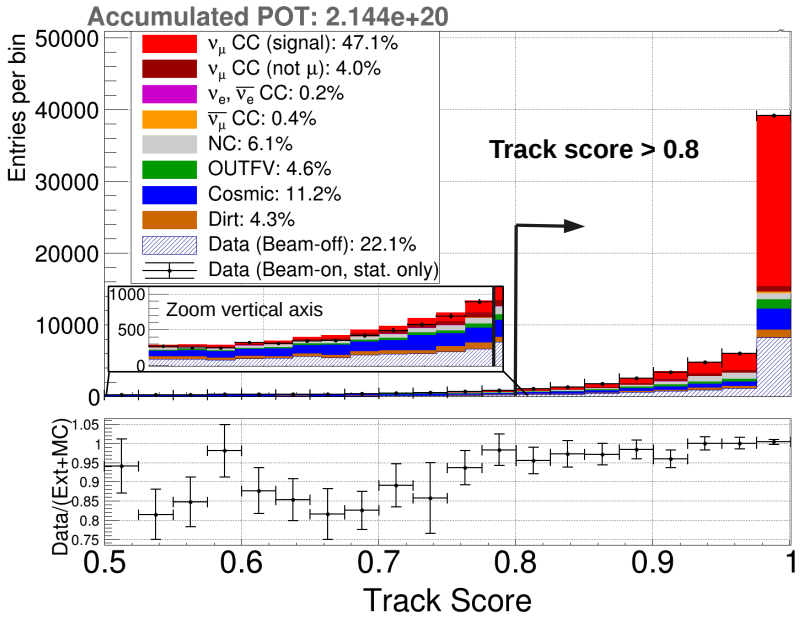

Figure 5.8.: Only objects with a track score above 0.8 are kept. Therefore electromagnetic showers and bad reconstructed events are rejected.

retain some efficiency at low muon momentum, the cut was loosened a bit to 20 cm which still ensures good momentum reconstruction, see Figure 5.9.

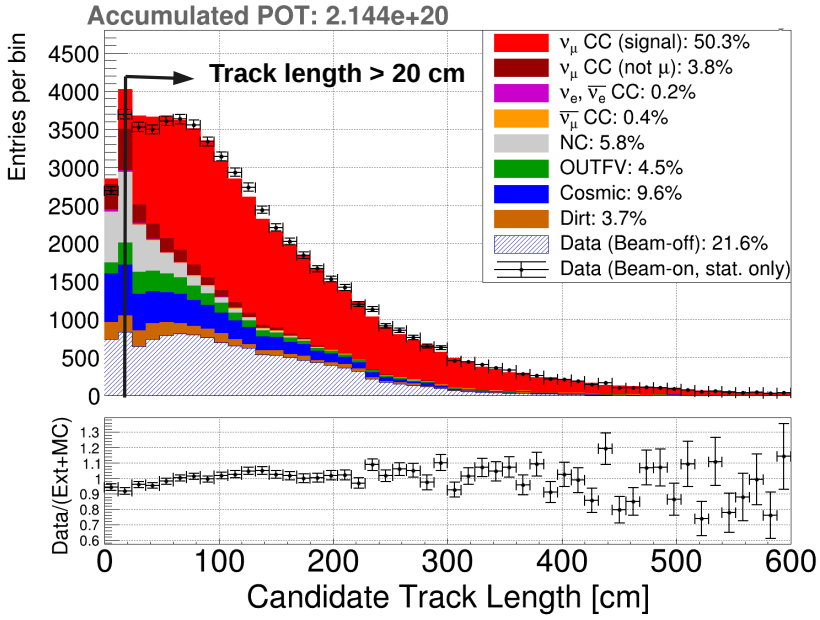

Figure 5.9.: The track length of the muon candidate of the events passing all the previous cuts. At low track lengths, the background events dominate and the momentum reconstruction becomes more challenging. Therefore all tracks with a length below 20 cm are rejected.

Next to the cosmic background and the events where the true interaction vertex lies outside the fiducial volume, neutral current events are the next dominating background. For these events, no muon track is present. It is difficult to clearly differentiate muons from pions but protons should leave a significantly different signal in the LArTPC. For this reason, the PID χ^2 under the proton assumption is used to reject events where the track looks clearly like a proton. The cut value is once again determined by optimizing purity $\cdot$ efficiency and the best value is 78. As one can see in Figure 5.10, nearly no signal events are lost with this cut but neutral current events and events where a track other than the muon is selected are rejected.

With these cuts, the background has been reduced while still retaining a lot of signal events. Apart from the cosmic background, all other sources of background are now at the few percent level. The careful use of the CRT and its low coverage do not allow us to drastically reduce this background much further. But, as one can see in Section 4.8, the cosmic track distribution and the neutrino induced signals have quite different topologies. The SVM described in Section 5.2 calculates a score on how much 'neutrino like' a charge signal looks like in the LArTPC and therefore can separate cosmic interactions from the neutrino induced ones. But the SVM is trained with simulated data and therefore requires a prior assumption of how a neutrino

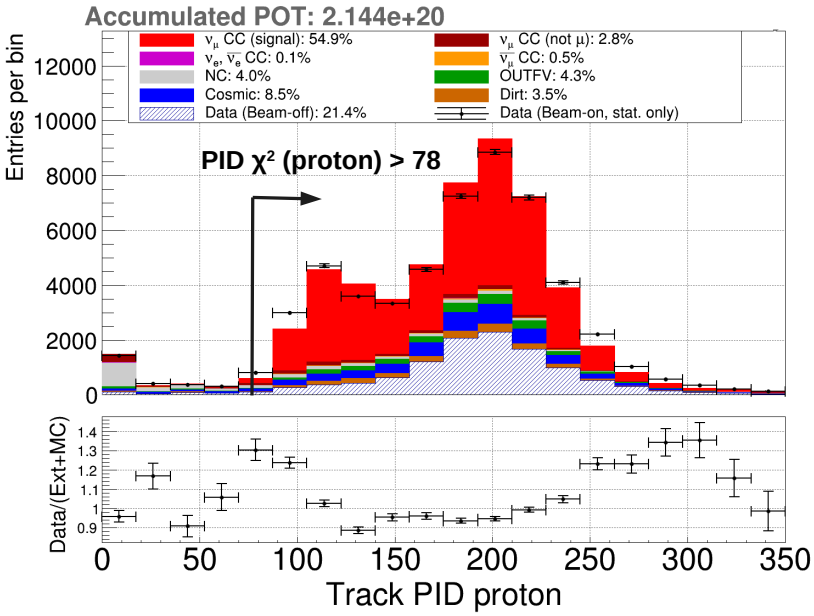

Figure 5.10.: The PID χ^2 values under the proton assumption for the muon candidate track. At low values, background events are dominant, especially neutral current events and events where not the right muon track was selected. All events with a χ^2 below 78 are rejected. As one can see there are some MC/data differences. But this cut does only remove a small number of interactions where the differences are not very prominent.

interaction looks like in the detector. This can introduce some model dependence and can cut into the phase space which wants to be measured. For this reason, this cut is applied only in the end and with great care although a value of 0.06 of this score is already required in the neutrino candidate preselection. A value of 0.1 was chosen although an optimization of purity · efficiency would lead to a harsher cut on this variable. As one can see in Figure 5.11, the purely cosmic interactions populate the low-value bins while the signal peaks at high values.

Now follows a summary of all the cuts developed for this analysis.

First, a reconstructed neutrino candidate is taken from the 3D event topology, see Section 5.2. At least one track is required to belong to the neutrino candidate. Out of these, one track is selected as the muon candidate track following the procedures in Figure 5.2. Further, the following selection is applied in order to reject background:

- Top cosmic ray veto: No CRTHit (see Section 4.8) is present in the Top CRT plane within the beam window (Figure 5.4), which would point to a cosmic ray entering the LArTPC from above
- CRT-LArTPC Z position selection: No CRTHit is present with a position upstream of the vertex in the beam window (Figure 5.5), which could arise

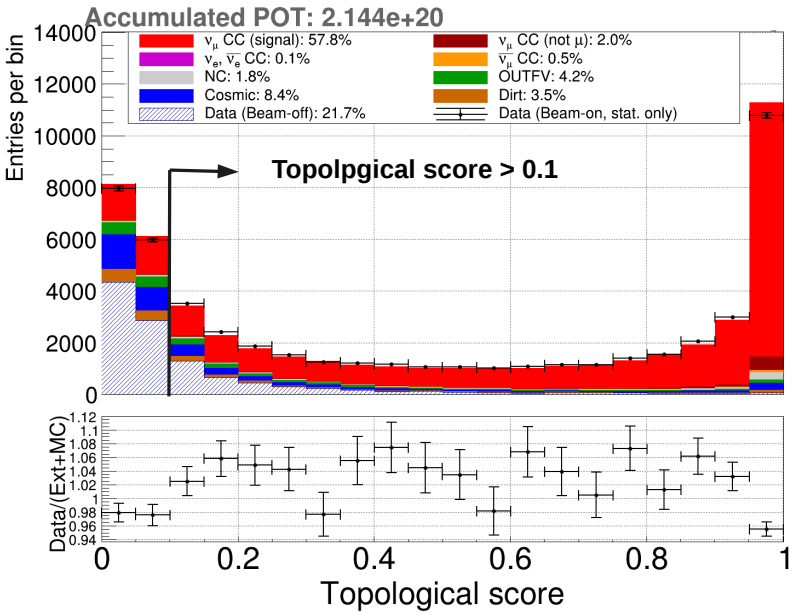

Figure 5.11.: The topological score calculated using the topological information of a grouped charge cluster in the LArTPC can separate neutrino signals from cosmic signals using a SVM. A cut value of 0.1 is chosen to further reduce cosmic background.

from a cosmic ray, but is unlikely to be produced by muons from neutrino interactions which are mostly forward-going

- CRT veto for contained muon: No CRTHit is present within the beam time window in events where the muon track from the neutrino interaction is contained within the LArTPC (Figure 5.6) to avoid overlapping cosmic ray activity
- CRT association: If the muon track from the neutrino interaction is associated with a CRTHit, its time needs to be in the beam window (Figure 5.7) to confirm that it could come from beam activity
- Track score: the muon track score is required to be greater than 0.8 (Figure 5.8) to reject events with wrong association of the track
- Track length: the muon track length is required to be greater than 20 cm (Figure 5.9) to separate muon neutrino interactions from other neutrino events
- Proton PID: the muon track PID under the proton assumption is required to be greater than 78 (Figure 5.10) to reject wrong track associations and other neutrino interactions, mainly NC events

- Topological score: a topological score defined to further reject background events from cosmic rays is required to be greater than 0.1 (Figure 5.11)

Now follows the discussion of the performance of these selection cuts.

5.6. Performance

In this section, the performance of the selection described in Section 5.5 is discussed. The cuts are described in the list in Section 5.5. Figure 5.12 shows the performance visually while tables in this section state the exact numbers. Generally, first an overview of all cuts is given, summarizing the CRT related cuts together as CRT cuts followed by a breakdown for each CRT cut individually. The overall efficiency and purity for the signal events are given in Table 5.2 and 5.3 while the following Tables 5.4 and 5.5 including the type of background as well as the signal.

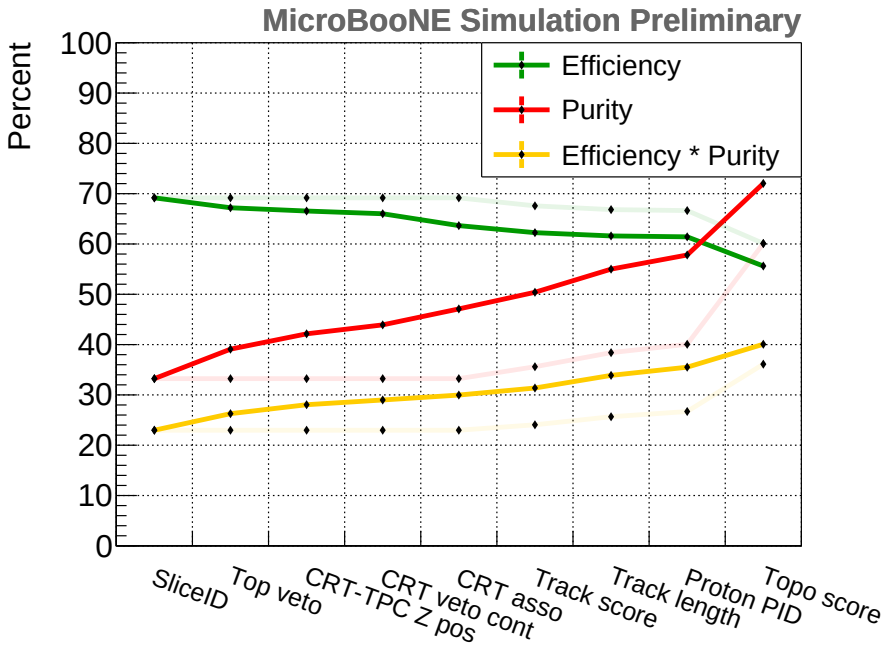

Figure 5.12.: The efficiency and the purity as well as their product for each cut. The transparent lines are for the case when the CRT cuts are not applied indicating the performance without CRT.

The biggest impact is due to the preselection, as one can see in Figure 5.12. While there is a loss of around one third of all signal events, the SliceID could remove so many background events that the signal makes now around one third of all the events. The largest background contribution remains the events where no neutrino has interacted in the LArTPC. This can be cut in nearly half by using the CRT cuts while only a small amount of signal events are lost. Some background channels seem

to increase after certain cuts, but this is only an effect coming from the large rejection of the overall background.

Cuts:	preselection	CRT cuts	track score	track length	track PID	Topo.
efficiency	69.17%	63.65%	62.25%	61.60%	61.42%	55.62%
purity	33.18%	47.09%	50.40%	55.00%	57.81%	72.04%
pur · eff	22.95	29.97	31.37	33.88	35.51	40.07

Table 5.2.: The efficiency and purity as well as their product after each cut.

Cut:	Top veto	CRT-LArTPC Z pos	CRT veto (cont.)	CRT asso.
efficiency	67.20%	66.55%	66.01%	63.65
purity	39.09%	42.14%	43.92%	47.09
pur · eff · 100	26.27%	28.05%	28.99%	29.97

Table 5.3.: The efficiency and purity as well as their product, here specifically for the CRT cuts.

As one can see in Table 5.4, cosmic interactions are the dominant background after the preselection as well as after all selection cuts are applied. After the background discussion in Section 3.4, one can imagine how much background already has to be removed by the SliceID preselection. The only cuts which really could reduce this background are the CRT cuts as well as the topological score cut while the other cuts either remove some other neutrino-related backgrounds or act as quality cuts for the signal events. Since ν_μ interactions are the most abundant in this beamline they should dominate over the other neutrino interactions.

With the CRT cuts and ignoring the topological score cut, one can reach nearly a selection as good as with the topological score cut but no CRT cut. But as one can see in the next section, where the efficiency is discussed in more detail, the CRT cuts have a much flatter response over a large fraction of the phase space while the topological score directly depends on some of the variables. By using the CRT cuts one can avoid a strong cut on the topological score and therefore reduce model dependencies or biases.

The events passing all the selection cuts for the beam-on data, estimated signal, and estimated background are stated in Table 5.6 with only the statistical uncertainty given. Here, the data and the expectation for the full Run 3 are given, which corresponds to $2.144 \cdot 10^{20}$ POT. One can clearly see that the number of background events could be drastically reduced while most signal events could be kept.

Now follows a discussion about the efficiency in more detail.

Cut:	presel.	CRT cuts	track score	track len.	track PID	Topo.
ν_μ CC	33.18%	47.09%	50.40%	55.00%	57.81%	72.04%
beam-off	40.15%	22.06%	21.52%	21.26%	21.68%	10.81%
dirt	4.66%	4.29%	3.78%	3.48%	3.46%	2.35%
cosmic	10.66%	11.16%	9.59%	8.51%	8.38%	5.64%
OUTFV	3.57%	4.61%	4.52%	4.37%	4.25%	3.51%
NC	4.25%	6.12%	5.80%	4.01%	1.81%	2.27%
$\overline{\nu_\mu}$	0.28%	0.40%	0.43%	0.47%	0.50%	0.61%
$\nu_e/\overline{\nu_e}$	0.15%	0.22%	0.20%	0.14%	0.07%	0.10%
ν_μ CC (not μ)	3.10%	4.05%	3.77%	2.76%	2.04%	2.66%

Table 5.4.: The amount of each channel after each cut.

Cut:	Top veto	CRT-LArTPC Z pos	CRT veto (cont.)	CRT asso.
ν_μ CC	39.09%	42.14%	43.92%	47.09%
beam-off	29.69%	26.03%	24.19%	22.06%
dirt	5.41%	4.58%	4.65%	4.29%
cosmic	12.45%	13.11%	12.95%	11.16%
OUTFV	4.18%	4.29%	4.34%	4.61%
NC	5.05%	5.45%	5.66%	6.12%
$\overline{\nu_\mu}$	0.33%	0.36%	0.37%	0.40%
$\nu_e/\overline{\nu_e}$	0.18%	0.19%	0.20%	0.22%
ν_μ CC (not μ)	3.61%	3.84%	3.73%	4.05%

Table 5.5.: The amount of each channel after each cut, here specifically for the CRT cuts.

Name	variable	# events ± stat. error	
		preselection	final selection
Measured data	N^{data}	99970 ± 316.18	38351 ± 195.83
Measured cosmic (beam-off)	-	41022.56 ± 157.02	4092.76 ± 49.60
ν_μ signal (MC)	N^{MC}	33924.00 ± 75.73	27280.42 ± 67.91
neutrino background (MC)	-	22499.28 ± 61.68	5604.33 ± 30.78
dirt background (MC)	-	4766.85 ± 89.87	890.39 ± 38.84
Total background	N^{bkgd}	68288.69 ± 191.14	10587.48 ± 70.11
Total data - background	-	31681.31 ± 369.47	27763.52 ± 208.01

Table 5.6.: Number of events used for the total integrated flux cross-section for data, backgrounds as well as the signal expectation from the simulation. This results in a total efficiency of 56% and a purity of 72%.

5.6.1. Discussion of the Efficiency of the Selection

Since the cross-section will be done in bins of muon momentum and the $\cos(\theta)$ angle of the muon track this section contains a detailed look into the efficiency of the selection for these two variables after each cut. As already discussed the preselection has the biggest impact. For this reason, Figure 5.13 shows the total efficiency on the left side while the right side shows the efficiency drop with respect to the preselection. The general shape of the efficiency for both, muon momentum and $\cos(\theta)$ is mainly given by the preselection.

The SliceID which acts as the preselection is described in A.2 and removes a very large amount of cosmic interactions. Lower energetic signals have a lower optical signal which leads to generally more difficulties in the charge to light matching. Neutrinos with lower energy populate also more the region of low muon momentum and therefore a decrease in efficiency in the muon momentum is visible in Figure 5.13. Also the topological score described in A.3 is used in this process as described in A.2. Since this SVM is trained to separate cosmic interactions from neutrino interactions it will reject neutrino interactions where comic tracks are most present. This is the case for tracks with $\cos(\theta)$ around zero (nearly vertical tracks) where also a decrease in efficiency is visible. Since higher momentum tracks are also generally more forward-boosted, going from forward-going muons to backward muons results also in general decreasing efficiency.

With the additional cuts, one can see that the efficiency decreases further towards lower momentum. Especially with a length cut of 20 cm on the muon candidate track, one starts to reject all muons with a momentum below 150 MeV. This is also exactly the point where the efficiency drops to zero as one can see in Figure 5.14. Since the efficiency drop is rather fast only all signals below 150 MeV are excluded. The selection still has an efficiency of around 25% for events with muons below 180 MeV/c in momentum, which will be the lowest momentum bin for the results.

The CRT cuts have a rather flat efficiency while the other cuts cutting more towards low momenta or $\cos(\theta)$ around zero. For the impact of the topological score itself, the same arguments as mentioned for the efficiency of the preselection are true. The impact of each CRT cut will be discussed next individually.

5.6.2. Discussion of the Efficiency of the CRT Cuts

In Figure 5.15 one can see the efficiency with respect to the preselection over different true variables. The overall efficiency for all CRT cuts is flat over the neutrino energy while small dependencies are visible for the muon momentum as well as the angles θ and ϕ. High momentum muons are more likely to be forward boosted where they will not be rejected by any of the CRT cuts as one can see in Figure 5.15 (b) and (c). The most cosmic interactions are seen in the CRT Top and Bottom planes since most of the cosmic flux goes through them. For this reason, the probability for a wrong accidental matching of a CRTHit and a track in the LArTPC is higher for up

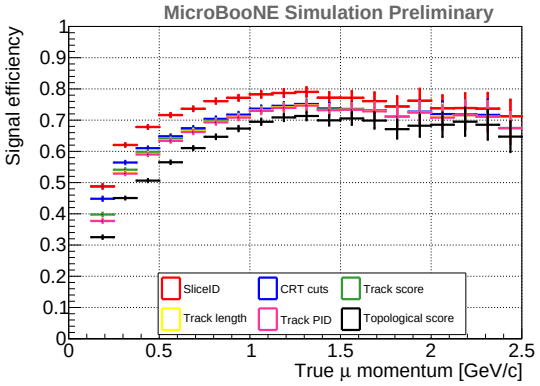

(a) True μ momentum: absolute

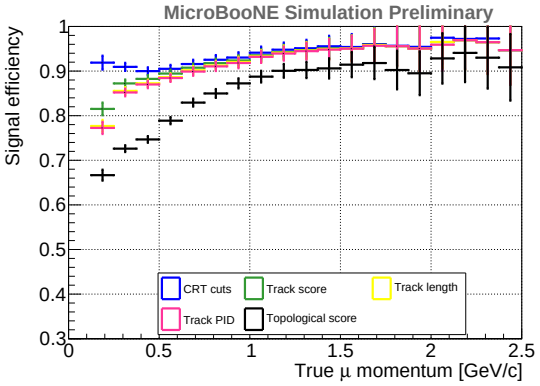

(b) True μ momentum: relative slideID

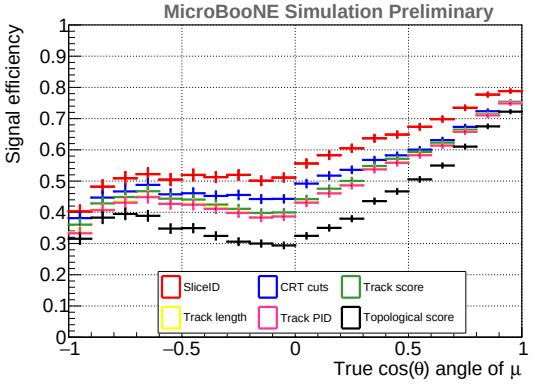

(c) True μ $cos(\theta)$: absolute

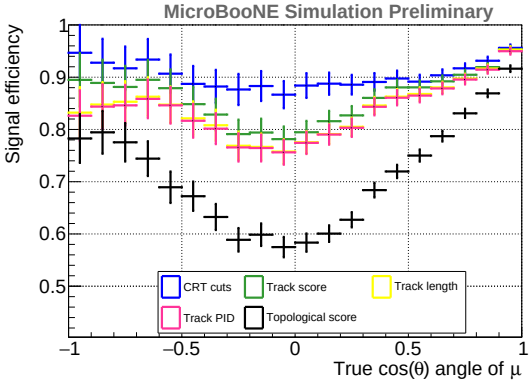

(d) True μ $cos(\theta)$: relative slideID

Figure 5.13.: The biggest effect on the efficiency has the slideID process which is here used as the preselection. To see the effect of the other cuts in more detail on the right side the efficiency is shown relative to the preselection. Be aware that the vertical axis shows different ranges on the right side figures.

and downward going tracks. Also, only the upward going muons from a neutrino interaction eventually reach the top CRT plane where they veto the event. For this reason, the ϕ distribution has these dips around $\pm\pi/2$.

5.6.3. Discussion of the Efficiency by Interaction Channel

By looking at the final efficiency grouped by interaction channel (QE, MEC, RES, DIS) one can see that this analysis has a similar efficiency for all interaction modes and therefore is truly inclusive (see Figure 5.16). Regardless of what form of ν_μ CC

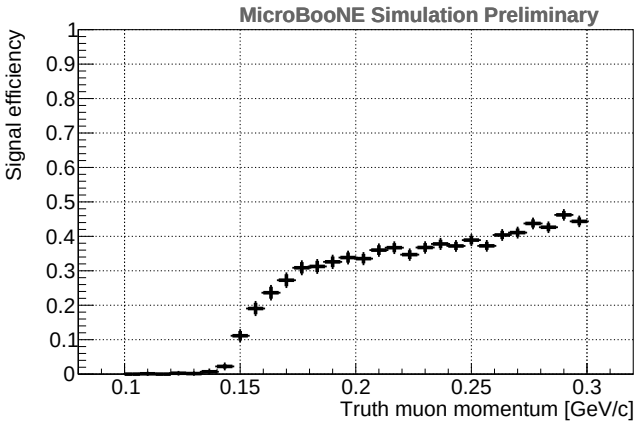

Figure 5.14.: The efficiency for the signal definition in 5.5 when no minimum muon momentum is required. The efficiency drops to zero at 150 MeV.

interaction happens, the analysis should be sensitive to it The amount of the total interactions predicted in the model used to predict this analysis are 53% QE events, 14% MEC events, 27% RES events and 6% DIS events.

As one can see in Figure 5.16 the efficiency drops below 500 MeV in neutrino energy or below 200 MeV in muon momentum. The main cause of this drop is the 20 cm track length cut which is applied in this analysis. Since for exiting muons, the momentum is calculated using the MCS method, this is a trade-off between keeping interactions at low muon momenta and the ability to properly reconstruct them as well reject the backgrounds dominating in the low track length region.

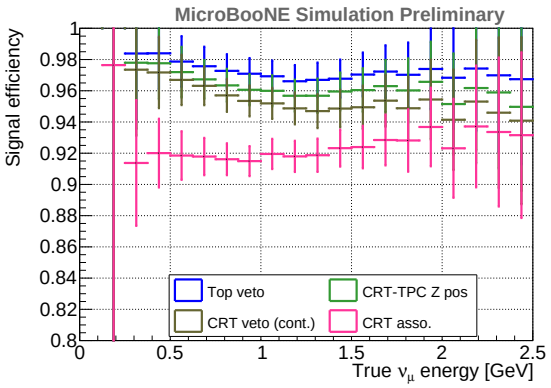

(a) True ν_μ energy: relative slideID

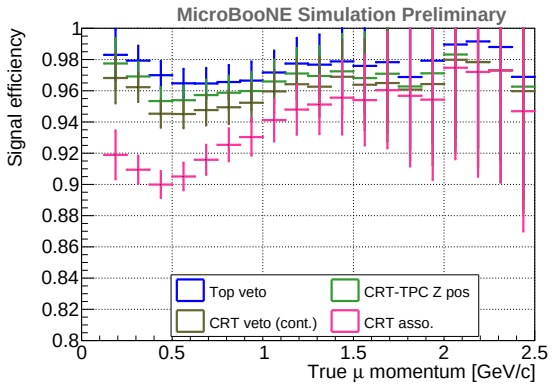

(b) True μ momentum: relative slideID

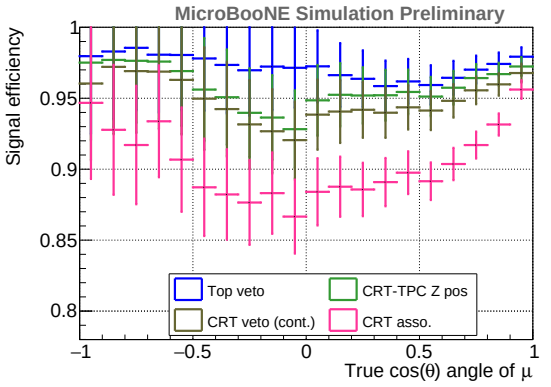

(c) True μ $cos(\theta)$: relative slideID

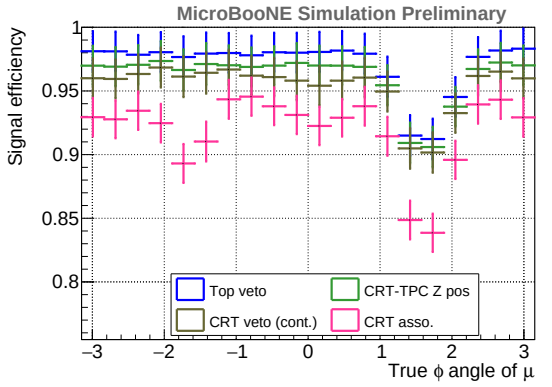

(d) True μ ϕ: relative slideID

Figure 5.15.: The efficiency for each CRT cut itself relative to the preselection. Be aware that the vertical axis shows different ranges.

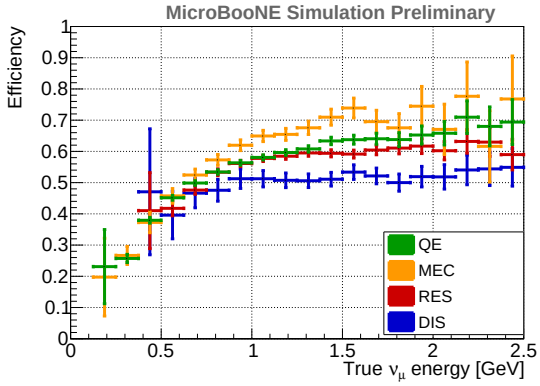

(a) True ν_μ energy

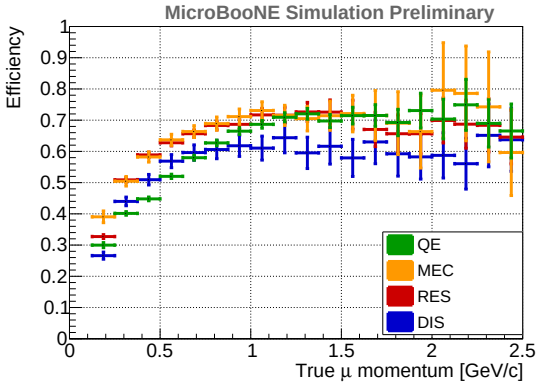

(b) True μ momentum

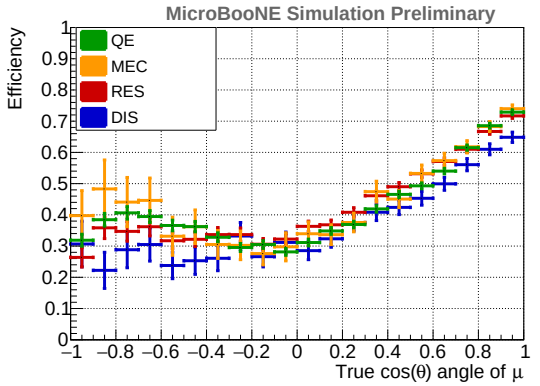

(c) True μ $cos(\theta)$

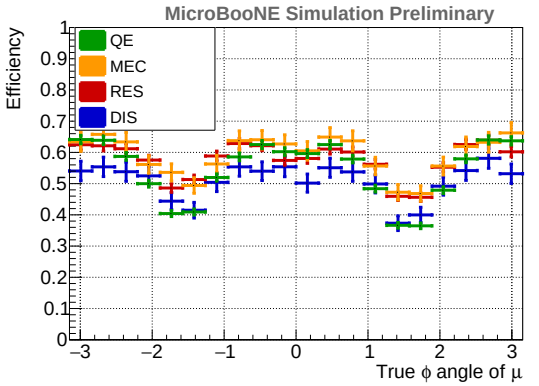

(d) True μ ϕ

Figure 5.16.: The efficiency for the different interaction channels over (a) true neutrino energy, (b) true muon momentum, (c) true $cos(\theta)$ of the muon track and (d) the ϕ angle of the true muon. The relative abundance of QE events is 53%, MEC accounts for 14%, RES for 27% , and DIS accounts for 6% of all selected signal events.

5.7. Kinematic Distributions from Muon Neutrino Candidate Interactions

Figures 5.17 to 5.25 show the distribution of selected kinematic quantities for the final selection of muon neutrino interactions presented in this thesis. The event rate plots are just after the reconstruction of a muon neutrino by Pandora and the muon track selection (here called as preselection) as well as after all cuts are applied (indicated by before cuts and after cuts). One can see in which regions the most background was present before the majority of selection cuts were applied.

The figures contain the measured beam-on distributions and stacked the expectation from the beam-off and simulation samples. The background is split into several groups according to the definition in Section 5.4. This ν_μ CC inclusive analysis measures the kinematics of the outgoing muon from the neutrino interaction.

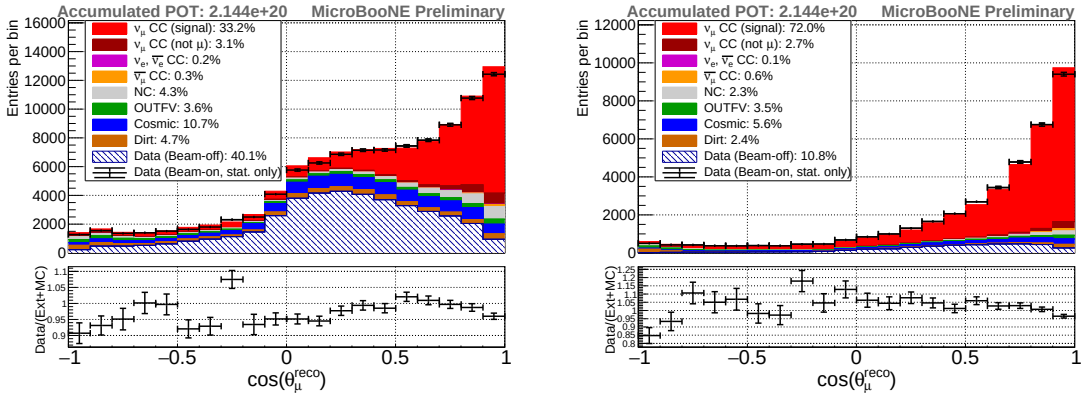

(a) before cuts

(b) after cuts

Figure 5.17.: The event rates in bins of $cos(\theta)$. The background contribution could be reduced over the full phase space and signal interactions are now dominating for almost all bins. While there is a good agreement between the data and the prediction in the forward direction, some fluctuations appear in the backward region with lower statistics.

In Figure 5.17 one can see the distributions in bins of cos(θ). The majority of the cosmic background appears in the vertical direction. We see that the selection cuts have effectively reduced this background such that it is no longer the dominant type of event. While having good data to Monte Carlo agreement within 10% overall values of $cos(\theta)$ before, the discrepancies generally increase after the selection cuts are applied. The difference between the data and the prediction is mainly present in the backward region where fewer events are present per bin. Since here only statistical errors are drawn on the data points, the discrepancies are not yet covered by the uncertainty.

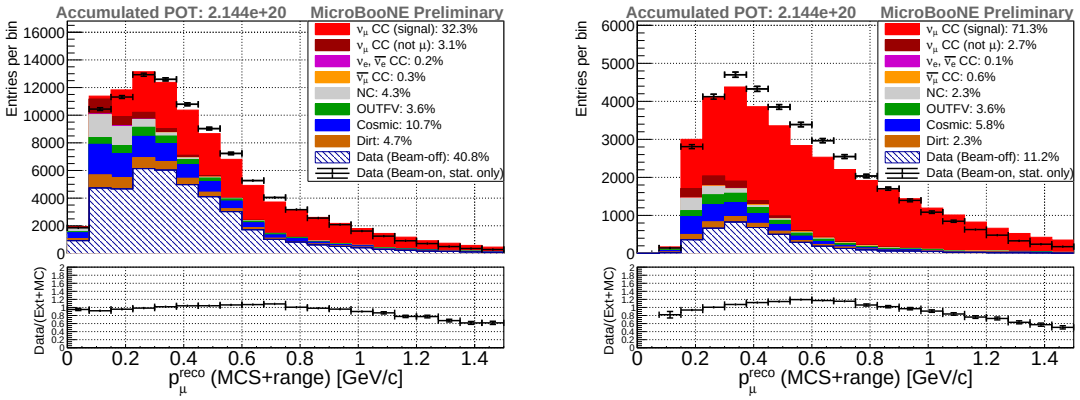

(a) before cuts (b) after cuts

Figure 5.18.: The event rates in bins of momentum. A clear shape disagreement is present in both distributions but more dominant after all cuts are applied.

The momentum (see Figure 5.18) distribution has the most background in the low momentum region but a nearly negligible contribution towards higher momenta. As explained in Section 5.2, the range-based method is used for the momentum reconstruction for contained muon candidate tracks while the MCS method is used for exiting tracks and therefore dominates at higher momentum. Also here, the discrepancies slightly increase after applying the selection cuts. There is a clear shape difference between the measured data and the prediction. A closer study has shown that this disagreement mainly comes from uncontained tracks at higher energies reconstructed using the MCS method. Other studies in MicroBooNE which have reconstructed the total neutrino energy have also seen a shape disagreement with a similar shape when they compared the data with the prediction [101].

The ϕ angle distribution of the muon from the ν_μ CC interaction is expected to be flat. The Figure 5.19(a) also shows where the most cosmic background enters which is then rejected to a large extent in Figure 5.19(b). The strong cosmic rejection together with difficulties in the reconstruction for tracks parallel to the collection wires leads to a smaller efficiency at these angles ($\pm\frac{\pi}{2}$) as one can see previously in Figure 5.16(d). Most of the data bins agree with the simulation within around 5%..

Figure 5.20 shows the track length of the muon candidate track. One can see that at shorter track lengths, the contribution from events where the muon does not belong to the ν_μ CC interaction rises. Also, other background contributions populate this region. Since no restriction for uncontained events was made, the track length here corresponds only to the length of a particle trajectory inside the LArTPC and not necessary to the total track length.

Analyses selecting more exclusive final states and event topology are looking at

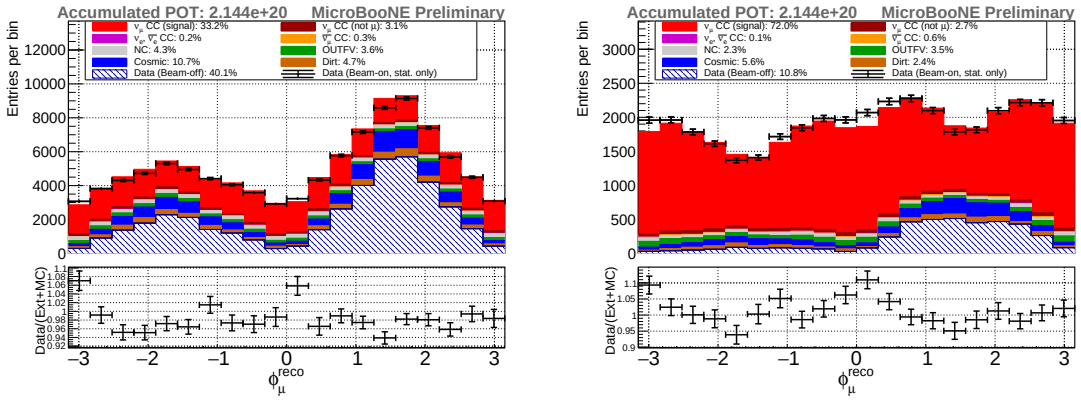

(a) before cuts (b) after cuts

Figure 5.19.: The event rates in bins of the angle ϕ. The cosmic background comes clearly from specific angles but can be largely be reduced by the selection cuts.

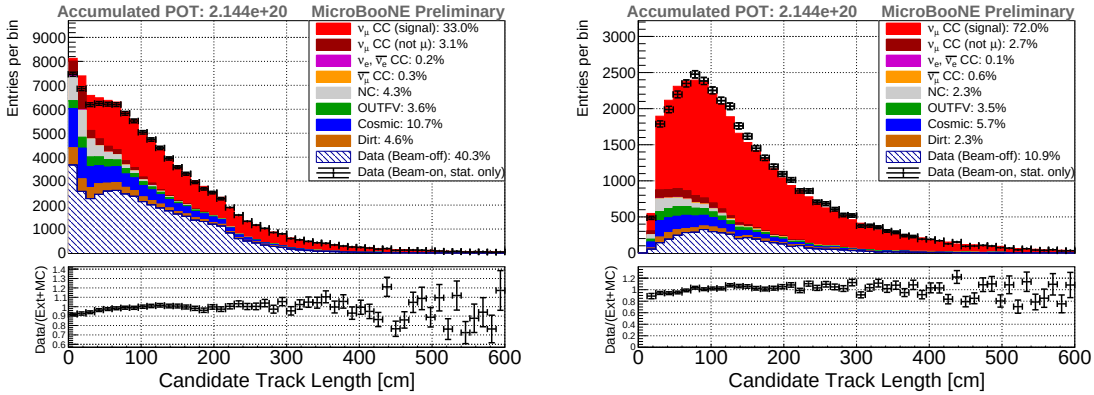

(a) before cuts (b) after cuts

Figure 5.20.: The event rates in bins of track length. The backgrounds are populated towards smaller track lengths. The data agrees quiet well with the prediction.

additional particles originating from the neutrino vertex. To indicate the background rejection for more exclusive analyses, the distribution of the reconstructed neutrino daughter particles in Figure 5.21 is shown. There is reasonable agreement with the expectation from simulation.
The dominant background comes from cosmic muons. They leave mainly one track signals inside the LArTPC as one can see in Figure 5.22. Also, the dirt background

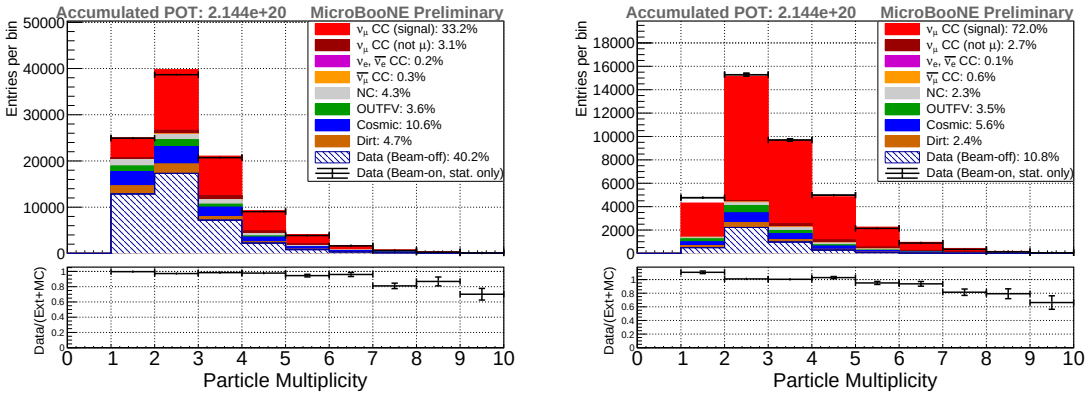

(a) before cuts (b) after cuts

Figure 5.21.: The event rates in bins of number of reconstructed daughter particles of the neutrino. The good agreement between data and prediction would allow also a good study of more exclusive interactions.

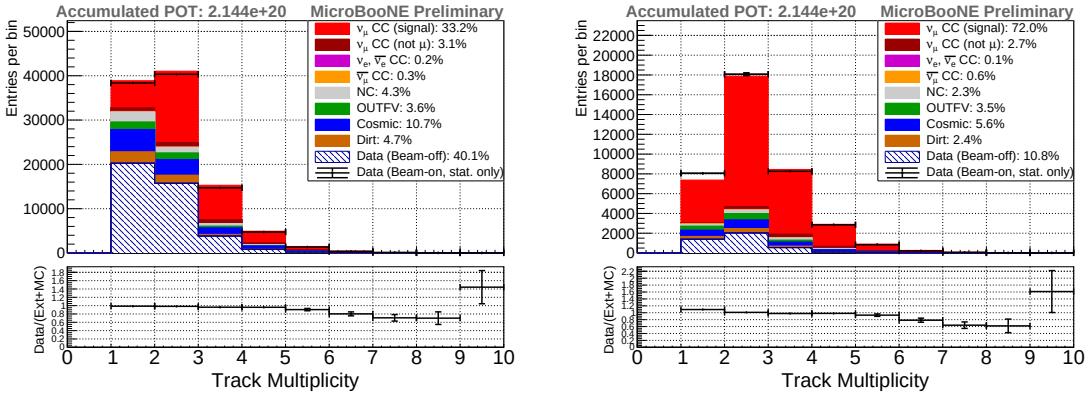

(a) before cuts (b) after cuts

Figure 5.22.: The event rates in bins of number of tracks. The single track background events could be largely reduced using the selection cuts.

(interactions not in the LArTPC) leaves mainly only one reconstructed track inside the LArTPC. Except for the region with very many reconstructed tracks, the prediction looks the same as the data distribution.

If one looks at the spatial distribution of the reconstructed vertex one can also observe features. While the distributions at the stage after the Pandora reconstruction is more or less flat in drift direction (vertex X position, Figure 5.23) as well as along the beam (vertex Z position, Figure 5.25), in the vertical direction (vertex Y position,

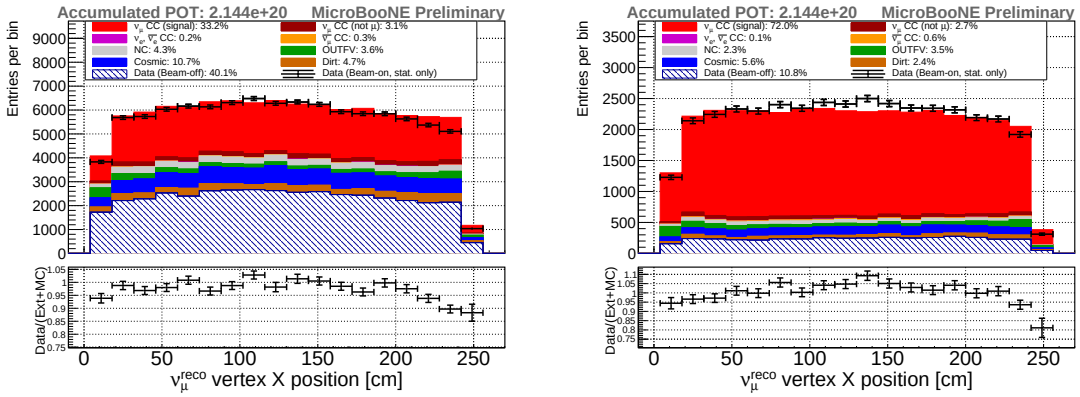

(a) before cuts (b) after cuts

Figure 5.23.: The event rates in bins of reconstructed vertex in drift direction. The flat response shows that the light-charge matching in the LArTPC works also for interactions happening far away from the PMTs behind the readout plane.

Figure 5.24) one can see the incoming cosmic background coming from above. The X position indicates the vertex distance to the light readout mounted behind the anode wires. The flat distribution along the drift direction (vertex X position) shows that the light to charge matching works also at the cathode, there is no loss in signals nor an increase of background events. By looking along the beam direction one can see that the main contribution of the dirt events enters the LArTPC from upstream. Some changes in the event rate along the beam direction can be explained by unresponsive collection wires in the LArTPC, also these are well represented in the simulation.

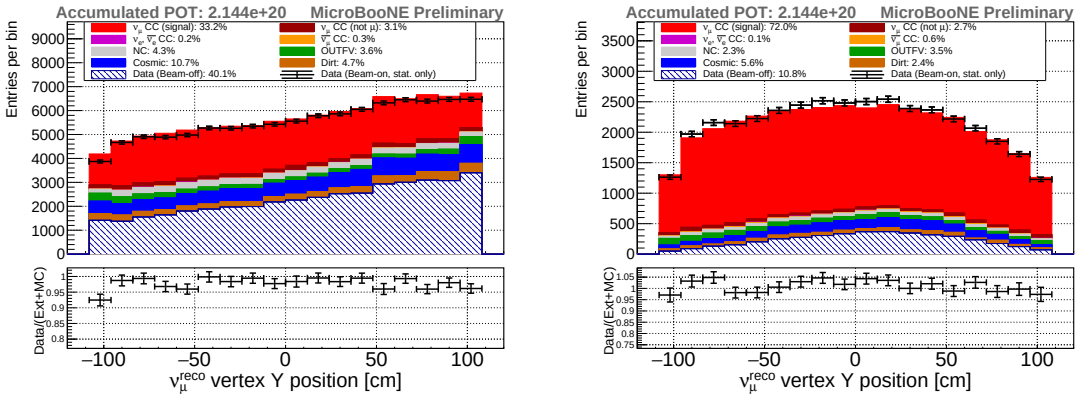

(a) before cuts (b) after cuts

Figure 5.24.: The event rates in bins of reconstructed vertex in Y direction. One can see the incoming cosmic background from above before the cuts. The selection removes more tracks higher in the LArTPC.

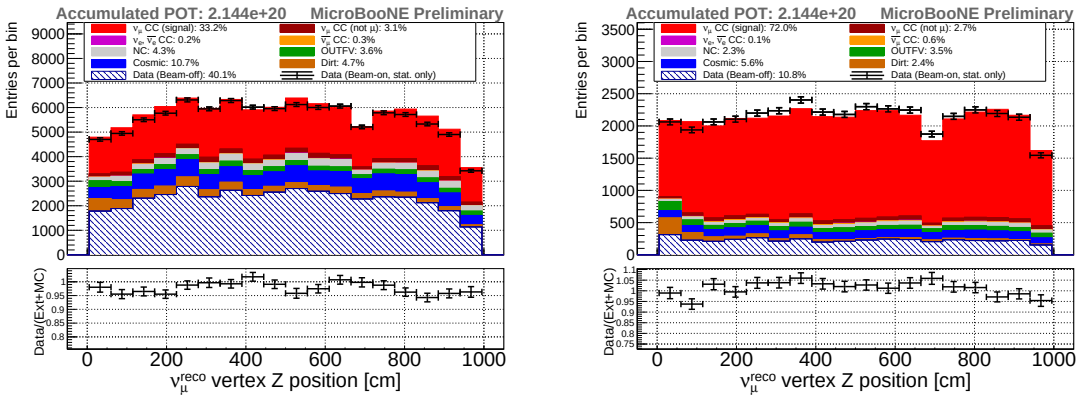

(a) before cuts (b) after cuts

Figure 5.25.: The event rates in bins of reconstructed vertex along the beam direction. The drop of reconstructed vertices at around z=680 cm is due to a non-responsive wire region as shown in Figure 3.8.

6. Cross-section Measurement

As we have seen in Section 2.5, for future experiments to be successful, the models have to describe the reality better which only can be reached when more cross-section measurements can be taken into account by the scientist who provides neutrino generators for the simulation.

There are various possibilities of how a cross-section measurement can be carried out or more precisely how it can be presented. A general problem is that a detector always measures a smeared version of the underlying unreachable true interaction which theory tries to approximate. Therefore there are distinct approaches to how a cross-section can be represented: an unfolded result, where the smeared measurement is unsmeared using an unfolding technique like D'Agostini unfolding [102] or profiled likelihood fitting [103]. The result can then be directly compared to theory. Or, the theoretical prediction is smeared and then compared to the data, which is called forward-folding [104]. Both of these methods have their advantages and disadvantages and are commonly used in different variations among the neutrino community.

The presentation which is used in this work uses the forward-folded approach and follows the slogan "we measure what we measure!". And this is not a cross-section but a count of events with measured characteristics. Therefore the result is presented in a forward-folded way; in reconstructed space and the form of a binned event rate since this is what we measure. Presenting the number of events in a form that looks like a cross-section (the normalization over total flux and number of targets) does not bring any advantage but can obfuscate the result for others trying to use the data. Furthermore, it does not allow a clear separation of data and uncertainties from predictions. More on this topic can be found in Appendix A.4.

In Equation 2.11, one can see that the forward folded cross-section is nothing but a background-subtracted event rate normalized to the total flux, the number of targets, and the bin width. The event rate is what an experiment actually can measure, therefore it makes sense to directly compare this to the prediction of a theory. This can be done by calculating an event rate from the model prediction using Equation 2.10 for each bin. This event rate is then still based on true variables, so one has to apply the detector smearing which also accounts for the efficiency to get the prediction for the reconstructed variables. This is done by multiplying the event rate in true variables with the smearing matrix S_{ij} given as follows:

$$S_{ij} = P(\text{observed in bin i}|\text{true value in bin j}) \cdot \epsilon_j \tag{6.1}$$

This gives us the predicted number of signal events for the reconstructed variable, now only the background has to be added which is usually given directly by the experiment.

While there exists no proper way to calculate the efficiency for reconstructed variables, the efficiency for true variables is given as in Equation 5.3.

The smeared signal event rate prediction plus the background can then directly be compared to the measured number of data events. The comparison of these two distributions should give the same result as the comparison of the cross-section derived from data using Equation 2.12 and the forward folded cross-section predicted by the theory.

Now follows some subsections where the central values are given which are used for the event rate calculation. The way the total flux is estimated is given as well as the total number of targets. These values are used to bring the theory cross-section prediction to an event rate prediction. This is explained in Section 6.0.1. This is followed by the binning chosen for this analysis in 6.0.2. Finally, the smearing matrix is presented in 6.0.3 and the background prediction in 6.0.4.

6.0.1. Total Flux and Number of Targets

The total flux is needed to calculate the event rate. The flux can be calculated by using simulated neutrinos from the beam simulation and count how many of them go through the fiducial volume. This is done by checking if the neutrinos are produced at the source with a direction that points through a plane (A_{TPC}) in the middle of the detector of the active TPC. For the simulated neutrinos, the number of POT is also calculated. The flux is then given by:

$$\phi = \frac{\#\ \nu \text{ through } A_{TPC}}{POT_{sim}} \cdot POT_{data} \cdot \frac{1}{A_{TPC}} \tag{6.2}$$

The following parameters given in Table 6.1 are used as an input resulting in the also given total flux.

Name	Variable	Value
# neutrinos through active area	N_{ν_μ}	110078620
Total POT	POT_{sim}	$2.5 \cdot 10^{12}$
Area of active volume	A_{TPC}	256.35 $cm \cdot$ 233 $cm = 59729.55 cm^2$
POT data	POT_{data}	$2.144 \cdot 10^{20}$
Total flux per POT	ϕ/POT	$7.3718 \cdot 10^{-10}\ cm^{-2} POT^{-1}$
Total flux	ϕ	$1.58051 \cdot 10^{11}\ cm^{-2}$

Table 6.1.: Parameters used for the total flux calculation.

So the total flux for the full data sample of Run 3 is estimated to be 1.58e11 neutrinos/cm^2. Uncertainties regarding this number are discussed in Section 6.1.3.

The number of target nucleons is given by the definition of the fiducial volume and the density of the liquid argon. With these values and additional constants one can calculate the number of target nucleons as follows:

$$N_T = \frac{\rho_{Ar} \cdot V_{fiducial} \cdot N_A \cdot N_{nucleons}}{m_{mol}} \tag{6.3}$$

In this analysis the values in Table 6.2 are used.

Name	Variable	Value
Argon density	ρ_{Ar}	1.3836 g/cm^3
molar mass Argon	m_{mol}	39.95 g/mol
Avogadro constant	N_A	$6.022140857 \cdot 10^{23}$ $atoms/mol$
Number of nucleons	$N_{nucleons}$	40
Fiducial volume	$V_{fiducial}$	49184671.35 cm^3
Number of target nucleons	N_T	$4.10331 \cdot 10^{31}$

Table 6.2.: Parameters and their value for the calculation of the number of target nucleons.

6.0.2. Binning

Here the binning chosen in this analysis is presented. It is based on a previous analysis done in MicroBooNE [13] and more information is given in A.6. Figure 6.1 shows the double differential binning and the assignment of the bin number.

In principle, one could bin as fine as the statistics allow which means when the statistical uncertainty overcomes the systematic uncertainty finer binning does not make sense anymore. But at some point, the bins start to be very correlated and one does not add much more information to the measurement by finer binning due to limited detector resolution. Therefore the smearing matrix without efficiency correction should contain most of its entries on the diagonal (a value around 68% is the goal). This is the case for this analysis as it can be seen in Figure A.6 in the appendix. Finer binning adds only small information and makes the plots very hard to read for the human eye.

One other thing one wants to avoid is a strong change of efficiency within one bin to avoid eventual model dependence and uncertainties. As one can see in Figure 6.2(a) within the chosen bins, there is no strong change of efficiency. The backward high momentum bins seem to have no events, but the detector smearing distributes events in these bins as well as to the excluded phase space region below 150 MeV. The number of data events per bin in the used data sample ($2.15 \cdot 10^{20}$ POT) is shown in Figure 6.2(b).

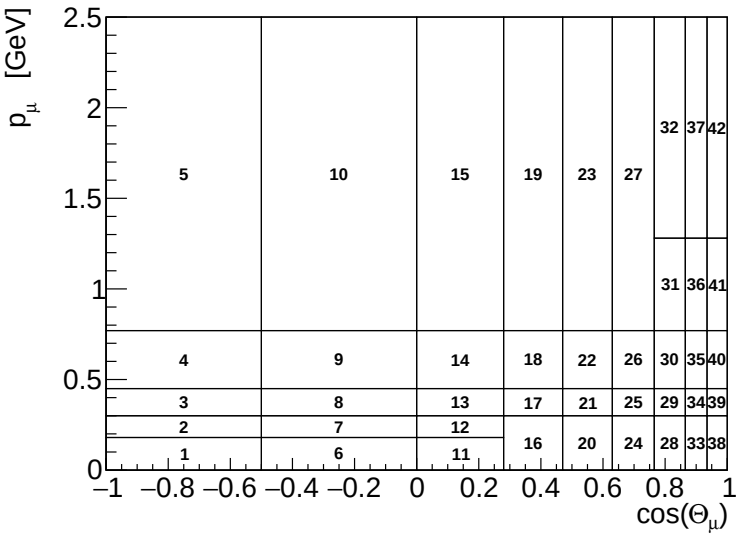

Figure 6.1.: The binning chosen for this analysis. The 2D binning was chosen according to the 1D binning with some of the bins are merged.

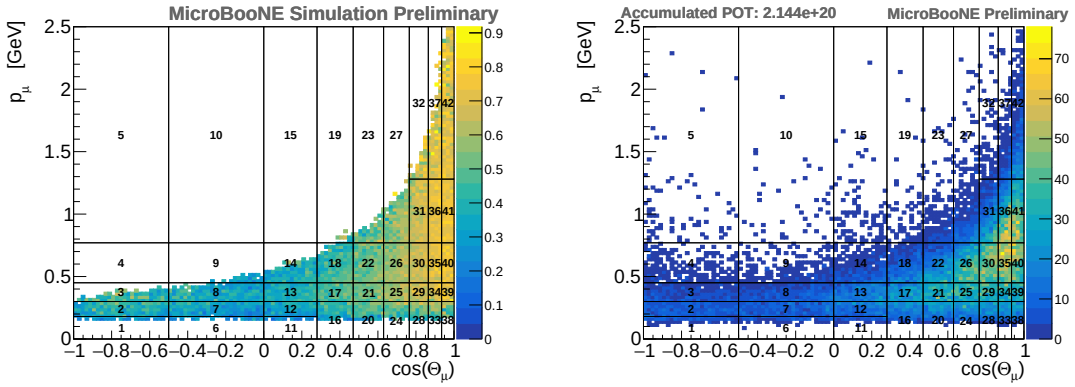

(a) Efficiencies within the bins

(b) data event rate in each bin

Figure 6.2.: Left: the efficiency within each bin is shown for entries where at least 10 events are selected. There are only small changes of efficiency within each bin. Right: the measured number of data events passing the selection for each bin. The events are distributed in all bins due to detector smearing.

6.0.3. Detector Smearing Matrix

With the chosen binning one can use the detector simulation to see which true values get reconstructed where.

This results in the smearing matrix, as given by Eq. 6.1 and shown in Figure 6.3. That matrix will be used to transfer true theory values into detector reconstructed variables by multiplying the matrix to true event rate using the binning presented in Section 6.0.2.

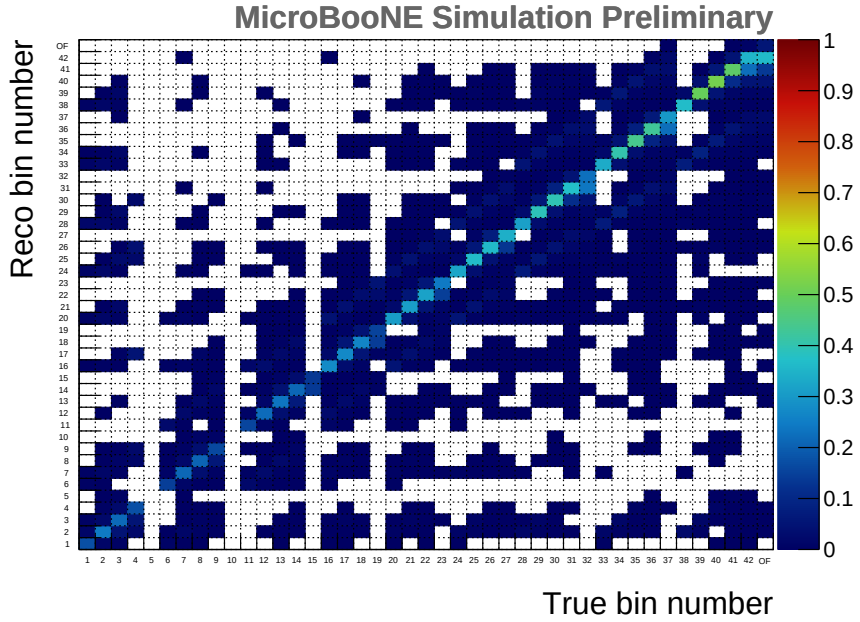

Figure 6.3.: The detector smearing matrix for the double differential event rate. The sum of all reconstructed bins (including the overflow bin) gives the efficiency for an event in this true bin to be reconstructed. As one can see, the used model does not predict any events in bin 5 and 10, nevertheless, some events are reconstructed in these bins due to detector smearing.

As one can see in Figure 6.3, the probability for each true bin to be reconstructed in the same reconstructed bin is the highest. This is done by design as one can read in 6.0.2 or better in A.6. Also, the efficiency grows towards more forward-looking bins and higher momentum bins.

This detector smearing together with the background presented in the next subsection is used on a model event rate to compare it to the measured event rate in data.

6.0.4. Background Prediction

To compare the measurement to different model predictions, one needs not only the smearing matrix to take the detector effects into account but also all the expected backgrounds. Since the modeling and the proper detector smearing for all sources of background would make the procedure very complicated and, since the beam-related

background is not dominating, background model differences are expected to be sub-dominant. So the same background prediction is used for all predictions even if another model is used. Since this background includes also beam-related background events which are modeled with the tuned GENIE version 3, a small model dependence is introduced. The uncertainties of this model are added to the background, so some of the differences should be covered by the uncertainties of the background estimation.

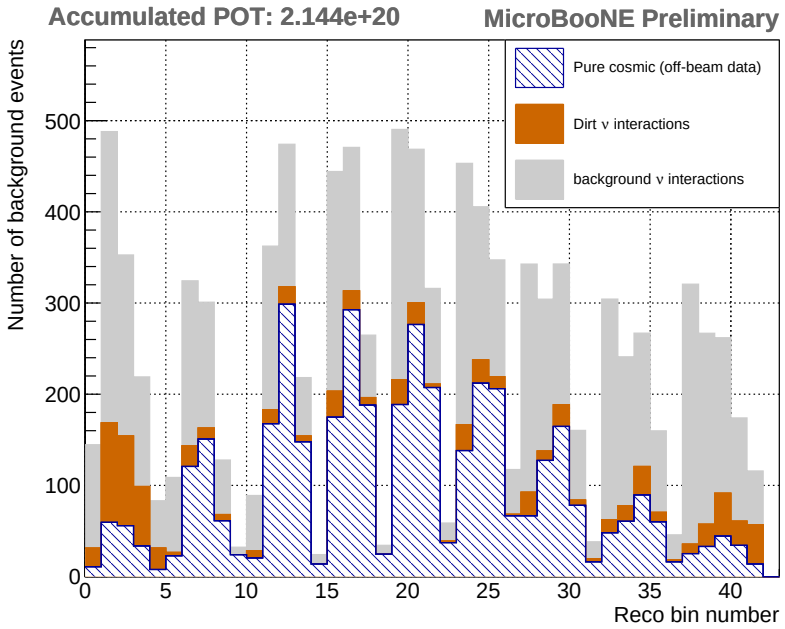

Figure 6.4.: The number of background events coming from different sources used in this analysis.

As one can see in Figure 6.4 a large fraction of the background events are pure cosmic events that are estimated using measured data where no beam neutrinos are present in the detector. For this reason, this background is free from any model uncertainty while the other background sources have associated model uncertainties which are discussed in Section 6.1.

6.0.5. How to Forward-fold

As we have seen in the previous Sections 6.0.1 to 6.0.4 there are a few ingredients needed to compare a model to the data. Now follows a description of how to apply all these together to compare a model or generator to the data of this analysis ignoring the uncertainties which are explained in the next Section 6.1.

As an input one needs a theoretical prediction of the neutrino energies which enters the data presented in this analysis. This means one needs the prediction of the muon angle and its momentum coming from a ν_μ CC interaction for neutrino energies from

0.15 GeV to the end of the BNB neutrino energy spectrum around 7 GeV. Further one needs to convert the predicted cross-section to a normalized event rate by multiplying the MicroBooNE flux to it. This is usually (and also here) done using an event generator which translates a theory into an event rate including the information needed, here the θ angle and the muon momentum for the signal in the specified energy range.

The generators can include usually the incident neutrino flux energy spectrum and then calculated the events accordingly. But to get to the proper event rate prediction for the signal events in the data, the numbers have to be multiplied by the POT or the total flux and the number of targets which are given in Section 6.0.1. Including this scaling one ends up with a so-called true event rate distribution which can be binned in the binning presented in Section 6.0.2. This step is shown in Figure 6.5.

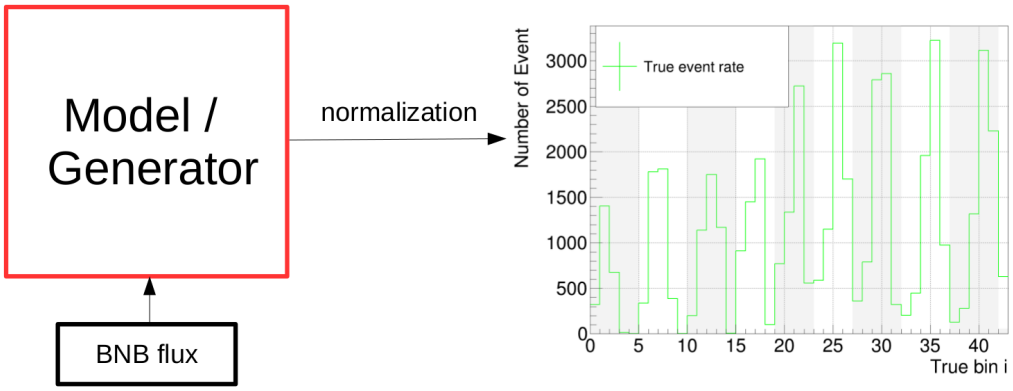

Figure 6.5.: A generator using a specific model predicts the number of events expected fro the BNB flux. Eventually, some scaling has to be applied to account for the number of targets in the fiducial volume or the total flux used for the data analysis.

Once one has the true event rate distribution in hand one has to apply the detector smearing. This is done by multiplying the event rate distribution by the smearing matrix where the efficiency is included, see Figure 6.6. The smearing matrix presented in Section 6.0.3 takes the true event rate and smears it to the distribution as the detector will reconstruct it. Some events will not be reconstructed and therefore the smeared event rate contains fewer events in all bins than the true distribution. Bin number 43 acts as the overflow bin where events outside of the phase space covered by the binning are placed, here events with a muon momentum above 2.5 MeV/c. These events eventually can enter the analysis due to detector smearing.

With the smeared true distribution representing the expected signal to be measured by the detector one still needs to add the expectation of the number of background events in each bin. The background distribution presented in Section 6.0.4 originates from the model used for the simulation of the experiment. Since the background has a large variety of sources the distribution is directly given in reconstructed bins

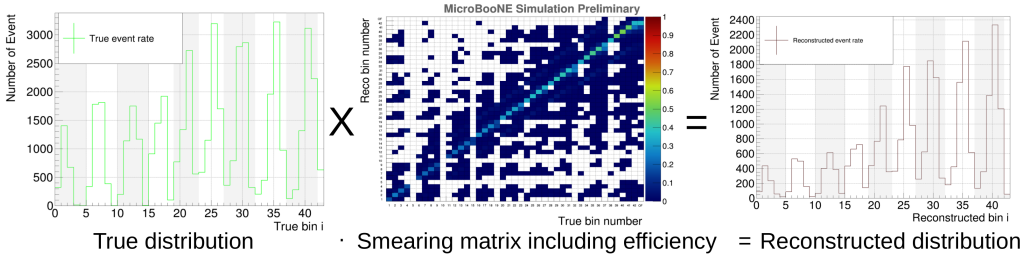

Figure 6.6.: The expected true event rate for a given flux and detector volume has to be smeared to a distribution as the detector will reconstruct it. This is done by multiplying the smearing matrix to the true distribution which included the binned efficiency.

therefore no smearing matrix has to be applied. Including the background, the event rate prediction is now complete and can be compared to the data distribution as seen in Figure 6.7. Although all the uncertainties still have to be taken into account for a quantitative comparison of the two distributions. This explained in the next Section 6.1.

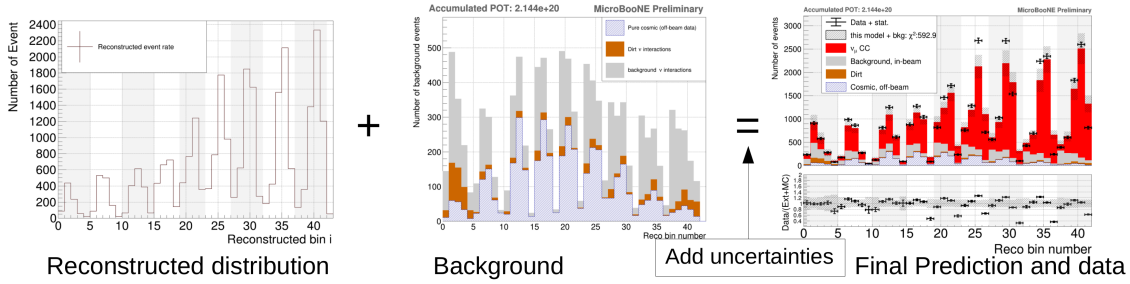

Figure 6.7.: The expected signal rate as seen by the detector includes no background contributions. Therefore this needs to be added before it can be compared to the measured data points. For a quantitative comparison the uncertainties has to be included which is explained in the Section 6.1.

6.1. Systematic Uncertainties

As we have seen in the previous Section 6, instead of a cross-section normalized distribution, the event rate is compared. The predicted event rate is built out of three different samples as explained in Section 5.1. There are different sources of uncertainty for each sample.

The overlay sample contains the most events which passing the selection. This sample contains background events as well as signal events, both have uncertainties assigned to them regarding detector modeling, cross-section modeling, and flux modeling. These are discussed in detail in Subsections 6.1.1, 6.1.2 and 6.1.3 respectively.

The beam-off sample consists of measured data where no neutrino has interacted in or around the detector. Its uncertainty is discussed in the Subsection 6.1.4.

The uncertainty assigned to events coming from the 'Dirt' sample is discussed in Subsection 6.1.5.

Generally, a covariance matrix E_{ij} is calculated as given in Equation 6.4 for each source of uncertainty which is then added together to get the total uncertainty on the prediction:

$$E_{ij} = \frac{1}{N_s} \sum_{s=0}^{N_s} (\sigma_i^s - \sigma_i^{cv}) \cdot (\sigma_j^s - \sigma_j^{cv}) \tag{6.4}$$

Since we deal here with event rates the σ_i^s is the varied number of all events (signal and background) in bin i for the universe s and σ_i^{cv} is the central value of that bin. This is the multiverse approach where N_s is the number of universes that are smeared according to the uncertainty of a specific effect or an ensemble of effects. Some uncertainty is estimated by only using one varied universe where the specific effect is changed according to one standard deviation. For this case, N_s is simply one.

Since this way of calculation of the uncertainties is chosen a few assumptions are made about the uncertainties. Since we calculate for each source the covariance matrix we assume Gaussian error distribution. The uncertainty is assigned symmetrically which is an approximation especially for a bin with low event rates.

While the uncertainty on the signal is newly calculated for each model prediction, the background distribution with its uncertainties remains the same. Here comes the assumption that the background does not change dramatically for different models. As mentioned in 6.0.4, one could calculate also the smearing matrix for each background and calculate the new prediction according to a new model but this makes the procedure complicated without bringing many advantages. Also, this analysis has a purity of around 72%, and around 15% of the background comes from beam-off data, so the modeling of the background events plays only a minor role.

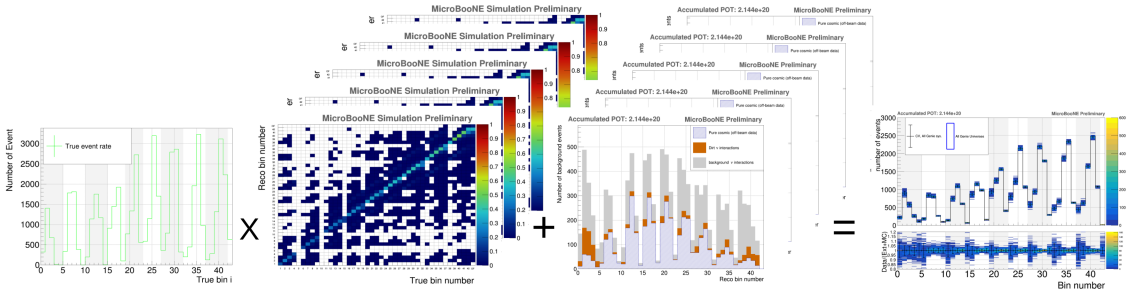

Figure 6.8.: Depending on the uncertainty, a specific amount of varied smearing matrices and background predictions are used to form varied predictions using a given true distribution. The difference between the central value prediction and all the varied predictions is used to assign the uncertainty due to the cause of the variation.

In Figure 6.8 one can see an example of how the uncertainties are calculated. For each variation ($\mathcal{O}(100)$ for multiverse approach, one for single variation) a new smearing matrix and background prediction is calculated. These are correlated and forms a new prediction. The difference between the varied prediction and the central value prediction is then used for the estimation of the uncertainty.

6.1.1. Detector Uncertainties

This section discusses the uncertainties associated with differences between the simulated detector response and its real response. The uncertainties regarding the charge and light system of the LArTPC are evaluated using a completely new detector simulation for each effect considered. This is discussed first. Then the uncertainties related to the CRT are discussed. Here a first estimation of the difference between the CRT detector modeling and the real response is estimated for the first time in MicroBooNE.

LArTPC Uncertainties

Detector uncertainties are assessed by modifying underlying characteristics of the simulation or low-level reconstruction quantities and re-extracting the number of passing events. A covariance E is calculated for each source of uncertainty x by taking the difference of the event rate of the modified simulation σ^x and the central value σ^{CV} for bin i and j:

$$E_{ij}^x = (\sigma_i^x - \sigma_i^{CV}) \cdot (\sigma_j^x - \sigma_j^{CV}) \tag{6.5}$$

The same events are used to minimize the effect of statistical fluctuations in the samples. For each treated effect, the simulation is redone by using the same unbiased off-beam event for overlaying and the same interaction of the neutrino simulation. Using this procedure, the uncertainty for each source is assumed to be Gaussian and the varied simulation is treated as a change of one sigma symmetrically applied in both directions. An overview of which parameters were taken into account is given in Table 6.3. A detailed description of the samples can be found in [105].

Uncertainties on the optical model arise from variations to the overall light yield, the attenuation model, and a different parameter for Rayleigh scattering in argon. The central values are given in the Table 2.1 with all the properties of LAr. For the light yield, a general decrease of 25% at the photo production stage is implemented. This is motivated by a study of the light yield of anode and cathode piercing tracks. For the uncertainty on the Rayleigh scattering, an alternative scattering length of 120 cm is used, the nominal simulation is based on a 60 cm scattering length. Different measurements of the Rayleigh scattering in LAr are covered by this uncertainty. The light attenuation is not modeled in the nominal simulation, therefore the alternative simulation uses a 10 m absorption length to account for the eventual difference between the simulation and the real data.

Detector variation	rel. diff. of the tot. event rate
Space charge	-0.62 %
Light yield Down	0.47 %
Light yield Attenuation	1.70 %
Light yield Rayleigh	0.01 %
Wire modification θ_{XZ}	0.29 %
Wire modification θ_{YZ}	0.65 %
Wire modification drift direction	-0.07 %
Wire modification YZ direction	0.60 %
Wire modification dE/dx	0.90 %
Recombination	1.70 %
Total (quadratic sum)	**2.85%**

Table 6.3.: The difference in the total flux integrated event rate for the different detector variation samples.

Space charge is based on an in situ measurement provided by cosmic rays and UV-laser system, see Section 3.5. The UV laser can introduce completely straight ionization tracks in the LArTPC, any deviations in the reconstruction can be translated in a correction map. Also, cosmic muons provide a source of nearly straight tracks, so one can also estimate the effect of the space charge based on deviations seen in cosmic muon tracks. The uncertainty reported here reflects the uncertainty in that measurement derived in a data-driven way.

The wire modification samples include variations in the waveform measured by the wire readout of the TPC. The modification covers the difference observed between data and simulation depending on the position of the charge deposition (X and YZ modification) or the angle of the trajectory of a particle to the wires (Θ_X or Θ_{YZ} modification). The dE/dx sample accounts for uncertainty due to the energy deposition of a particle in liquid argon and the corresponding charge which then drifts inside the TPC. Finally, the recombination sample represents the uncertainty in the number of initially produced electrons, so the amount of initially produced free electrons which then recombine again with the argon ions before reaching the wire readout.

As one can see in Table 6.3 the light attenuation has the biggest effect on this analysis. Since the light signal from the PMTs is matched to the collected charge on the wire planes a mis-modeling of the light signal can lead to losses during the reconstruction process.

In Figure 6.9 one can see the effect of the different detector variations on the double differential event rate. The uncertainty bars on the central value are then the quadratic sum of the difference of each variation corresponding to the total detector systematic uncertainty due to the detector systematics. To see the difference in more detail, the ratio plot shows the fractional difference.

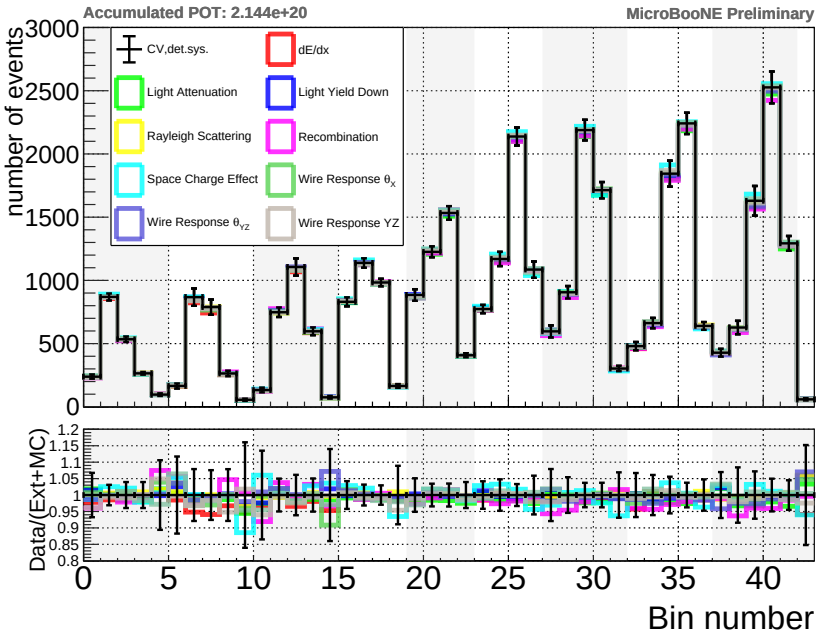

Figure 6.9.: The event rate passing the selection for the different detector-varied samples. The error bars are the resulting uncertainties including the variation of all the samples shown.

CRT Uncertainties

The CRT uncertainty is not included in the detector variation samples mentioned above. Its associated uncertainty is evaluated by assuming a 10% difference in the tagging efficiency between the simulation and data. The 10% difference is a conservative estimation based on the data-MC comparison. A tagging efficiency was measured to be above 95% for all locations on a CRT panel [6]. By looking at the histograms where the CRT cuts are explained (Figure 5.4 to 5.7) one can see that an eventual difference between the prediction and the data is well below a 10% difference. The number of passing signal events for the efficiency and passing background events for the subtraction for simulated samples (dirt and overlay) was adjusted resulting in a difference of the total event rate of 0.63%. This is taken as the uncertainty due to the CRT on the total event rate. The same procedure is applied to the bins of the double differential event rate results. The change is shown in Figure 6.10.

A comparison to the previous ν_μ CC inclusive analysis of MicroBooNE [13] shows that the detector systematic uncertainty could be heavily reduced from 16.2% to the values presented here. This could be achieved by improving the detector model by including various effects as an induced charge of neighboring wires and the space charge effect.

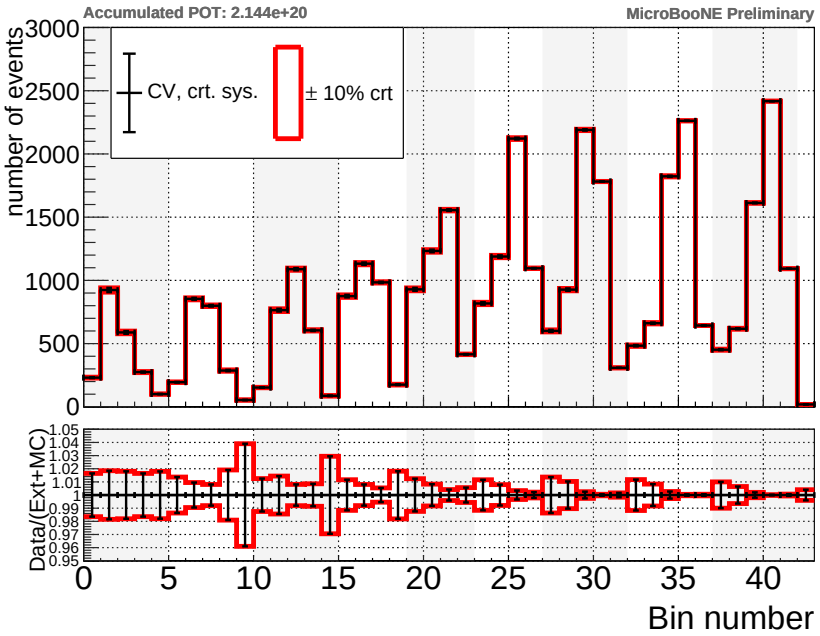

Figure 6.10.: The event rate passing the selection for the central value and ± 10% efficiency of the CRT for the simulated events.

6.1.2. Cross Section Model Uncertainties

The uncertainties for most of the cross-section model processes are calculated by generating 600 'universes' in which various model parameters are varied randomly according to Gaussian distributions with one-sigma uncertainties as described in [55]. The parameters were varied simultaneously in each universe to allow for correlations between parameters. Uncertainties not included in this procedure were calculated by using two universes and taking the difference between the two. They are stated in [55] and are shown in Figure A.2, the reason for this special treatment is that for these uncertainties a different model is used as an estimation of the uncertainty.

Uncertainty	rel. diff. of the tot. event rate
cross-section	2.15%

Table 6.4.: The uncertainty on the total event rate due to cross-section uncertainties.

In Figure 6.11 one can see the variations on the double differential event rate due to the variations of the cross-section input parameters. The total uncertainty is then given by the standard deviation of the variations to the central value. Not all input parameters are considered in the variation shown in Figure 6.11. Detailed information about what parameters were varied can be found in [55].

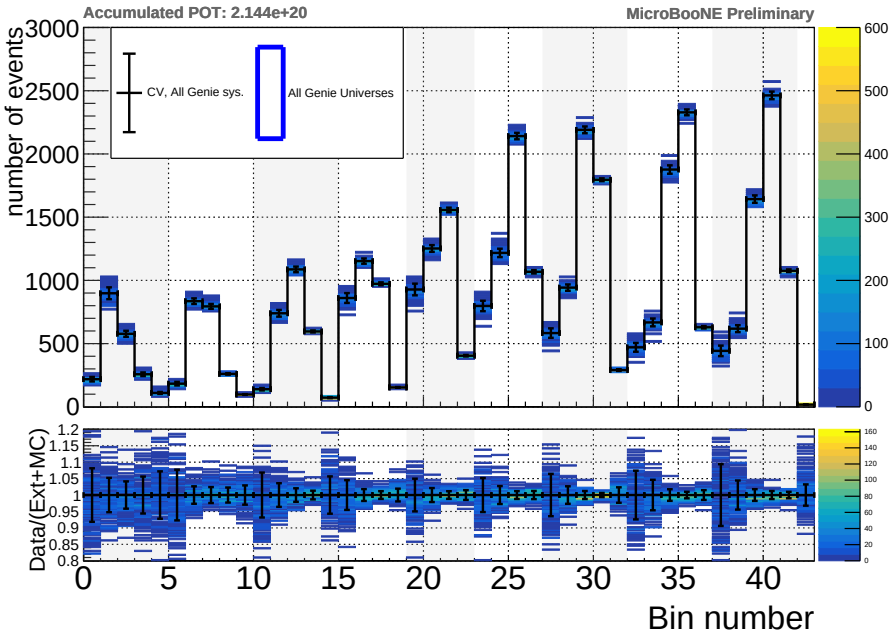

Figure 6.11.: The event rate passing the selection for the central value and 100 universes where an ensemble of cross-section modeling parameters were varied simultaneous.

The remaining parameters were included by taking the difference of two universes where one universe corresponds to the central value for most cases. The effect of these variations is shown in Figure 6.12. The ratio plot below shows the difference of a variation to the central value. The error bars in these figures show the total uncertainty for each bin calculated the variation in the figures. The description of these parameters can be found in [55].

6.1.3. Flux Uncertainties

MicroBooNE reuses the beam simulation from the MiniBooNE experiment which is based on a GEANT4 simulation. The flux uncertainty is evaluated by taking the number of background events into account as well as the change of the total flux on ν_μ neutrinos through the active volume of the TPC. We calculate here the varied event rate according to this equation:

$$N^i_{pred} = \left(N^i_{signal} + N^i_{bkg(MC)}\right) \cdot \frac{\phi_i}{\phi^{CV}} + N^i_{cosmic} \tag{6.6}$$

Here, N^i_{pred} is the new predicted number of events estimated by the varied number of signal (N^i_{signal}) and background ($N^i_{bkg(MC)}$) events normalized by the difference of the total flux of the central value (ϕ_{CV}) and the varied total flux (ϕ^i). The number of

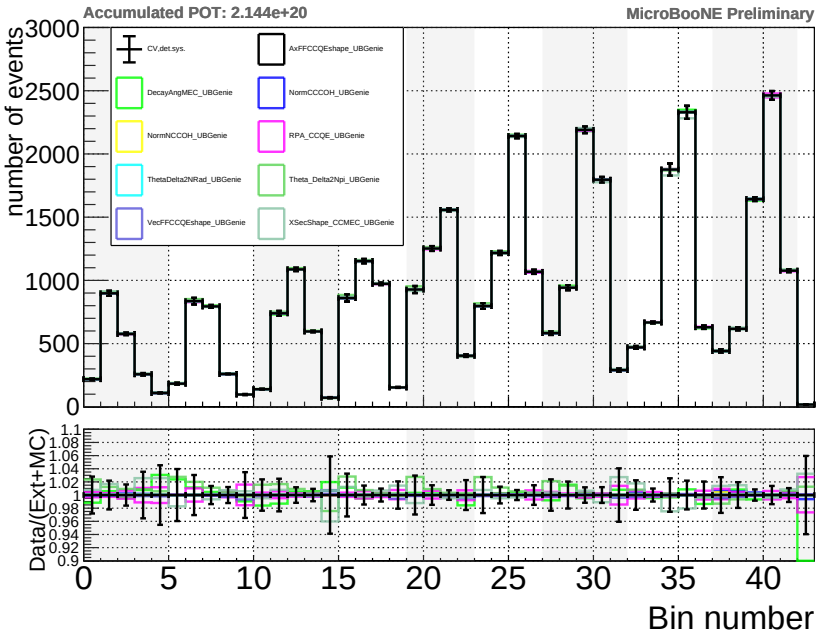

Figure 6.12.: The event rate passing the selection for the central value and the distribution where each cross section variation represents the impact of using a different model for the relevant process.

off-beam cosmic interaction N^i_{cosmic} remains the same since its originates from real off-beam data. The i represents a specific universe, the total number of universes used for the calculation is 1000.

Included are the uncertainties due to the hadron production of secondary particles after the protons hit the target as well as non-hadronic uncertainties like the uncertainties in the horn current which focus the secondary particles in the decay pipe. The π^+ and π^- production uncertainties are evaluated by using the HARP measurements. Also considered are the pion and nucleon cross-sections where pion production (10.32%) contributes the most to the total flux uncertainty. Table 6.5 summarizes the source of uncertainties where the uncertainty for others includes uncertainties on the cross-section of pions and nucleons on beryllium and aluminum as well as uncertainties related to the horn current.

In Figure 6.13 one can see the variations on the double differential event rate due to the flux variations. The total uncertainty is then given by the quadratic sum of the standard deviation of each variation to the central value. So a bias between the mean of the variations and the central value would lead to increased uncertainty.

Uncertainty	rel. diff. of the tot. event rate
π^+	10.32%
π^-	0.10%
K^+	0.19%
K^-	0.01%
K^0	0.04%
Other	4.12%
Total flux	11.12%

Table 6.5.: The uncertainty on the total event rate due to flux uncertainties.

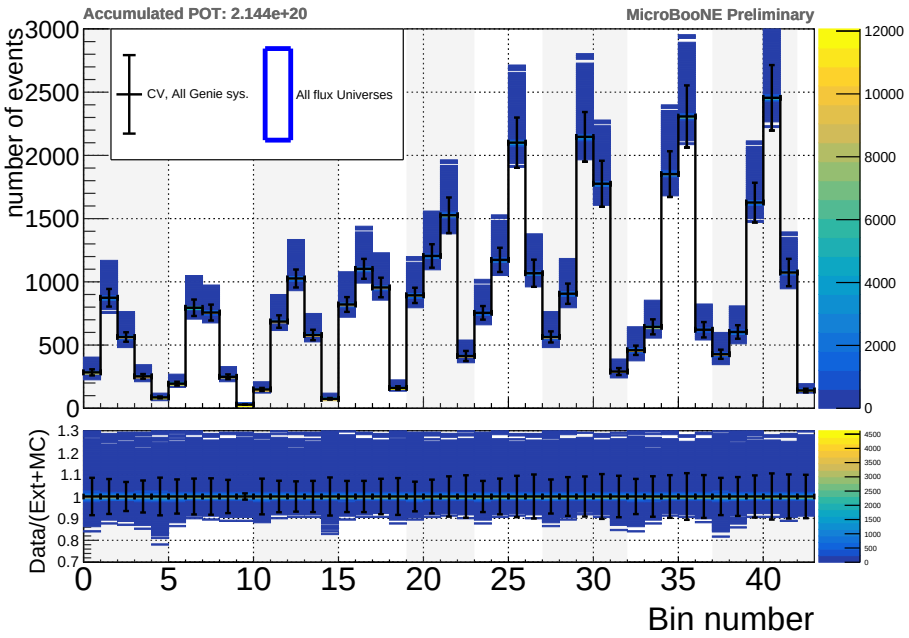

Figure 6.13.: The event rate passing the selection for the central value and 1000 universes for each of the 13 parameters on which the flux uncertainty is evaluated.

6.1.4. Other Uncertainties

Around 10% of the background comes from cosmic interactions which have triggered the readout of the detector. The amount of these events is evaluated using events where no beam neutrinos are present in the detector but the state of the detector is the same as when the beam is on. The number is evaluated by scaling the number of events of possible readouts of the off-beam sample to the number of possible on-beam readouts. For this reason, no significant difference between the off-beam cosmic events and the events where no neutrino has interacted in or close to the detector is

expected. Therefore no systematic uncertainty is associated with these interactions since both are real data taken in the same detector configuration.

A study on the effect of re-interaction of the outgoing particles in the argon on the total cross-section has shown that the uncertainty is less than 0.2% and therefore negligible compared to the other sources of uncertainty [106].

To take into account uncertainties due to POT counting, an overall 2% uncertainty is added to the flux uncertainty. This corresponds to the difference of two independent measurements of the proton intensity per pulse. For the total event rate, this accounts for a 1.86% uncertainty since the beam-off contribution is not affected by this.

6.1.5. Dirt Uncertainties

The amount of events where the neutrino has interacted outside the cryostat ('dirt') is estimated using the POT information. Since the total contribution of these events is difficult to validate a conservative assumption of 100% on these interactions is used in this analysis. The variations in the total event rate are shown in 6.14.

Due to improved rejection power of these events using the CRT (see Figure 4.32 in Section 4.8 and Section 5.5), this ends up only with a 1.51% uncertainty on the total event rate.

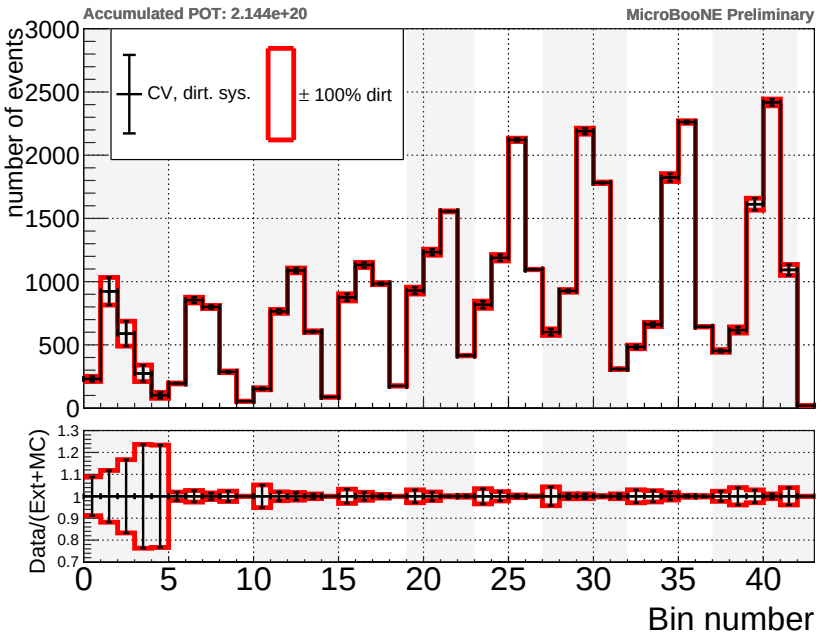

Figure 6.14.: The event rate passing the selection for the central value ± 100% contribution from the dirt sample.

6.1.6. Statistical Uncertainty

For this counting experiment that counts events passing the selection in certain bins, the statistical uncertainty is taken as the square root of the number of events in a given bin.

All uncertainties are assigned to the prediction since the data is looked at as a throw of this model (see discussion at Appendix A.4). For this reason, the statistical uncertainty on the bins of the prediction has to be taken into account and not the statistical uncertainty of the data itself. Therefore the statistical error is given by the square root of the number on the total predicted events in each bin (using all the different samples).

In principle, one has also to take the statistical uncertainty of the prediction itself into account but then there is a risk of double counting the statistical uncertainty. Also, the statistical uncertainty of each sample is well below the statistical uncertainty of the total prediction. This is the case since a greater number of events for each signal or background channel is used and scaled down for the prediction. One exception is the dirt sample where the equivalent POT is not much higher than the POT in data. But as we have seen in Section 6.1.5, a 100% uncertainty is added for the dirt amount. For this reason, any statistical uncertainty of this sample should be well covered in the additional 100% uncertainty.

As one can see in Figure 6.15, the statistical uncertainty of the sub-samples is well below the statistical uncertainty of the final prediction. For one bin (bin 9) the cosmic contribution peaks above 60% but for this bin, the statistical error is well below the total uncertainty as shown in Figure 6.15. For this reason, any additional uncertainty coming from statistical fluctuations in the sample used for the prediction is neglected.

6.1.7. Summary Uncertainties

Here is a summary of all the uncertainties used in this analysis on the total number of events as well as on the total cross-section calculated using Equation A.1 is presented in Table 6.6.

The correlation and covariance matrix as well as a figure for the fractional uncertainties in each bin are given in Appendix B. The uncertainty for the total normalized cross-section is given here because the result is presented in Section 6.2.1 and gives a better intuition on the size of each uncertainty since the total event rate uncertainty is significantly smaller due to the cosmic ray background fraction where the uncertainty is neglected.

Figure 6.16 shows the prediction of the Monte Carlo simulation used for the simulation of the experiments with all uncertainties included. The values are stacked together and since they are added quadratically, the influence of some uncertainties is hardly visible. What prominently shows up is the large contribution due to the dirt interactions in the most backward bins.

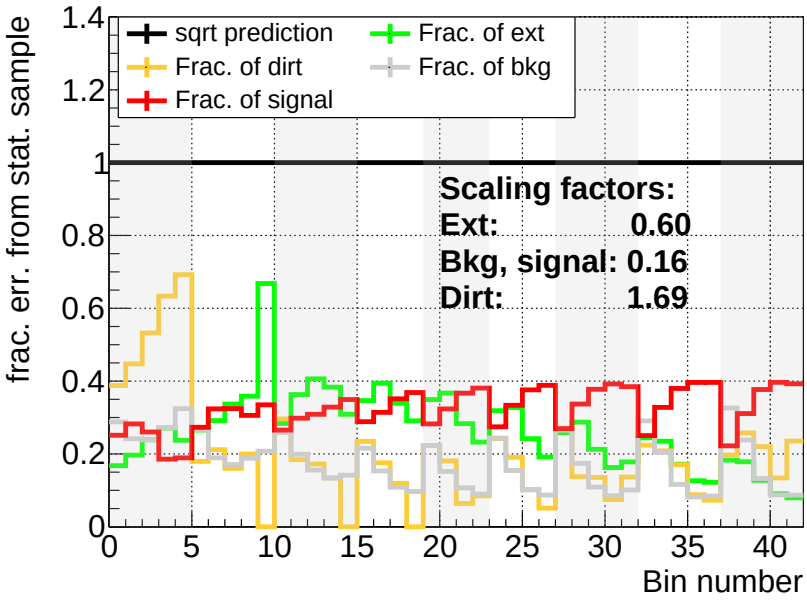

Figure 6.15.: The statistical uncertainty of each sample normalized by the statistical uncertainty of the final prediction. For the dirt sample a 100% uncertainty covers eventual statistical contributions and for the other samples the statistical uncertainty is much lower than the statistical uncertainty of the final prediction.

Source	Uncertainty	
	Total event rate	Total cross-section
Detector response	2.85%	3.92%
Cross section	2.27%	3.06%
Flux	11.12%	12.87%
Dirt background	2.37%	3.20%
Cosmic ray background	N/A	N/A
POT counting	1.78%	2.41%
CRT	0.63	2.64%
Statistics	0.51%	0.71%
Total (Quadratic Sum)	**12.10%**	**14.62%**

Table 6.6.: Summary of all uncertainties for the predicted event rate and the measured total flux integrated cross-section. The cosmic ray background has no uncertainty assigned to it (see 6.1.4.)

To see which uncertainties are dominant for specific bins one can look at the unstacked distribution in Figure 6.17. As one can see, the dirt contribution is only

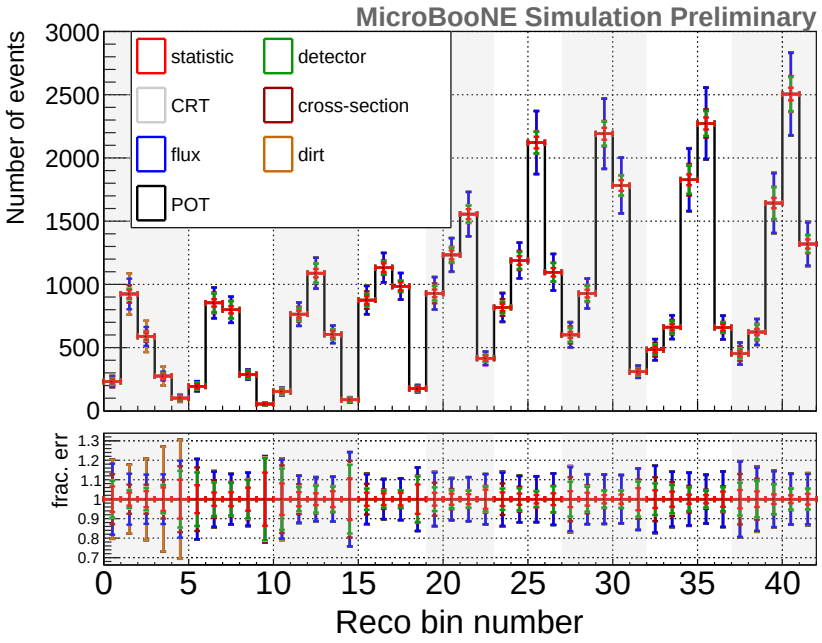

Figure 6.16.: The predicted event rate is shown with the uncertainty bars according to each source. The uncertainties are quadratically added from left to right and top to bottom as given in the legend. The dirt uncertainty dominates in the most backward bins but is nearly negligible for the others.

dominant for the most backward bins but only a very minor uncertainty for the other bins. For most bins, the flux uncertainties are dominant. Only for the bins with lower statistics is the detector modeling a leading uncertainty. As one can see the CRT contribution is nearly negligible for all bins.

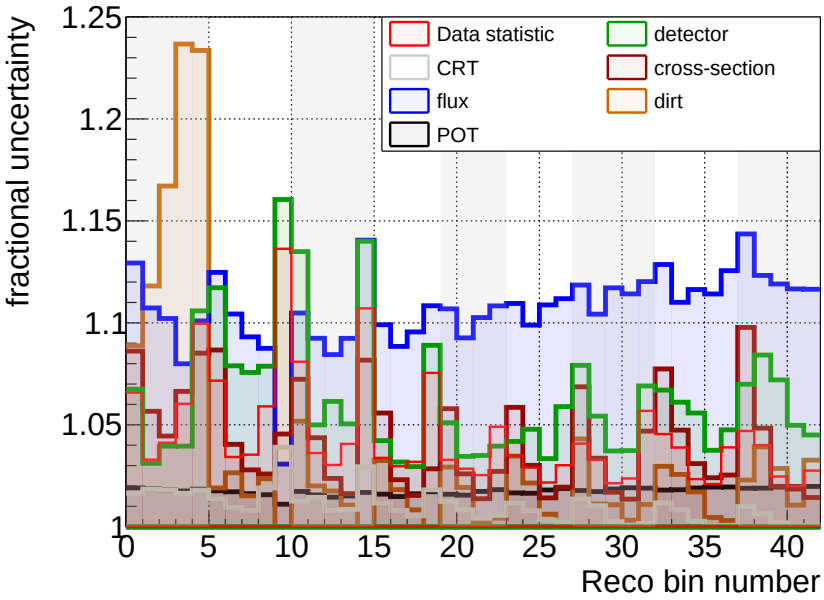

Figure 6.17.: The fractional uncertainties from all the different sources are shown individually (not stacked). For most bins the flux uncertainty dominates but for the most backward bins (dirt) and for some low statistic bins (detector).

6.2. Result

To give a compact overview of the result obtained in this analysis, first, the total cross-section with its uncertainty is shown. The prediction of different models is also obtained. For the calculation, the background prediction is subtracted from the data and the smearing matrix is used for the calculation of the detector smearing. Therefore this result is quite model dependent since the efficiency is calculated using the shape of the GENIE V3 tuned model and appears in the denominator for the calculation of the total cross-section obtained in data.

The less model-dependent result is represented as a double differential event rate with a clear separation between data and model. This measurement is presented in Section 6.2.2 following the Section 6.2.1 with the total cross-section result.

How to get this measurement for further comparison is explained in A.1.

6.2.1. Total Cross Section

The measured total cross-section including the efficiency correction calculated using the nominal simulation (GENIE V3 MicroBooNE tuned) is:

$$\sigma = 0.770 \pm 0.005 \text{ (stat)} \ \pm 0.113 \text{ (sys)} \cdot 10^{-38} \text{ cm}^2 \tag{6.7}$$

How this result compares to different generators is shown in Figure 6.18.

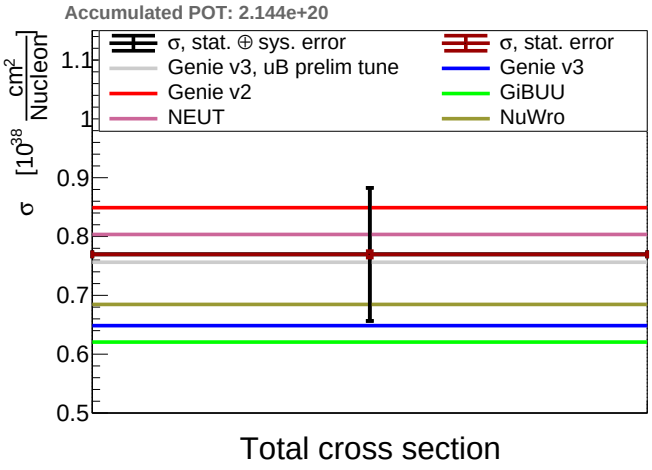

Figure 6.18.: Total cross-section plot: The data shows the total flux integrated cross-section with the assigned uncertainties. The line shows the MC predictions for different models, remark the vertical axis does not start at zero.

As one can see in Figure 6.18, the measured cross-section using the GENIE V3 uB tune for the background prediction and the efficiency estimation agrees best with the same model prediction. NEUT predicts the cross-section also very close to the measured value. While GENIE V2 and NuWro are still within the one sigma uncertainty, the other models GENIE V3 and GiBUU are not in agreement with the measurement.

To see where this result stands in comparison to other experiments, Figure 6.19 shows this measurement in red together with the results already shown in Figure 2.3. This direct comparison was done by dividing the total cross-section by the mean energy of the BNB neutrinos, the uncertainty corresponds to one sigma. The values were taken from [107].

Since such a result depends on the model used for the prediction it is also not very surprising that the model used for the prediction and its cross-section itself agrees best. To reduce model dependencies introduced by the cross-section calculation, the double differential result is shown as an event rate where some of these dependencies can be avoided. Also, the information is limited for the total cross-section while much more information is available by the double differential distribution presented next.

6.2.2. Double Differential Event Rate

The double differential result of the analysis is presented as an event rate and the comparison to the model used for the simulation of the background events and the

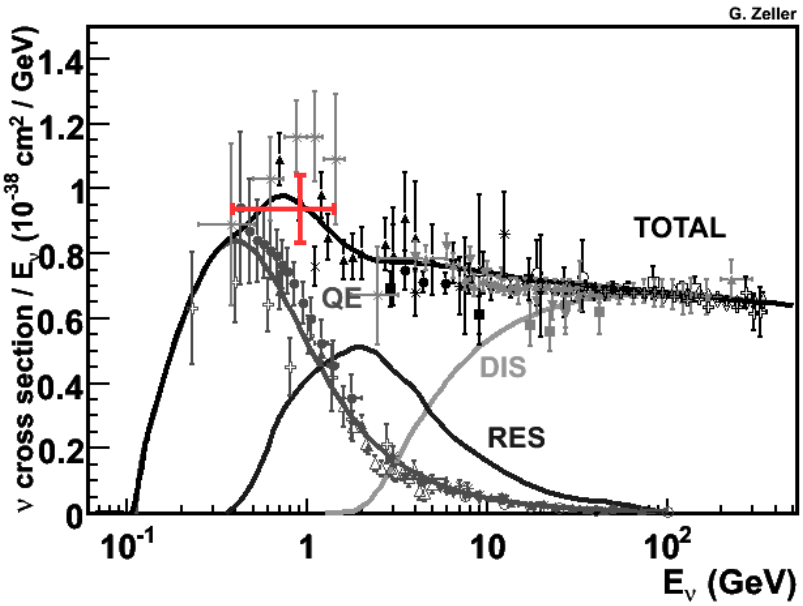

Figure 6.19.: The total cross-section divided by the BNB energy compared to other measurements.

detector smearing (GENIE MicroBooNE tune). Also, the true distribution of this model is used for the calculation of the signal prediction.

In Figure 6.20 we can see the different parts of the prediction of the data event rate. In blue is the contribution estimated by the off-beam events and in brown is the estimated amount coming from the dirt sample. In gray and red are the events from the overlay sample representing the background and the signal events respectively. On top of the stacked prediction, the systematic error bars are drawn as dashed black areas. Below the event rate distribution, the ratio between the data and the prediction is shown, also with the systematic uncertainty on the prediction. The error bars on the data are only statistical. This error is not taken into account for any calculation since the statistical error is added to the prediction as described in Section 6.1.6.

As we can see in this Figure 6.20 most data points are within the uncertainty of the model prediction. But a general shape disagreement is visible according to the disagreement seen in the event rate figure for different momenta in Figure 5.18. Also now it is visible that the disagreement becomes more significant in the more forward direction. Against the intuition one could get after looking at the event rate figures in Section 5.7 Figure 5.17, the most backward bins (bin number 1 to 5) are in good agreement with the model prediction. Also, the next bins (6 to 10) are almost within the model prediction.

For all further bins, the shape disagreement seen in Figure 5.18 leads to a disagreement of the data and the model. Especially for the high momentum bins (19,

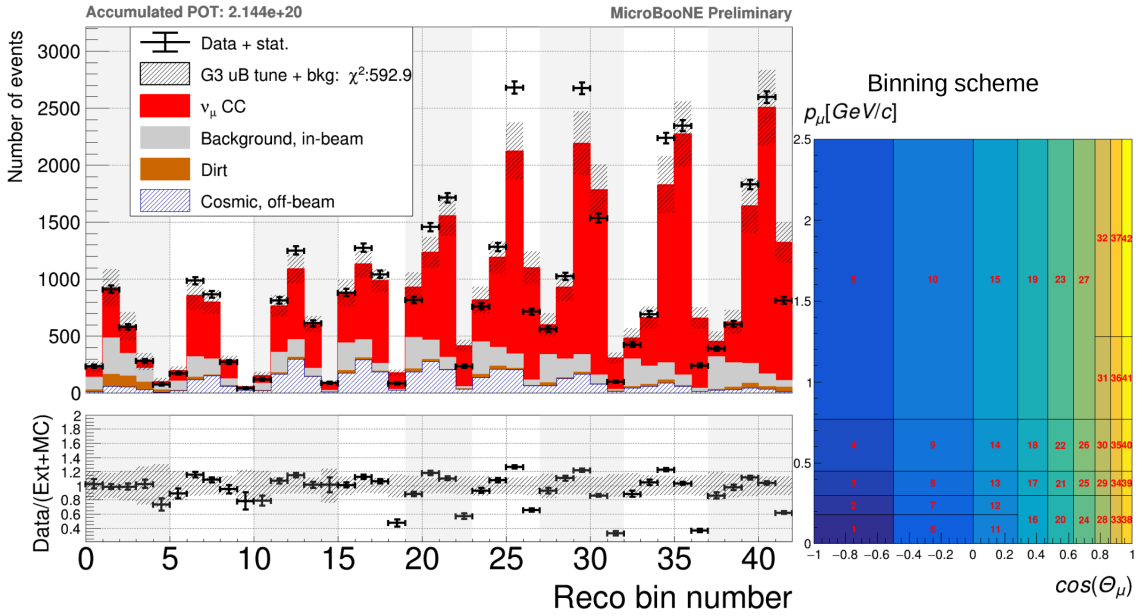

Figure 6.20.: The double differential event rate measured as well as the prediction using beam-off (blue), dirt (brown), neutrino background (grey) and signal events (red). The horizontal axis shows the bin number according to the binning shown on the right side or in 6.1.

23, 27, 32, and 37), the prediction is well above the measured value. Also, the underestimation of the model for medium momenta is visible in some bins (e.g 13, 22, 26, and 30).

While Figure 6.20 shows all the double differential bins in one plot by bin number, Figure 6.21 shows for each value of $\cos(\theta)$ the histogram for the momentum bins resulting in nine different histograms. The value of the $\cos(\theta)$ angle is given for each histogram and now the backgrounds are split into the groups introduced earlier. It shows the same information as Figure 6.20 but with more details for the backgrounds.

In the next section, the signal distribution is split by the different interaction channels occurring at these energies and compared to data. Also, a study of different model predictions is done in the following section.

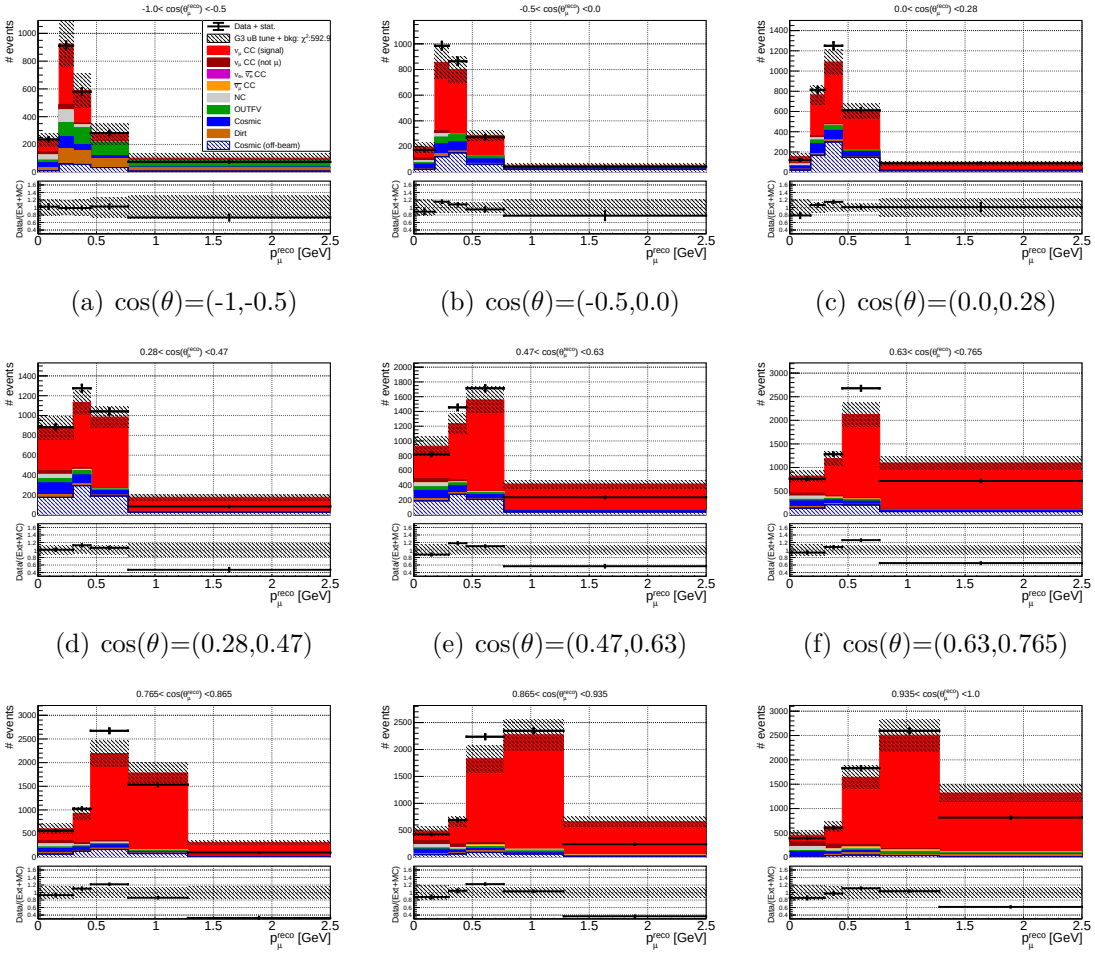

(a) cos(θ)=(-1,-0.5) (b) cos(θ)=(-0.5,0.0) (c) cos(θ)=(0.0,0.28)

(d) cos(θ)=(0.28,0.47) (e) cos(θ)=(0.47,0.63) (f) cos(θ)=(0.63,0.765)

(g) cos(θ)=(0.765,0.895) (h) cos(θ)=(0.895,0.935) (i) cos(θ)=(0.935,1)

Figure 6.21.: Double differential event rate with the different background contributions as shown in 5.7. Each histogram represents a certain bin of cos(θ) angles.

6.3. Split by Interaction Channel

To see the contribution of each interaction channel within the GENIE model MicroBooNE tune used for the simulation of the experiment, the distribution of the data with the subtracted background as well as the stacked contribution of each interaction channel is shown in Figure 6.22.

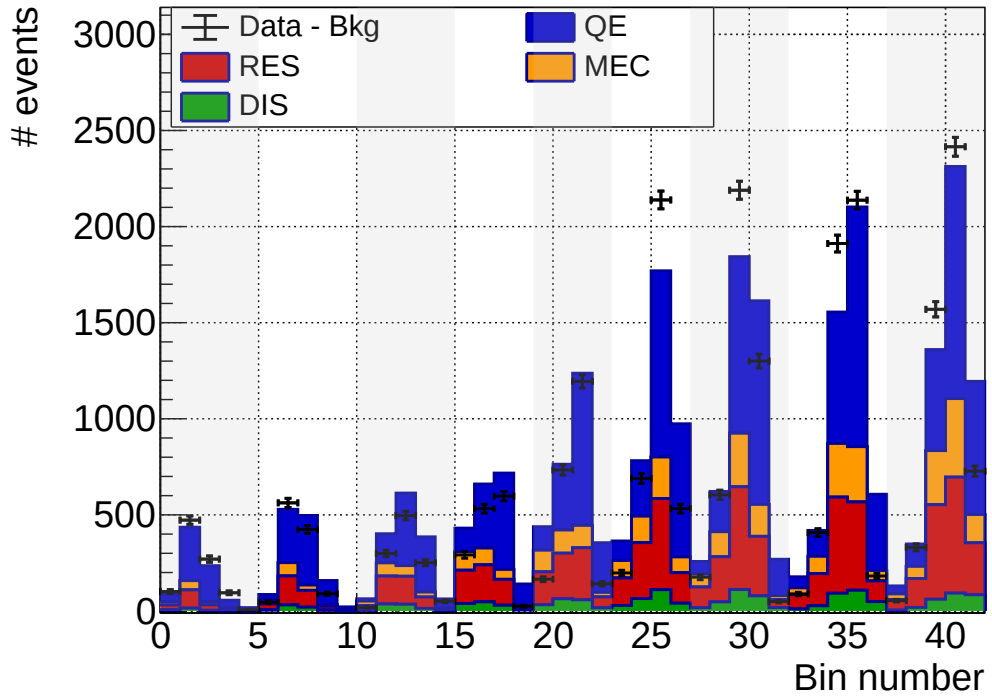

Figure 6.22.: The double differential event rate measured with all background events subtracted. The stacked histogram shows the expected contribution of each interaction channel: QE, RES, MEC and DIS.

As one can see in Figure 6.22, bin 5 has a negative number of events. This is caused by a lower number of events than the number of expected backgrounds in this bin. Since with the subtraction, simulated events are mixed with measured events the calculation of the size of the error bars is not straightforward anymore, and therefore, they are not drawn here. The negative number of events here represents already one problem when the result is presented not as an event rate but as a mixture of simulation and measured data. These negative values would lead to a negative cross-section. Both, a negative number of signal events as well as a negative cross-section are not physical. But by looking at Figure 6.20 one can see that the event rate for these bins is within the uncertainty.

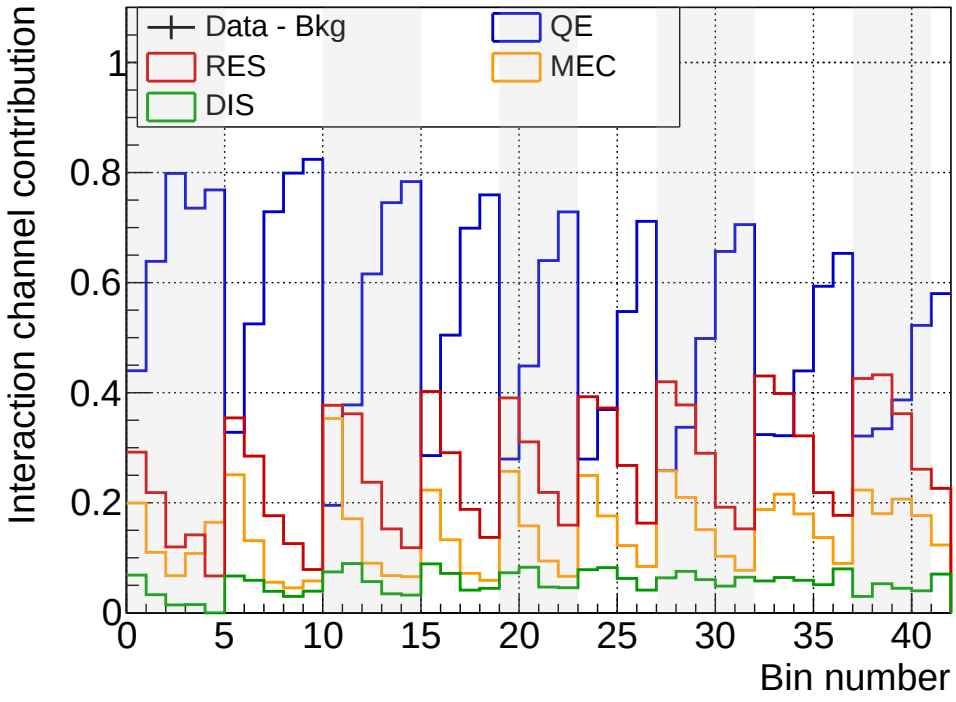

Figure 6.23.: The fractional double differential event rate distribution for each interaction channel: QE, RES, MEC and DIS.

If one checks the fractional contribution of each interaction channel for the double differential bins in Figure 6.23 one can see that the QE events are dominating at higher muon momentum bins while the contribution of DIS events is for all bins similar. The amount of RES and MEC events is higher for the low momenta bins and the RES events are even dominating over the QE events for some low momentum bins. This is expected since the QE channel dominates at low energy transfer, therefore these are the events where the muon has still most of the initial neutrino energy.

One can not conclude that the differences between the measured data and the prediction comes from a certain interaction channel. A try to fit the data distribution with different normalization of the interaction channels led to no reasonable result. For completeness is in Appendix A.5 the forward-folded cross-section shown since there one can also draw the contribution of each interaction channel for each bin. This is done although without showing the uncertainties as discussed in 6.

6.4. Comparison to Different Generators

As we have seen in the discussion at the beginning of Section 6 introducing the cross-section representation, the way of showing the result of this analysis is based on the measured event rate rather than some calculated estimation of a cross-section based on the event rate.

This comes at the cost of not showing a forward-folded cross-section but brings the advantage of strictly separated uncertainties between the data and a prediction. This pays off especially when one wants to compare the measurement to different models as it is done here.

Here the predicted event rate of different models is compared to the data. The event rate prediction is calculated by using the framework NUISANCE [108] together with the MicroBooNE flux and the prediction of different generators for this flux. The used generators are the following and discussed in more detail in 2.6.1:

- GENIE v2_12_10 (Version 2)
- GENIE v3.00.04 (Version 3)
- NEUT Version 5.4.0.1
- NuWro Version 19.02.1
- GiBUU release 2019

The true event rate prediction for the MicroBooNE flux coming from these different generators is then used for the calculation of the uncertainty. The background is expected to have a sub-dominant effect and therefore is not newly modeled. For all different signal models, the background estimation originates from the tuned GENIE Version 3 including the estimated uncertainty on it. The signal prediction is smeared with the detector smearing matrix and therefore also corrected for the detection efficiency. To get the uncertainty estimation right, the background according to each varied universe (as discussed in the different uncertainty sections) is used as well as the varied detector smearing matrix. By doing this we receive a new estimation of the uncertainty according to each model while in the case where only a covariance matrix would be presented, such a recalculation would not be possible. But this procedure needs the publication of all varied background estimations as well as all the detector smearing matrices. REMU [104] would be a tool that allows all of this in a prepared way but is not directly applicable in the way the detector uncertainties are usually calculated in MicroBooNE. It provides a forward-folding framework with flexible binning where the measurement including the uncertainty estimation can be implemented for easy use by people external of the experiment.

If one would like to argue that the recalculation of the uncertainties brings only a small advantage and does not change the conclusion one should have a look at Appendix A.7. There it is shown that indeed, the preference for which model fits does not change, but the χ^2, and therefore the absolute level of agreement, does change.

The χ^2 agreement is calculated the following way:

$$\chi^2 = \sum_{ij} \left[\sigma_i^{\text{data}} - \sigma_i^{\text{pred}}\right] \cdot \left[E_{ij}^{\text{pred}}\right]^{-1} \cdot \left[\sigma_j^{\text{data}} - \sigma_j^{\text{pred}}\right] \tag{6.8}$$

Where i and j are the bins numbers and E_{ij}^{pred} is the total covariance matrix of the prediction which then has to be inverted. The σ_i^{data} and σ_i^{pred} stands for the events in bin i measured in the beam sample and its prediction, respectively.

The different models and the comparison of their prediction including their uncertainty to the data are given in Table 6.7.

Model	Genie tune	Genie V3	Genie V2	Neut	NuWro	GiBUU
total χ^2	592.9	652.5	632.7	507.9	588.5	781.2
χ^2/NDF	14.12	15.54	15.06	12.09	14.01	18.60

Table 6.7.: Summary of the χ^2 values of the data to MC comparison using different models. The uncertainties are recalculated for each model using the varied detector smearing matrices and the true distribution of the model. The full distributions are shown in A.7. The number of degrees of freedom is 42 since that many bins are used.

The event rate predictions for the different models and their recalculated uncertainties are shown in A.8, Figure A.7 in the same as Figure 6.20. By looking at the event rate distributions one can see that no model predicts the same shape as the data regarding the different momenta. No model achieves chi^2/NDF of around one which means that none agree with the data within the uncertainty. The conclusion is either the uncertainties are underestimated or all models do not predict the data correctly.

To see the differences between the models better, Figure 6.24 shows the predictions of the different models (including all backgrounds) and the data in the same histogram. One can see that Genie V2 generally over-predicts the data in the more forward region while GiBUU under-predicts it for most of the backward bins. Drawing uncertainties in this Figure 6.24 would make the histogram unreadable. Another way that allows some indication of the uncertainty is to draw it at the data points and divide each prediction by the data distribution. This is technically not correct but allows an estimation of the uncertainty and the model to data comparison in one histogram. This is done in Figure 6.25. A correct comparison would be the data divided by the model with the model uncertainty also drawn. This is shown in the ratio plots below the event rate plots in Figure A.7 for each model individually.

As one can see in Figure 6.25, the difference between the data and the models is within 20% for most bins. Clear outliers are the highest momentum bins (19, 23, 27, 32, and 37). While the difference between the models and the data is mainly covered by the uncertainty for the backward region, the disagreement becomes significant in the more forward region. Generally one can see that all models predict the event rate with a similar shape. Since in Figure 6.25 the model predictions are divided by the

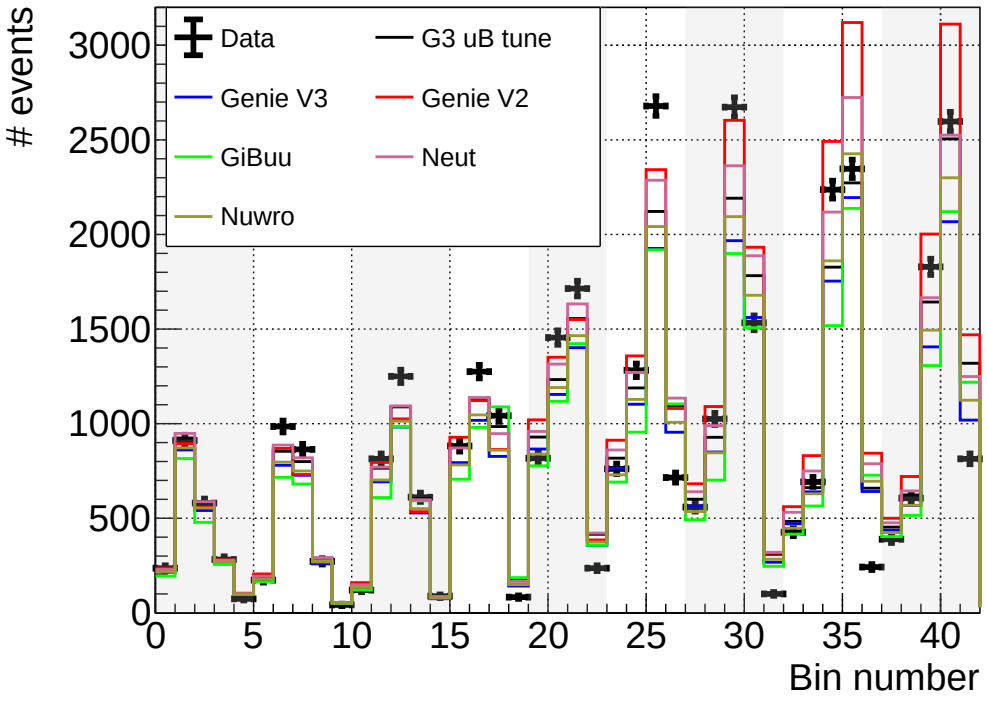

Figure 6.24.: The event rate measured and the different model prediction including all background events.

data one sees the shape disagreement in the general path of all the models around one.

Surprisingly, the best agreement in terms of the χ^2 value is not the tuned Genie Version 3 model. It is NEUT which describes the data best from all these models, although the χ^2 is still large. This model is used for the T2K experiment which operates at similar energies. The base model used for the simulation is the tuned GENIE Version 3 which was fit to T2K data, but it seems that the generator NEUT still outperforms the tuned GENIE version. Even the model NuWro describes the data slightly better. The untuned GENIE versions 2 and 3 perform both similarly, although by eye the discrepancies of Version 2 looking larger in the more forward region. In the end comes GiBUU. In Figure 6.25 one can see that the prediction of this model often is most far away from the data points.

All in all, one can say that no model describes the data satisfactorily, especially given the large shape discrepancies in the forward region.

In order to see if the disagreement comes only from certain bins, Figure 6.26 shows the χ^2 values if only $N-1$ bins are considered. One can see that no specific bin dominates the χ^2 value. Some high momentum bins (e.g bin 37) have some effect in all models but generally, the $N-1$ χ^2 values are close to the total χ^2 value. NEUT

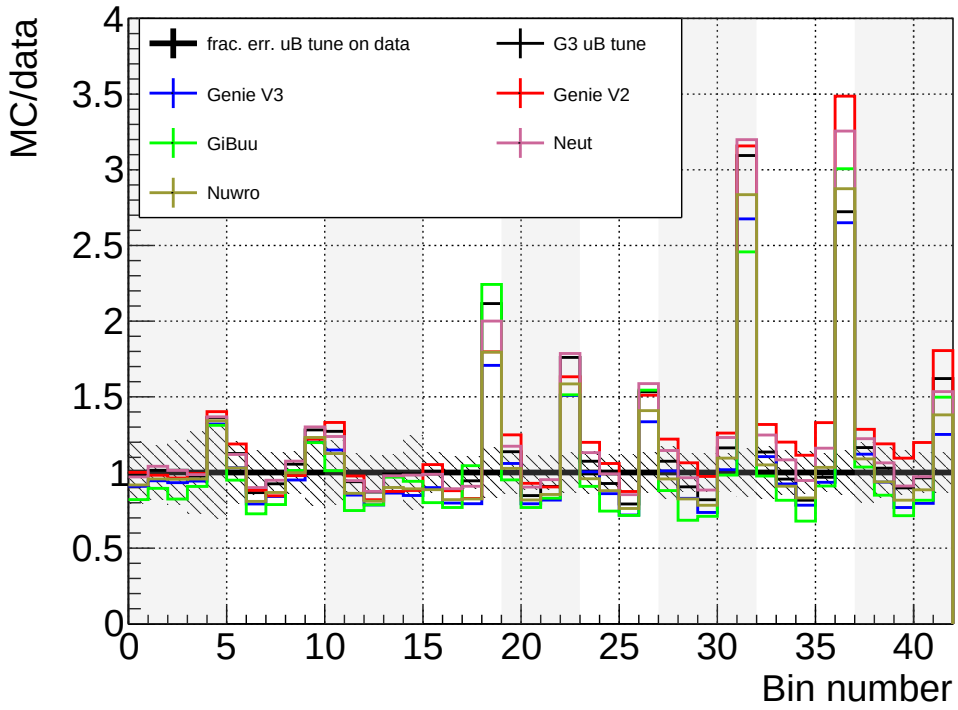

Figure 6.25.: The ratio of the different model prediction including all background events divided by the measured data. The fractional uncertainty of the tuned Genie model is added as an indication for the uncertainty on the data.

performs better than the other models while the order of the model with the highest χ^2 would change if certain bins would be excluded. The tuned GENIE model has a very similar performance as the model used by NuWro.

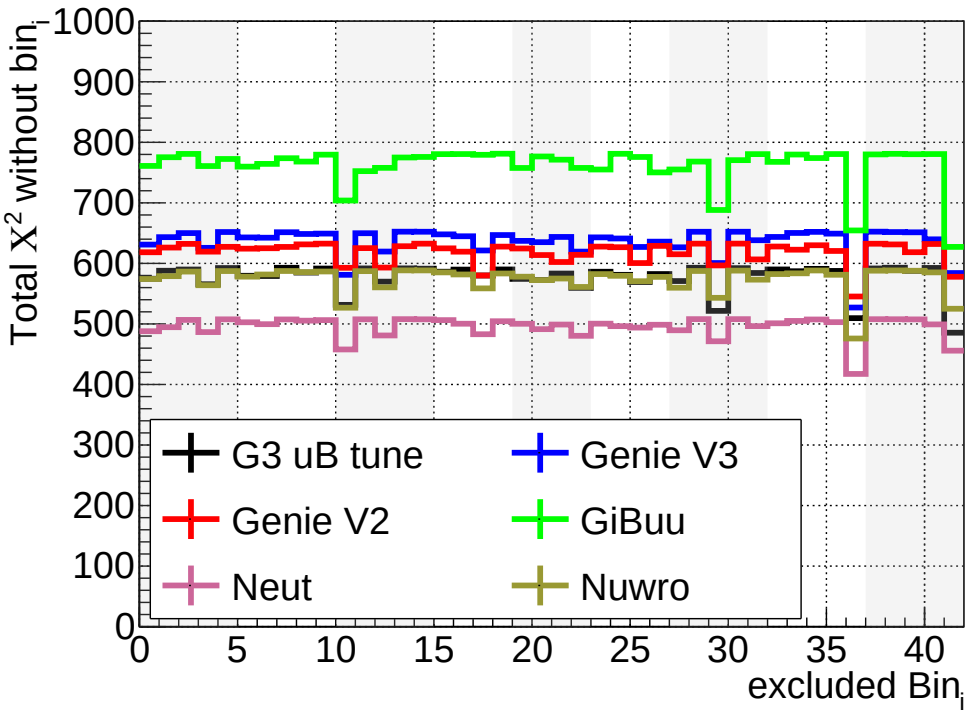

Figure 6.26.: The total χ^2 value is calculated by ignoring the specific bin i. In this way one can check if the χ^2 value is mainly driven by certain bins. Although bin 37 and 42 stick a bit out, ignoring these bin would not lead to a significant improvement of agreement.

7. Conclusion

With a better understanding of neutrino beams and the detectors used for measuring the neutrino interactions, the modeling of neutrino interactions potentially becomes a dominant source of uncertainty. Nuclear effects can distort the initially produced particles and make the prediction harder for heavy nuclei such as argon. This work presents a measurement of neutrino interactions at intermediate energies, where the modeling uncertainties are especially large, using the MicroBooNE detector with improved cosmic rejection using the newly implemented CRT.

Due to the detectors' location on the surface of the earth and the long readout time (2.3 ms) with respect to the beam spill (1.6 µs) and relatively low beam intensity ($\sim$ 1 ν per 600 spills), a large amount of cosmic induced signals will enter MicroBooNE or the other detectors in the SBN program at FNAL.

For this reason a CRT is built around the existing MicroBooNE detector and will also be built around the SBND detector. I assembled the CRT modules at the University of Bern and contributed to the installation around the MicroBooNE detector as well as the installation of the SBND test stand. With my reconstruction code, the CRT data is reconstructed to CRTHits in 3D space and time in a format that can be combined with the readout information of the LArTPC in MicroBooNE. The CRT integration for MicroBooNE is described in a publication [109].

I corrected several effects that were discovered to be drastically reducing the functionality of the CRT data. This enabled the cosmic rejection in MicroBooNE using the CRT. I have shown that, after my corrections, the performance of the CRT fulfills the requirements of a timing resolution in the order of a few nanoseconds and a position resolution in the order of a few centimeters.

With this performance, I have presented several possibilities of cosmic removal cuts depending on the topology of the signal and background contribution. A majority of these cuts are applied in a ν_μ CC inclusive selection, where they successfully remove a large part of the remaining comic background after an initial preselection. By using the CRT for cosmic removal, a flat efficiency over a large phase space after the cuts could be maintained. An additional set of cuts finalizing the selection lead to an efficiency of 56% and a signal purity of 72%. With this selection, I obtained a total cross-section as well as an intermediate single differential cross-section result in $\cos(\theta)$ and muon momentum which is described in a public note [106]. These results were shown at the 29th International Conference on Neutrino Physics and Astrophysics (Neutrino 2020). As one can see in Figure 7.1, the uncertainties on the total cross-section could significantly be reduced due to the use of the CRT and a better understanding of the detector response.

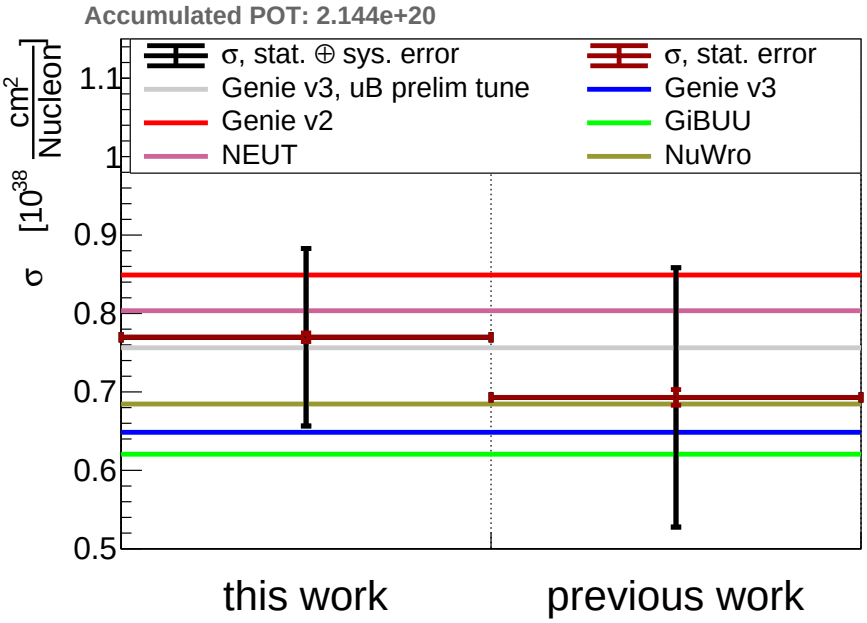

Figure 7.1.: Total cross-section plot: The data shows the total flux integrated cross-section with the assigned uncertainties obtained in this work as well as one of the previous work in [13]. The line shows the MC predictions for different models.

The final result that I obtained is represented as an event rate, allowing the clear separation of simulated and measured interactions. With this separation, the assignment of uncertainties to the simulated prediction could be achieved, ensuring minimal model dependence of the measurement.

The measured data points were compared to different predictions of commonly used neutrino generators. The recalculation of the covariance matrix minimizes the influence of the model initially used by the experiment itself. This is done by using the true event rate distribution as an input together with a set of varied smearing matrices and the correlated background predictions. The calculation of the χ^2 agreement between the data distribution and the predicted event rate distribution showed insufficient agreement for all considered models proving the need for more accurate modeling of neutrino interactions.

Since the publication of such a result requires the recalculation of the uncertainty according to the input distribution, a script is provided along with the information needed to compare any binned distribution to the data measured in this work. This reduces the workload on external people to a minimum and makes the measurement more useful for the community.

A driving factor of the disagreement between the different models and the measured data was the bins with higher momenta. No conclusive answer to this discrepancy

could be found during this work and it will be interesting to see what the cause of it could be.

Although a great portion of the cosmic background could be removed by using the CRT, there is room for multiple improvements. If I could do such an experiment again I would include the CRT from the beginning in the detector design. The limited coverage reduces the performance of the cosmic rejection significantly while the effort on the software side remains the same. Since the CRT was realized later and has a completely independent DAQ, the data integration could not be done immediately. Therefore, important cross-checks were delayed which indeed revealed issues in the installation of the CRT. For this reason, it would be better to ensure the data integration immediately after the installation including the simulation. This would allow a broad set of cross-checks and comparison of the different detector systems and even their expected behavior by simulation without a large delay. Luckily, all of these points seem to be implemented in the SBND experiment, the results of which I am really looking forward to.

By performing more precise measurements in neutrino physics, the issue of model dependence gains in importance. The model has to describe the data in great detail since even small effects can be measured. The development of multidimensional cuts has a potential risk of picking up a model dependence in a very non-trivial way. Although, these cuts often have a great performance and can include a large fraction of the information provided by the detector, the impact of differences between real data and simulation is difficult to judge. Detector systems like the CRT keep the efficiencies flat and reduce potential model dependence of either the simulation of the interactions or the induced detector response.

The representation of a result should have the maximal impact on the community. Both unfolding and forward-folding, have their advantages and disadvantages. I think it would be good if there were a general agreement between experiments and theorists of how a result should be presented. It would also help if this decision could happen within a collaboration so that a common way can be supported and be cross-checked by a variety of people. The translation of an event selection to a physics result including all systematic uncertainties could be shared to minimize the potential risk of errors in the case of individual coding for each analysis.

Acknowledgements

A great thanks go to my supervisor **Michele Weber** and former supervisor **Antonio Ereditato** who gave me the opportunity to do this work at LHEP. It was great to have such a nice balanced work of hardware and analysis.

I am very thankful for my examiners **Hirohisa Tanaka** and **Gilberto Colangelo**.

I am really grateful to **Igor Kreslo** for numerous discussions about the CRT and physics problems in general.

A special thank you goes to **David Lorca**. His support guided me from the beginning to nearly the end of my work.

Many thanks to **James Sinclair** and **Callum Wilkinson**. Their expertise helped me during the analysis as well as in the writing of this thesis.

I very much appreciated the time with my PhD colleagues **Yifan Chen**, **Patrick Koller**, **Roman Berner**, as well as **Patrick Stähli**. The numerous discussions over the lunch breaks were very enjoyable and precious.

A great thank goes to the workshop, especially **Gregor Pfäffli** who told me a lot about mechanical work and the handling of various materials.

The help of the secretariat by **Ursula Witschi** and **Marcella Esposito** and of the IT group by **Jeremy Singh**, **Gianfranco Sciacca** and **Marco Indermühle** was always appreciated.

Many thanks go to my family, especially my parents **Klara** and **Rolf**. I always could count on their support, either morally or financially which enabled me to do this great work in the very beginning.

Last but not least I want to thank **Carina** for her endless support during good as well as stressful times.

Bibliography

[1] F. Reines and C. L. Cowan. 'Free anti-neutrino absorption cross-section. 1: Measurement of the free anti-neutrino absorption cross-section by protons'. In: *Phys. Rev.* 113 (1959), pp. 273–279. DOI: 10.1103/PhysRev.113.273 (cit. on pp. vi, 4).

[2] Q. R. Ahmad et al. 'Measurement of day and night neutrino energy spectra at SNO and constraints on neutrino mixing parameters'. In: *Phys. Rev. Lett.* 89 (2002), p. 011302. DOI: 10.1103/PhysRevLett.89.011302. arXiv: nucl-ex/0204009 [nucl-ex] (cit. on pp. vi, 1, 5).

[3] Y. Fukuda et al. 'Evidence for oscillation of atmospheric neutrinos'. In: *Phys. Rev. Lett.* 81 (1998), pp. 1562–1567. DOI: 10.1103/PhysRevLett.81.1562. arXiv: hep-ex/9807003 [hep-ex] (cit. on pp. vi, 5).

[4] T. Katori and M. Martini. 'Neutrino–nucleus cross sections for oscillation experiments'. In: *J. Phys.* G45.1 (2018), p. 013001. DOI: 10.1088/1361-6471/aa8bf7. arXiv: 1611.07770 [hep-ph] (cit. on pp. vi, 1, 11).

[5] R. Acciarri et al. 'Design and Construction of the MicroBooNE Detector'. In: *JINST* 12.02 (2017), P02017. DOI: 10.1088/1748-0221/12/02/P02017. arXiv: 1612.05824 [physics.ins-det] (cit. on pp. vi, 25, 27–30).

[6] M. Auger et al. 'A Novel Cosmic Ray Tagger System for Liquid Argon TPC Neutrino Detectors'. In: *Instruments* 1.1 (2017), p. 2. DOI: 10.3390/instruments1010002. arXiv: 1612.04614 [physics.ins-det] (cit. on pp. vi, 2, 32, 41, 60, 62, 66, 112).

[7] H. Bethe and R. Peierls. 'The 'neutrino''. In: *Nature* 133 (1934), p. 532. DOI: 10.1038/133532a0 (cit. on pp. 1, 4).

[8] A. D. Sakharov. 'Violation ofCPin variance,Casymmetry, and baryon asymmetry of the universe'. In: *Soviet Physics Uspekhi* 34.5 (May 1991), pp. 392–393. DOI: 10.1070/pu1991v034n05abeh002497. URL: https://doi.org/10.1070/pu1991v034n05abeh002497 (cit. on p. 1).

[9] F. P. An et al. 'Observation of Electron-Antineutrino Disappearance at Daya Bay'. In: *Physical Review Letters* 108.17 (Apr. 2012). ISSN: 1079-7114. DOI: 10.1103/physrevlett.108.171803. URL: http://dx.doi.org/10.1103/PhysRevLett.108.171803 (cit. on pp. 1, 7).

[10] D. Collaboration et al. *The DUNE Far Detector Interim Design Report Volume 1: Physics, Technology and Strategies*. 2018. arXiv: 1807.10334 [physics.ins-det] (cit. on pp. 1, 12).

[11] H.-K. Proto-Collaboration et al. *Hyper-Kamiokande Design Report*. 2018. arXiv: 1805.04163 [physics.ins-det] (cit. on pp. 1, 12).

[12] R. Acciarri et al. 'The Pandora multi-algorithm approach to automated pattern recognition of cosmic-ray muon and neutrino events in the MicroBooNE detector'. In: *Eur. Phys. J.* C78.1 (2018), p. 82. DOI: 10.1140/epjc/s10052-017-5481-6. arXiv: 1708.03135 [hep-ex] (cit. on pp. 2, 72).

[13] A. et. al. 'First Measurement of Inclusive Muon Neutrino Charged Current Differential Cross Sections on Argon at $E_\nu \sim 0.8$ GeV with the MicroBooNE Detector'. In: *Phys. Rev. Lett.* 123 (13 Sept. 2019), p. 131801. DOI: 10.1103/PhysRevLett.123.131801. URL: https://link.aps.org/doi/10.1103/PhysRevLett.123.131801 (cit. on pp. 2, 103, 112, 134, 155).

[14] M. Antonello et al. 'A Proposal for a Three Detector Short-Baseline Neutrino Oscillation Program in the Fermilab Booster Neutrino Beam'. In: (2015). arXiv: 1503.01520 [physics.ins-det] (cit. on pp. 2, 8, 25, 26, 34, 68).

[15] J. Chadwick. 'Intensitätsverteilung im magnetischen Spectrum der β-Strahlen von radium B + C'. In: *Verhandl. Dtsc. Phys. Ges. 16* (1914), p. 383 (cit. on p. 4).

[16] W. Pauli. 'Pauli letter collection: letter to Lise Meitner'. Typed copy. URL: http://cds.cern.ch/record/83282 (cit. on p. 4).

[17] E. Fermi. 'An attempt of a theory of beta radiation. 1.' In: *Z. Phys.* 88 (1934), pp. 161–177. DOI: 10.1007/BF01351864 (cit. on p. 4).

[18] J. Chadwick. 'The Existence of a Neutron'. In: *Proc. Roy. Soc. Lond. A* 136.830 (1932), pp. 692–708. DOI: 10.1098/rspa.1932.0112 (cit. on p. 4).

[19] B. Pontecorvo. 'Inverse beta process'. In: *Camb. Monogr. Part. Phys. Nucl. Phys. Cosmol.* 1 (1991), pp. 25–31 (cit. on p. 4).

[20] M. Goldhaber, L. Grodzins and A. Sunyar. 'Helicity of Neutrinos'. In: *Phys. Rev.* 109 (1958), pp. 1015–1017. DOI: 10.1103/PhysRev.109.1015 (cit. on p. 5).

[21] G. Danby et al. 'Observation of High-Energy Neutrino Reactions and the Existence of Two Kinds of Neutrinos'. In: *Physical Review Letters* 9 (1962), pp. 36–44 (cit. on p. 5).

[22] R. Davis Jr., D. S. Harmer and K. C. Hoffman. 'Search for neutrinos from the sun'. In: *Phys. Rev. Lett.* 20 (1968), pp. 1205–1209. DOI: 10.1103/PhysRevLett.20.1205 (cit. on p. 5).

[23] J. Bahcall. 'The solar neutrino problem'. In: *Comments Nucl. Part. Phys.* 5.2 (1972), pp. 59–64 (cit. on p. 5).

[24] J. N. Bahcall and R. Davis. 'Solar Neutrinos - a Scientific Puzzle'. In: *Science* 191 (1976), pp. 264–267. DOI: 10.1126/science.191.4224.264 (cit. on p. 5).

[25] M. L. Perl et al. 'Properties of the Proposed tau Charged Lepton'. In: *Phys. Lett. B* 70 (1977), pp. 487–490. DOI: 10.1016/0370-2693(77)90421-X (cit. on p. 5).

[26] R. Becker-Szendy et al. 'Neutrino measurements with the IMB detector'. In: *Nucl. Phys. B Proc. Suppl.* 38 (1995), pp. 331–336. DOI: 10.1016/0920-5632(94)00765-N (cit. on p. 5).

[27] D. Decamp et al. 'A Precise Determination of the Number of Families With Light Neutrinos and of the Z Boson Partial Widths'. In: *Phys. Lett. B* 235 (1990), pp. 399–411. DOI: 10.1016/0370-2693(90)91984-J (cit. on p. 5).

[28] K. Kodama et al. 'Observation of tau neutrino interactions'. In: *Physics Letters B* 504.3 (2001), pp. 218–224. ISSN: 0370-2693. DOI: https://doi.org/10.1016/S0370-2693(01)00307-0. URL: http://www.sciencedirect.com/science/article/pii/S0370269301003070 (cit. on p. 5).

[29] M. Lüthi. 'A Novel UV Laser System for Electric Field Calibration in Liquid Argon Time Projection Chambers'. PhD thesis. University of Bern, 2019 (cit. on pp. 7, 22, 23).

[30] K. Abe et al. *Constraint on the Matter-Antimatter Symmetry-Violating Phase in Neutrino Oscillations*. 2019. arXiv: 1910.03887 [hep-ex] (cit. on pp. 7, 12).

[31] D. Adey et al. 'Measurement of the Electron Antineutrino Oscillation with 1958 Days of Operation at Daya Bay'. In: *Physical Review Letters* 121.24 (Dec. 2018). ISSN: 1079-7114. DOI: 10.1103/physrevlett.121.241805. URL: http://dx.doi.org/10.1103/PhysRevLett.121.241805 (cit. on p. 7).

[32] K. A. et. al. 'Combined Analysis of Neutrino and Antineutrino Oscillations at T2K'. In: *Phys. Rev. Lett.* 118 (15 Apr. 2017), p. 151801. DOI: 10.1103/PhysRevLett.118.151801. URL: https://link.aps.org/doi/10.1103/PhysRevLett.118.151801 (cit. on p. 8).

[33] K. Abe et al. 'The T2K Experiment'. In: *Nucl. Instrum. Meth. A* 659 (2011), pp. 106–135. DOI: 10.1016/j.nima.2011.06.067. arXiv: 1106.1238 [physics.ins-det] (cit. on p. 8).

[34] D. S. Ayres et al. 'The NOvA Technical Design Report'. In: (Oct. 2007). DOI: 10.2172/935497 (cit. on p. 8).

[35] R. D. McKeown. 'The daya bay reactor neutrino experiment'. In: *AIP Conf. Proc.* 1182.1 (2009). Ed. by M. L. Marshak, pp. 68–71. DOI: 10.1063/1.3293901 (cit. on p. 8).

[36] C. Palomares. 'Double-Chooz Neutrino Experiment'. In: *PoS* EPS-HEP2009 (2009), p. 275. DOI: 10.22323/1.084.0275. arXiv: 0911.3227 [hep-ex] (cit. on p. 8).

[37] J. K. Ahn et al. 'RENO: An Experiment for Neutrino Oscillation Parameter θ_{13} Using Reactor Neutrinos at Yonggwang'. In: (Mar. 2010). arXiv: 1003.1391 [hep-ex] (cit. on p. 8).

[38] J. Shirai. 'KamLAND-Zen'. In: *PoS* NEUTEL2017 (2018), p. 027. DOI: 10.22323/1.307.0027 (cit. on p. 8).

[39] M. G. Aartsen et al. 'The IceCube Neutrino Observatory: Instrumentation and Online Systems'. In: *JINST* 12.03 (2017), P03012. DOI: 10.1088/1748-0221/12/03/P03012. arXiv: 1612.05093 [astro-ph.IM] (cit. on p. 8).

[40] M. Ageron et al. 'ANTARES: the first undersea neutrino telescope'. In: *Nucl. Instrum. Meth. A* 656 (2011), pp. 11–38. DOI: 10.1016/j.nima.2011.06.103. arXiv: 1104.1607 [astro-ph.IM] (cit. on p. 8).

[41] M. Aker et al. 'The Design, Construction, and Commissioning of the KATRIN Experiment'. In: (Mar. 2021). arXiv: 2103.04755 [physics.ins-det] (cit. on p. 8).

[42] K. H. Ackermann et al. 'The GERDA experiment for the search of $0\nu\beta\beta$ decay in ^{76}Ge'. In: *Eur. Phys. J. C* 73.3 (2013), p. 2330. DOI: 10.1140/epjc/s10052-013-2330-0. arXiv: 1212.4067 [physics.ins-det] (cit. on p. 8).

[43] N. Abgrall et al. 'The Majorana Demonstrator Neutrinoless Double-Beta Decay Experiment'. In: *Adv. High Energy Phys.* 2014 (2014), p. 365432. DOI: 10.1155/2014/365432. arXiv: 1308.1633 [physics.ins-det] (cit. on p. 8).

[44] Y. Gando. 'First results of KamLAND-Zen 800'. In: *J. Phys. Conf. Ser.* 1468.1 (2020). Ed. by M. Nakahata, p. 012142. DOI: 10.1088/1742-6596/1468/1/012142 (cit. on p. 8).

[45] M. Agostini et al. 'Final Results of GERDA on the Search for Neutrinoless Double-β Decay'. In: *Phys. Rev. Lett.* 125.25 (2020), p. 252502. DOI: 10.1103/PhysRevLett.125.252502. arXiv: 2009.06079 [nucl-ex] (cit. on p. 8).

[46] A. A. Aguilar-Arevalo et al. 'Updated MiniBooNE Neutrino Oscillation Results with Increased Data and New Background Studies'. In: (June 2020). arXiv: 2006.16883 [hep-ex] (cit. on p. 9).

[47] A. B. McDonald. 'Nobel Lecture: The Sudbury Neutrino Observatory: Observation of flavor change for solar neutrinos'. In: *Rev. Mod. Phys.* 88.3 (2016), p. 030502. DOI: 10.1103/RevModPhys.88.030502 (cit. on p. 9).

[48] K. Zuber. *Neutrino Physics*. 978-0-7503-0750-5. Denys Wilkinson Laboratory, University of Oxford, 2004 (cit. on p. 9).

[49] C. Patrignani et al. 'Review of Particle Physics'. In: *Chin. Phys.* C40.10 (2016), p. 100001. DOI: 10.1088/1674-1137/40/10/100001 (cit. on p. 9).

[50] L. Zambelli. 'Constraints on T2K neutrino flux predictions with NA61/SHINE experimental data'. In: *49th Rencontres de Moriond on QCD and High Energy Interactions*. 2014, pp. 249–252 (cit. on p. 13).

[51] J. A. Formaggio and G. P. Zeller. 'From eV to EeV: Neutrino Cross Sections Across Energy Scales'. In: *Rev. Mod. Phys.* 84 (2012), pp. 1307–1341. DOI: 10.1103/RevModPhys.84.1307. arXiv: 1305.7513 [hep-ex] (cit. on p. 15).

[52] S. Agostinelli et al. 'GEANT4–a simulation toolkit'. In: *Nucl. Instrum. Meth. A* 506 (2003), pp. 250–303. DOI: 10.1016/S0168-9002(03)01368-8 (cit. on pp. 16, 27).

[53] M. Betancourt et al. 'Comparisons and Challenges of Modern Neutrino Scattering Experiments (TENSIONS2016 Report)'. In: *Phys. Rept.* 773-774 (2018), pp. 1–28. DOI: 10.1016/j.physrep.2018.08.003. arXiv: 1805.07378 [hep-ex] (cit. on p. 17).

[54] C. Andreopoulos et al. 'The GENIE Neutrino Monte Carlo Generator'. In: *Nucl. Instrum. Meth. A* 614 (2010), pp. 87–104. DOI: 10.1016/j.nima.2009.12.009. arXiv: 0905.2517 [hep-ph] (cit. on pp. 17, 71).

[55] T. M. Collaboration. '[Public Note 1074] Neutrino Interaction Model and Uncertainties for MicroBooNE Analyses'. In: *https://microboone.fnal.gov/publicnotes* () (cit. on pp. 17, 71, 113, 114).

[56] C. H. Llewellyn Smith. 'Neutrino Reactions at Accelerator Energies'. In: *Phys. Rept.* 3 (1972), pp. 261–379. DOI: 10.1016/0370-1573(72)90010-5 (cit. on p. 17).

[57] C. Andreopoulos. 'GENIE Physics and User Manual'. In: *Genie-doc-2-v5* (). URL: https://genie-docdb.pp.rl.ac.uk/cgi-bin/ShowDocument?docid=2 (cit. on p. 17).

[58] D. Rein and L. M. Sehgal. 'Neutrino Excitation of Baryon Resonances and Single Pion Production'. In: *Annals Phys.* 133 (1981), pp. 79–153. DOI: 10.1016/0003-4916(81)90242-6 (cit. on p. 17).

[59] A. Bodek and U. K. Yang. 'Modeling neutrino and electron scattering inelastic cross- sections in the few GeV region with effective LO PDFs TV Leading Order'. In: *2nd International Workshop on Neutrino-Nucleus Interactions in the Few GeV Region*. Aug. 2003. arXiv: hep-ex/0308007 (cit. on pp. 17, 18).

[60] J. Nieves, I. Ruiz Simo and M. J. Vicente Vacas. 'Inclusive Charged–Current Neutrino–Nucleus Reactions'. In: *Phys. Rev. C* 83 (2011), p. 045501. DOI: 10.1103/PhysRevC.83.045501. arXiv: 1102.2777 [hep-ph] (cit. on p. 17).

[61] Y. Hayato. 'A neutrino interaction simulation program library NEUT'. In: *Acta Phys. Polon. B* 40 (2009). Ed. by A. Ankowski and J. Sobczyk, pp. 2477–2489 (cit. on p. 17).

[62] N. T. H. Van. 'NEUT as a Neutrino Event Generator'. In: *International Symposium on Neutrino Frontiers* (2018). URL: https://indico.in2p3.fr/event/17344/contributions/61549/attachments/49324/62634/NTHVan_ISoNF.pdf (cit. on p. 17).

[63] K. M. Graczyk and J. T. Sobczyk. 'Form Factors in the Quark Resonance Model'. In: *Phys. Rev. D* 77 (2008). [Erratum: Phys.Rev.D 79, 079903 (2009)], p. 053001. DOI: 10.1103/PhysRevD.79.079903. arXiv: 0707.3561 [hep-ph] (cit. on p. 17).

[64] G. Co'. 'Random phase approximation and neutrino-nucleus cross sections'. In: *Acta Phys. Polon. B* 37 (2006). Ed. by K. M. Graczyk and J. T. Sobczyk, pp. 2235–2242. arXiv: nucl-th/0605051 (cit. on p. 18).

[65] T. Golan, J. Sobczyk and J. Żmuda. 'NuWro: the Wrocław Monte Carlo Generator of Neutrino Interactions'. In: *Nuclear Physics B - Proceedings Supplements* 229-232 (2012). Neutrino 2010, p. 499. ISSN: 0920-5632. DOI: https://doi.org/10.1016/j.nuclphysbps.2012.09.136. URL: http://www.sciencedirect.com/science/article/pii/S0920563212003532 (cit. on p. 18).

[66] H. Jones and M. Scadron. 'Multipole gamma N- delta form factors and resonant photo- and electroproduction'. In: *Annals of Physics* 81.1 (1973), pp. 1–14. ISSN: 0003-4916. DOI: https://doi.org/10.1016/0003-4916(73)90476-4. URL: https://www.sciencedirect.com/science/article/pii/0003491673904764 (cit. on p. 18).

[67] A. Nikolakopoulos et al. 'Modeling neutrino-induced charged pion production on water at T2K kinematics'. In: *Phys. Rev. D* 97.9 (2018), p. 093008. DOI: 10.1103/PhysRevD.97.093008. arXiv: 1803.03163 [nucl-th] (cit. on p. 18).

[68] K. Niewczas and J. T. Sobczyk. 'Nuclear Transparency in Monte Carlo Neutrino Event Generators'. In: *Phys. Rev. C* 100.1 (2019), p. 015505. DOI: 10.1103/PhysRevC.100.015505. arXiv: 1902.05618 [hep-ex] (cit. on p. 18).

[69] N. Metropolis et al. 'Monte Carlo Calculations on Intranuclear Cascades. I. Low-Energy Studies'. In: *Phys. Rev.* 110.1 (1958), p. 185. DOI: 10.1103/PhysRev.110.185 (cit. on p. 18).

[70] T. Golan, C. Juszczak and J. T. Sobczyk. 'Final State Interactions Effects in Neutrino-Nucleus Interactions'. In: *Phys. Rev. C* 86 (2012), p. 015505. DOI: 10.1103/PhysRevC.86.015505. arXiv: 1202.4197 [nucl-th] (cit. on p. 18).

[71] J. T. Sobczyk. 'NuWro at NUSTEC 2019'. In: *NUSTEC Board Meeting* (2019). URL: https://indico.fnal.gov/event/22614/contributions/68619/attachments/43198/52102/nuwro-nustec-2019.pdf (cit. on p. 18).

[72] O. Buss et al. 'Transport-theoretical description of nuclear reactions'. In: *Physics Reports* 512.1 (2012). Transport-theoretical Description of Nuclear Reactions, pp. 1–124. ISSN: 0370-1573. DOI: https://doi.org/10.1016/j.physrep.2011.12.001. URL: http://www.sciencedirect.com/science/article/pii/S0370157311003619 (cit. on p. 18).

[73] C. J. Horowitz, D. P. Murdock and B. D. Serot. 'The Relativistic Impulse Approximation'. In: *Computational Nuclear Physics 1: Nuclear Structure*. Ed. by K. Langanke, J. A. Maruhn and S. E. Koonin. Berlin, Heidelberg: Springer Berlin Heidelberg, 1991, pp. 129–151. ISBN: 978-3-642-76356-4. DOI: 10.1007/978-3-642-76356-4_7. URL: https://doi.org/10.1007/978-3-642-76356-4_7 (cit. on p. 18).

[74] C. Thorn. 'Catalogue of Liquid Argon properties'. In: *DocDB 412-v4* () (cit. on p. 20).

[75] S. Kubota et al. 'Dynamical behavior of free electrons in the recombination process in liquid argon, krypton, and xenon'. In: *Phys. Rev. B* 20.8 (1979), p. 3486. DOI: 10.1103/PhysRevB.20.3486 (cit. on p. 20).

[76] C. Adams et al. 'Deep neural network for pixel-level electromagnetic particle identification in the MicroBooNE liquid argon time projection chamber'. In: *Physical Review D* 99 (May 2019). DOI: 10.1103/PhysRevD.99.092001 (cit. on p. 21).

[77] A. Rubbia. 'Future liquid Argon detectors'. In: *Nuclear Physics B - Proceedings Supplements* 235-236 (Feb. 2013), pp. 190–197. ISSN: 0920-5632. DOI: 10.1016/j.nuclphysbps.2013.04.010. URL: http://dx.doi.org/10.1016/j.nuclphysbps.2013.04.010 (cit. on p. 22).

[78] V. L. Highland. 'Some Practical Remarks on Multiple Scattering'. In: *Nucl. Instrum. Meth.* 129 (1975), p. 497. DOI: 10.1016/0029-554X(75)90743-0 (cit. on p. 22).

[79] G. R. Lynch and O. I. Dahl. 'Approximations to multiple Coulomb scattering'. In: *Nucl. Instrum. Meth. B* 58 (1991), pp. 6–10. DOI: 10.1016/0168-583X(91)95671-Y (cit. on p. 22).

[80] R. Acciarri et al. 'First Observation of Low Energy Electron Neutrinos in a Liquid Argon Time Projection Chamber'. In: *Phys. Rev. D* 95.7 (2017), p. 072005. DOI: 10.1103/PhysRevD.95.072005. arXiv: 1610.04102 [hep-ex] (cit. on p. 23).

[81] P. A. Machado, O. Palamara and D. W. Schmitz. 'The Short-Baseline Neutrino Program at Fermilab'. In: *Ann. Rev. Nucl. Part. Sci.* 69 (2019), pp. 363–387. DOI: 10.1146/annurev-nucl-101917-020949. arXiv: 1903.04608 [hep-ex] (cit. on p. 25).

[82] T. M. Collaboration. '[Public Note 1031] Booster Neutrino Flux Prediction at MicroBooNE'. In: *https://microboone.fnal.gov/public-notes* () (cit. on p. 27).

[83] S. J. Brice. 'MiniBooNE'. In: *Nucl. Phys. B Proc. Suppl.* 143 (2005). Ed. by J. Dumarchez, F. Vannucci and T. Patzak, pp. 115–120. DOI: 10.1016/j.nuclphysbps.2005.01.095 (cit. on p. 27).

[84] M. D. Tutto and N. Foppiani. 'How to Normalise Data and MC'. In: *DocDB 15204-v2* () (cit. on p. 27).

[85] J. Li and A. S. Miquel Nebot-Guinot. 'The Light-Yield Measurement Analysis'. In: *DocDB 33742-v1* () (cit. on p. 30).

[86] A. Surdo. 'Measurement of the Cosmic Ray spectra by the ARGO-YBJ experiment'. In: *Nucl. Part. Phys. Proc.* 265-266 (2015). Ed. by P. Bernardini, G. Fogli and E. Lisi, pp. 255–257. DOI: 10.1016/j.nuclphysbps.2015.06.066 (cit. on pp. 32, 36).

[87] P. A. Zyla et al. 'Review of Particle Physics'. In: *PTEP* 2020.8 (2020), p. 083C01. DOI: 10.1093/ptep/ptaa104 (cit. on p. 32).

[88] M. collaboration et al. *Neutrino Event Selection in the MicroBooNE Liquid Argon Time Projection Chamber using Wire-Cell 3-D Imaging, Clustering, and Charge-Light Matching*. 2020. arXiv: 2011.01375 [physics.ins-det] (cit. on p. 33).

[89] C. Adams et al. 'A method to determine the electric field of liquid argon time projection chambers using a UV laser system and its application in MicroBooNE'. In: *JINST* 15.07 (2020), P07010. DOI: 10.1088/1748-0221/15/07/P07010. arXiv: 1910.01430 [physics.ins-det] (cit. on p. 35).

[90] A. Ereditato et al. 'A steerable UV laser system for the calibration of liquid argon time projection chambers'. In: *JINST* 9.11 (2014), T11007. DOI: 10.1088/1748-0221/9/11/T11007. arXiv: 1406.6400 [physics.ins-det] (cit. on p. 35).

[91] M. Auger et al. 'Multi-channel front-end board for SiPM readout'. In: *Journal of Instrumentation* 11.10 (Oct. 2016), P10005–P10005. DOI: 10.1088/1748-0221/11/10/p10005. URL: https://doi.org/10.1088%2F1748-0221%2F11%2F10%2Fp10005 (cit. on pp. 39, 40).

[92] I. Kreslo. 'CRT Measurements in SBND pit'. In: *SBND-doc-3923-v1* () (cit. on p. 66).

[93] T. M. Collaboration. 'Supporting Note: MCC9 Overlay GENIE simulated BNB and Cosmic data'. In: *MicroBooNE-doc-27003-v2* () (cit. on pp. 71, 75).

[94] C. Adams et al. 'Ionization electron signal processing in single phase LArTPCs. Part I. Algorithm Description and quantitative evaluation with MicroBooNE simulation'. In: *JINST* 13.07 (2018), P07006. DOI: 10.1088/1748-0221/13/07/P07006. arXiv: 1802.08709 [physics.ins-det] (cit. on pp. 72, 74).

[95] C. Adams et al. 'Ionization electron signal processing in single phase LArTPCs. Part II. Data/simulation comparison and performance in MicroBooNE'. In: *JINST* 13.07 (2018), P07007. DOI: 10.1088/1748-0221/13/07/P07007. arXiv: 1804.02583 [physics.ins-det] (cit. on pp. 72, 74).

[96] L. E. Sanchez. 'Updates on SVM-based track/shower identification in Pandora'. In: *DocDB 14039-v1* () (cit. on p. 72).

[97] W. V. D. Pontseele. 'Pandora Neutrino ID and numu CC inclusive in MCC9.1'. In: *DocDB 24535-v1* () (cit. on pp. 73, 147, 149).

[98] T. M. Collaboration. '[Public Note 1056] Selection of muon neutrino charged–current induced interactions with N>0 protons and performance of events with N=2 protons in the final state in the MicroBooNE detector from the BNB'. In: *https://microboone.fnal.gov/public-notes* () (cit. on p. 73).

[99] P. Abratenko et al. 'Determination of muon momentum in the MicroBooNE LArTPC using an improved model of multiple Coulomb scattering'. In: *JINST* 12.10 (2017), P10010. DOI: 10.1088/1748-0221/12/10/P10010. arXiv: 1703.06187 [physics.ins-det] (cit. on p. 73).

[100] B. List. 'Why and When to Optimize Efficiency times Purity'. In: *ETH Zurich, Institute for Particle Physics* (2002) (cit. on p. 77).

[101] MicroBooNE. 'Measurement of electron neutrino interactions at low energy with the MicroBooNE Experiment'. In: *DocDB 27738-v10* () (cit. on pp. 96, 147).

[102] G. D'Agostini. 'A Multidimensional unfolding method based on Bayes' theorem'. In: *Nucl. Instrum. Meth. A* 362 (1995), pp. 487–498. DOI: 10.1016/0168-9002(95)00274-X (cit. on p. 101).

[103] K. Abe et al. 'Measurement of the inclusive muon neutrino charged current cross section on carbon in the near detector of the T2K experiment'. In: *Phys. Rev. D* 87.9 (2013), p. 092003. DOI: 10.1103/PhysRevD.87.092003. arXiv: 1302.4908 [hep-ex] (cit. on p. 101).

[104] L. Koch. 'A response-matrix-centred approach to presenting cross-section measurements'. In: *Journal of Instrumentation* 14.09 (Sept. 2019), P09013–P09013. ISSN: 1748-0221. DOI: 10.1088/1748-0221/14/09/p09013. URL: http://dx.doi.org/10.1088/1748-0221/14/09/P09013 (cit. on pp. 101, 128).

[105] T. M. Collaboration. 'Novel Approach for Evaluating Detector Systematics in the MicroBooNE LArTPC'. In: *https://microboone.fnal.gov/public-notes* () (cit. on p. 110).

[106] T. M. Collaboration. '[Public Note 1069] Single differential muon neutrino charged-current cross section with the MicroBooNE detector using the Cosmic Ray Tagger'. In: *https://microboone.fnal.gov/public-notes* () (cit. on pp. 117, 133, 155).

[107] T. M. Collaboration. '[Public Note 1045] First Muon-Neutrino Charged-Current Inclusive Differential Cross Section Measurement for MicroBooNE Run 1 Data'. In: *https://microboone.fnal.gov/public-notes* () (cit. on p. 122).

[108] P. Stowell et al. 'NUISANCE: a neutrino cross-section generator tuning and comparison framework'. In: *Journal of Instrumentation* 12.01 (Jan. 2017), P01016–P01016. DOI: 10.1088/1748-0221/12/01/p01016. URL: https://doi.org/10.1088/1748-0221/12/01/p01016 (cit. on p. 128).

[109] C. Adams et al. 'Design and construction of the MicroBooNE Cosmic Ray Tagger system'. In: *Journal of Instrumentation* 14.04 (Apr. 2019), P04004–P04004. DOI: 10.1088/1748-0221/14/04/p04004. URL: https://doi.org/10.1088/1748-0221/14/04/p04004 (cit. on p. 133).

A. Cross Section: Additional Information

A.1. How to Use this Analysis

A majority of the data is presented here as histograms. Also, some comparisons to specific models are made within this work. But to get the most out of this measurement the data has to be presented to analyzers easily. Therefore is the data also available in a git repository as ROOT histograms together with a library for the treatment of the uncertainties.

`https://github.com/thomasmettler/numuCC_uBooNE_result`

There are various functions available that take the information out of the ROOT histograms needed for further analysis. A list of the functions can be seen in the README file in the repository.

An example script is also provided which does the analysis with the event rate distribution predicted by the MicroBooNE tuned GENIE Version. It also calculates the χ^2 between the data and the model prediction including all uncertainties described in this work.

A.2. Pandora Neutrino ID

The goal of the Pandora Neutrino ID [101], also called SliceID process is to efficiently select neutrino signals out of the signals from the LArTPC coming mainly from cosmic muon tracks. The SliceID tries to select all kinds of neutrinos and is usually used for a Pandora based analysis of the MicroBooNE data.

The following requirements have to be fulfilled by a grouped charge signals (also called a slice) reconstructed by the Pandora framework [97]:

- There is an optical flash in the beam window
- The YZ position of the slice is compatible with the flash
- The flash intensity corresponds to the charge signal of the slice taking the X position into account
- The slice does not contain a track with starts or stops at the anode or cathode if shifted in the drift direction to the time of a nearby optical signal

- The slice does not contain a stopping muon track which is checked by the MCS behavior of this track and the check for a Bragg peak and Michel electron under the cosmic hypothesis.
- The topological score (see Appendix A.3) has to be larger than 0.06 and if the flash-charge matching is bad (χ^2>10) the topological score has to be even larger than 0.25
- Reject the whole event if the flash signal matches an obvious cosmic track by calculating the χ^2 of the flash-charge matching. The χ^2 of the slice has to be 5 times larger than the obvious cosmic one.

In Figure A.1 one can see an example how the SliceID process works. At least one optical signal needs to be registered during the beam window (yellow) while any number of light can be registered outside of the beam (orange). After grouping the charge signals belonging together in slices (green ellipses), the obvious cosmic ones are removed. In this figure, this would be slice 1 and 2 since they have charge signals outside the active area during the beam spill. The other slices are reconstructed under the cosmic hypothesis and the neutrino hypothesis. In this example slice 3 could be identified as a stopping muon with a decay to a Michel electron although no light information is available for this cluster. Slice number 4 could be matched to the flash outside the beam window where its track would go through the cathode when the shift in the drift direction would be corrected. The last slice 5 can be matched to the light flash inside the beam window with enough confidence and is therefore selected as the neutrino candidate slice of this event for further analysis. Zero or one candidate slice is reconstructed per readout since the probability that more than one neutrino interacts in one spill is very small.

This SliceID process builds the start point of many analyses using the Pandora reconstruction.

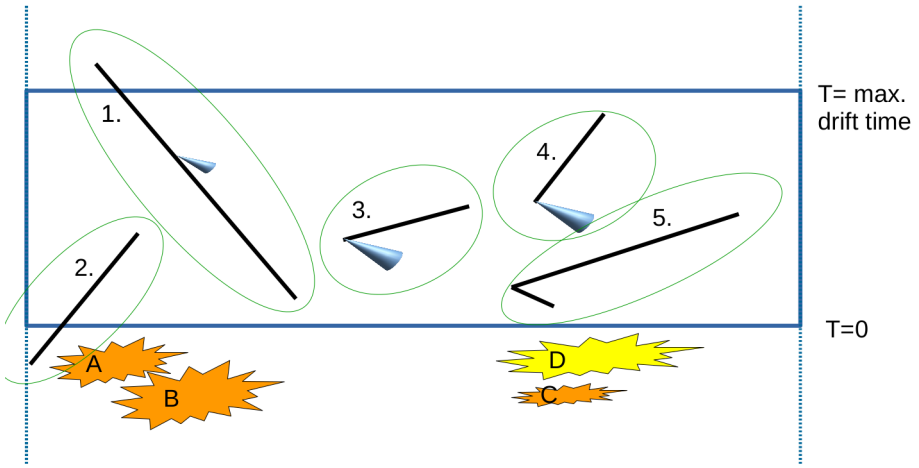

Figure A.1.: The selection of a neutrino candidate slice in the SliceID process. First, the charge clusters are grouped in slices (green ellipses) and the obvious cosmic signals are removed. The rest of the slices are reconstructed under the cosmic assumption and the neutrino assumption. The slice which fulfills all requirements best listed in this section will act as the neutrino candidate. The flashes represent the optical signal registered outside (orange) of the beam window or inside (yellow).

A.3. Topological Score

The cosmic originating tracks have a different topological distribution than the signal induced originating from beam neutrino interaction. This knowledge can be used to reject cosmic tracks efficiently. To find good rejection without losing a large amount of neutrino signal interactions a SVM was trained with topological properties reconstructed the Pandora framework [97]. Pandora has two reconstruction chains for the charge signals of the LArTPC. One is the neutrino hypothesis where Pandora tries to reconstruct a neutrino vertex with all its daughter particles. The other is the cosmic hypothesis where only cosmic muon tracks are reconstructed with eventual delta rays and Michel electrons.

The following variables are used to train the SVM coming from the Pandora reconstruction under the neutrino hypothesis [97]:

- Number of direct neutrino daughters
- Number of wire hits in the grouped charge signal
- The Y position of the reconstructed neutrino vertex
- The Z component of the wire hit weighted by the direction of the neutrino daughters

- Number of space-points within 10 cm of the neutrino vertex
- Ratio of the first two eigenvalues of a Principle Component Analysis (PCA) fit of the position of the space-points within 10 cm of the neutrino vertex

The following variables are used coming from the cosmic hypothesis:

- The Y position of the longest track
- Difference between the direction of the start and end of the longest track in the cosine angle
- Number of hits in the longest track
- Fraction of all hits which belong to the longest track from the grouped hits.

As shown in Figure 5.11, the calculated score is between 0 (cosmic like) and 1 (neutrino like). A value of at least 0.06 of this score is needed that a slice is considered as a possible neutrino slice of the SliceID process.

A.4. Forward-folded Cross Section Representation

In this section, the different representations of a cross-section result will be discussed with the main focus on the data to prediction comparison of different models as a cross-section normalized event rate or as an event rate directly.

The total cross-section of a process is given by the following expression:

$$\sigma = \frac{N^{data} - N^{bkgd}}{\epsilon \cdot \phi \cdot N_T} \tag{A.1}$$

Where σ is the total cross-section, N^{data} is the number of measured events passing the selection, and N^{bkgd} is the number of expected background events passing the selection derived from the simulation of the whole experiment. The efficiency ϵ can also be derived from the simulation for the total cross-section since no smeared variable has to be used in its calculation. Finally, ϕ is the total flux of neutrinos which can be measured by the experiment and N_T is the total number of target nucleons.

For the single differential cross-section in the forward folded case the equation looks similar:

$$\left(\frac{d\sigma}{dX_\mu}\right)_i = \frac{N_i^{data} - N_i^{bkgd}}{\phi \cdot N_T \cdot \left(\Delta X_\mu\right)_i} \tag{A.2}$$

Here i is the bin number and $\left(\Delta X_\mu\right)_i$ is the bin width of the bin i. X is now the reconstructed variable over which the differential cross-section is calculated. Since we have now to deal with a reconstructed variable, the efficiency is not clearly defined. There are different methods of how a reconstructed efficiency can be approximated

but here we simply do not correct for the efficiency on the reconstructed variables. Such a correction always introduces model dependence and does not bring new information into the measurement. Therefore it is better to avoid a summed up efficiency correction and smear the true distribution including the efficiency by multiplying the distribution by the smearing matrix given in Equation 6.1. By doing that model dependence can be minimized but the theorist loses the intuition about the values since each bin is scaled down by the experimental efficiency and the values are now detector smeared. An example of such a representation is given in Figure A.2(a) with arbitrary uncertainties and values.

Also, the experimentalist intuition can be disturbed since now values from a model are mixed with data. By the total scaling and the bin-dependent scaling, one starts to hide what actually determines the measurement which is the measured event rate. Statistical errors and also other errors are scaled and it is hard to see if the numbers make sense by looking directly at the cross-section histograms which increase the risk of errors without bringing new information. Also one has to add model-dependent errors on the data points. So not only the model prediction has errors assigned but also the data points. These errors are also correlated and a clear separation of what is modeled and what is measured is not possible anymore.

A way to avoid these problems without losing information is to look directly at the event rate. Since the result is any way in reconstructed variables each experiment distribution looks differently. By directly looking at event rates one can get an idea of which bins are more trustful than others and one gets some intuition of the expected size of the error bars especially for the statistical uncertainty. Also one can directly see the amount of expected background for each bin. Unphysical bins with negative values can be avoided which would be possible for a background-subtracted representation. An example of an event rate representation is given in A.2(b) with arbitrary values and uncertainties.

To compare a forward-folded measurement with a given theory/model one has to calculate anyway the expected event rate using the flux prediction of the experiment and smear this distribution according to the detector smearing. So instead of normalizing both (data and theory) to a cross-section-like distribution one can also directly compare the event rates without losing any information. But the clear separation of data and simulation allows the assignment of the uncertainty to the proper distribution, speaking of the simulated parts since uncertainty is designed to cover the difference of the model to the 'real world'. For this reason, measured data points should not have any uncertainty on them. This can not be done when the normalized representation is used since there the (measured) data points are subtracted by the (simulated) background. In Section A.5 the cross-section for this analysis is also given in the normalized version for completeness, although no uncertainties are given there.

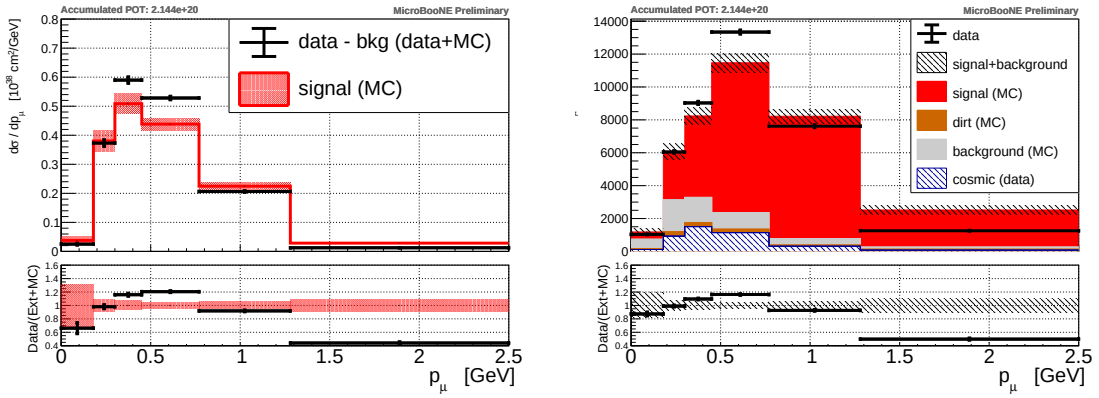

(a) cross-section normalized

(b) event rate

Figure A.2.: Two different representations of a single differential cross-section: cross-section normalized (left) and as an event rate (right). While the cross-section normalized representation looks-like a cross-section, the event rate contains the same information but with clear separation between data and simulation. The values and uncertainties are arbitrary but the same for both figures.

A.5. Cross Section Result Forward-folded

The forward-folded cross-section result is represented as a forward-folded cross-section. Only the statistical uncertainty of the data is drawn. For the background and the signal prediction, the tuned GENIE model V3 was used. Also shown is the contribution from each interaction channel.

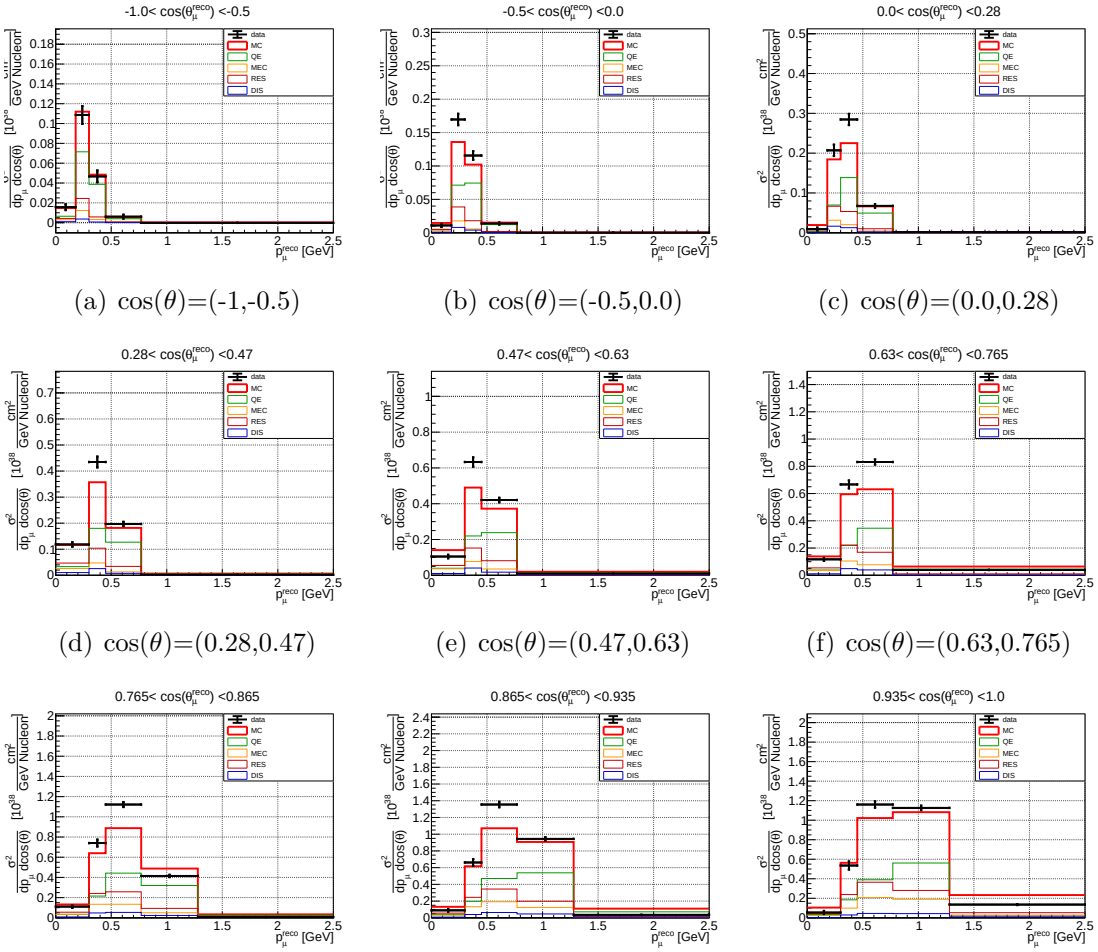

(a) cos(θ)=(-1,-0.5) (b) cos(θ)=(-0.5,0.0) (c) cos(θ)=(0.0,0.28)

(d) cos(θ)=(0.28,0.47) (e) cos(θ)=(0.47,0.63) (f) cos(θ)=(0.63,0.765)

(g) cos(θ)=(0.765,0.895) (h) cos(θ)=(0.895,0.935) (i) cos(θ)=(0.935,1)

Figure A.3.: Double differential forward-folded cross-section with the contribution from each interaction channel predicted by the tuned GENIE model.

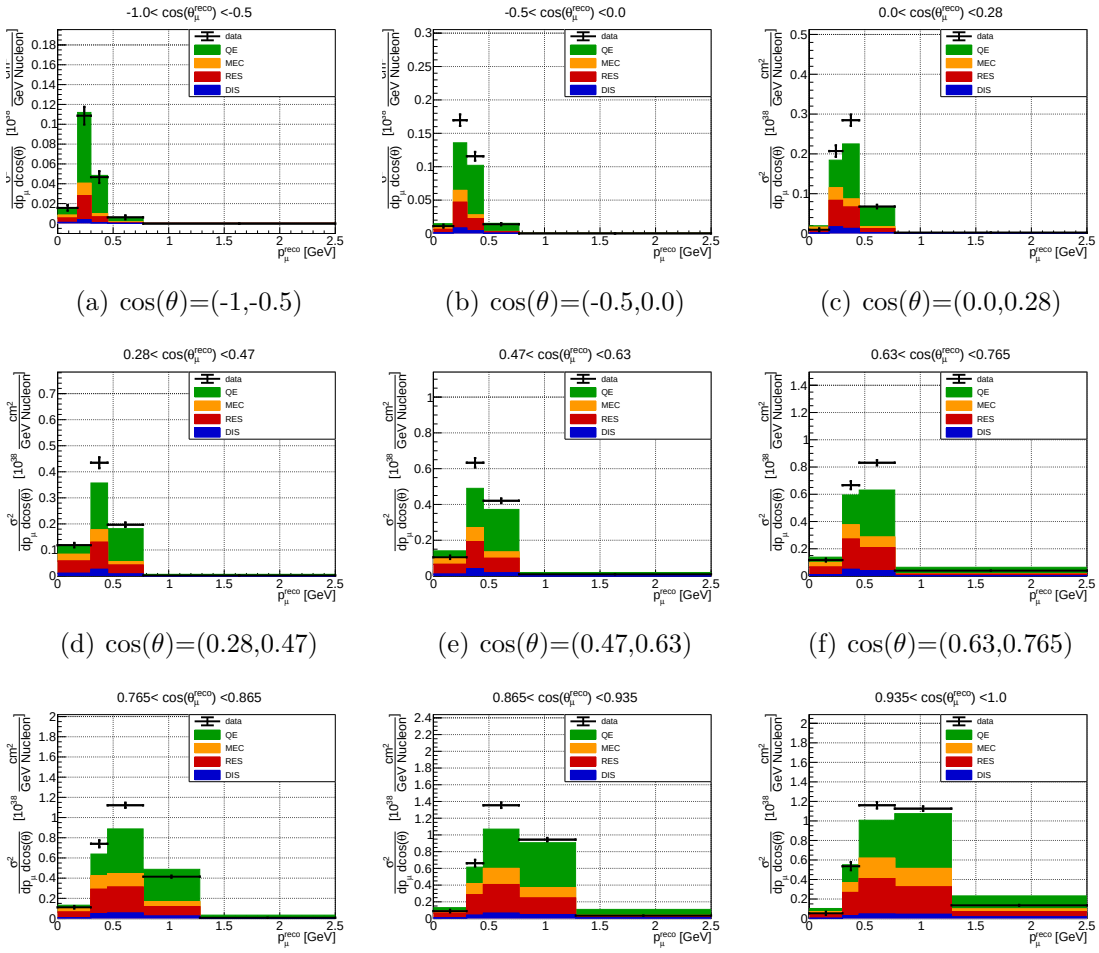

(a) cos(θ)=(-1,-0.5) (b) cos(θ)=(-0.5,0.0) (c) cos(θ)=(0.0,0.28)

(d) cos(θ)=(0.28,0.47) (e) cos(θ)=(0.47,0.63) (f) cos(θ)=(0.63,0.765)

(g) cos(θ)=(0.765,0.895) (h) cos(θ)=(0.895,0.935) (i) cos(θ)=(0.935,1)

Figure A.4.: Double differential forward-folded cross-section with the stacked contribution from each interaction channel predicted by the tuned GENIE model.

A.6. Binning Study

The double differential binning is chosen by combining the two single differential binning and merging bins where the statistic is too low. The binning chosen for the single differential distributions is oriented on a previous analysis done in MicroBooNE [13] and the result for an analysis I have done is in [106]. The reason for this adoption is the following:

- Same reconstructed variables are used ($\cos(\theta)$ and momentum of the muon track)
- The muon momentum is calculated in the same way (MCS) for the exiting tracks
- Same binning allows for direct comparison (the result are in [106])
- Binning is close to optimal for most bins

For the two single differential cross-section the following binning are used:

$$bins\ in\ p_{\mu} = [0.00, 0.18, 0.30, 0.45, 0.77, 1.28, 2.50] \tag{A.3}$$

$$bins\ in\ cos(\theta_{\mu}) = [-1.00, -0.50, 0.00, 0.28, 0.47, 0.63, 0.765, 0.865, 0.935, 1.00] \tag{A.4}$$

The binning should be chosen not to be much finer than the detector resolution since then the neighboring bins only become more correlated and no new information is added to the distribution. One way of doing it is to check that the detector smearing keeps around 67% in the correct bin. These histograms are shown in Figure A.5 for the single differential distributions and A.6 for the double differential case. As one can see in Figure A.6 the detector smearing is in this order for most of the bins. Therefore, although the statistics would allow a finer binning, there is no big advantage due to the detector resolution. The chosen 2D binning is shown in 6.0.2.

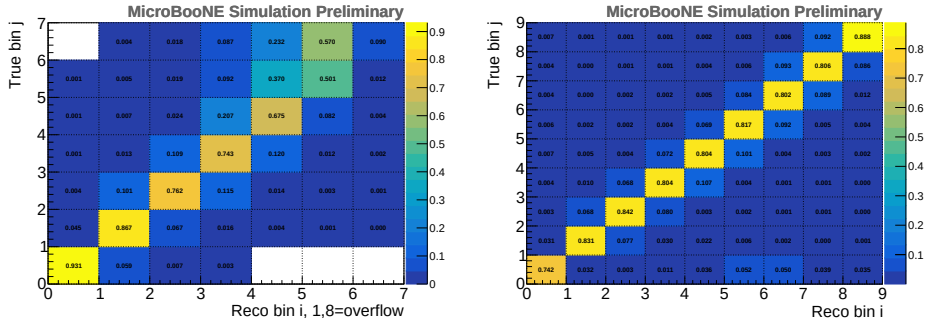

(a) momentum (b) $\cos(\theta)$

Figure A.5.: The detector smearing without including the efficiency for the single differential distribution over muon momentum and $\cos(\theta)$. For these distribution the detector resolution would in principle allow a finer binning.

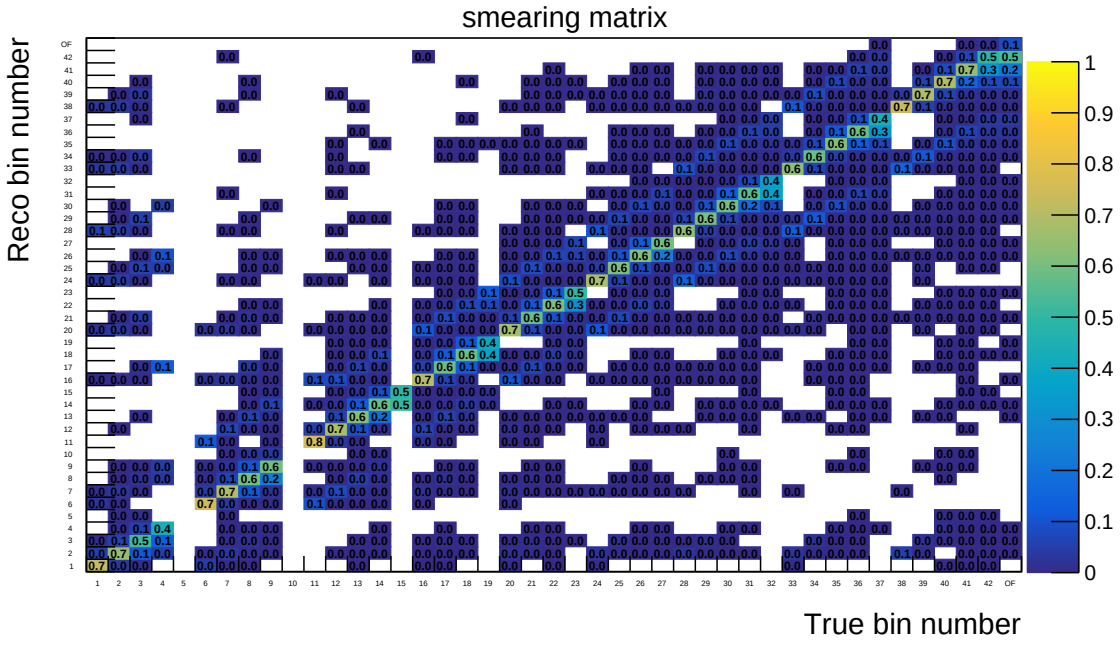

Figure A.6.: Detector smearing matrix without including the efficiency for the 2D binning in momentum and $\cos(\Theta)$. The probability that a reconstructed event has also its true value in the same bin is for most bins between 60% and 70%. Finer binning which would be statistically allowed would not bring a big advantage since the detector resolution is limited.

A.7. Model Comparison with Fractional Uncertainties

Since the uncertainty is calculated using a true distribution of the event rate of a distinctive model, the sizes of the uncertainty depend on the input distribution. Since the background is considered as constant as well as the purely cosmic background, the uncertainty depends on the input distribution in a non-trivial way. For this reason, the uncertainty is recalculated for each true event rate distribution of a model and returned as a fractional covariance matrix. Naively one could assume that the difference in the size of the uncertainty for each model is only a minor aspect either for the total size of the uncertainty or the fractional.

Here are the result presented which show that indeed the order in which model fits the data best does not change if the fractional uncertainty of one model is applied to another model. But what change is the order of models that fits the data best if one compares the χ^2 value between the models when the uncertainty is calculated using the right model. Or in other words, it does matter that for the GENIE V3 χ^2 calculation also the uncertainty for this model is used.

Table 4 gives an overview of the χ^2 values for different models where the uncertainty is calculated also with different models:

Model	GENIE tune	GENIE V3	GENIE V2	GiBUU	NEUT	NuWro
GENIE tune	593	696	619	852	417	500
GENIE V3	549	653	574	803	467	581
GENIE V2	616	723	633	878	513	639
GiBUU	531	631	566	781	457	566
NEUT	600	709	626	862	508	634
NuWro	555	659	585	808	474	589

Table A.1.: Summary of the χ^2 values of the data to MC comparison using different models and using different models for the calculation of the uncertainty.

If one checks the χ^2 values for each model where the uncertainty is calculated with always the same model for each one, the conclusion of which model fits best does not change. The correct way would be to check the χ^2 for each model where the uncertainty is also evaluated with the same model. In Table A.1 one has to look at the diagonal values. By doing this one remark that the order of models which fits best is: NEUT, NuWro,GENIE tune, GENIE V2, GENIE V3, and GiBUU. This is not the order one would get if the fractional covariance is evaluated using a different model. In these cases, the tuned GENIE model fits better than NuWro for example.

Since the χ^2 values are all high and close to each other, this is not that a big change in the conclusion. But since it makes a difference one should always compare the model to data agreement with the uncertainty calculated by using the same model.

A.8. Event Rate Distributions for Different Models

Here are the event rate distributions given for the different models. The uncertainty is always calculated with the given model. The given χ^2-values and the discussion of the outcome of this comparison are all given in the main section at 6.4. Here, simply the event rate distributions are given for the different models if the reader wants the differences for the different predictions in a nice way. The uncertainty is always calculated with the given model.

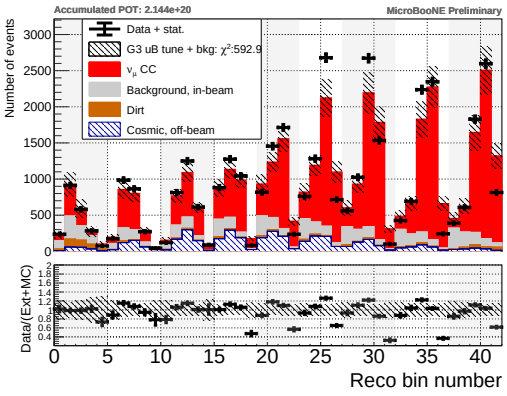

(a) GENIE uB tune

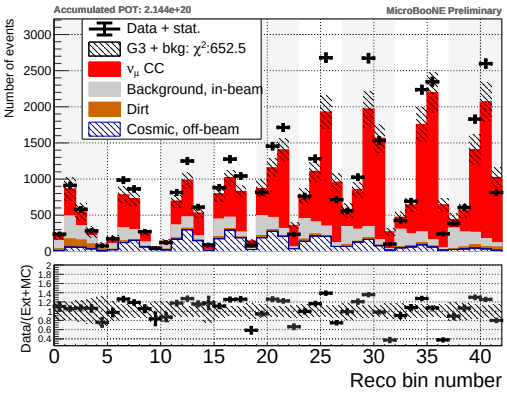

(b) GENIE V3

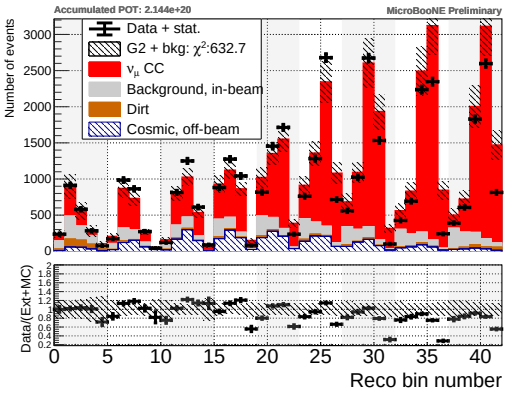

(c) GENIE V2

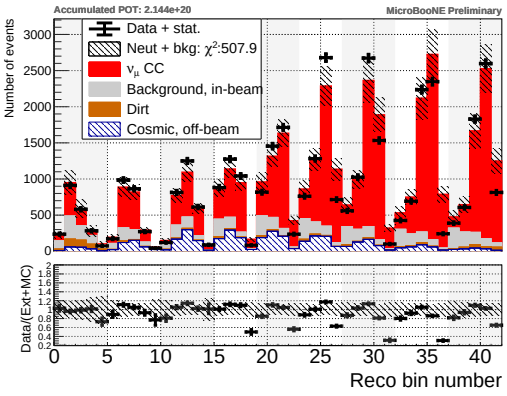

(d) NEUT

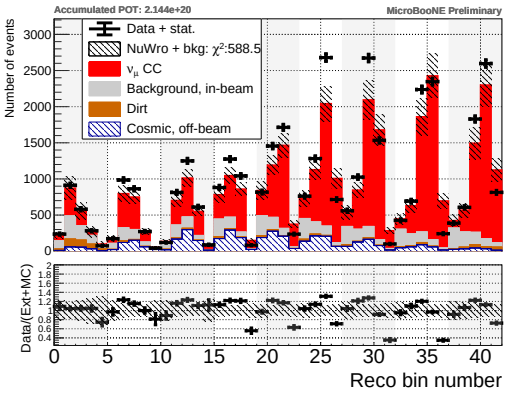

(e) NuWro

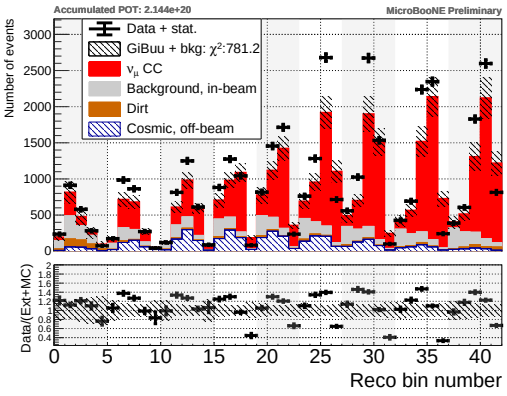

(f) GiBUU

Figure A.7.: Double differential event rate using different forward folded model predictions.

A.9. Fake Data Studies

In this chapter, several fake data studies are shown. Since here we compare the measured event rate to a model prediction, one would like to see whatever the model prediction goes in also is represented in the froward-folded event rate prediction. For this, the reweighed reconstructed double-differential event rate is taken as the fake data and compared by the forward-folded correspondingly reweighed true distribution. Small differences are expected since the detector smearing matrix eventually brings in a small model dependence as well as the background which remains always the same. The expected background is calculated using the tuned GENIE model, for this reason, a reweighing of the signal and the background leads to deviation of the forward folded prediction. Nevertheless one wants to check that the χ^2 value between the fake data distribution and the predicted event rate is in agreement with the uncertainties. This will be indicated by a χ^2 value per degree of freedom below 1. With the 42 bins and therefore 42 degrees of freedom the χ^2 value should be well below 42 even with drastic changes of the input model.

A.9.1. Fake Data: no MicroBooNE tune

In Figure A.8, the untuned GENIE model V3 is used instead of the tuned one. As one can see, all the points are within the uncertainty band. The χ^2 value does not allow a distinction between the two distributions. By comparing the distribution of the tuned and untuned model (see Figure A.8 and Figure A.7) one can see that especially in the forward region the event rate prediction is quite different for this model.

A.9.2. Fake Data: no MEC

In Figure A.9, the tune GENIE model V3 is used but the total MEC contribution is put to zero. As one can see, all the points are within the uncertainty band. The χ^2 value does not allow a distinction between the two distributions. The MEC contribution accounts for 10% to 20% for most bins as shown in Figure A.2. Even with this contribution completely turned of, the χ^2 value does not allow a distinction between the two distributions.

A.9.3. Fake Data: double MEC

In Figure A.10, the tuned GENIE model V3 is used and all MEC interactions are double counted. All the points are within the uncertainty band. So also a modeling within the total contribution of MEC interactions of the tuned GENIE V3 by $\pm$ 100% would result in the same conclusion.

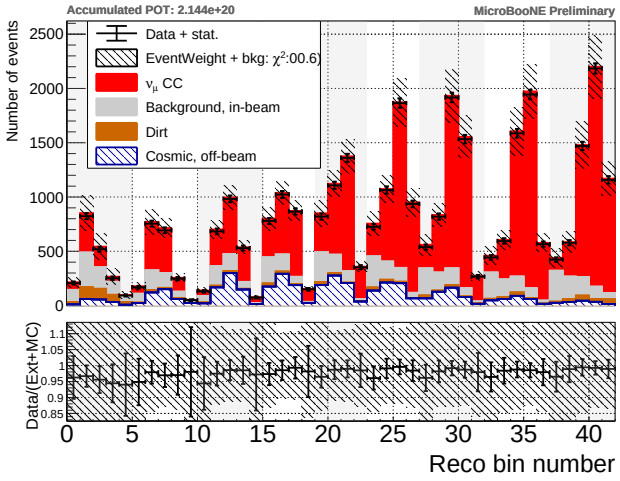

Figure A.8.: The untuned GENIE V3 model is used here. The reweighted signal and background prediction build the event rate of the fake data set while the prediction uses the CV background prediction and the forward-folded true distribution of the untuned model.

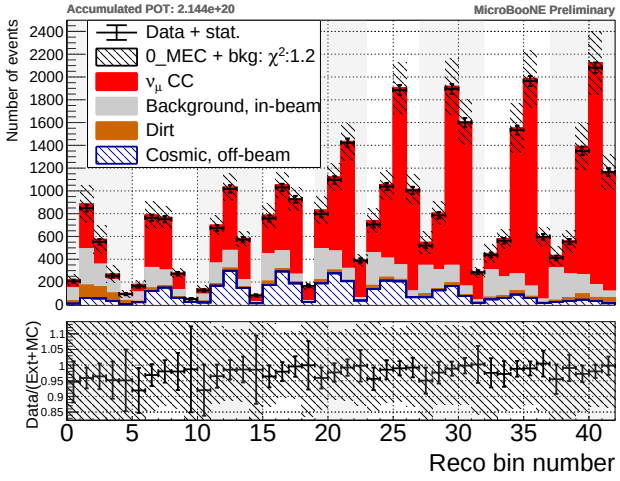

Figure A.9.: The tuned GENIE V3 model is used here but all MEC interactions are ignored.

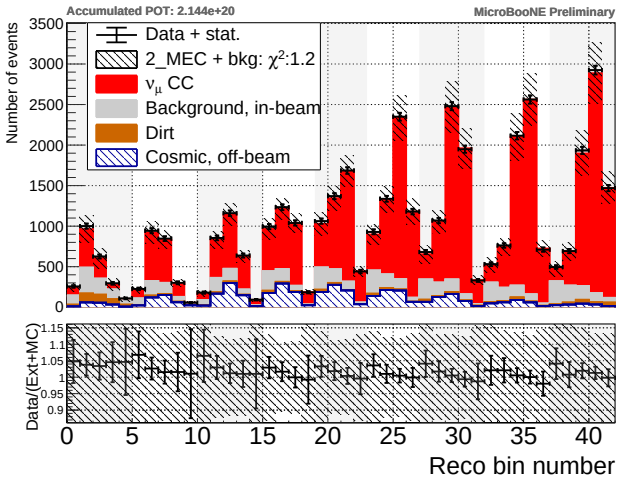

Figure A.10.: Here, the contribution of the MEC interaction is doubled.

A.9.4. Fake Data: Ratio Change 1

In Figure A.11, the tuned GENIE model V3 is used instead but a reweighing of the different interaction channels is done. The QE contribution is scaled up by 20%, the RES as well. The MEC interactions are completely neglected and the DIS interactions are doubled. All points are within the uncertainty band but some points show a difference of up to around 15%. Nevertheless, even with these large changes the chi^2 is well below indicating a disagreement between the models.

A.9.5. Fake Data: Ratio Change 2

In Figure A.12, again the contributions of the different interaction channels are changed. Now, the QE contribution is scaled down to 80% while the RES and MEC contributions are scaled up by 20%. The DIS events are again doubled. The difference between the forward-folded and true distribution are looking similar as in Figure A.11 indicating that the change comes probably from the RES interactions. Nevertheless, also for these changes, the χ^2 does not allow a distinction of the two distributions, and all the points are within the uncertainty band.

So after these few fake data tests, one could see that there are some changes as expected but they are well covered by the uncertainties. So even a model which predicts the distributions quite differently than the tuned GENIE V3 does which is used for the calculation of the background contribution as well as for the calculation of the smearing matrix, the distribution would agree with the data in the case where the model describes the data correctly.

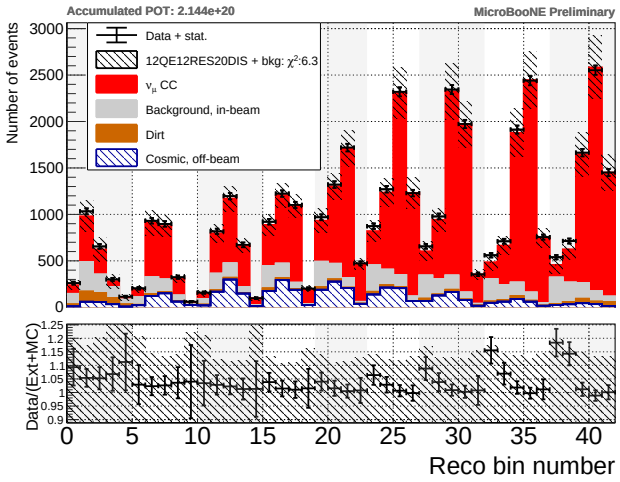

Figure A.11.: The contributions of the different interaction channels is changed by quite a bit: QE and RES are scaled by 1.2 while MEC is turned off and DIS are doubled. The forward-folded prediction agrees still with the true distribution.

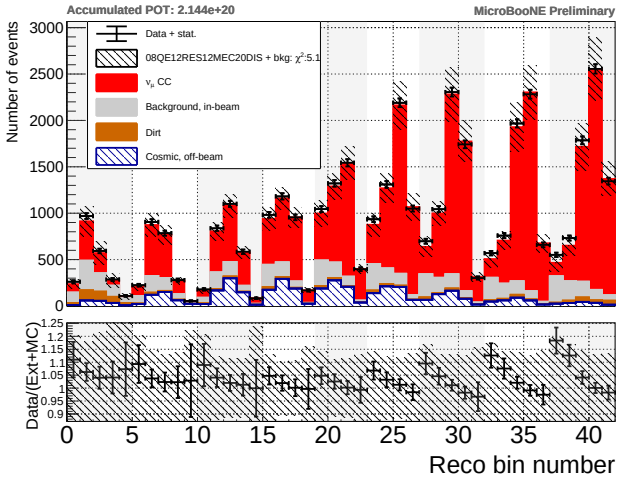

Figure A.12.: The contributions of the different interaction channels is changed again but now according to: MEC and RES are scaled by 1.2 while QE is scaled down by 0.8, DIS is again doubled. The forward-folded prediction agrees still with the true distribution.

B. Uncertainties: Covariance, Correlation and fractional Uncertainty

This chapter contains additional information about the uncertainties. For each source of uncertainty, the covariance matrix is given as well as the correlation matrix. These matrices are evaluated using the tuned GENIE model. The difference between the different models is shown in the fractional uncertainty for each bin. The difference comes from the static background prediction and its associated uncertainty as well as the uncertainties in the smearing matrices together with the different event rate predictions.

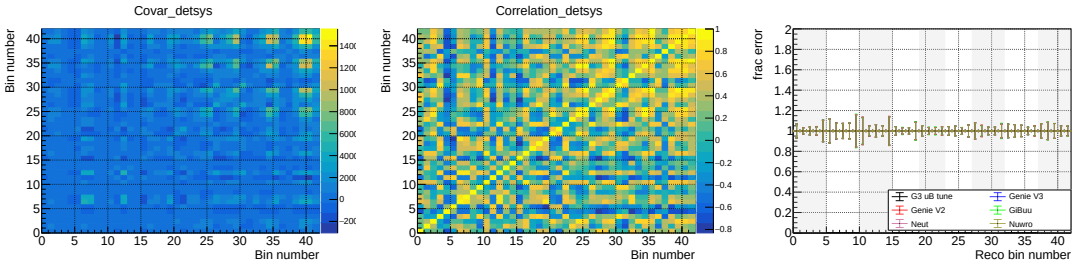

(a) covariance matrix (b) correlation matrix (c) fractional uncertainty

Figure B.1.: **Detector uncertainties**: the covariance matrix as well as the correlation matrix evaluated using the tuned GENIE model. Also shown are the fractional uncertainty differences between the models. Here the uncertainties related to the simulation of the LArTPC are shown.

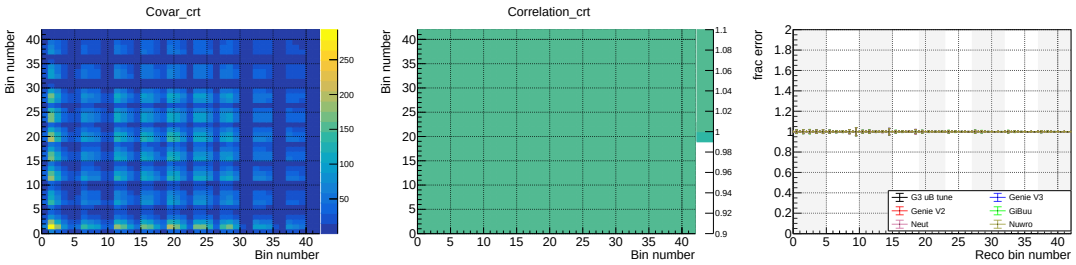

(a) covariance matrix (b) correlation matrix (c) fractional uncertainty

Figure B.2.: **CRT uncertainties**: the covariance matrix as well as the correlation matrix evaluated using the tuned GENIE model. Also shown are the fractional uncertainty differences between the models. Here the uncertainties related to the simulation of the CRT are shown.

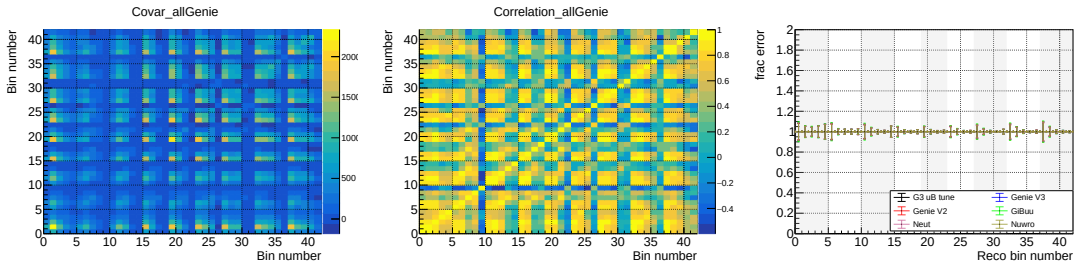

(a) covariance matrix (b) correlation matrix (c) fractional uncertainty

Figure B.3.: **Cross section uncertainties**: the covariance matrix as well as the correlation matrix evaluated using the tuned GENIE model. Also shown are the fractional uncertainty differences between the models. Here the uncertainties related to the cross section simulation is shown using 600 multi-verses with a simultaneous varied parameter set.

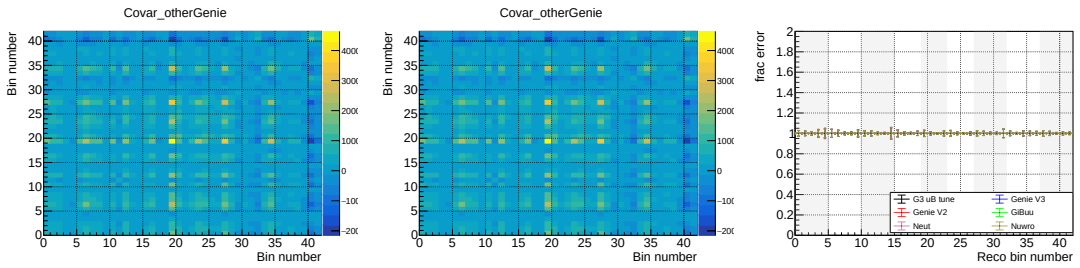

(a) covariance matrix (b) correlation matrix (c) fractional uncertainty

Figure B.4.: **Additional cross section uncertainties**: the covariance matrix as well as the correlation matrix evaluated using the tuned GENIE model. Also shown are the fractional uncertainty differences between the models. Here the uncertainties related to the cross section are shown using 2 universes variation of certain parameters.

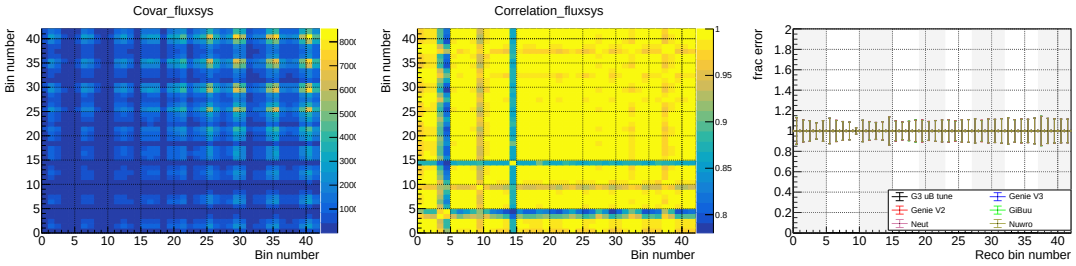

(a) covariance matrix (b) correlation matrix (c) fractional uncertainty

Figure B.5.: **Flux uncertainties**: the covariance matrix as well as the correlation matrix evaluated using the tuned GENIE model. Also shown are the fractional uncertainty differences between the models. Here the uncertainties related to the simulation of the flux are shown.

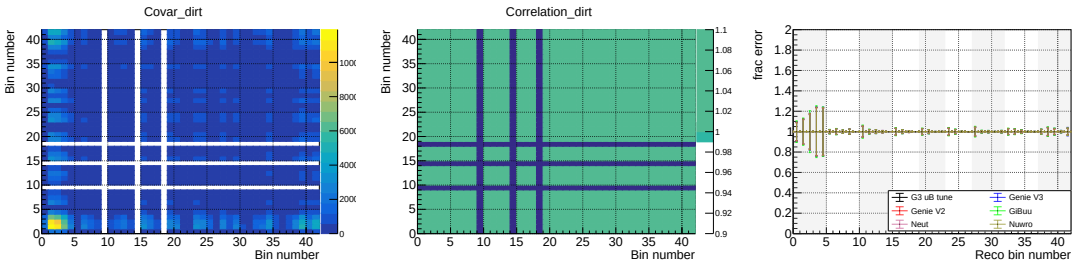

(a) covariance matrix (b) correlation matrix (c) fractional uncertainty

Figure B.6.: **Dirt uncertainties**: the covariance matrix as well as the correlation matrix evaluated using the tuned GENIE model. Also shown are the fractional uncertainty differences between the models. Here the uncertainties related to the simulation of the dirt interactions are shown.

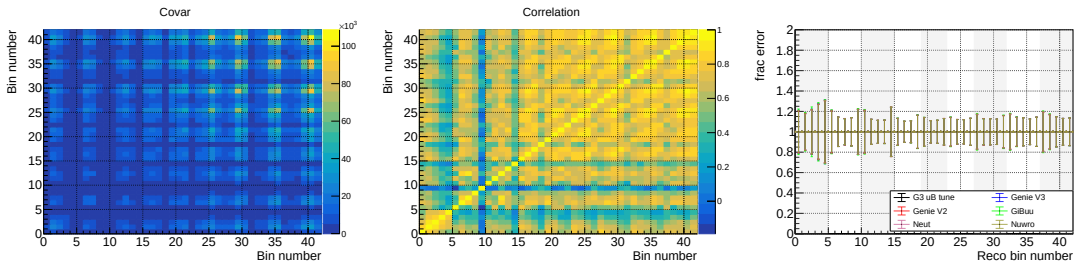

(a) covariance matrix (b) correlation matrix (c) fractional uncertainty

Figure B.7.: **Total uncertainties**: the covariance matrix as well as the correlation matrix evaluated using the tuned GENIE model. Also shown are the fractional uncertainty differences between the models. Here the total uncertainties are shown by adding the covariance matrices together.